Titan's upper atmosphere composition and temperature from Cassini-ultraviolet imaging spectrograph stellar and solar occultations

Fernando Capalbo

UNIVERSITÉ PARIS-EST

Thèse présentée pour obtenir le grade de

Docteur de l'Université Paris-Est

Spécialité: Sciences de l'Univers et Environnement

par

Fernando Javier Capalbo

Ecole Doctorale : SCIENCES, INGÉNIERIE ET ENVIRONNEMENT

Composition et température de l'haute atmosphère de Titan à partir des occultations stellaires et solaires mesurées par l'Spectrographe d'Imagerie Ultraviolet de Cassini

Thèse soutenue le 26 novembre 2013 devant le jury composé de:

Courtin Régis	*Rapporteur*
Pascal Rannou	*Rapporteur*
Emmanuel Lellouch	*Examinateur*
Antoine Jolly	*Examinateur*
Veronique Vuitton	*Examinateur*
François Raulin	*Examinateur*
Roger Yelle	*Examinateur*
Yves Bénilan	*Directeur de thèse*

Titan's upper atmosphere composition and temperature from Cassini Ultraviolet Imaging Spectrograph stellar and solar occultations

Fernando J. Capalbo
fernando.capalbo@lisa.u-pec.fr

PhD Thesis:
University Paris Est, France

Supervisor: Professor Yves Bénilan
yves.benilan@lisa.u-pec.fr

Defense Jury:

- Mr. Régis Courtin, LESIA, Observatoire de Paris-Meudon. Reporter.
- Mr. Pascal Rannou, Groupe de Spectrométrie Moléculaire et Atmosphérique, Univ. Reims. Reporter.
- Mr. Emmanuel Lellouch, LESIA, Observatoire de Paris-Meudon. Examiner.
- Mr. Antoine Jolly, Laboratoire Interuniversitaire des Systèmes Atmosphériques. Examiner.
- Mme. Veronique Vuitton, Institut de Planétologie et d'Astrophysique de Grenoble, Université Joseph Fourier. Examiner.
- Mr. Roger Yelle, University of Arizona. Examiner.
- Mr. François Raulin, Laboratoire Interuniversitaire des Systèmes Atmosphériques. President of Jury.
- Mr. Yves Bénilan, Laboratoire Interuniversitaire des Systèmes Atmosphériques. PhD supervisor.

Date of defense: November 2013.
Manuscript version: February 2014.

Foreword

The ultimate objective of the author of this work is to study nature and life. Without giving a definition of this last, controversial word, limiting the concept to that for which humans are an example will be enough for the purpose of this work. One of the motivations of this study is curiosity. However, the main motivation comes from the author's personal belief that the understanding of life in a wider context than that given by the experiences we face everyday here on Earth, for example in the context of other celestial bodies, may radically change the concepts and attitudes of many people in our society.

Of course any work is somehow related with nature and life, but a focus on a restricted subtopic is mandatory. One of these subtopics is the building blocks of what we know today as examples of life. Restricting the topic even more, the interests of this work are focused on basic organic compounds that may give rise to more complex, prebiotic molecules. In particular, the interest is focused on their identification, interrelation and their environmental conditions in the upper atmosphere of Titan. One could wonder: why Titan?, why the thermosphere and not the stratosphere or even the surface?. The answer to the first question is given in the Introduction. An ideal or logical development of motivation to perform this work would maybe imply a study of Titan's surface and atmosphere, the state of knowledge about them and then, based on its importance, relevance, need and/or personal interest a decision that a study of the upper atmosphere in the VUV domain was necessary. But the truth is that, as in many other cases concerned with any other topic, there are other reasons which are rarely stated although unavoidably present. The particular interest/focus in the thermosphere and particularly in VUV observations was influenced by practical and worldly events of the author's personal life. This changed a bit the order of things with respect to the ideal motivation development commented above (change which is normal), without diminishing the interest or the relevance of this topic; relevance which is going to be exposed mainly in the Introduction.

This final report describes the work done by the author as part of his doctorate in philosophy (PhD) course, as student and employee during 3 years at the University Paris Est. The work was developed in the Groupe de Physico-Chimie Organique Spatiale (GPCOS), at the Laboratoire Inter-Universitaire des Systèmes Atmosphériques (LISA), and combined with teaching activities in the Université Paris Est Créteil (UPEC), in Créteil, France.

The document describes the analysis of Titan's thermospheric composition and temperature, derived from the analysis of data from the Ultraviolet Imaging Spectrograph (UVIS) on board the Cassini orbiter. It comprises also laboratory measurements of absorption cross sections of the benzene molecule.

Abstract

The origin, distribution and evolution of organic molecules and life are the main subjects of a recent scientific field known as astrobiology. One interesting subtopic is the identification of organic compounds and the chemical and physical processes they are part of, in places other than Earth. One particularly interesting object from this point of view is Titan, Saturn's largest moon and the only one in the Solar System known to have a thick N_2/CH_4, planet-like atmosphere. This atmosphere is long ago known to be rich in organic compounds of high interest for astrobiology. The NASA-ESA-ASI mission Cassini-Huygens, was designed to explore the Saturnian system, with particular interest in Titan. The instruments in Cassini provided large amounts of information about the atmosphere. Data from the Ion Neutral Mass Spectrometer (INMS) and the Cassini Plasma Spectrometer showed the existence of heavy organic neutrals (with up to 7 C atoms) and ions (bigger than 13000 Da) in the thermosphere. Observations along the mission showed a complex atmospheric variability depending on many variables like solar activity or magnetospheric interactions, among others. The organic molecules in the atmosphere give rise to a complex chemistry that leads to the formation of organic aerosols in the lower stratospheric layers. These aerosols precipitate to the surface in Titan and continue their chemical evolution. This is one of the characteristics that makes Titan interesting from an astrobiological perspective.

The Ultraviolet Imaging Spectrograph (UVIS) aboard Cassini is a valuable tool that allows studying composition, species distribution and temperatures in Titan's upper atmosphere. It can detect molecules using their absorption features, in the region known as ignorosphere (500 - 950 km), between the ranges covered by the Composite InfraRed Spectrometer (CIRS) and INMS. The detection is dependent on the absorption cross section of the molecules and aerosols, which are measured in laboratory or calculated from theory. This PhD project focuses on the study of the upper atmosphere of Titan from the analysis of Cassini-UVIS data and laboratory measurements of absorption cross sections.

A characterization of the UVIS instrument and observations was necessary. Data from the Far UltraViolet (FUV) and Extreme UltraViolet (EUV) channels of UVIS were analyzed and corrected for instrument effects. From the analysis of 8 solar occultations in EUV, N_2 and CH_4 number density profiles were derived with an inversion regularization method. Temperatures were obtained from the N_2 profiles assuming an isothermal upper atmosphere. Stellar occultations in FUV were modeled and a density retrieval technique characterized. The possibility of detection for different molecules (some of them not detected by this technique before) was analyzed. Then, using a Levenberg-Marquardt minimization algorithm, column density profiles for different hydrocarbons and nitriles, and optical depth of aerosols were obtained from simulated data. The column densities and optical depth were inverted with a regularization method to obtain number density profiles for the molecules and extinction profiles for the aerosols. The procedure was finally applied to 2 stellar occultations measured by UVIS. The species studied are CH_4, C_2H_2, HCN, C_2H_4, C_4H_2, C_6H_6, HC_3N, CH_3, and aerosols. The profiles from the stellar and solar occultations were obtained for different times and locations. The temperatures derived were analyzed as a function of geographical and temporal variables—latitude,

longitude, date of observation, etc.—without a clear correlation with any of them, although a trend of decreasing temperature towards the poles could be observed. The globally averaged temperature obtained is (144 ± 2) K. Atmospheric variability was discussed on the light of these results.

Benzene (C_6H_6) is an important molecule detected in Titan's atmosphere because it is thought to be intermediate between the gas and solid particle formation. Measurements of absorption in the ultraviolet by benzene gas, at temperatures covering the range from room temperature to 215 K, were performed in different international facilities. From them, benzene absorption cross sections were derived and analyzed in terms on the transitions observed. No significant variation with measurement temperature was observed. Implications of this results for the identification of benzene in Titan's thermosphere by UVIS were discussed. The absorption cross sections were used in the derivation of C_6H_6 abundances in Titan's thermosphere commented above.

In summary the analysis of UVIS observations presented contribute to the characterization of the upper atmosphere through N_2 density profiles, thermospheric temperatures, density profiles of minor species and extinction profiles of aerosols. This observational data will help to constrain and contrast photochemical models. The abundance profiles and temperatures given for different geographical and temporal coordinates can be used to further study the atmospheric variability. As a whole, the results of this work are expected to help in the understanding of Titan's upper atmospheric composition and dynamics. This knowledge, combined with information about Titan's lower atmosphere and surface, will help to understand the evolution of organic molecules in this neighboring abiotic celestial body.

Contents

List of Figures

List of Tables

Chapter 1

Introduction

The origin, evolution and distribution of life in the universe, including Earth, are the focus of a research field known as astrobiology. This wide field of study requires an interdisciplinary approach to get a global picture and understand the interrelations of the complex processes involved. Any contribution to this field will focus on a sub-topic, studied from a particular point of view, framed by a particular discipline, but without disregarding the interrelations with the others. One of these subtopics is the 'building blocks' of what we know today as examples of life, organic molecules. It is believed that these carbon-containing molecules, taking part in increasingly complex organic chemistry, under particular conditions, can lead to matter that is alive. Organic molecules are the very basic constituents of living organisms here on Earth, where their presence and interactions can be readily studied. But a comprehensive study of the role of this molecules in the development of life cannot be limited to Earth or a present state. These molecules are distributed across the universe, under different environments, changing in different time scales, without the influence of human activity. In spite of their relevance to the origin of life, our knowledge about the distribution, interactions and the conditions this molecules are subject to in extraterrestrial environments is limited. Increasing this knowledge is the objective of this work. To help us to get a wider picture of nature and make a modest contribution to astrobiology that, together with the results from other studies and disciplines, could shed light over the processes that led to life here on Earth.

Among the organic molecules of interest for astrobiology there are those that take place in prebiotic chemistry. This is an organic chemistry (chemistry involving organic molecules) in liquid water that produces what can be called prebiotic molecules (e.g. sugar, amino acid, and nitrogenous base), sensible to form compounds of biological interests (Raulin, 2005,b). Organic molecules include volatiles like hydrogen cyanide (HCN), formaldehyde (HCHO), cyanoacetylene (HC_3N) and their oligomers. A next step in prebiotic chemistry is the formation of organic macromolecular products. These are formed systematically in laboratory simulations of atmospheric gas mixtures leading to the formation of organic products. The exact composition of these muddy compounds depends on the formation conditions. Interestingly, when hydrolyzed they are capable of letting out a wide variety of organics and oxygenated compounds, including many of biological interest, such as amino acids. On certain celestial bodies (as the case of Titan as explained below) macromolecular material created in the atmosphere can precipitate to the surface and further evolve. Therefore, prebiotic molecules and the organic compounds obtained from them are primordial to be characterized in extraterrestrial environments.

Atmospheres are an important target in the study of organic chemistry. Old theories considered the possibility that prebiotic compounds were formed in a primitive reducing Earth atmosphere, and that prebiotic chemistry took place with the precipitated compounds in the surface oceans (Miller, 1953). Although nowadays this idea has been abandoned, the early Earth atmosphere probably not being reducing enough for atmospheric organic synthesis to take place; atmospheric organic chemistry is still of interest, as it can take place in many extraterrestrial environments, mainly in atmospheres of giant planets[1]. It takes place in atmospheres in our Solar System and allows us to test theories about this type of chemistry 'in the field'. Moreover, atmospheric composition is fundamental for the adaptation of living organisms on the surface. In this context the study of any atmosphere is relevant, and particularly one rich in organic compounds. Organic compounds in atmospheres (like methane (CH_4), acetylene (C_2H_2), to mention some) and nitrogenated compounds (like molecular nitrogen (N_2), ammonia (NH_3), etc.) could lead to the formation of more complex molecules, including prebiotic ones. All this makes the identification and characterization of organic compounds in the universe, and in planetary atmospheres in particular, a very interesting topic, and the focus of this work.

[1]For a discussion about early Earth atmosphere and a comparison with Titan's see for example Selsis and Parisot (2005) and Reisse (2005).

Table 1.1: Titan characteristics. Most of the values are taken from Coustenis and Taylor (2008). Third column is expressed in Earth units.

Mass	1.346×10^{23} kg	0.0226
Equatorial radius	2575 km	0.202
Mean distance from Saturn	1,221,850 km	-
Mean distance from Sun	1.422×10^{9} km	9.55
Solar Flux	15.1 W m^2	0.01
Orbital period	15.95 Earth days	15.95
Rotaional Period	15.95 Earth days	15.95
Month duration (period around Saturn)	0.58 Earth months	0.58
Titan year (period around Sun)	29.5 Earth Years	29.5
Orbital eccentricity	0.029	1.74
Orbital inclination to Saturn's Equator	0.33°	-
Orbital inclination to Ecliptic	29.6°	1.3
Axial Tilt	0°	0
Mean surface Temperature	94 K	0.33
Surface pressure	1.5 bar	1.5
Surface gravity	1.35 m s^{-2}	0.14

One of the bodies in our Solar System is particularly relevant to the interests outlined in the previous paragraphs. Titan, Saturn's biggest satellite, is similar to some models of the early Earth and its characteristics can teach us about our home world and other celestial bodies in general. Some orbital and physical characteristics of Titan are given in Table 1.1. Titan's bulk composition is mainly water ice and rocky material (ESA, 2005). It has a rocky center and several layers of ice at different pressures, with a possible liquid layer of water and ammonia between low and high pressure ice layers (Tobie et al., 2005). In this sub-surface ocean, chemical evolution may also occur and early conditions inside Titan could have fostered the development of prebiotic chemistry and the possible emergence of life (Raulin et al., 2009). The surface is composed mainly of water ice and organics (Soderblom et al., 2009a). It is smooth, with few impact craters. It presents low height variation with the exception of some mountains of several hundred meters and several possible cryovolcanoes (Jaumann et al., 2009). Radar experiments about Titan's surface revealed signs of land-like surfaces spattered with lakes, the only large, stable bodies of surface liquid known to exist anywhere other than on Earth. The lakes are made of liquid hydrocarbons (Stofan et al., 2007), which are an interesting environment from the astrobiological point of view, due to their potential to concentrate macromolecular species. Although the surface temperature (94 K, Fulchignoni et al., 2005) is too low for prebiotic chemistry to take place in Titan's surface, the possibility of being warmed up by cometary impacts or internal heating during periods long enough to allow some kind of chemical evolution (Raulin, 2005), as well as the possible presence of sub-surface liquid water-ammonia solution, are thrilling. Additionally, Titan is the only satellite in the Solar System known to have a thick, planet-like atmosphere. Even in the absence of life, the prebiotic conditions of the Titanian environment and the associated organic chemistry are of great interest. Complex and still not fully understood chemical reactions among a whole 'zoo' of organic molecules higher in the atmosphere produce organic aerosols, that precipitate to the surface. The formation of a UV-protective aerosol layer would protect eventual organics in the surface, the possibility of this mechanism taking place in a body with more life-friendly surface conditions, like a prebiotic Earth, adds relevance to the study of these processes. The production, evolution and delivery of these 'basic blocks' for life in the atmosphere is one of the main motivations of the studies of Titan from the astrobiological point of view. Titan can be considered as a frozen planetary-scale chemical reactor, some of the processes taking place in it having maybe taken place in early Earth

(in the atmosphere or other places, like oceanic hydrothermal vents (Reisse, 2005)). Consequently, characterizing and understanding Titan, and particularly its atmosphere, might help understand the processes that can lead to prebiotic chemistry in a planet.

1.1 Titan's atmosphere

1.1.1 A short tale about an intriguing atmosphere

The interest about Titan's atmosphere can be emphasized by a quick chronological review of some discoveries, studies and experiments that contributed to the actual knowledge of it. This short review focused on the upper atmosphere (although comments on lower layers will also be made) is intended to provide an historical context, as well as a short tale of progressive discovery of this fascinating atmosphere. Many important aspects will be omitted for simplicity and the reader is referred to the existing bibliography for further information. For example, Coustenis et al. (2009b), on which this section is largely based.

José Comas Solà claimed in 1908 to have observed limb darkening on Titan, and therefore an atmosphere. A few decades later James Jeans concluded, from his analysis of escape processes in atmospheres, that heavy gases could have been retained by Titan after its formation if temperatures between 60 - 100 K prevailed (Jeans, 1931). These gases could be, among others, ammonia, argon (Ar), neon (Ne), molecular nitrogen and methane. The presence of the atmosphere was confirmed by Gerald Kuiper in 1944, who actually detected methane in it (Kuiper, 1944). The detection of methane implied a chemically evolved atmosphere, as methane requires carbon (C) and hydrogen (H), and the latter should have escaped from Titan long ago. The presence of the atmosphere was soon recognized as a unique characteristic of Titan among the other satellites.

New information about Titan atmosphere had to wait till the 1970s, when the main components of the atmosphere started to be elucidated. Trafton announced the detection of molecular hydrogen through infrared spectroscopic studies (Trafton, 1972b), implying the presence of a molecular hydrogen (H_2) escape inhibiting gas. At the same time, Trafton (1972a) determined a higher absorption than Kuiper in one of the IR bands of methane, meaning a higher abundance of CH_4 or, again, the presence of another undetected but abundant gas which would broaden CH_4 bands via collisions. Hunten (1973b,a) considered N_2 or CH_4 as the main constituent of the atmosphere, but the low abundances of methane and high effective pressure estimates in Titan derived shortly afterwards (Lutz et al., 1976) constrained methane to a minor component. Moreover, the absence of substantial quantities of NH_3 led to the assumption that it could have been dissociated into N_2 and H_2, supporting the idea of N_2 as the main component of the atmosphere. Contemporaneously, low albedo (Danielson et al., 1973) and polarization measurements of reflected radiation measured for Titan implied the presence of a visible-ultraviolet (VIS-UV) absorbing haze, which turned to be distributed around Titan (Veverka, 1973). Hypotheses on the composition of the haze pointed to complex organics. This ideas were supported by experiments and identification via observations in the thermal range of not only CH_4 but also ethane (C_2H_6), ethylene (C_2H_4), and C_2H_2 (Gillett et al., 1973; Gillett, 1975). Thus the picture of condensed CH_4 and a 'fog' of polymers formed from the fragments of methane UV photolysis took form. The properties of this haze not being well known, any attempt of interpretation of spectroscopic observations was (and still is) dependent on the assumptions about the haze particles. The '70s first models of Titan's atmosphere concentrated on CH_4 and hydrocarbons as main components (e.g. Strobel, 1974). On the other hand, models about the formation of Titan including a N_2 atmosphere (Lewis, 1971) and a high surface temperature derived from observations (Conklin et al., 1977), led Hunten and Morrison (1978) to propose a model in which dissociation of NH_3 would lead to N_2, with surface pressures of

tenths of bars. Subsequently, it was Strobel in 1982 who first modeled Titan's atmospheric chemistry with N_2 as the main species. At the end of the '70s then, a few measurements and a lot of hypothesis set the temperature and pressure spanning a few order of magnitudes around actual values. The terrain was set, but new measurements were desperately needed.

The Voyager 1 flyby in 1980 shocked with an unpleasant surprise: the satellite was completely shrouded by the thick (optical depth 5) atmosphere. Nevertheless, the observations helped in finding some answers to the many questions about Titan's atmosphere. Voyager images showed an hemispheric asymmetry, explained at that time in terms of variations in haze density, particle size and composition, as well as seasonal effects (Smith et al., 1982). A haze layer detached from the main haze was observed at about 300 km, although the properties of the haze were minimally constrained, and no model could reconcile the different measured properties of the haze. Analyses of the Voyager/Radio Science System (RSS) and Voyager/Infrared Interferometer Spectrometer (IRIS) data in the '80s (e.g. Samuelson et al., 1981; Lindal et al., 1983; Lellouch et al., 1989) allowed to derive a satellite radius, surface pressure and temperature in close agreement with actual values. Combining different constraints from the experiments in Voyager, N_2 was confirmed as the main constituent of the atmosphere. As they provide a method to directly probe N_2 densities in the upper atmosphere, solar occultation measurements performed with the Voyager/UltraViolet Spectrometer (UVS) instrument played an important role in this determination (see e.g. Smith et al., 1982). Results from UVS also provided a value of thermospheric temperature of 186 K at 1265 km and a CH_4 abundance of 8% at 1125 km. CH_4 and other minor hydrocarbons were also confirmed from Voyager infrared data (e.g. Coustenis et al., 1989a). The confirmation of the presence of complex organics motivated the generation of lab experiments and of 1-D photochemical models. These models were also the basis of the knowledge of the thermal structure of the middle and upper atmosphere, much less characterized than the lower atmosphere. These new models (Strobel, 1982; Yung et al., 1984) were based on chemical reactions in a N_2-CH_4 atmosphere, vertical transport modeled with an eddy diffusion coefficient profile. The main reactions were established and the results were the irreversible destruction of N_2 and CH_4 (the latter should have been completely destroyed by photolysis in some 10^6 years time), the production of many hydrocarbons and nitriles and H_2, the latter escaping to space. The possible inventory of the chemical constituents kept growing, and the ideas of molecular complexity leading to solid phase products gain support, as more molecules and aerosols with properties similar to those of Titan were detected in new laboratory experiments, trying to reproduce the conditions in Titan's atmosphere (Raulin et al., 1982; Khare et al., 1984, 1986; Mckay et al., 1989). One decade after the flyby, the molecules detected from Voyager data seemed to fall short compared to the variety of organics and derived macromolecules obtained in experiments and models, but this would not last for long.

By the end of the 20th century a more comprehensive picture and interpretation of the atmosphere emerged, supported by new observations. The complex hydrocarbons predicted in models, observed in laboratories or unexpected from these two sources started to be detected in the satellite. In addition to the analysis of IRIS data (Coustenis et al., 1989a,b) the detections were achieved using ground or Earth orbit observations, thanks to the development of high resolution capability instrumentation in the last 20 years of the 20th century, especially in the thermal infrared and mm/sub-mm ranges (and therefore limited to the lower atmospheric layers in Titan). This made it possible to obtain more precise abundance and temperature profiles, to detect new molecules and to probe the atmosphere at lower levels than Voyager. Examples of this detections are those of water (H_2O) and benzene (C_6H_6) (Coustenis et al., 1989a, 2003) from ISO observations. Nevertheless the Voyager 1 observations continued to be exploited for more than 2 decades after the flyby. From the analysis of IRIS data recorded over the north (winter) pole, Coustenis et al. (1991) showed an abundance of hydrocarbons increasing with altitude, consistent with species forming in the upper atmosphere and sinking in the

lower stratosphere. Still from IRIS data, an enhance towards northern (winter) latitudes of most of the minor hydrocarbons was observed (Coustenis and Bézard, 1995). The new molecules detected motivated updates to the 1-D photochemical models in the '90s (e.g. Toublanc et al., 1995; Lara et al., 1996) and the observed latitudinal variations and associated temperature differences originated different explanations (Flasar and Conrath, 1990; Bézard et al., 1995). General circulation models (Hourdin et al., 1995) attacked these topics and provided a picture of summer pole to winter pole circulation above the stratosphere and opposite below it. During equinoxes this circulation would break into two circulation cells with upwelling at the equator. At the same time new efforts in the study of the haze lead to reconcile its properties measured by Voyager some 15 years before. This was achieved thanks to models that treated the aerosols as conglomerates of small (hundredths of μm) spherical particles (West and Smith, 1991; Rannou et al., 1995). As for the upper atmosphere, temperature profiles up to some 500 km altitude derived from a stellar occultation measured from the ground in 1998 (Sicardy et al., 1999) showed local structure with two inversion layers at 425 and 450 km. The observed structure motivated an interpretation based on waves braking in the upper stratosphere. Thus, when the 21st century started, thanks to Voyager and ground based measurements, main composition, trace gases, pressure and temperature were constrained, although with a large span of values. But topics as the origin of N_2 and methane remained open, and a vertical profile of CH_4 uncertain. Whereas the first close taste of the satellite had provided constrains and confirmations for some of the old theories, the complex picture associated with Titan required more observations to understand it.

In the first years of the 2000s Titan was experiencing its northern winter solstice, two thirds of a Titan year had passed from the Voyager 1 encounter and seasonal changes could be better studied, giving rise to new interpretations. Ground and Earth orbit measurements had been performed at different moments since the northern spring around 1980, when Voyager flew by the satellite. The latitudinal asymmetry observed by Voyager reversed during this period (Caldwell et al., 1992; Coustenis et al., 2001). The circulation in the atmosphere was interpreted to be coupled with the distribution of haze and minor constituents (Rannou et al., 2002; Lebonnois et al., 2003), and better explained by a global circulation model coupled with a haze microphysical model (Rannou et al., 2004). More photochemical models contributed to the knowledge about the haze (Wilson et al., 2003; Wilson and Atreya, 2003), explaining Titan's haze as the result of coupled hydrocarbon-nitrile polymers and Polycyclic Aromatic Hydrocarbons (PAH). This fact assigned particular importance to benzene as link between the gas and the haze. But the pathways to haze formation were still missing. The models kept updating with new constraints, like the new profiles for N_2 and other hydrocarbons provided by Vervack et al. (2004) from a reanalysis of Voyager 1/UVS data, measured more than 20 years before. They derived thermospheric temperatures of $\sim$ 155 K, more in agreement with current values than the 186 K from Smith et al. (1982). Notwithstanding the better knowledge of the thermal structure, the experiments simulating Titan's atmosphere (e.g. Coll and Raulin, 1998; Coll et al., 1999; Ramírez et al., 2001; Ramirez and Navarro Gonzalez, 2002; Imanaka et al., 2004) kept surprising due to the high order hydrocarbons and nitriles obtained, compared to the inventory detected in Titan. What is the degree of complexity achieved by the chemistry on Titan? What parameters dictate the circulation of the atmosphere? How variable is it? What is the origin of Titan's methane? What is the nature of the surface, its composition and topography? These questions were still opened before the Cassini/Huygens mission, which would provide new answers, and questions.

The thirst for a new close look of Titan had to wait till the arrival to the Saturnian system of Cassini/Huygens in the end of 2004. Measurements from the Cassini orbiter and the Huygens probe to Titan have been analyzed since then, with new information becoming available after each Titan flyby, which continue in the present days (September 2013). These analyses contributed to solve some of the questions about Titan as well as to expand in location and time the measurements of the atmosphere.

Long after N_2 was postulated as main atmosphere constituent, Cassini measurements support the idea that N_2 was not primordial, but probably produced from photolyzed NH_3. The Composite Infrared Spectrometer (CIRS) instrument on Cassini, with improved spectral resolution with respect to IRIS on Voyager, incremented our knowledge of the composition and temperature structure in the stratosphere. The trends observed in the stratosphere from Voyager data, with abundance of some hydrocarbons increasing with height and with an enrichment towards the north (winter) pole, were confirmed and the studies extended (see for example Vinatier et al., 2007, 2010). Neutral and ionic composition and temperature in the thermosphere above some 900 km were measured with unprecedented spatial resolution and frequency by the Ion and Neutral Mass Spectrometer (INMS). The Ultraviolet Imaging Spectrograph (UVIS) experiment complemented the mentioned instruments in altitude coverage, providing composition and temperature measurements of the thermosphere (Shemansky et al., 2005; Koskinen et al., 2011; Capalbo et al., 2013), although published results derived from UVIS are fewer than those derived from CIRS and INMS. But new puzzling measurements arrived also with Cassini. Since 2005 INMS and the Cassini Plasma Spectrometer (CAPS) measured heavy organic neutrals (with up to 7 C atoms, including C_6H_6, e.g. Magee et al., 2009) and ions (of more than 13000 Da, e.g. Coates et al., 2009) in the atmosphere, above 900 km. This led to a re-formulation of thermospheric chemistry and photochemical models, which started to include ion chemistry (Vuitton et al., 2007, 2008) and to re-analyze the paths to macromolecule formation (Lavvas et al., 2008a,b). Models before Cassini included hydrocarbons and nitriles, a few included thermosphere minor neutral. After Cassini, new species and reactions were included, particularly in the thermosphere. Observations along the Cassini mission showed interesting temporal and geographical/horizontal variability in the upper atmosphere. The dependence of this variability on parameters like solar activity or magnetospheric interactions is still under study. Müller-Wodarg et al. (2008) suggest that Titan's thermosphere is highly variable and dominated by strong dynamics, which are accompanied by an oblate shape of the atmosphere at those thermospheric heights. This picture diverges considerably from the global structure predicted in the pre-Cassini era by general circulation models which considered solar heating alone (like Muller-Wodarg et al., 2000). Magnetospheric influence on thermospheric temperatures was also suggested (Westlake et al., 2011). The efforts to reconcile the measurements and understand the atmosphere continue till the present day, with new information arriving from Cassini and lab experiments, and new interpretation and models that let us layout a picture of the atmosphere in general, and the thermosphere particularly.

1.1.2 General description - state of knowledge

Composition

From all the experimental evidence and studies developed in the last century we can have a good idea about Titan's atmosphere. In what follows, this text will focus on composition, temperature structure and variability of the upper atmosphere (above ∼500 km), referring to lower layers when suitable to underline a possible connection or explanation. The surface gravity of about 0.14 g makes Titan's atmosphere much more extended than in the case of Earth, with an exobase around 1500 km (e.g. Westlake et al., 2011). It is composed mainly of N_2, the main trace gas being CH_4, followed by H_2. Dissociation and ionization of N_2 and CH_4 in the upper atmosphere by UV radiation from the Sun and precipitating electrons, following by recombination of the products, give rise to different hydrocarbons (which in turn can give rise to polycyclic aromatic hydrocarbons) and nitriles (including the prebiotic HCN). Oxygenated species like H_2O and carbon monoxide (CO) are also present, though less abundant than the species previously mentioned. Just as an example of the complexity of the composition, a table comparing some measurements and models from the bibliography is shown in

Figure 1.1.

Species	Lebonnais	Wilson and Atreya	INMSTa	INMSW07	INMSglob–Cui-unc	INMSglob–Cui-corr	INMSglob-Magee	UVISTb	Vuitton
CH_4	7.100%	9.400%	2.19 ± 0.0002%	1.550%	2.20 ± 0.01%	2.20 ± 0.01%	2.45 ± .366%	5.700%	
H_2	0.270%	0.220%	0.410 ± 0.005%	0.400%	0.390 ± 0.01%	0.390 ± 0.01%	0.409 ± .034%		
C_2H_2	0.039%	0.063%	0.019 ± 0.005%	0.025%	0.012 ± 0.01%[b]	0.0310% ± 0.01%[b]	0.0378–.0571%	0.340%	
C_2H_4	0.080%	0.110%	0.053 ± 0.008%	0.072%	[b]	[b]	0.007–0.065%	0.430%	
C_3H_4[a]	11 ppm	18 ppm	3.9 ± 0.22 ppm	11 ppm	6.3 ppm	140 ± 90 ppm	10.7–13.0 ppm		
HCN		900 ppm					192–561 ppm	5520 ppm	200 ppm
^{40}Ar			7.1 ± 0.1 ppm		11.0 ± 0.3 ppm	11.0 ± 0.3 ppm	15.2–16.1 ppm		
C_2H_6	37 ppm	197 ppm	121 ± 6 ppm	20 ppm	27 ± 1.9 ppm	73 ± 26 ppm	44–102 ppm	4480 ppm	
HC_3N		2 ppm[d]			<0.8 ppm	32 ± 7 ppm	1.32–2.02 ppm		40 ppm
C_6H_6		0.1 ppm[d]		3.3 ppm	0.9 ± 0.04 ppm		3.22–3.34 ppm		3 ppm
C_4H_2		3 ppm[d]		5.1 ppm	2.5 ± 0.1 ppm	6.4 ± 2.7 ppm	6.09–7.37 ppm	740 ppm	10 ppm
C_6H_2		0.03 ppm[d]							0.8 ppm
C_7H_4									0.3 ppm
C_7H_8					<0.13 ppm		0.006–0.08 ppm		0.2 ppm
C_8H_2		5E-4 ppm[d]							0.2 ppm
C_2N_2				3.3 ppm	1.5 ± 0.09 ppm	48 ± 8 ppm	1.72–2.83 ppm		
CH_3CN		0.9 ppm[d]			<1.48 ppm	31 ± 7 ppm[c]			3 ppm
C_2H_3CN		1 ppm[d]			<0.57 ppm	<18 ppm	0.24–0.61 ppm		10 ppm
C_2H_5CN							0.218–0.46 ppm		0.5 ppm
C_4H_3N									4 ppm
HC_5N									1 ppm
C_5H_5N									0.4 ppm
C_6H_3N									0.3 ppm
C_6H_7N									0.1 ppm
NH_3		0.04 ppm[d]			29.9 ± 7.8 ppm				6.7 ppm
CH_2NH									10 ppm

Lebonnois et al. (2001) model – 1180 km.
Wilson and Atreya (2004) model – 1180 km.
INMSglob-Magee – global average 1000–1100 km. min and max values (Magee et al., 2009).
INMS Ta (Waite et al., 2005) – 1176 km.
INMSW07 (Waite et al. 2007; z=960 km, 71° lat; just one example).
UVIS Tb (Shemansky et al., 2005); reported relative to CH_4; converted here with n_{tot}=5.8E9 cm^{-3}; 1006 km.
INMSglob – Cui –unc: uncorrected global average 1077 km (Cui et al., 2009a)
INMSglob–Cui-cor: corrected values 1077 km (Cui et al., 2009a).
Vuitton (Vuitton et al., 2006, 2007) ionospheric model; just deduced values – 1100km
[a] C_3H_4 (CH_3C_2H and $CH_2C_2H_2$).
[b] Combined C_2H_2 and C_2H_4.
[c] altitude of 1025 km.
[d] altitude of 1000 km.

Figure 1.1: Titan's upper atmosphere composition from different measurements and models. From Soderblom et al. (2009b). Header of second column should read Lebonnois.

As a general rule for the trace gases, the higher the complexity of a molecule the less its abundance in the atmosphere. The vertical abundance profiles of the different species are affected by molecular diffusion in the upper atmosphere and by eddy mixing in lower layers, the borderline of these effects being the homopause. The homopause has been placed somewhere between 850 and 1100 km (Yelle et al., 2008; Cui et al., 2009; Vervack et al., 2004). N_2, as the main component, can be considered in hydrostatic equilibrium, the abundance of other minor species are subject to source/sinks and transport phenomena. Sinks and sources greatly affect the vertical profiles of chemically active species. Those with a short chemical lifetime have its presence determined by chemical processes, those with a long chemical lifetime, are distributed according to transport and dynamical processes. Photochemical models predict that the molecular vertical mixing ratio profiles increase with height in the stratosphere, as the molecules are formed in the upper atmosphere, diffuse downwards and generally condense in the lower stratosphere. The abundance then decreases with altitude in the thermosphere above the production region. Models that are one dimensional should be representative of what is observed at mid latitudes. Mixing ratios of some species have been observed to increase with altitude in the stratosphere for southern (summer) and mid latitudes (see for example Vinatier et al., 2007, 2010), supporting the described behavior, although this is not the same for all latitudes as will be commented below. In the lower thermosphere number density profiles from UVIS (Koskinen et al., 2011) show maxima near the predicted production region for some species, and Shemansky et al. (2005) showed a depletion in the upper thermosphere for the same species. However the abundance profiles are not always monotonically increasing/decreasing with altitude below/above this 'creation layer', other interesting phenomena are observed. Shemansky et al. (2005) show two changes in the scale height of

the species (at about 700 and 1000 km), and the number density profiles from Koskinen et al. (2011) present a wavy behavior. Although they are not going to be treated in this essay, ions are another important component of Titan's upper atmosphere (see e.g. Vuitton et al., 2009). Although limited to only one dimension, the characterization of the vertical distributions of atmospheric constituents is of fundamental importance to add to the global picture of the atmosphere. The main characteristics of the gaseous phase of the neutral upper atmosphere is somehow established, but the measurements and models of composition available today present some inconsistencies when contrasted with each other (see discrepancies in the following sections). Moreover, the consequences of such composition and its fluctuations around the average observed is still under study.

Aerosols

According to models, hydrocarbons and nitriles will form polyacetylene polymers, nitrile polymers, PAH polymers as well as aliphatic and aromatic copolymers (see for example Wilson and Atreya, 2003; Lavvas et al., 2008b). These polymers could agglomerate and form organic haze particles or aerosols. The implications of this haze are manifold. It plays an important role in the atmospheric radiative balance, affecting the temperature structure; it also affects the radiative transfer and thus influences photolysis. The aerosol surface could also host heterogeneous processes (Lavvas et al., 2011). The astrobiological importance of this haze has been recognized since its detection some 40 years ago. The haze can precipitate onto the surface (and lakes) and undergo further chemical evolution according to surface conditions. Moreover, its UV protective nature can shield the surface from harmful radiation. The path to haze formation appears to take place all across the atmosphere, from seed particles to coagulation and then aggregation, to end up in a haze layer (see Lavvas et al. (2011) and Figure 1.2). What is the composition of Titan's aerosols?, how are they formed? The efforts to answer these key

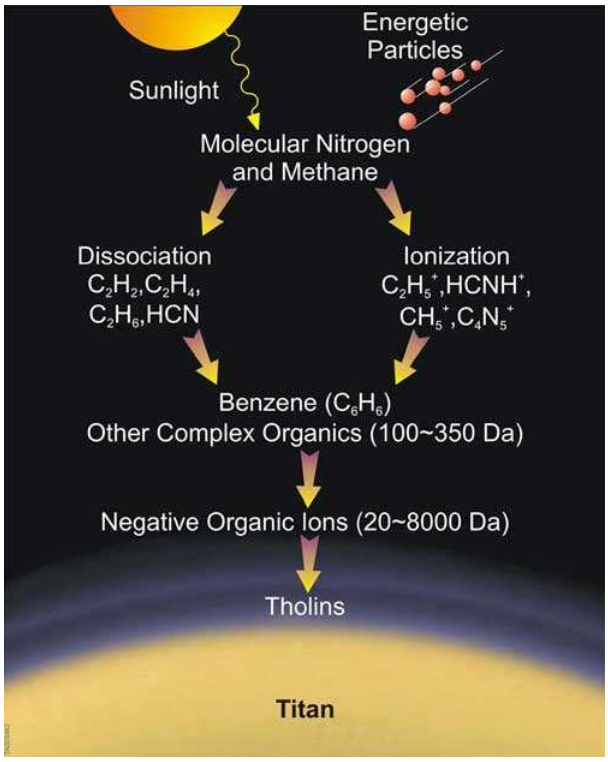

Figure 1.2: Complexification of Titan composition, from gas to aerosols (from Waite et al., 2007)

questions about Titan's atmosphere include laboratory experiments trying to reproduce the conditions in Titan's atmosphere (Raulin et al., 1982; Khare et al., 1984, 1986; Mckay et al., 1989). They pro-

vided evidence that the complex organics formed out of the gas mixture can lead to solid compounds called 'tholins', with similar optical properties to those observed in Titan's haze. However, it should be noted that the haze production mechanisms and resulting haze optical properties depend largely on the pressure, temperature and initial mixture (CH_4/N_2) of the experiment. This might imply that in different altitudes of the atmosphere the haze formation processes vary, leading to other key question: what are the aerosol distributions in time and space on Titan? Aerosols have been observed at altitudes as high as 1000 km (Liang et al., 2007) and down to the surface. Moreover, particles detected with mass >> 13000 Da at some 950 km and above (Coates et al., 2009) are likely aerosol precursors. But although their presence is unquestionable, their characteristics are elusive. Aerosol size and shape are important for their microphysics, but size depends on ion charge and a range of values are possible. High polarization and high forward scattering measured from Voyager and Pioneer lead to postulate that the particles were non spherical (West et al., 1983). The high polarization suggested loose aggregates, with small monomers of about 50 nm. The high forward scattering suggested a large area (equivalent sphere of 2 μm radius) with about 3000 monomers per each (Tomasko et al., 2008). FUV stellar occultations provide little constraints for the aerosols characteristics (Koskinen et al., 2011). Nevertheless they can provide extinction vertical profiles in the lower thermosphere (600 - 800 km) and help characterize the aerosols' horizontal/temporal distribution combining occultations measured for different geographical locations at different times. Either because of their astrobiological implications or their influence in Titan's atmosphere thermal structure and dynamics, aerosols are a primary component of the atmosphere which can not be left aside in the efforts to understand it.

Vertical structure

The composition and vertical distribution of the gases and aerosols largely determine the vertical structure of Titan's atmosphere. Heating and cooling from gases and haze balance in different ways at different altitudes and, although derived vertical profiles vary from model to model and from model to measurements, a rough temperature profile can be described. From 94 K at the surface, the temperature decreases with height in the troposphere, getting as low as about 70 K at a tropopause at approximately 50 km. The temperature increases in the stratosphere, avoiding N_2 to condensate, and reaches values of about 180 K at the stratopause, located around 300 km. The existence of a mesosphere is not clear, although the presence of a temperature inversion at about 500 km due to the detached haze layer centered at around 550 km has been observed. Above this tentative mesopause the temperature increases with height in the thermosphere, until the profile becomes mainly isothermal with temperatures measured around 150 - 170 K. In this text the author will loosely refer to the lower thermosphere for altitudes roughly between 600 and 900 km and to the upper thermosphere meaning altitudes ranging from 900 to 1400 km. The Huygens Atmospheric Structure Instrument (HASI) experiment aboard the Huygens probe provided a one time/one location temperature profile from the surface up to 1400 km. Another unique measurement came from UVS on Voyager, from a solar occultation (Vervack et al., 2004). From UVIS occultations Shemansky et al. (2005) derived a temperature profile for the thermosphere. The main, regular, upper atmosphere temperature determinations come from INMS measurements.

The thermosphere is particularly important in the global picture of Titan's atmosphere. Based on what has been exposed above, it can be thought of as a chemical factory that forms complex and heavy positive and negative ions and molecules (e.g. aromatic and nitrile species) in its upper layers, as a consequence of interaction with EUV radiation, energetic ions and electrons. This is the region where photolysis of N_2 and CH_4 occurs. The molecules and ions formed are thought to start the haze

formation processes, with aerosols detected as high as 1000 km (Liang et al., 2007). These particles fall through the upper layers and grow, and eventually become ubiquitous throughout the stratosphere, playing a fundamental role in heating Titan's stratosphere and perhaps the thermosphere (Lavvas et al., 2009). UVIS solar occultations can provide an independent and reliable measurement of temperature in the upper atmosphere through the measurements of N_2 profiles. Measured at different locations/times they are a valuable addition to the study of the thermal structure and its variability. This will be one of the main results of the present manuscript. All things considered, the average composition and temperature structure of the upper atmosphere of Titan is well characterized. At the same time, it presents a variability far from being completely interpreted.

Variability

Titan's upper atmosphere presents a marked variability. Added to the variations observed before the arrival of Cassini to the Saturnian system, commented previously, the analyses of INMS data show that the abundances and temperatures can vary from flyby to flyby (see for example Cui et al., 2009; Magee et al., 2009). The models also predict variability in the atmosphere based on different factors, like solar zenith angle (De La Haye et al., 2008). For the purpose of analysis, one could try to classify the abundance and/or temperature variability in horizontal and temporal, according to the factors that might cause it, keeping in mind that the observed behavior can be the result of an inseparable combination of all of them and a correlation with any of these parameters might be absent. Moreover, the possibility of a bias in a reduced data set should be kept in mind.

The horizontal variability can be divided in latitudinal and longitudinal. There are several manifestations of variations as a function of latitude. One of the manifestations is in composition. Vinatier et al. (2010) showed an enrichment of many hydrocarbons and nitrile species at low stratospheric altitude near the north (winter) pole. They also showed that the vertical profile of some species changes for northern latitudes and the general increase with altitude observed for equatorial or southern latitudes is not maintained. For the higher layers, INMS measurements of the thermosphere, above 1100 km, show a density increase towards the equator for some of the heavy hydrocarbons (Müller-Wodarg et al., 2008). This is reflected in the oblateness of the atmosphere obtained in the empirical model in the cited work and commented before. The latitudinal variations manifest also in temperature. Titan has a difference in temperature between the hemispheres at the stratospheric level. According to CIRS measurements, the stratosphere is colder in the winter pole, the stratopause being higher and warmer in this pole. In the thermosphere, some INMS measurements and models based on them also showed a decreasing temperature towards the winter pole (Cui et al., 2009; Müller-Wodarg et al., 2008). However, Snowden et al. (2013) find no correlation between temperatures measured in the upper atmosphere and latitude in their analysis of INMS data. Thanks to general circulation models we know now that Titan presents a meridional circulation: at solstice, there is air flow and transport from summer pole to winter pole in the stratosphere and above and winter pole to summer pole below. During equinoxes the circulation breaks into two, with upwelling in the equator and downwelling in the poles, and there is a symmetry between north and south hemispheres. This ought to change over the course of Titan's year (30 terrestrial years). The latitudinal transport also allows haze particles to remain in the atmosphere for a longer time until they are deposited in the polar regions. The transport and accumulation of the haze (and hydrocarbons in a less important way) towards the winter hemisphere increases cooling there and powers the transport effect. This circulation takes part mainly in the stratosphere and mesosphere, the thermosphere being less affected by it. At the same time, recent seasonal changes in the altitude of the detached haze provide a strong argument for circulation-induced modification of the haze (Teanby et al., 2012). An origin in a transition from

monomer to fractal haze particles, combined with higher-altitude haze production and subsequent modification by high-altitude dynamical circulation, is required to provide a complete explanation. Their measurements show that the radiative effects of this complex chemistry are sufficient to drive dynamics up to very high altitudes, effectively linking chemical and dynamical processes well into the thermosphere (above 500 km), providing another motivation to study temperature in the upper atmosphere and its contribution to aerosol formation. Again, a variability analysis of composition and temperature in the low/mid thermosphere is lacking. UVIS measurements can provide valuable information in this topic, to be added to the existing datasets. In sum, while the latitudinal variability in Titan's stratosphere is a combined effect of the dynamics of the atmosphere and the chemistry, the behavior of the thermosphere with latitude is still elusive.

The longitudinal variability is considered in this work as the variation in composition and temperature with Titan longitude. As Titan is tidaly locked to Saturn the same side of Titan faces Saturn at all times during its orbit, making longitude on Titan correspond directly to a region of interaction with the Saturn plasma environment (Saturn, anti Saturn, ram, or wake). Therefore any longitudinal variation would be related to magnetospheric interactions. Cui et al. (2009) divided the data from INMS into longitude bins and found that the Saturn side of Titan was warmer than the anti-Saturn side and the magnetospheric ram side was warmer than the wake side. However, the small number of samples available for the study made it impossible to determine a general latitude trend. The sparsity of longitude sampling also kept Müller-Wodarg et al. (2008) from deriving conclusions on the variability with these coordinates. No trends with longitude was observed in the analysis by Snowden et al. (2013). In short a variation of the thermosphere with longitude has not been observed.

Titan's atmosphere presents also a temporal variability. For the purpose of analysis it can be divided into seasonal, solar cycle, diurnal and secular effects. The $\sim 27^{\circ}$ tilt provide Titan seasonal effects. One Titan year equals some 30 Earth years and therefore more than one year passed from the Voyager 1 flyby till the present day (September 2013). Evidence of the seasonal effects started to be evident with a clear north/south albedo switch in 1980-1990 (Caldwell et al., 1992). The darker hemisphere in the blue spectral region being the one with more absorbing haze. As already commented, hemispheric differences in the stratosphere are consistent with a higher concentration of gases and haze in the winter pole (Bézard et al., 1995; Lebonnois et al., 2003; Rannou et al., 2002), accompanied by an increase in cooling in this region. The changes observed are explained by the change in circulation in the lower atmosphere commented above. The thermosphere reacts faster than the lower layers, washing out seasonal effects, hindering their study. Apart from the mentioned Titan's tilt, Saturn's orbital eccentricity and associated 20% variation of solar radiation received at different points in the orbit affects the seasonal variations, mainly in the troposphere and stratosphere. The different distance to the Sun (9.03 to 10.04 AU between perihelium and aphelium) produces an hemispheric asymmetry for the same season. The southern summer has more solar input and is therefore hotter but shorter (at perihelion). Finally, it is worth mentioning that seasons don't repeat perfectly, as there is interanual variability due to the solar cycle phase shift with respect to the seasons (Lockwood and Thompson, 2009).

Like other atmospheres, Titan's is also influenced by the solar cycle. Since the ultraviolet input is the main driver of Titan's photochemical gas and haze production, variations in UV and EUV solar radiation due to the solar cycle may produce a change in the thermosphere, with an 11-year periodicity. Long periods of observation are required to decorrelate such effects, and the relationship of Saturn magnetosphere with the solar cycle has to be considered too. The Voyager 1 flyby and most of the Cassini mission, which are the main sources of information we have on the thermosphere, occurred during solar maximum an minimum conditions, respectively. Although valuable as the only measurement of this kind for that period, the data from Voyager 1 flyby is understandably limited for

an analysis of variability. Finally, as the solar influence over Titan's upper atmosphere has been at its relative weakest during most of the Cassini observations, no variability caused by variations in solar activity is expected for this more recent and extended data set.

Diurnal variability is defined by day/night differences. During 1 Titan day (16 Earth days) the atmosphere is exposed to different illumination conditions. De La Haye et al. (2008) presented a one-dimensional rotating model, at constant latitude and varying local-time, to take into account the diurnal variation effects, such as the ceasing of the solar flux induced mechanisms on the night side. The model showed large variations in the processes prevalent on the day compared to the night side. Surprisingly, the thermosphere day side is observed to be cooler than the night side in De La Haye et al. (2007) and Cui et al. (2009). Westlake et al. (2011) found that the higher the Solar Zenith Angle of the observation the higher the temperature they get from a particular flyby. This is contradictory to what would be expected for a solar driven atmosphere. Diurnal variations are therefore present although, counterintuitively, not driven by solar input.

Apart of the diurnal cycle, other consequence of the rotation of Titan around Saturn is the interaction with different environments of its magnetosphere and with the solar wind. Based on an analysis of INMS data from 32 flybys, Westlake et al. (2011) suggested a correlation of the thermospheric temperature with the position of Titan in Saturn's magnetosphere. They found that measurements performed in the plasma sheet lead to hotter temperatures than those in the plasma lobe, suggesting that magnetospheric particle precipitation causes the temperature variations observed. On the other hand, Snowden et al. (2013) found no correlation between the temperature of Titan's thermosphere and ionospheric signatures of enhanced particle precipitation, suggesting that the correlation is not indicative of a physical connection. As the importance of the energy deposition rate of EUV photons becomes less important than that of ions/electrons above some 1350 km, a different behavior of the temperature structure in different regions of the thermosphere could be a possibility. New measurements at the relevant altitudes and results from models including the effects of magnetospheric particles might shade some light to this controversial type of variability.

As a natural element, Titan's atmosphere is subject to variations that do not fit in any of the classifications made here, and that could be misinterpreted as one of them. Secular variation, long-term non-periodic variations, are possibly present but obviously impossible to characterize. Lockwood and Thompson (2009) report on 34 years of visible wavelength photometry of Titan, the most recent 4 years of observations, overlapping in seasonal phase with the first 4 years of the observation period. They find that Titan's brightness varied from one Titan year to the next at the same seasonal phase, in this case largely due to the high stratospheric hazes. Moreover, upward waves can produce localized compositional and temperature changes. Waves have been observed in titan's mesosphere and thermosphere (Fulchignoni et al., 2005; Müller-Wodarg et al., 2006), although the problem of wave forcing is currently under-constrained by observations. In any case, irregular phenomena are not to be discarded as explanation of some of the observed variations, especially when the data set analyzed is sparse.

The exposed general picture of Titan's atmosphere, particularly its thermosphere, accounts for a complex system, at some 1500 million kilometers away from Earth, with a complex environment, studied by our scientific community for more than a century, and a bunch of measurements. Many of the measurements we are in possession of today were obtained in the last decade by an artificial satellite called Cassini. New data arrive periodically and new efforts in the form of laboratory studies and models are done continuously to improve the state of knowledge of Titan's atmosphere.

1.2 Cassini investigations

On October 1997 the Cassini-Huygens spacecraft was launched, starting one of the most challenging and fruitful endeavors of human space exploration. Its mission was to provide information to better understand the Saturnian system, with a particular interest in Titan. After several flybys and a Jupiter encounter the spacecraft entered the saturnian system. On January 2005 the Huygens probe, ejected from the spacecraft almost one month before, reached Titan. The first farthest ever human device at the surface of a celestial body, the probe collected information about Titan's atmosphere along its passage through it. The Cassini spacecraft continued orbiting the saturnian system, visiting Titan regularly. A diagram of the Cassini missions coverage is shown in Figure 1.3. Currently in the middle of the Cassini Solstice mission (the second mission extension after the nominal and Equinox missions) these flybys are at the moment of writing still providing a mound of information about the satellite.

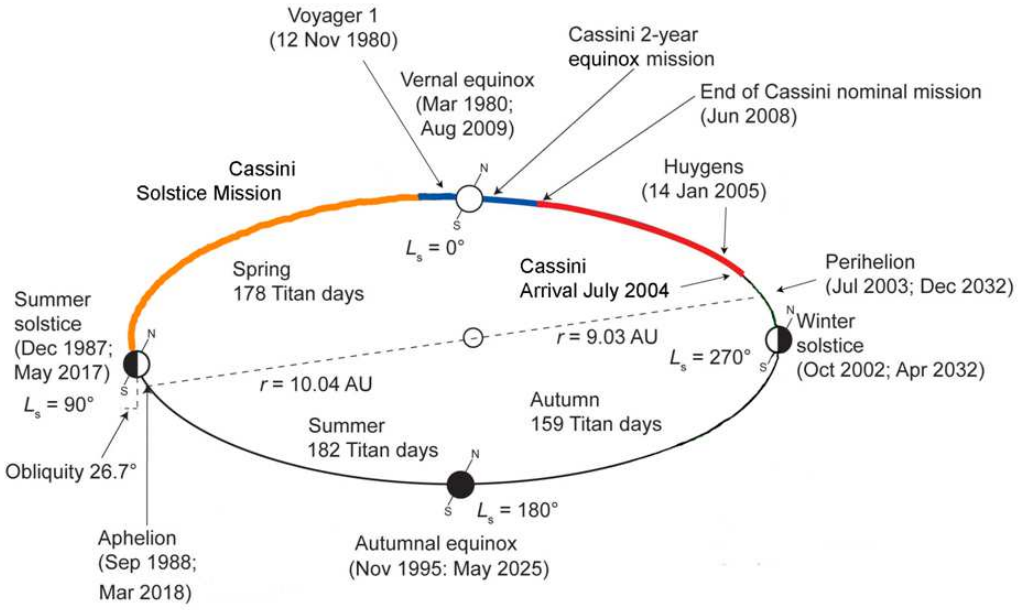

Figure 1.3: The entire primary, equinox, and solstice phases of the Cassini mission cover just half of a Saturn/Titan year (29.5 Earth days) (Credit: Ralph Lorenz).

Measurement requirements for the Cassini mission included:

- Determine the abundances of atmospheric constituents (including any noble gases).
- Observe vertical and horizontal distributions of trace gases.
- Detect new molecules.
- Study the formation, composition and distribution of aerosols.
- Map the global temperatures.
- Investigate seasonal effects in Titan's atmosphere.

The Cassini 'era' provided lots of new tools to analyze Titan and its atmosphere. Among the instruments in the Cassini remote sensing plate, three of them are very relevant for the study of

the atmosphere and will be referenced in this work. The Composite Infrared Spectrometer (CIRS, Kunde et al., 1996) consists of dual interferometers that measure infrared emission from atmospheres, rings, and surfaces over wavelengths from 7 to 1000 micrometers (1400 to 10 cm^{-1}) to determine their composition and temperatures. It performs, among other measurements, nadir and limb observations to derive composition and temperature structure profiles of Titan's lower atmosphere, from the surface up to some 500 km. The Ion and Neutral Mass Spectrometer (INMS, Waite et al., 2004) measures in-situ positive ion and neutral species to derive composition and structure in the upper atmosphere of Titan, from the altitude of closest approach (some 900 km in some cases) up to the limit of the atmosphere. The capabilities of the Ultraviolet Imaging Spectrograph (UVIS, Esposito et al., 2004) include measuring ultraviolet radiation (∼560 - 1900 Å) from and through Titan's atmosphere. This allows to derive composition and temperature in the upper thermosphere, from some 500 km to 1400 km (limb viewing), complementing the ranges covered by the other two instruments. The synergy between these instruments is one of the main advantages given by Cassini to study the whole atmosphere.

After almost 9 years from the first Titan encounter a region of the atmosphere remains barely explored. The region between 500 - 900 km received the name of ignorosphere because very little is known apart from theoretical photochemical modeling and some measurements (Coustenis et al., 2009a). As stated before, heavy molecules, ions and aerosols present in the lower atmosphere are predicted to form in this region. This makes its characterization important to better understand the atmosphere as a whole. To discover how intimately coupled is the upper thermosphere with the stratosphere, and what is the role of this upper region in the atmospheric chemistry are some of the main objectives of the Cassini mission. UVIS is the only remote sensing system in Cassini that can probe the hydrocarbon homopause region of the thermosphere on Titan and some hundreds of kilometers above. Data from UVIS can shed light on the energetics, composition, structure and variability of this region, that couples the ionospheric and stratospheric phenomena. The instrument observes ultraviolet light reflected or emitted by aerosols or atomic and molecular species in Titan's atmosphere; it also observes UV light transmitted during occultations of the Sun and occultations of stars by Titan's atmosphere. Titan's reflectance spectrum is best fit with scattering from a combination of aerosols and hydrocarbons (Ajello et al., 2008). The observed extreme ultraviolet and far ultraviolet airglow of Titan allowed to derive a wealth of information on solar driven processes involving molecular nitrogen (N_2) as well as geometric albedo in the upper atmosphere (Ajello et al., 2007, 2008; Stevens et al., 2011). Molecular nitrogen profiles in the ignorosphere and temperatures for an isothermal atmosphere were recently derived from UVIS EUV solar occultation measurements (Capalbo et al., 2013). Apart from the main components of Titan's atmosphere (N_2 and CH_4), some of the first hydrocarbons and nitrile species in the chain of reactions considered in photochemical models from the dissociation and ionization of these two species (like C_2H_2, C_2H_4, C_2H_6), as well as important intermediate molecules in the path to polymer formation (like C_4H_2, C_6H_6, HCN, HC_3N), were detected in the ignorosphere from UVIS measurements. This was done using the stellar occultation technique in the FUV spectral region (Shemansky et al., 2005; Koskinen et al., 2011) in the range 400-1600 km approximately. Analysis of UVIS data also provided profiles of aerosol extinction at these altitudes (Koskinen et al., 2011). With time, if the analysis of more UVIS observations fill in the experimental gap in our knowledge about the lower and middle thermosphere of Titan, the ignorosphere denomination will no longer apply.

1.3 Motivations and focus of the present work

Considering the author's interests about life origins and evolution in space, commented in the foreword and the first paragraphs of this introductory chapter, the preceding short history and description of Titan's atmosphere provide enough motivation for the present work. The above exposed relevance of the thermosphere and convenience of UV observations, motivate the focus on that region of the atmosphere and on that technique, respectively.

Being at the middle of the Cassini Solstice mission, we have a good knowledge of the composition and thermal structure of the atmosphere, but, as exposed on the previous section, the 500 - 1000 km region remains a bit elusive. Although HASI inferred the thermal structure at equatorial latitudes through this region, it did not yield a pronounced mesopause widely expected from theory. Ground-based millimeter-wavelength observations provided limited, globally averaged, composition measurements, in contrast to the detailed altitudinal and latitudinal composition and temperature measurements by CIRS for the stratosphere and INMS for the upper thermosphere and ionosphere. The UVIS stellar occultations provided composition and thermal structure in the ignorosphere region. Although this studies remain scarce compared to the others mentioned, the abundances and density profiles derived from UVIS are an addition to the UVS profiles (for N_2, CH_4, C_2H_2, C_2H_4, HCN, and HC_3N), the only ones available before Cassini. UVIS results represent in this way a significant advance in the characterization of Titan's upper atmosphere gaseous (Shemansky et al., 2005; Koskinen et al., 2011) and solid (Liang et al., 2007) composition. These new measurements will be described in more detail in following chapters. However there are some limitations and drawbacks among the results obtained. Shemansky et al. (2005) first derived column density profiles for CH_4, C_2H_2, C_2H_4, C_2H_6, C_4H_2 and HCN, and estimated number densities for some altitudes from the first UVIS stellar occultations. The uncertainties in column densities and number densities reported for some hydrocarbons and HCN are very high, up to 100% in some number densities. Neither Shemansky et al. nor Liang et al. presented detailed number density profiles for the minor species identified in the data and their analysis did not include all of the species that are detectable. Koskinen et al. (2011) added HC_3N and C_6H_6 to the list of molecules detectable by UVIS, and derived number density profiles from two stellar occultations. Although the general trend with altitude of the mixing ratios of hydrocarbons and nitriles (increasing with altitude up to the production region and then decreasing) in UVIS results broadly agree with the general trend implied by the CIRS and INMS measurements, there are still some discrepancies in absolute values, particularly at low altitudes. Finally, none of these analyses could derived N_2 directly from the measurements, and a reliable retrieval of CH_4 was limited to altitudes below 1200 km due to the characteristics of the FUV absorption. An independent assessment of upper atmosphere nitrogen densities are also helpful to confirm the systematic factor of ~ 3 difference among HASI, INMS, and the Attitude and Articulation Control System (AACS) densities (see for example Müller-Wodarg et al. (2008)). UVIS solar occultations can provide an independent and reliable measurement of temperature in the upper atmosphere through the measurements of N_2 profiles, as well as extend the CH_4 profiles higher than 1200 km. Even when Cassini/UVIS has performed several solar occultations during the whole Cassini mission, the first publish results are recent (Capalbo et al., 2013). Different measurements pertain to different locations, times or observational conditions, which make it difficult to compare them. Measured at different locations/times, solar occultations in the UV are a valuable addition to the study of the thermal structure and its variability.

The general objective of this work is to contribute to the knowledge of Titan's upper atmosphere. Within this main goal, and based on the considerations and background exposed in this Chapter 1, it will focus on three high level objectives:

1. To provide observational data to constrain photochemical models. This will include new measurements of relevant absorption cross section in laboratory, determination of thermospheric temperature, characterization of distribution of gases abundances and aerosol extinction profiles as a function of variables like latitude, longitude, solar/magnetospheric activity, time.

2. To contribute to the interpretation of thermospheric dynamics and the relationships of the upper atmosphere with the stratospheric aerosols. A focus will be made on upper atmosphere temperature variability.

3. To analyze the detectability of new molecules and confirmation of already detected molecules in the thermosphere of Titan by means of VUV observations. Particularly those molecules taking place in prebiotic chemistry and those considered intermediate in the path to aerosols (case of C_6H_6)

To fulfill these objectives different studies and experiments were performed, which will be expanded in the different chapters of this manuscript:

- The understanding and processing of UVIS data and ancillary data, and the implementation of the atmospheric absorptive occultation technique. These topics, developed in Chapter 2, include corrections of instrument effects, fundamental to the derivation of trustful data and interpretation. The chapter ends with a presentation of the observations analyzed.

- The implementation of the techniques used to retrieve atmospheric composition and temperature from the UVIS measurements form the first part of Chapter 3.

- A study of the possible and relevant molecules to be detected with UVIS, based on the molecule absorption cross section in the spectral range relevant for UVIS observations, and based on instrument characteristics. Molecules in models and laboratory experiments were used as a guide. This shapes the second part of Chapter 3, also including data simulations to test the retrieval routines.

- Laboratory measurements of C_6H_6 absorption cross section in the VUV and as a function of temperature, at temperatures as low as 215 K. Presented in Chapter 4, this is followed by the implementation of the measured absorption cross section in the analysis of atmospheric absorption and detection of C_6H_6 in the thermosphere.

- Retrievals of density profiles of main (N_2 and CH_4) and minor (hydrocarbons, including C_6H_6, and nitriles) compounds, as well as aerosol extinction profiles, in the thermosphere through the analysis of stellar and solar occultations in the FUV and EUV channels of UVIS, respectively. A comparison with previous work is also presented. The results constitute the first part of Chapter 5.

- The last part of Chapter 5 includes a thermospheric temperature variability analysis and a comparison with existing measurements.

Conclusions derived from this work are presented in Chapter 6, together with perspectives and suggestions for further work. It is worth noting that the interpretation and correction of UVIS instrument effects, and the experimental work (acquisition, processing and interpretation) to obtain the absorption cross section data demanded a big deal of time and efforts of different kind. These first steps are fundamental to derive trustful data by means of which the analysis above could be performed and the objectives commented achieved. For these reasons a big part of the present work is dedicated to these tasks.

Chapter 2

UVIS stellar and solar occultation data analysis

This chapter deals with the data and methods used to derive the results concerning stellar and solar occultations, presented in Chapter 5. A description of the UVIS instrument and data is first presented. This will be followed by comments on absorptive UV occultations, the type of observations performed by UVIS analyzed in this work. Since solar and stellar occultations were analyzed, a comparison between their characteristics is followed by a detailed description of their relevance, past efforts in the field and first steps in the processes involved in their analysis. The present chapter ends with a presentation of the observations analyzed and their geographical and temporal characteristics, as a database for further reference in the reading of the manuscript.

2.1 UVIS instrument and data

2.1.1 UVIS instrument

One of the instruments in the remote sensing payload of the Cassini spacecraft is the Ultraviolet Imaging Spectrograph (UVIS). This instrument was designed to measure ultraviolet light reflected/transmitted by or emitted from atmospheres, rings, and surfaces to determine their composition, the altitude distribution of their components, aerosol content, and temperatures. UVIS is composed of two spectrographs, a high speed photometer (HSP), and an Hydrogen Deuterium Absorption Cell (HDAC). These instruments, together with an electronic assembly, are mounted over the spacecraft interface plate. The two spectrographs provide images and spectra covering the extreme ultraviolet (EUV: 561 - 1182 Å) and the far ultraviolet (FUV: 1115 - 1913 Å) ranges of the electromagnetic spectrum. The HSP is used for high signal-to-noise-ratio stellar occultations by rings and atmospheres. The HDAC measures the relative abundance of deuterium and hydrogen from their Lyman-α emission. The UVIS science objectives include investigation of the chemistry, aerosols and composition of the atmospheres of Titan and Saturn, the deuterium-to-hydrogen (D/H) ratio for Titan and Saturn, icy satellite surface properties,; and the structure of Saturn's rings. This work deals with data from the FUV and EUV spectrographs of UVIS.

The FUV and EUV instruments consist each of a 20 x 20 mm aperture, 133 mm in front of an off-axis section of a parabolic mirror with a 100 mm focal length. The mirror is followed by an entrance slit and a toroidal grating with a 300 mm horizontal radius of curvature, used in a Rowland circle mount. For each channel there is a set of 3 interchangeable entrance slits providing 3 different fields of view and resolutions. The dispersed radiation incises in a multi-element detector in a chord of the circle. This is an imaging, pulse-counting microchannel plate detector, with a planar 25.6 x 6.4 mm^2 sensitive area. The FUV detector is in a vacuum housing with an MgF_2 window. A windowless detector is required for the EUV wavelength range. For each detected photon, the electronics coupled to the Coded Anode Array Converter (CODACON) detector generates a photon count for the corresponding hit pixel in the anode array. The photon counts are accumulated in a memory to build a picture. This data are periodically read out for transfer to the spacecraft memory and eventually to ground. The two-dimensional format for the detector allows simultaneous spectral and one-dimensional spatial coverage. The second dimension in the imaging mode is given by spacecraft movement. The detector format is 1024 x 64 (spectral by spatial) with a pixel size of 25 x 100 μm^2. A scheme of the spectrograph is shown in Figure 2.1, a table with reference values is presented in Figure 2.2. The telescope is equipped with a sunshade and baffle system to minimize background from scattered light during limb scan measurements. In addition, the EUV channel has a solar occultation port. This is an aperture with boresight 20 degrees away from the main telescope boresight. A pick off mirror redirects the radiation towards the main telescope mirror. For a more detailed description of the instrument see Esposito et al. (2004).

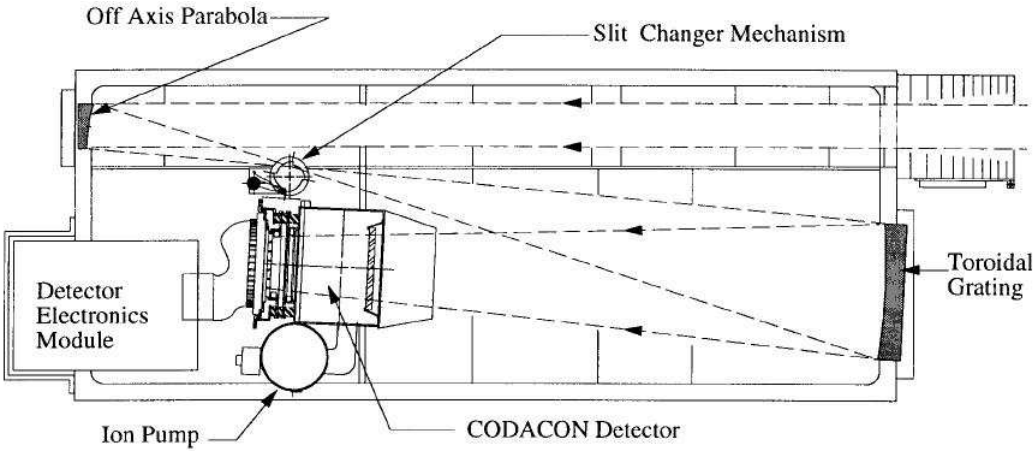

Figure 2.1: Scheme of UVIS FUV/EUV channel. From Esposito et al. (2004)

	FUV (1115-1912Å)	EUV (563-1182Å)
TELESCOPE		
Focal length Size(mm)	100	100
Entrance pupil size (mm)	20 x 20	20 X 20
Reflecting surface	Al + MgF_2	Boron carbide
TOROIDAL GRATINGS		
Size (mm)	60 x 60	60 x 60
Grating radii (mm)	300, 296.1	300, 296.8
Grating surface	A1 + MgF_2	Boron carbide
Grooves/mm	1068	1371
Input angle α (degrees)	9.22	8.03
Out angles β (degrees)	±2.9	-4.08, + 1.72
3-POSITION SLITS		
Slit widths (microns)	75, 150, 800	100, 200, 800
Δλ (Å) (Extended source)	2.75, 4.8, 24.9	2.75, 4.8, 19.4
Field of View (mrad)	(.75, 1.5, 8) x 60	(1, 2, 8) x 59
DETECTORS		
Photocathode	CsI	KBr
% Maximum QE	8	25
Detector window	MgF_2	none
Detector size (mm)	25.6 x 6.4	25.6 x 6.4
Pixel format (λ x θ)	1024 x 64	1024 x 64
Pixel size (μ)	25 x 100	25 x 100
Pulse resolution	10μsec	10μsec

Figure 2.2: UVIS EUV/FUV channel characteristics. From Esposito et al. (2004).

The UVIS instrument presents several improvements with respect to the UVS instrument onboard Voyager 1, including an improved spectral resolution and sensitivity. Therefore a more trustworthy identification of absorption features is expected, especially in the case of C_2H_2, C_2H_4 and C_4H_2, which spectral features are not easily seen in UVS data but are clearly identifiable in UVIS' (Shemansky et al., 2005; Koskinen et al., 2011).

2.1.2 UVIS data

The channels in UVIS can operate in different configurations and this results in different types of data products. The result of the measurements performed during a time range and with a particular instrument configuration is called observation, and has a unique identifier. The data in a UVIS observation are a copy of unprocessed data in the UVIS memory buffer, in binary format. An observation corresponds to one of four different types of data product: a spectrum, a time series of spatial-spectral images, a time series of detector counts, or an image at one wavelength. One or more of these data products and associated ancillary data products (1 ancillary product for many data products is possi-

ble) are stored in a data volume. Several volumes form a data set. Data products conform to Planetary Data System (PDS) standards and therefore have data objects and an associated PDS object label, which completely defines the product. This includes instrument configuration information, window and binning (see below) and integration time specifications. For a more detailed description of the different product types the reader is referred to the data documentation in the PDS. The observations dealt with in this work correspond to the time series of spatial-spectral images product type. This type of data is called spatial spectral cube. For a description of the spatial spectral cubes and their processing see Esposito et al. (2004) and Capalbo (2010).

A UVIS spatial spectral cube is a time ordered sequence of 1024 x 64 matrices. Each element of a matrix is the number of detector counts for an individual detector pixel during a fixed time interval or integration time. In more complex cases, to reduce data size, windowing and/or a binning of the spatial and/or spectral dimensions are defined in the 1024 x 64 matrices. See Figure 2.3 for a representation of data from an observation in the form of a PDS cube. In these cases, the detector is divided into

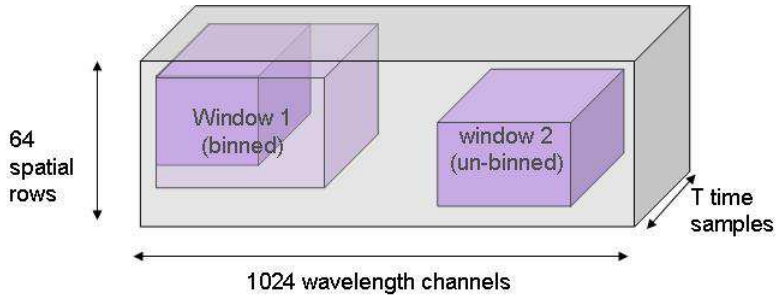

Figure 2.3: Graphic representation of a PDS data cube with raw data counts from an observation. The number of samples depends on the observation time. The useful data are divided into two windows, and the data in one of them was binned in the spatial and spectral dimensions.

a set of active rectangular sub-regions (windows). Each window can also be binned. The result is that some integers in the cube correspond to a range or 'window' of detector cells and their values are derived by summing over the spatial and/or spectral dimensions accordingly to the windowing and binning. The resulting data are located in the upper-left corner of the defined windows, and the rest of the locations have non-valid values. For a detailed description of the format see the PDS data documentation.

2.1.3 Ancillary data

The knowledge of the geometry configuration during observations is important for interpreting the data. It permits the derivation of useful quantities like the tangent altitude corresponding to a particular measurement time, and the corresponding planetary coordinates. Ancillary information about the instrument, spacecraft, planets, etc., are essential to derive geometry configurations. This information includes pointing, position and attitude of the instrument and spacecraft, position and motion of the sources of radiation, the target objects, angles and distances to calculate parameters that determine the characteristics of an observation, etc. The Navigation and Ancillary Information Facility (NAIF) provides an information system for this and other purposes. The SPICE system assists scientists in planning and interpreting scientific observations from space-based instruments. A description of SPICE and its use in this work can be found in Acton (1996), Capalbo (2010), and references therein. SPICE provides the ancillary data needed for the calculations of necessary information (like geometry) and also a toolkit to process the ancillary data. The primary SPICE data sets are called "kernels". SPICE kernels are composed of navigation and other ancillary information that has been prepared to be easily used by the planetary science and engineering communities. They

should include or be accompanied by metadata that provide pedigree and other descriptive information needed. The SPICE system includes the SPICE Toolkit, a large collection of allied software. The principal component of this Toolkit is a library of portable subroutines needed to read the kernel files and to calculate observation geometry parameters of interest. Users can integrate these SPICE Toolkit subroutines into their own application programs. The SPICE Toolkit was originally implemented in ANSI FORTRAN 77, but is now available in C, IDL and MATLAB as well. Some of the routines in the Toolkit IDL version, called ICY, were used in the present work to compute geometry related quantities.

2.2 Absorptive UV occultations

Several physical and chemical processes can take place in an atmosphere. An important factor driving those processes is the energy input/output. In the case of the upper atmosphere, this input can be due to radiation from stars (mainly from the Sun for Solar System bodies), the interstellar medium (γ and X-rays), or energetic particles from the interstellar or interplanetary medium (e- and ions from surrounding bodies, protons from stellar wind).

Lavvas et al. (2011) comment on several of the sources mentioned above for the case of Titan. Solar photons dominate energy deposition and ionization/dissociation processes on the day side (Galand et al., 2010). Some of these photons will generate photoelectrons that will provide a smaller but important contribution to ionization and dissociation processes. Magnetospheric electrons have in general a smaller contribution than photons. Although the former can dominate ionization on the night side in some occasions (Cravens et al., 2009), their importance is always less than solar ionization on the day side. The contribution to neutral dissociation by energetic ions (O^+, H^+) in 500 - 1000 km is small under typical Titan conditions. The altitude of maximum energy deposition of pickup ions is in general above the solar EUV/UV energy deposition (as shown in Figure 5 of Westlake et al., 2011). There is a contribution to ionization in the 500 - 700 km by meteoroids ablation, but small. Galactic cosmic rays contribute to ionization in the lower atmosphere, with a peak at 65 km. Other sources of energy for the upper atmosphere can be particles from the solar wind, and breaking waves from the mesosphere into the thermosphere (Müller-Wodarg et al., 2008).

The characteristics of the atmosphere can be elucidated by studying its interaction with these sources. In this work the upper atmosphere of Titan is studied by means of its interaction with the radiation received from the Sun or other stars. These photons can interact with the atmosphere, more precisely exciting the molecules composing it. The interaction can be called:

absorption: the energy from the photons in the radiation field can be converted to internal energy leading to molecular excited states (electronic, vibrational, rotational). Some of the electronic levels can lead to dissociation or ionization. Part of the energy absorbed can also be converted to kinetic energy, increasing the temperature of the medium.

scattering: the molecule returns spontaneously to the original energy state, re-emitting the photon. This emission can be of the same wavelength (scattering) or of different wavelengths (Raman scattering). In the general case the intensity of the re-emitted radiation depends on the angle of emission; this distribution of energy depends in turn on the relative size of the molecule (or particle) with respect to the incident wavelength. Particular cases occur when the direction of emission is the same as that of incidence (forward scattering), opposite (backward scattering), or following the laws of reflection (diffuse reflection or just scattering).

transmission: the part of the radiation field that has not been absorbed or scattered back.

Other processes in the atmosphere manifest as **emission** from it, for example:

thermal emission: the energy gained from collisions (kinetic energy) are emitted as photons.

airglow: emission of radiation caused by different processes. These can be chemiluminescence, in which photons are emitted by the recombination of ionized particles, or by the reactions between certain molecules; or photoluminescence (fluorescence and phosphorescence), which is an energy release mechanism similar to molecular scattering but in which longer times are involved between absorption and emission. Apart from the phenomena just described, the radiation suffers from **diffraction** when traversing the atmosphere, which has different refractive index at different heights. This produces a deviation in the direction of the radiation. The combination of these phenomena determines the interaction of the atmosphere with the radiation received.

The effects of radiation propagating through a medium can be modeled with the radiative transfer equation (see for example Rees, 2001). The spectral radiance L, in Watts per meter square per steradian, for a particular wavelength λ and propagating in a direction (θ, ϕ) is obtained solving the equation

$$\frac{dL(\lambda,\theta,\phi)}{dD} = -(\alpha_a(\lambda,T) + \alpha_s(\lambda,T))L(\lambda,\theta,\phi)R(\lambda) + \alpha_s J(\lambda) + \alpha_a B(\lambda,T). \tag{2.1}$$

Here dD measures distance in the propagation direction, α_a and α_s are the absorption and scattering coefficients, and R accounts for differential refractivity. The spectral radiance coming from emission from the medium is B. Equation (2.2) defines J, the radiation scattered into the direction of propagation from other directions. In this equation the primed angles reference the different directions that contribute to the propagation direction. The phase function of the scattering, $p(cos(\Theta))$, describes the angular distribution of the scattered radiation in terms of the angle Θ through which the radiation has been deflected (see Rees (2001) for details).

$$J = \frac{1}{4\pi}\int_{4\pi} L(\theta',\phi')\, p(\cos(\Theta))\, d\Omega'. \tag{2.2}$$

The dependences shown in equation (2.1) refer to wavelength (λ) and temperature (T). In the case of radiation through an atmosphere, the first term on the right side of the equation represents radiance from the source attenuated due to extinction over a differential distance. The second term accounts for contributions emitted from the surrounding of the differential distance. The third term accounts for the emission of the atmosphere itself. In many cases, the medium is supposed to be in thermal equilibrium with the radiation, and the atmospheric emission is considered to be equal to that of a black body at the temperature of the atmosphere. This equation can be simplified for the case of absorptive VUV occultations as will be seen below.

One of the effects of energy deposition and radiation interacting with the upper atmosphere of Titan, and the most relevant in the context of the present work, is the ionization and dissociation of N_2 and CH_4. As underlined in the introduction, this is very relevant to the whole chemical and physical processes occurring in the atmosphere. Lavvas et al. (2011) presented a detailed model for photodissociation and ionization of N_2 and CH_4 incorporating the latest photoabsorption cross sections at that time and including contribution from photoelectrons. The role of photoelectrons was overestimated in the past, but both photons and photoelectrons are necessary for accurate representation of chemical precursors in the upper atmosphere. The interactions of atmospheric constituents with the radiation input can be used to draw out atmospheric composition. Depending on atmospheric characteristics, geometry and observation technique, the measured phenomena might be a combination of those commented above: absorption, scattering, transmission, or emission.

2.2.1 Atmospheric composition from absorptive VUV stellar occultations

The overall picture of the procedure used in this work to derive composition and temperature is schematized in Figure 2.4. As Cassini performs a Titan flyby UVIS performs observations. These can include star occultations, particularly Sun occultations. The raw UVIS data are combined with ancillary data to calculate transmission as a function of altitude. At the same time absorption cross sections, model profiles, and the UVIS instrument function are combined according to analysis needs. Then the column densities and number densities are derived, and temperatures are calculated. The detailed procedure and particularities for stellar and solar occultations will be described in the remaining of this chapter.

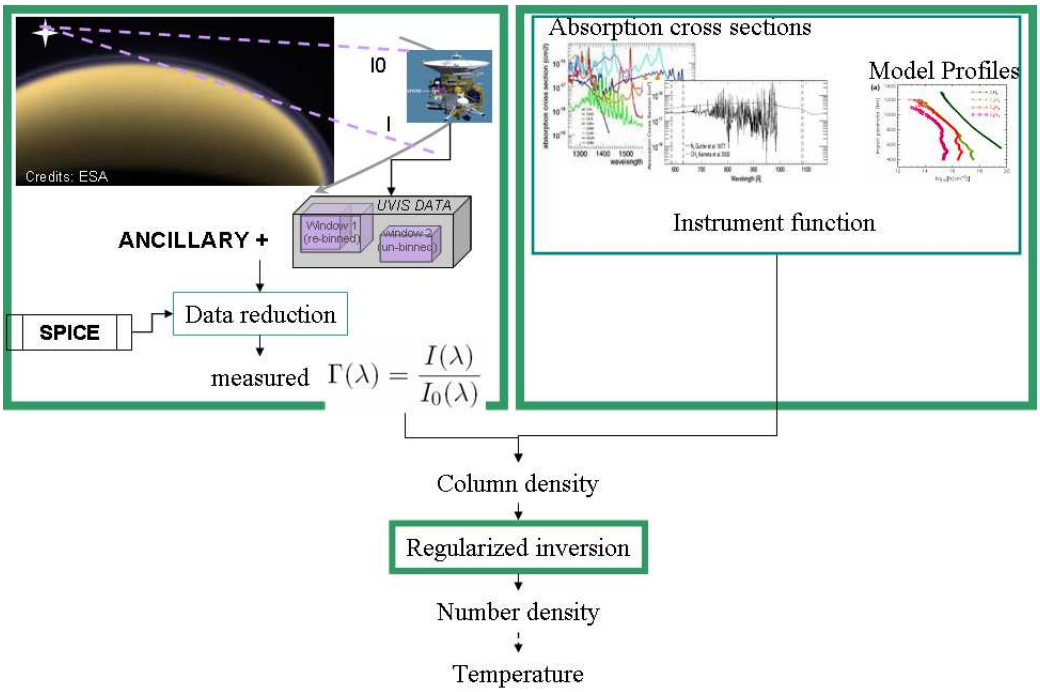

Figure 2.4: Workflow chart. The raw UVIS data measured during a flyby are combined with ancillary data to calculate transmission as a function of altitude. At the same time absorption cross section, model profiles and the UVIS instrument function are combined according to analysis needs. Then the column densities are calculated and from them the number densities. Temperatures are calculated when possible.

During an occultation the radiation from the source is measured before and during the time that the Line Of Sight (LOS) to the source traverses the atmosphere. From all the wavelengths that can be used, VUV is very popular because many gases present strong absorption features in this wavelength region. Almost all electronic transitions of molecules give rise to spectra in the visible and ultraviolet regions; only very few extend into the infrared region. Absorption is the dominant phenomena for the observations analyzed here, although extinction from aerosols is also considered. Information from UV absorption corresponds to the upper atmosphere, as the UV radiation is completely absorbed for the lower layers. Equation 2.1 can be simplified for the case of VUV occultations by Titan's atmosphere observed by UVIS. The emissions in the UV from Titan's atmosphere can be neglected when observing a star (see Koskinen et al., 2011 and Ajello et al., 2007, 2008), so the third term vanishes. Considering the Field of View (FOV) of the UVIS spectrographs (see Section 2.1) and the characteristics of occultations observed from an orbiting spacecrafts (for example, the distances involved), scattered radiation into the instrument FOV can be neglected (Smith and Hunten, 1990). Therefore the second term disappears, as well as the angular dependence. Finally, refractions effects are negligible (Smith and Hunten, 1990). So, expressing the radiation flux as an intensity I in Rayleigh

(instead of radiance L[1]), equation (2.1) can be written as

$$\frac{dI(\lambda)}{dD} = -\alpha I(\lambda). \tag{2.3}$$

Integrating equation (2.3) an expression for the attenuation of the radiation through the atmosphere can be reached, as shown in equation (2.4),

$$\frac{I(\lambda)}{I_0(\lambda)} = \exp(-\int \alpha dD) = \Gamma(\lambda), \tag{2.4}$$

where I_0 represents the intensity of radiation outside the atmosphere. The intensity measured above the atmosphere gives the source spectrum, the spectra observed while the LOS traverses the atmosphere, I, is the source spectrum modified by the extinction of the different components of the atmosphere. Γ is the transmission through the atmosphere, measured for the different altitudes probed by the LOS. The integral extends over the whole path of the radiation through the atmosphere. This path varies with the altitude from the surface. The extinction coefficient, α, is related to the extinction cross section σ via equation (2.5),

$$\alpha = \sigma n, \tag{2.5}$$

where n is the number density of the gas in the atmosphere. For the gaseous species considered, α this will be equal to the absorption cross section (the scattering cross sections being several orders of magnitude lower, see for example Ityaksov et al., 2008; Sneep and Ubachs, 2005); for the aerosols the extinction is considered to be a combination of absorption and scattering. The atmosphere might be composed of a mixture of gases of several species and aerosols, and the extinction due to each of them has to be taken into account. To express this in a convenient way for the purpose of data analysis and species retrieval it is useful to consider the atmosphere as spherically symmetric and stratified in L discrete layers. The idea is schematized in Figure 2.5, which shows four layers as an example, each with a constant and uniform density for a particular gas. The closest distance between Titan's surface and the boresight is called the tangent altitude, and is considered the altitude corresponding to the measurement. In the figure three layers are traversed by the instrument boresight when the tangent altitude corresponding to the third layer is being probed. This defines the distances $D_{i,j}$ that represent the optical path traversed through layer i when probing a tangent altitude in the middle of layer j. The distance D is given by equation (2.6),

$$\begin{aligned} D_{i,j} &= 2\left(\sqrt{r_{top,i}^2 - r_{mid,j}^2} - \sqrt{r_{top,(i+1)}^2 - r_{mid,j}^2}\right) \quad ; \quad i \neq j \\ D_{i,i} &= 2\left(\sqrt{r_{top,i}^2 - r_{mid,i}^2}\right) \quad ; \quad i = j \end{aligned} \tag{2.6}$$

where $r_{top,i}$ is the distance from Titan's center up to the upper end of the layer i and $r_{mid,j}$ is the distance from Titan's center up to the middle point of layer j. This is equal to Titan's radius plus the tangent altitude being probed. Then equation (2.4) can be rewritten as equation (2.7).

$$ln(\frac{I_l(\lambda)}{I_0(\lambda)}) = -\tau_l(\lambda) = -\sum_{l'=l}^{L}\sum_{s=1}^{S}\sigma_{l',s}(\lambda)n_{l',s}D_{l',l} = -\sum_{l'=l}^{L}\sum_{s=1}^{S}\sigma_{l',s}(\lambda)N_{l',l,s}. \tag{2.7}$$

The quantity $\tau_l(\lambda)$ is minus the logarithm of the transmission for a tangent altitude in layer l. It is called optical depth. For a particular layer (or altitude), this quantity can be expressed as a function

[1]There relation between them is $L = I\frac{10^{10}}{4\pi}$

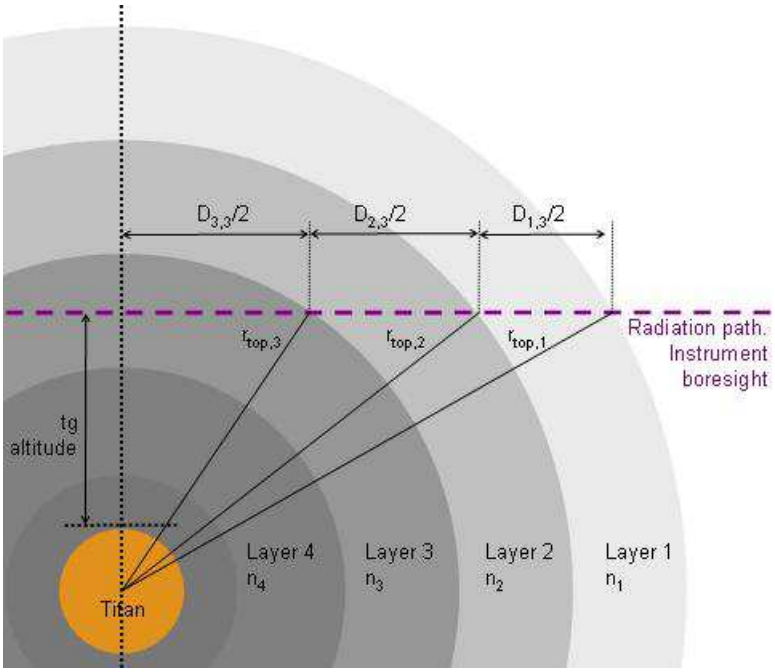

Figure 2.5: Schematics of the atmospheric layers created for the analysis. Layer i has a number density n_i. The distance from Titan's center up to the upper end of the layer is $r_{top,i}$. The distances $D_{i,j}$ represent the optical path traversed through layer i when probing a tangent altitude in the middle of layer j. In the figure the instrument boresight probes a tangent altitude corresponding to the middle point of layer 3.

of wavelength—giving a transmission spectrum. In Equations (2.7) the integral in equation (2.4) was replaced by a sum over the different atmospheric layers that the radiation goes through: the layer whose midpoint coincides with the tangent altitude under consideration and the ones above it. Equation (2.5) was used to replace the extinction coefficient. The distance traveled by the radiation through layer l' is $D_{l',l}$, and $N_{l,l',s}$ is the column density for species s considering this distance. Both quantities refer to the tangent altitude in the middle of layer l. The inner summation runs over the S species to be considered in the analysis. In the case of the cross sections, the dependence with altitude is a consequence of its dependence with temperature, which varies with altitude. In this work the absorption cross section will be considered independent of altitude, and absorption cross sections at a constant temperature will be used for the retrieval. This allows to take it outside the layer summation and get equation (2.8),

$$-\,ln(\frac{I_l(\lambda)}{I_0(\lambda)}) = \tau_l(\lambda) = \sum_{s=1}^{S} \sigma_s(\lambda) N_{tot_{l,s}}, \tag{2.8}$$

where N_{tot} is given by equation (2.9).

$$N_{tot_{l,s}} = \sum_{l'=l}^{L} N_{l',l,s}. \tag{2.9}$$

Equation (2.8) is the equation that will be solved numerically. In this way the column densities that best fit the observational data are determined as a function of altitude via a retrieval procedure; from them, a number density profile is calculated (see Section 3).

It is evident from equation 2.7 that the interpretation of spectra in the VUV can depend critically on the knowledge of the molecular absorption cross sections in conditions representative of a planetary environment. The absorption cross section can vary significantly with temperature, in

particular variation of band intensities can be observed (see for example Ferradaz et al. (2009) and Chapter 4). Sharp transitions are more affected by temperature effects than broad bands, thus the effect of temperature are more evident in high resolution spectra of sharp transitions. Therefore, it is desirable to have absorption cross section data corresponding to the temperature of the atmosphere. But the atmospheric temperature can vary with altitude; in this case, the optimal situation would be to count with a set of absorption cross section spectra for the different temperatures. Even when temperature dependent measurements of absorption cross section have been done for several molecules of planetological interest (Wu et al., 2001, 2004; Bénilan, unpublisheda, to cite some), their inclusion would complicate the retrieval procedure. On the other hand, for some molecules presenting broad absorption bands, the difference between room temperature and low temperature absorption cross sections is less important; less than 10% in the case of some C_6H_6 bands, as shown in Chapter 4. In these cases the absorption spectra at room temperature, more available than spectra measured at low temperatures, can be used without adding a significant source of error to the results. As for the temperature variation with altitude, the upper thermosphere of Titan is reasonably modeled in a first approximation with an isothermal profile, supporting the use of absorption cross sections at a fixed temperature for a given species. A preliminary analysis of the effect of the use of absorption cross sections measured at different temperatures in the derived transmission through Titan's thermosphere is presented in Capalbo (2010). In the present work absorption cross sections measured at low temperatures will be used when available. Measurements at room temperature will be used when the former are unavailable and/or the behavior of the absorption spectra is expected to be unaffected by temperature.

Occultation by Titan's atmosphere can be observed from the Earth. Measurements from the surface in the visible and near infrared probe the region 250 - 600 km above Titan's surface (see for example Sicardy et al., 1999), so they could be complementary to the type of occultations presented here. Measurements from an airborne or spaceborne platform orbiting Earth, would allow to extend the wavelength range to shorter wavelengths. But with very few opportunities of being at the right moment at the right place, these measurements remain rare. Titan subtends only 1 arcsec or so on the sky as seen from Earth, so the probability of the satellite passing in front of a star is small. Measurements from a spacecraft passing by or orbiting Titan present an optimal situation due to their better spatial resolution and proximity to the target. This is the kind of observations used in this work, observations obtained as Cassini flew by Titan.

Occultation measurements by UVIS complement and have many advantages with respect to measurements from other instruments. It has been commented before that the altitude range covered by UVIS occultation measurements lies in between of those covered by CIRS and INMS. In addition, the INMS instrument measures composition in-situ, while the spacecraft flies through the atmosphere, and UVIS occultation measurements require the spacecraft to be at a certain distance above the Top Of the Atmosphere (TOA). So, although measurements from the two instruments can happen in one flyby, this is rare, and the observations complement each other in time coverage. Furthermore, as noted by Müller-Wodarg et al. (2008), a major difficulty in deriving atmospheric properties from any single flyby from INMS is the fact that the spacecraft moves both horizontally and vertically through Titan's atmosphere. Typically, the horizontal distance covered in Titan's atmosphere is at least a factor of 5 larger than the sampled height range. While density measurements from single flybys are often displayed as a function of altitude, it is dangerous to interpret such figures as height profiles because horizontal structures in the atmosphere also affect the measured profiles. Müller-Wodarg et al. (2008) warns on the effects of horizontal density variations on derived temperatures from INMS measurements. In addition, this means that we cannot necessarily assume isothermal conditions along any given in-situ measurements from flybys. Although a similar problem can affect UVIS derived data in

cases when the instrument line of sight does not move perpendicular to the surface, in general the span in longitude and latitude for the relevant altitudes is only a few degrees (see Tables 2.4 and 2.5). Hence, the profiles derived from UVIS data can be considered as real vertical profiles. The INMS and CIRS vertical resolution is roughly a few km (Cui et al., 2009) and some tens of km (Vinatier et al., 2007), respectively. The vertical sampling of the UVIS occultations can be less than a kilometer in some cases. The resolution of the final derived number densities is, however, degraded in the data reduction and retrieval processes used here to some tens of km in most cases.

The knowledge of the temperature of Titan's upper atmosphere is key to the understanding of both its chemistry and dynamics. From the solar UV absorptive occultations N_2 number density profiles will be derived in this work. Several methods have previously been used to determine the effective or inferred temperature of the upper atmosphere from a profile of number densities (see for example Westlake et al. (2011); Snowden et al. (2013) for examples of temperature extraction from INMS density profiles). Here the N_2 profiles will be used to derive temperature under the assumptions of hydrostatic equilibrium and assuming the N_2 profile is representative of the atmospheric density profile.

All things considered, absorptive UV occultations are a very convenient way to derive composition profiles and temperature of the upper atmosphere, adding a valuable complement to measurements from other instruments. But the formalism above described is framed in a bigger context (see Figure 2.4). Ancillary data, preliminary data processing and processing of the derived column densities are necessary to provide physical information from a UV occultation. The following pages of this chapter describe procedures developed and implemented by the author to interpret UVIS occultations.

2.2.2 First steps in occultation analysis

To get relevant information about the atmosphere from the formalism described in the previous subsection, auxiliary but fundamental information and calculations are needed; for example the geometry of observation: satellite position, angles, ground points, context in Saturn system, etc. Other important issues are instrument corrections needed to derive proper transmission. These are the topics of the present and following subsections in this chapter, starting with first steps: geometry calculations and preliminaries of data analysis.

Geometric quantities

The first step in the analysis is to determine the geometric conditions for the observation. The spacecraft trajectory and attitude during the occultation is obtained with the help of SPICE kernels and ICY Toolkit. The start of the observation is given by the start time in the PDS label of the observation, the stop time is determined from this time, the number of samples in the observation and the integration duration of each sample. Integration time is 1 s for solar occultations, 5 s for the T41 stellar occultation, and 1.75 s for the T53 stellar occultation. The integration duration and the spacecraft velocity and attitude determine the vertical sampling of the atmosphere. The tangent altitude is calculated as the closest point of the boresight to the surface of Titan. This tangent altitude corresponds to the altitude probed (see Figure 2.5). The tangent altitude point trajectory in the atmosphere will determine the measured altitude profile of the species detected. As commented before, in most of the cases the drift of this point in latitude and longitude is only a few degrees, giving an accurate representation of an altitude profile, independent of horizontal variations—this is one of the advantages of the UVIS solar and stellar occultations. Also calculated was the distance from the spacecraft to the center of Titan and from the spacecraft to the tangent altitude point. These distances vary from one observation to another from some 10^3 to 10^5 km. As an example,

Figure 2.6 shows these distances for the T53 stellar occultation. Other derived geometric quantities

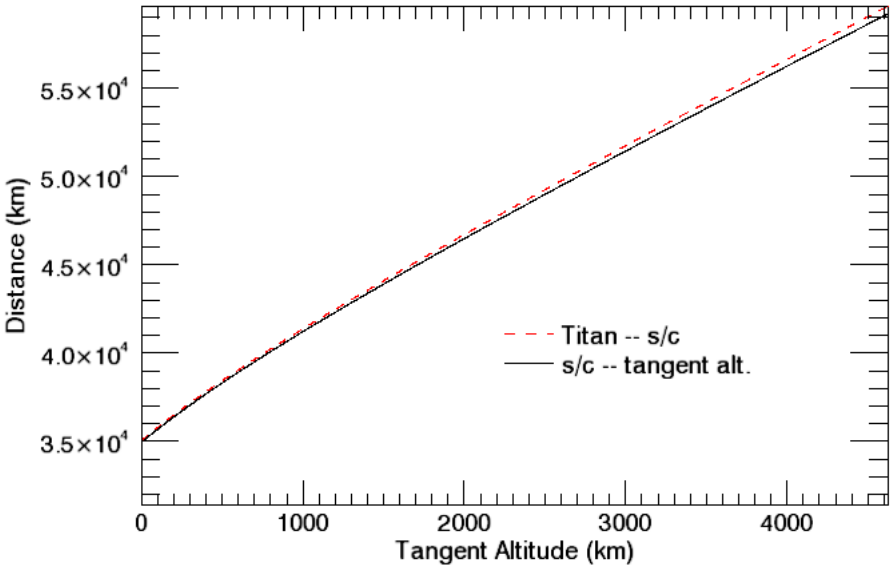

Figure 2.6: Distances between the spacecraft and the center of Titan, and between the spacecraft and the tangent altitude point, as function of tangent altitude, for a stellar occultation measured during the T53 flyby.

include sub solar point on the surface of Titan, Titan Local Solar Time (LST), position of Titan in terms of Saturn Local Time (SLT), illumination angles (useful, among other uses, to determine if the atmosphere is in shadow during a stellar occultation), and the size of the source (Sun or other star) and the size of the UVIS FOV, at the atmospheric level. The position and size of the source in the x-y FOV reference frame is another important quantity derived. It determines the position of the image in the detector, x representing the dispersion direction of the grating (spectral dimension) and y the cross dispersion direction (spatial dimension). The wavelength calibration available in the PDS corresponds to a source centered in the dispersion dimension. Thus, if the source is not centered in the x direction, the registered spectrum can be wavelength shifted with respect to the PDS wavelength scale (see Section 2.4). The relative position of the source in the FOV during the observations is also important. Pointing instabilities might cause the source image to fall in different rows/columns of the detector along the observation. Apart from the wavelength shifts commented, this might result in uneven intensity spectra, from one altitude to the other, due to the non-flat response of the detecting plate. In worse cases the source might even drop out of the field of view rendering the observation useless. An examination of the position in the slit is therefore mandatory. Examples of these geometric quantities are shown in the following sections when calculated for the particular cases of a star or solar occultation.

First steps common to UVIS FUV and EUV data cube analysis

The different steps in the UVIS data analysis can be consulted in the NASA-PDS (2012). The procedures described here, although based in this reference, are tailored to the particular experience and issues encounter by the author during the processing. The common (or very similar) procedures to be done for both FUV and EUV channels are summarized in the following. The coming sections will deal in more detail with corrections specific for each channel.

The dark current of the instrument comes principally from the Radioisotope Thermal Generator (RTG, Ajello et al., 2007) in the Cassini spacecraft and is negligible for the integration time used for

occultations, being some 10^{-4} cts/pix/sec (Holsclaw, personal communication). For the occultation data products analyzed in this work, a few detector rows correspond to useful data. This is a result of the point spread function of the instrument and the pointing attitude of the spacecraft during the observation. The corresponding rows in the data spatial spectral cube, representative of the spatial dimension of the observation, were summed up. Some channels in the extremities of the 1024-channel detector present no counts systematically, and are therefore eliminated from the data array. The result is a 2-D matrix containing count values for wavelength-time (or tangent altitude[2]) coordinates. This was done taking into account the windowing and binning of the data (see section 2.1). For one wavelength, the matrix contains the intensity measured as the LOS swapped the atmosphere probing different altitudes. This can be represented as the signal as a function of time (or altitude). These are called 'light curves'. Each row in the matrix represents an intensity spectrum collected during the integration time for a certain height range. These will be referred to as 'samples'. In all cases the light curves were inspected for anomalies. For example, the wavelength shift commented above can result in a light curve with a clear slope above the TOA, caused by the shift in photon flux from one detector pixel to the other. For each wavelength channel, low dispersion of the values around the mean value measured above the atmosphere (less than 15 and 30 % for solar and stellar occultations, respectively), and a small slope as a function of altitude (some 10^{-2} and 10^{-3} counts/km for solar and stellar occultations, respectively) assure a proper light curve. From the values measured above the atmosphere the quantity I_0 in equation 2.8 is calculated. The TOA is identified well above the altitude for which absorption starts to be evident. For most of the occultations analyzed the data were binned in altitude, each resulting value being the average of the values in the bin. This reduces the number of values available to calculate I_0, nonetheless the values used for this calculation were in all cases large enough to derive a representative I_0 value (see for example Figure 2.11). The altitude binning also gave an effective sampling of the atmosphere different from that in the raw data. This will not affect the final vertical resolution, as it is mainly determined by the number density retrieval process (see Chapter 3). However, in cases of heavy binning the smoothing effect in the light curve could lead to an overestimation of the derived abundances at high altitudes and an underestimation for low altitudes. In the case of N_2 this could further imply an overestimation of the calculated temperature. As a consequence, the results obtained averaging many altitudes should be interpreted with caution. This is the case of some of the solar occultations analyzed. Apart from these basic steps common to both stellar and solar occultations, other corrections and procedures are particular to each of them, as are the advantages and disadvantages of each of these types of observation.

2.2.3 Stellar vs. solar occultations

The stellar and solar occultations have advantages and disadvantages with respect to each other, both types of observations being, indeed, complementary. EUV radiation probes higher layers in the thermosphere, up to some 1500 km in Titan (the approximate altitude of the exobase, see for example Westlake et al., 2011); FUV radiation probes lower layers, down to Titan's mesosphere. In this work solar occultations measured with the UVIS/EUV channel were used to derive N_2 and CH_4 number densities, stellar occultations measured with the UVIS/FUV channel were used to derive number densities for CH_4 and other hydrocarbons and nitriles. Table 2.1 presents some pros and cons of stellar and solar occultations, that will be discussed following. The characteristics of the UV occultation are not to be confused with instrument limitations. Although the EUV channel can be used to measure radiation from stars, the FUV channel in UVIS does not have an occultation port

[2]For simplicity, altitude will sometimes be used instead of tangent altitude, the meaning remaining clear from the context.

and, consequently, cannot measure radiation from the Sun due to saturation limitations.

Stellar occultations have several advantages. One of them is the coverage of the occultations. There can be many opportunities during a spacecraft mission, among its different flyby orbits in the case of Cassini. Stellar occultations from an orbiting spacecraft can happen at different latitudes and longitudes. Therefore, if enough of them are available, a global 3D characterization of the atmosphere can be performed, and day-night variations can be studied. The received intensity is appropriate to detect it with normally developed detectors, i.e, without any problems of saturation—the Ly-α emissions might be strong but are attenuated by the interplanetary medium (IPM). The fact that measured stars can be considered point sources translates into high vertical resolution and ease of analysis. On the other hand the spectral coverage is limited to wavelengths above 912 Å, as shorter wavelengths are absorbed by the interstellar medium (interstellar hydrogen ionizes and cuts off the stellar UV flux below 912 Å). Therefore, UVIS/FUV occultations do not measure N_2, which absorbs only at shorter wavelengths. Cassini/UVIS also observes stellar occultations in the EUV, which do measure the N_2 absorption of Titan's atmosphere. But stellar EUV occultations are still limited by ISM absorption to wavelengths longward of 912 Å, where absorption is by highly complex N_2 electronic band systems (Lewis et al., 2008). These are very difficult to interpret at UVIS spectral resolution, as all the sharp lines must be modeled before convolution with the instrument function. Nevertheless, N_2 profiles have been recently determined from UVIS/EUV stellar occultations (Kammer et al., 2013). Unfortunately, the recent publication of the cited work did not allow a thorough comparison with it to be included in the present manuscript. Finally, the low stellar flux (compared with the solar flux) can derive in low signal-to-noise ratio (S/N).

In a Solar occultation the full solar spectrum is available to be detected, there are no wavelength limitation like that imposed by the interstellar medium absorption, as in the case of stellar occultations. Therefore the dissociation and ionization continuum absorptions of some elements can be used (e.g. N_2, see subsection 2.4.2) in addition to absorption in discrete bands at longer wavelengths (e.g. some hydrocarbons). The high intensity of the signal provides a good S/N. On the other hand solar occultations have some limitations with respect to other star occultations. Solar occultations can only take place at the terminator. There are normally less solar occultation opportunities than stellar occultation opportunities. The signal is sometimes very strong, risking saturation and requiring an extra mechanism to be implemented (like a filter or a pick-off mirror out of axis). The finite size of the Sun can compromise altitude resolution and complicate the analysis, especially if it is about or larger than the scale height of the species whose absorption is to be measured. But this disadvantage can be minimized by particular observation geometries when the observer is close to the atmosphere. Non-uniform intensity in the solar disk can also be a problem.

Table 2.1: Stellar and solar occultation characteristics.

Stellar occultation (FUV, EUV)	**Solar occultation (EUV)**
Happen at different latitude/longitude.	Happen only at the terminator, less frequent.
No need to reduce source flux.	Strong signal cannot strike the detector directly, need pick-off mirror.
Point source: higher vertical resolution, ease of analysis.	Finite size, lower vertical resolution, complicates analysis.
Limited to wavelength $>$ 912 Å by ISM absorption.	Full wavelength range available.
Low S/N.	High S/N.

2.3 Stellar occultations measured by UVIS FUV

2.3.1 Introduction to stellar occultations measured in the FUV

As shown in previous sections, stellar occultations are a powerful technique to identify molecules and to derive their vertical profiles in planetary upper atmospheres. Many molecules in Titan's atmosphere present strong absorption features in the FUV region and can therefore be detected by UVIS occultations. From the many molecules measured or predicted in Titan's upper atmosphere, here the focus is on CH_4, C_2H_2, HCN, C_2H_4, C_4H_2, C_6H_6, HC_3N, CH_3, and aerosols (AER). These were chosen based on an analysis of theoretical detectability of different species (see Chapter 5) and the visual inspection of spectra measured during occultations. This type of occultation can cover altitudes from 500 to 1300 km, which include several interesting regions in the middle and upper atmosphere. The altitudes below the homopause, which in Titan can be placed around 850 -1000 km (Cui et al., 2009; Vervack et al., 2004), include the region where a detached aerosol layer of varying height was observed (see for example Lavvas et al., 2010; West et al., 2011). The region above the homopause is a photochemically active region for several hydrocarbons and nitriles. Finally, the upper layers probed include the ionosphere, where the neutral abundances are determined in part by ion-chemistry. Therefore, different layers with different physics and chemistry are represented in a profile from a FUV occultation.

Stellar UVIS/FUV occultations by Titan were first presented by Shemansky et al. (2005). From the occultations measured during the flyby called Tb, they derived column density profiles for CH_4, C_2H_2, HCN, C_2H_4, C_2H_6, and C_4H_2. The observations cover altitudes from 450 to 1600 km above the surface. They observed a change in scale height of the retrieved hydrocarbons at 700 and 1000 km. Below 600 km, the density of the species mentioned drops precipitously to undetectable levels, to mixing ratios four to six orders of magnitude below that of CH_4. This result is in strong disagreement with inferred measured densities of higher order hydrocarbons and HCN from the Voyager experiment (Vervack et al., 2004) below 600 km. It should also be noted that the C_4H_2 absorption cross sections used by Shemansky et al. (2005) were saturated at 1445 Å and 1645 Å, which might have led to an overestimation of the abundance for this species. From the measured CH_4 abundances they inferred a temperature profile above 400 km. The profile contains a convective region around 450 km where the temperature gradient is adiabatic and a mesopause at 615 km with a temperature of 114 K. The asymptotic kinetic temperature at the top of the atmosphere determined from this experiment is 151 K. By comparison, the HASI temperature was $\sim$ 175 K there. Liang et al. (2007) used the same UVIS data from the Tb flyby to detect and characterize aerosols at altitudes between 500 and 1000 km. The detection of aerosols in this region implies that they are formed at higher altitudes in the thermosphere.

Stellar occultations by Titan's upper atmosphere observed by UVIS/FUV were also analyzed by Koskinen et al. (2011). These authors presented an analysis of other stellar occultations measured by UVIS: T53 and T41. The presence and profiles of some hydrocarbons in the upper atmosphere was then established, adding C_6H_6 and HC_3N to the list of species detected by UVIS presented in Shemansky et al. (2005). Koskinen et al. identified absorption layers at 600 - 700 km dominated by hydrocarbons and nitriles and an absorption layer at 500 km dominated by aerosols. This last layer was less evident in the occultation occurring at higher northern latitudes among the two analyzed. From their CH_4 profile they inferred temperature profiles for the upper atmosphere and presented an analysis of the temperature fluctuations in terms of gravity waves.

The results from the works commented are an example of the already highlighted potential of this observations to contribute to the understanding of Titan's upper atmosphere variability and dynamics. The present work includes a thorough analysis and characterization of the retrieval techniques to derive

composition from UVIS/FUV stellar occultations. The technique was applied to data from flybys T41 and T53 with the intention to compare results with those from Koskinen et al. (2011), obtained with an almost identical technique. This work resulted in profiles in good agreement with those in the reference mentioned.

2.3.2 UVIS/FUV stellar occultation analysis

The geometric calculations and data handling procedures common to both channels were described in Section 2.2; results and particularities in the data reduction for the FUV are presented in this subsection, the relevant calculated quantities can be consulted in Table 2.4. The overall picture of the procedure used in this work to derive composition from stellar occultations is schematized in Figure 2.7. The pointing direction to the source in these cases is calculated from the solar system

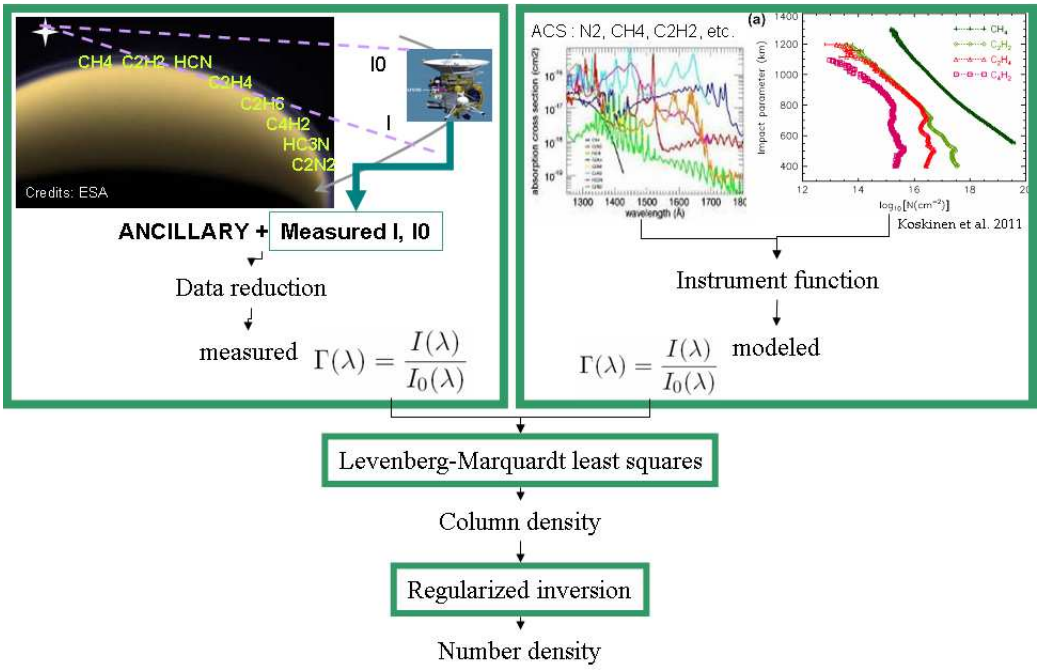

Figure 2.7: Workflow chart for stellar occultation analysis. The raw UVIS data measured during a flyby are combined with ancillary data to calculate transmission as a function of altitude. At the same time absorption cross section, model profiles and the UVIS instrument function are combined to generate a simulated transmission. From the comparison of these transmissions the column densities are calculated, and from them the number densities.

barycenter to the star of interest (as the distance to the star is much bigger than the distance from Cassini to the solar system barycenter, the error of this approximation is negligible). Although the reflexion and emission of the atmosphere is assumed to be negligible against the transmitted stellar light, at the moment to put the occultations in a bigger context it might be relevant to know if the atmosphere was in shadow during the observation. This was determined comparing, for all the samples in the observation, the nadir angle of the Sun from the tangent altitude point, with a critical nadir angle, defined between the normal to the surface passing by the tangent altitude point, and a tangent to Titan's surface passing by this point. If the nadir angle of the sun is bigger than the critical angle for a particular tangent altitude, that point in the atmosphere was not in shadow during the observation. The observation is in shadow if all the relevant tangent altitudes are.

The importance of the position and stability of the image of the source in the detector was stressed in Subsection 2.2.2. For all the stellar observations analyzed, the x position was only about a hundredth of mrad from the center of the slit and no wavelength shift was observed when comparing the measured star spectrum with a reference spectrum. Moreover, the position of the star in the field of view during

the whole observation was checked to be within the limits of the FOV and stable. An example of the calculated positions for T53 is shown in Fig 2.8. The angular size of the star is nil, and therefore the

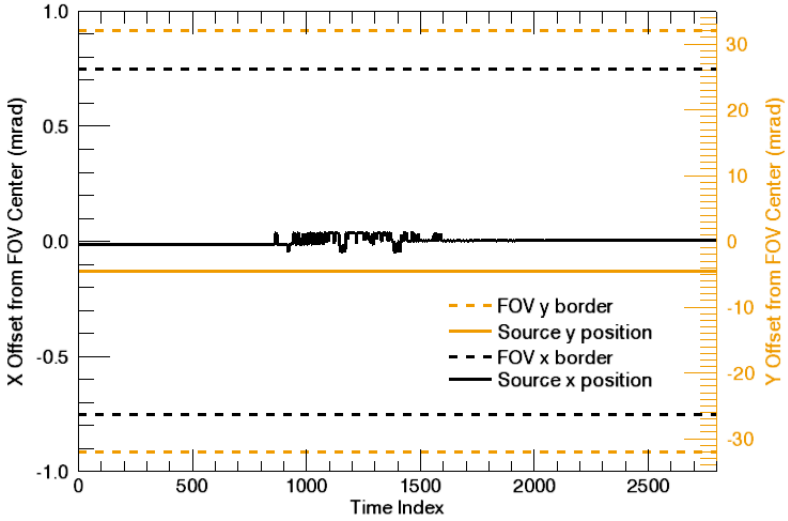

Figure 2.8: Star x and y position in the FOV of the UVIS/FUV low resolution slit, as a function of sample index (time), during the T53 flyby. The occultation is very stable, the small variations observed do not affect significantly the measured spectra—See section 2.4.2 for a discussion on pointing calculations accuracy.

altitude resolution is dictated by the altitude sampling of the atmosphere. This altitude sampling is, after altitude averaging, around 10 km for the stellar occultations analyzed.

The background for star occultations is determined from the counts measured low in the atmosphere, where no photons from the source are expected to reach the detector. Different ranges are used for different stellar occultations but all of them are comprised in between 15 and 300 km. The presence of low response ('evil') pixels in the detector is determined and the data corrected if those are present. If evil pixels are signaled in the PDS data, and the data presents moderate level of binning (which is the case for the stellar occultations analyzed), the pixels are linearly wavelength-interpolated, as suggested in the UVIS User's Guide (NASA-PDS, 2012). As only the relative intensity is the important quantity in the techniques used, no absolute intensity calibration is needed. Nevertheless, and with the only purpose of confirming the identity of the star being measured, the data was calibrated following the procedure in the PDS documentation. Figure 2.9 shows the UVIS calibrated spectrum of star Alpha Eridanus corresponding to an altitude of 2000 km, measured during flyby T53, compared with the spectrum measured by the International Ultraviolet Explorer (IUE), convolved with the UVIS/FUV instrument function and binned in UVIS/FUV wavelength channels. The IUE file used for this comparison was sp33528, retrieved from the IUE data archive[3].

In limb observations of Titan, absorption in the short wavelengths of the FUV range up to some 1400 Å is dominated by CH_4. In the region from 1400 to 1800 Å the absorption features of several hydrocarbons and nitriles overlap. The region above 1800 Å is dominated by aerosol extinction. Figure 2.10 show the absorption cross sections of several molecular species and the extinction cross sections of aerosols, used in the retrieval of atmospheric constituents performed from FUV observations. The characteristics of these data are shown in Table 2.2.

[3]http://archive.stsci.edu/iue/search.php

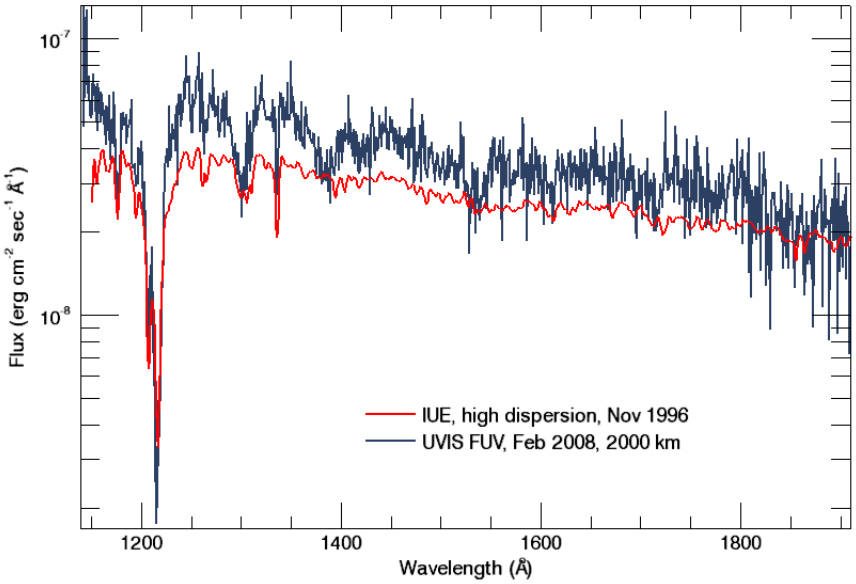

Figure 2.9: UVIS calibrated spectrum of star Alpha Eridanus, measured for an altitude of 2000 km during flyby T53; and the spectrum measured by the International Ultraviolet Explorer (IUE), convolved with the UVIS/FUV instrument function and binned in UVIS/FUV wavelength channels.

Table 2.2: The absorption cross sections used in the retrieval of atmospheric constituents performed from FUV observations. The species which absorption cross section was measured, the wavelength range, resolution, temperature for the measurements, and the corresponding references are shown. Extinction cross sections are listed for the aerosols.

Species	Wavelength Range (Å)	Temperature (K)	Resolution (Å)	Reference
CH_4	1200 – 1420	150	0.6	Chen and Wu (2004)
	1430 – 1520	295	1	Lee et al. (2001)
C_2H_2	1170 – 2109	150	0.05	Wu et al. (2001)
HCN	1150 – 1900	255	0.6	Bénilan (unpublisheda)
C_2H_4	1150 – 1900	140	0.6	Wu et al. (2004)
C_4H_2	1135 – 1698	173	0.5	Ferradaz et al. (2009)
	1700 – 1950	295	<0.8	Fahr and Nayak (1994)
HC_3N	1130 – 1630	203	0.5	Ferradaz et al. (2009)
	1650 – 2300	298	0.5	Ferradaz et al. (2009)
C_6H_6	1720 – 1910	215	1	this work
	1150 – 2050	298	1	this work
CH_3	1497 – 1504	n[a]	n[a]	Pilling et al. (1971)
	1127 – 1216	n[a]	7	Taatjes et al. (2008)
AER	1200 – 2000	n[a]	n[a]	(see Koskinen et al., 2011)

[a] n = Not available or not applicable.

The molecular absorption cross sections were measured in laboratory, the extinction for the aerosols were calculated for spherical aerosols with a radius of 100 Å, using Mie theory and assuming the optical properties of tholins (Khare et al., 1984; Koskinen et al., 2011).

The absorption of the different species at different altitudes is reflected in the measured transmission. As an example of the transmission measured by UVIS/FUV as function of altitude, curves for the stellar occultation T53 are shown in Figure 2.11. The sample curves correspond to bins [1200.00, 1362.23] Å, [1699.68, 1706.63] Å,[1740.38, 1818.63] Å, and [1800.00,1900.00] Å, dominated by CH_4, C_2H_4, C_6H_6, and AER absorption, respectively (see Table 3.1), although the contribution of other gases can not be completely neglected. Preliminary information can be derived already from

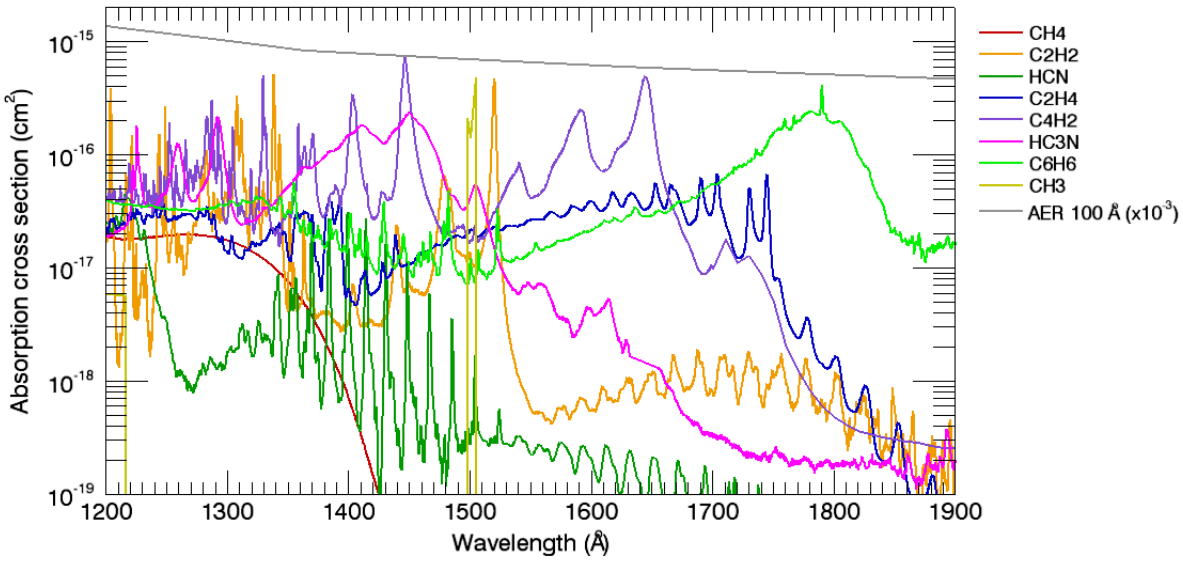

Figure 2.10: Absorption cross sections used in the retrieval of atmospheric constituents performed from FUV observations and extinction cross sections for spherical aerosols of 100 Å radius.

this early stage of analysis. CH_4 seems smoothly distributed in height, as if it were in hydrostatic equilibrium. C_2H_4 or, better said, the combination of gases absorbing in the second bin, form an absorption layer around 500 km (there are two absorption layers at about 500 km and 725 km in the corresponding T41 transmission curves). The last but one bin is expected to reflect the C_6H_6 abundance profile. An analysis of this kind using a bin similar to the last bin used here, where absorption is mainly due to aerosols, was used in Koskinen et al. (2011) to study the variations with time of the detached haze layer. An example of transmission spectra resulting from the combined absorption of the species, measured by UVIS/FUV during the stellar occultation T53 can be seen in Figure 2.12. Altitude averaged spectra corresponding to different altitudes are shown. Although the absorption of the different species are mingled, the characteristics of some of them are evident, like the absorption of C_2H_2 around 1520 Å. At the same time, it is also evident the difficulty of the identification of species with absorption bands above 1750 Å, where absorption is dominated by the featureless aerosol extinction. Particularly, this presents a challenge for the identification of benzene (see Chapter 4). Absorption spectra and transmission spectra like the ones shown, can be used in the determination of candidate molecules to be detected by UVIS/FUV in Titan. The spectra presented in this section are used for the retrieval of abundance vertical profiles, using the methods presented in Section 3.

2.4 Solar occultations measured by UVIS EUV

2.4.1 Introduction to solar occultations measured in the EUV

As shown in previous sections, solar occultations in the EUV are a powerful technique to identify molecules and derive their vertical profiles in planetary upper atmospheres. The EUV is the wavelength range where N_2 absorbs and is therefore of primary importance for studies of Titan's upper atmosphere. From the many molecules measured or predicted in Titan's upper atmosphere that could be detectable, in the present analysis of solar occultations the focus will be on N_2 and CH_4; the detection of less abundant molecules is complicated by the overwhelming absorption of these two in the whole EUV range. Knowledge of the distribution of these constituents with altitude, latitude, and longitude is key to constrain the atmospheric structure and dynamics, and thereby investigating energy and momentum

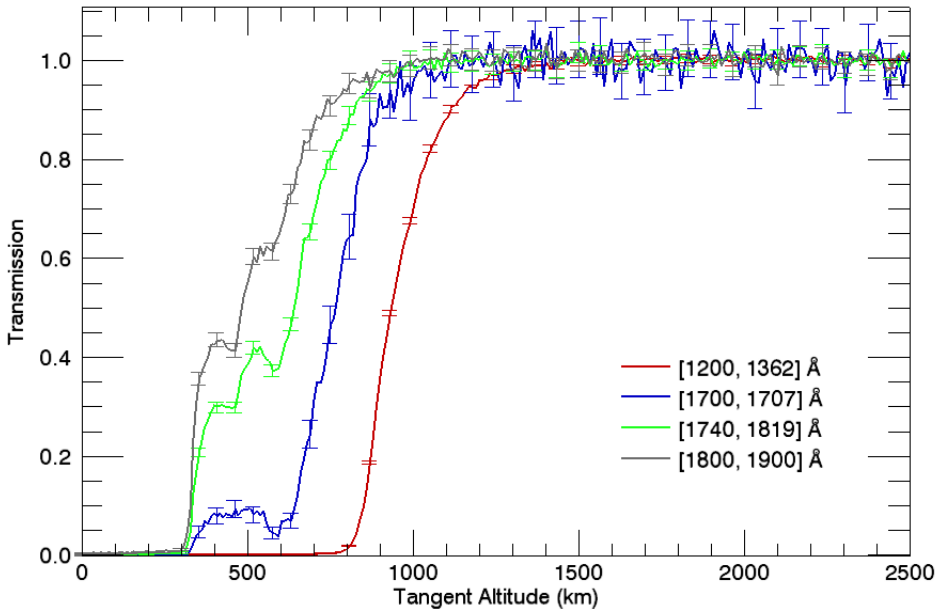

Figure 2.11: Transmission as a function of altitude, measured with UVIS/FUV for the wavelength bins shown in the graph, during the T53 stellar occultation.

balance in the upper atmosphere. EUV occultations can cover altitudes from 850 to 1500 km, which covers the upper thermosphere of Titan near and above the homopause (850 - 1000 km). The ionization and dissociation of N_2 and CH_4 happen in this upper region; moreover, the uppermost layers probed cover the ionosphere, where interactions with magnetospheric particles from Saturn can take place.

Until recently there were uncertainties about the absolute magnitude of the N_2 densities in the upper atmosphere, with disagreement among values inferred from *in situ* measurements by INMS in Cassini (Cui et al., 2009; Magee et al., 2009), from accelerometer measurements by the Huygens Atmospheric Structure Instrument (HASI, Fulchignoni et al. (2005)), and from the Attitude and Articulation Control System (AACS) on the Cassini spacecraft (Sarani, 2009). The fact that the densities from INMS are systematically smaller by about a factor 3 from HASI and AACS pointed to a need of recalibration in INMS. Therefore, independent assessments of upper atmosphere nitrogen densities are important in this respect, accurate and precise determination of the profiles of the main constituents being of primary importance. UV airglow measurements can be used to characterize the atmosphere (Stevens et al., 2011). However these results in the EUV have a vertical resolution of 120 km and are dependent on the accurate knowledge of the instrument function and the radiometric calibration of the Ultraviolet Imaging Spectrograph (UVIS), which has an uncertainty of ∼15%. The analysis of airglow data also depends on a complex model of the emission features, excitation cross sections and density profile of N_2. Therefore, solar occultations measured from a spacecraft and in-situ mass spectrometry are the most direct measurements of Titan's neutral upper atmospheric composition, providing a method to directly probe N_2 densities. UVIS solar occultations observed in the EUV measure absorption in the ionization and dissociation continuum of N_2 and the dissociation region of CH_4, where cross sections vary smoothly with wavelength and have been precisely measured in the laboratory. Data corresponding to these absorption regions are therefore relatively straightforward to analyze and should provide reliable results, largely free from systematic uncertainties.

The first solar occultation by Titan was measured by the UVS instrument (Broadfoot et al., 1977) onboard the Voyager 1 spacecraft. This instrument has a field of view (FOV) of 0.5 × 15 mrad and consists of a 128 detector array. It covers the range 500 - 1700 Å and has a resolution of 10 Å.

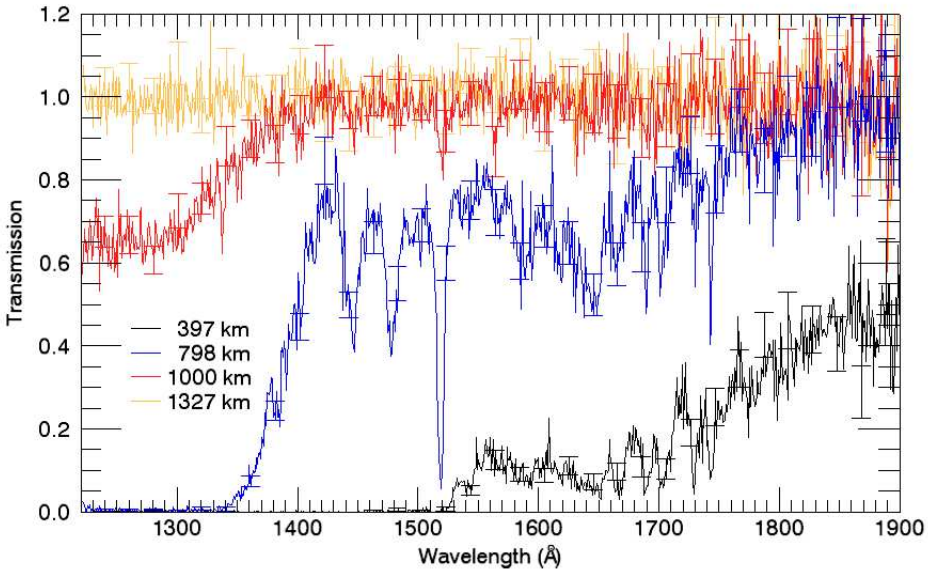

Figure 2.12: Transmission as a function wavelength for the tangent altitudes shown in the graph, measured with UVIS/FUV, during the T53 stellar occultation.

Although UVS measured an ingress and an egress occultations, Smith et al. (1982) concentrated on the ingress leg because it had better geometrical characteristics. The primary sources of uncertainties in this study were uncertainties in the reference intensity measured above the atmosphere, instrument specific uncertainties, including Ly-α scattering especially at long wavelengths. They used the data to confirm that the atmosphere is composed mainly of N_2 with a small abundance of CH_4, they also derived C_2H_2 abundances. They interpreted the data for wavelengths < 800 Å as N_2 absorption. The authors used a value of $2.5 \times 10^{-17} cm^2$ at a wavelength of 725 Å, but as was correctly observed by Vervack et al. (2004) later, the absorption cross section of N_2 presents structure in this region. Smith et al. (1982) derived number densities for CH_4 from the absorption at 1151, 1114, and 928 Å. Using the solar occultation data to constrain their model they derived an homopause at 925 km and a scale height for CH_4 of 149 km between 1265 and 1525 km altitude. Their results were used to constrain several subsequent models of the upper atmosphere (e.g., Yung et al. (1984); Lara et al. (1996); Yelle et al. (1997)). A reanalysis of the Voyager solar occultation made by Vervack et al. (2004) solved some inconsistencies noted by Strobel et al. (1992) in the Smith et al. (1982) opacity profiles, the new analysis found higher N_2 densities and lower CH_4 and C_2H_2 densities. Vervack et al. utilized a more sophisticated analysis technique and a more detailed model for the instrument to make corrections, improving the results. After forward modeling the transmission they used a Levenberg-Marquardt least squares routine to calculate the column densities. They assumed the absorption cross sections were temperature independent and a linear increase of the number densities in each atmospheric layer. Based on comparisons between the measured data and occultations simulated from photochemical models they chose 6 species to retrieve (N_2, CH_4, C_2H_2, C_2H_4, HCN, and HC_3N). It is important to consider that the Sun was ~ 8 km[4] in the atmosphere for this Voyager encounter and about 2 pixels in the UVS detector. They used the continuum N_2 absorption cross section below 650 Å to retrieve molecular nitrogen because the wavelength region presenting strong absorption bands was not well known. This impeded them from getting low altitudes N_2 densities and at the same time, due to the exclusion of the N_2 bands, this impeded them from getting high altitude densities for the other species. Fitting isothermal profiles to the derived number densities they found a temperature of (153 ± 5) K for

[4]Scale heights for N_2 measured in the present work vary in the range 60 – 80 km.

the thermosphere with no variation, taking into account the uncertainties, for the ingress and egress occultations. They observed differences of the CH_4 profile obtained at each terminator, and found a 'tentative' homopause at about 1000 km.

The higher spectral resolution of UVIS compared to UVS allows to better identify and use solar features for the retrieval. A closer observation and better spacecraft stability provide better altitude resolution and reduce the corrections needed when processing the data with respect to Voyager 1. In this work we present the first number density profiles of N_2 and CH_4, and temperatures in the thermosphere of Titan retrieved from solar occultations observed by UVIS (see also Capalbo et al., 2013). The measurements presented complement those from the references mentioned above since they were made at different times (28 years later in the case of the Voyager measurements) and correspond to different geographical locations. The methodology developed in the present work can be applied to future UVIS solar occultations to complement the temporal and spatial coverage of observations by this and other instruments.

2.4.2 UVIS/EUV solar occultation analysis

The geometric calculations and data handling procedures common to the FUV and EUV channels were described in Section 2.2; the results and particularities in the data reduction from the EUV channel are presented following, the relevant calculated quantities can be consulted in Table 2.5. The overall picture of the procedure used in this work to derive composition and temperature from solar occultations is schematized in Figure 2.13.

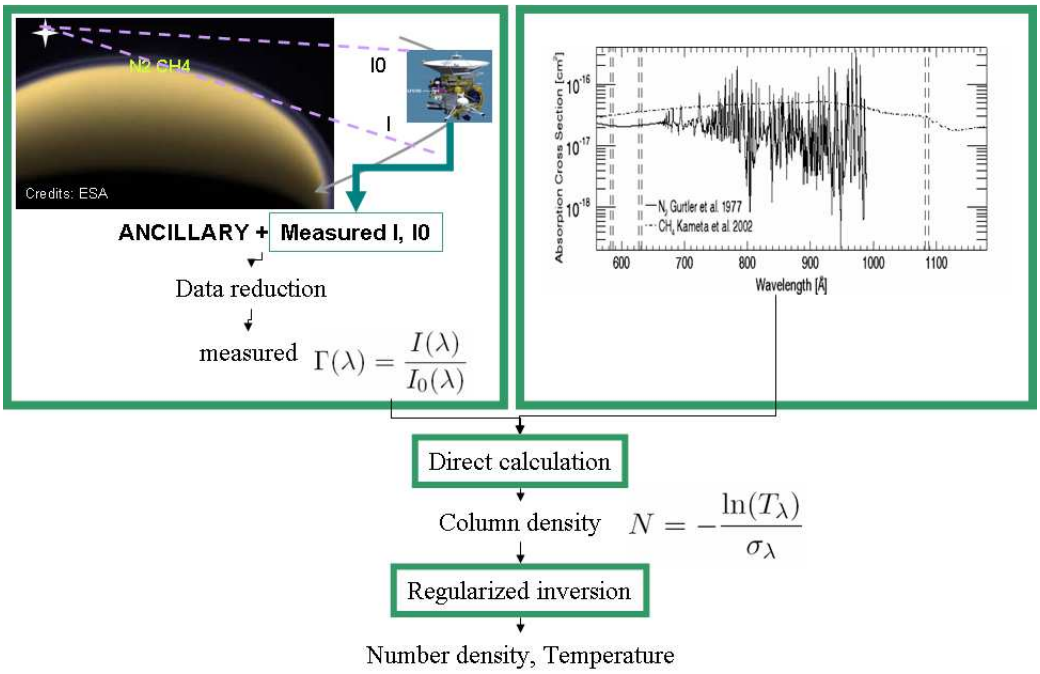

Figure 2.13: Workflow chart for solar occultation analysis. The raw UVIS data measured during a flyby are combined with ancillary data to calculate transmission as a function of altitude. From this transmission and experimental absorption cross sections the column densities are calculated and, from them, the number densities. From the N_2 number densities temperature for the upper atmosphere is derived.

The importance of the position, size and stability of the image of the source on the detector was stressed in Subsection 2.2.2. In the case of solar occultations, the position and the finite size of the Sun are mapped in the squared FOV of the solar occultation port. The angular size of the Sun in the FOV during the flybys is about 1 mrad. Based on this and the imaging performance of the instrument (McClintock et al., 1993), the spectral resolution is estimated to be 3.6 Å. The size of the

Sun at the atmosphere level depends on the distance from the spacecraft to the atmosphere and can be of the order of 1 - 20 km, which is most of the time bigger than the altitude sampling interval (see Table 2.5). In these cases the altitude resolution of the measured transmission is dictated by a combination of those quantities. Therefore binning of several samples was done, to produce a net sampling distance as to minimize the influence of overlapping solar projected disks. The criteria used was that the overlapping area at the borders of the averaged solar disk projections in the atmosphere had to be around 10% of the area covered by the averaged projections. This allows to take into account the finite size of the Sun in subsequent analysis while increasing the S/N. The reduction of sampling rate has in general no significant effect on the final altitude resolution for derived local densities, as this resolution is dominated by the inversion of column densities (Chapter 3). However, as commented in Subsection 2.2.2, cases of large altitude binning do degrade altitude resolution of the final results, could result in underestimated abundances at low altitudes and, therefore, overestimated temperatures. As a consequence the results obtained averaging many altitudes should be interpreted with caution. In the Voyager 1/UVS measurements the Sun had a size of 6 - 8 km at the atmosphere level. Simulations of the size of the Sun effect in Vervack et al. (2004) revealed that there were not significant differences between a single-segment uniform sun and a segmented non uniform one. For the solar occultations analyzed here, the Sun was assumed to be uniform. Finally, no variation of solar output during the occultations was assumed in the present work.

Some of the observations present significant drift in the x and/or y directions. Examples of the calculated positions and sizes in a case of good (flyby T58) and bad (flyby T62) pointing are shown in Fig 2.14. Although the flat filed response of the EUV detector is expected to be better than that

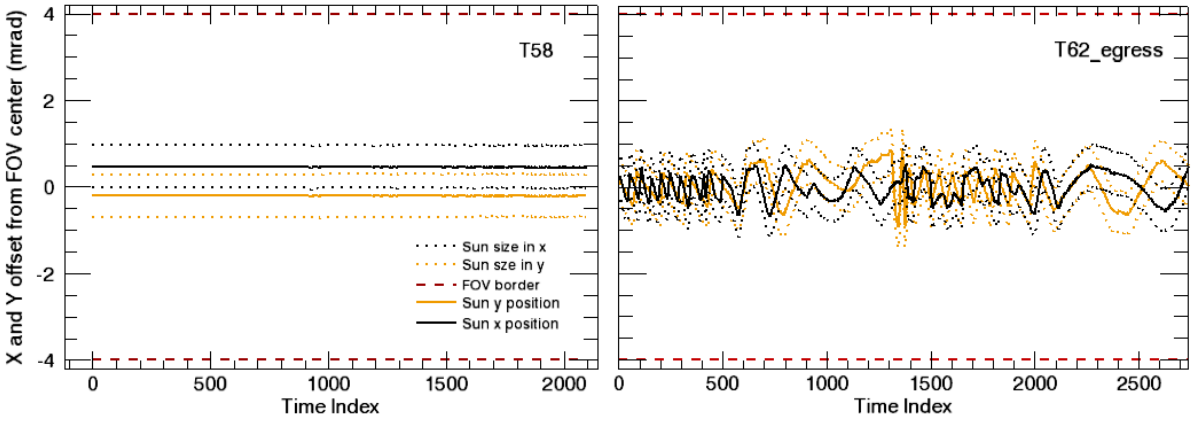

Figure 2.14: Sun position and size in the squared FOV of the UVIS solar occultation port for occultations T58 and the egress leg of T62.

of the FUV and, consequently, no significant variation in flux with position is expected; the time dependent wavelength shift associated with the drifts is significant for some of the observations (see transmission curves below). At this point the accuracy of the pointing calculated with SPICE and its relation with the wavelength shift become not only highly relevant, but traceable thanks to the strong emission lines in the solar spectrum. As stated in the SPICE documentation[5], because of the complexity of determining data accuracy, especially for time-dependent data, and also because of the complexity of processing any such data within SPICE, the SPICE system provides no numerical mechanisms for managing accuracy information. The accuracy of the derived data was then estimated

[5]http://naif.jpl.nasa.gov/pub/naif/toolkit_docs/C/info/intrdctn.html

from measurements of the solar spectrum and comparison with values of Cassini pointing stability. In the case of unstable occultations, like T62, the Sun can drift 0.89 mrad in 126 seconds (corresponding to 124 km in tangent altitude around 1200 km). As the instrument dispersion is ~ 2.4 Å/mrad, the drift would imply a wavelength relative shift of some 2.1 Å. This is approximately the shift in the 977 Å solar line that can be measured in the spectra corresponding to the two extreme positions of the Sun in those 126 seconds. Moreover, the drift of the line across UVIS wavelength channels measured independently during the wavelength registration procedure (see below) gives approximately the same result when translated to wavelength units. In cases of more stable occultations, like the case of T53, the calculated drift of the Sun in the FOV is 5×10^{-4} mrad in 700 s. This is curiously some 65 times smaller than values for Cassini's pointing stability under reaction wheels, which are around 56×10^{-3} mrad/1200 s (Macala, 2002). Again, considering the instrument dispersion, the drift would imply a wavelength relative shift of some 0.0012 Å. The shift is in this case imperceptible in the measured spectra. However, the solar line drifts across approximately 0.3 UVIS wavelength channels, as measured independently during the wavelength registration procedure (see below), which translates to 0.18 Å, or 0.075 mrad in the FOV x direction, orders of magnitude bigger than the drift derived with SPICE. The average position of the Sun in the x direction of the FOV, on the contrary, corresponds well with the observed absolute shift in the PDS-calibrated spectra (some 1.1 Å for T53); shift that was corrected (when possible) with the wavelength registration procedure described below. In sum, an interpretation of this is that the SPICE derived pointing calculations for big displacements of the source in the FOV are accurate, and can be traced to wavelength shifts in the spectra. On the contrary, small displacements are apparently not reproduced in the calculated position of the source in the FOV—the tenths of μrad measured commented above not being real variations in pointing, but calculation artifacts. In these cases the detection of eventual, more subtle wavelength shifts relies on the wavelength registration procedure. Finally, it is important to note that the image of the Sun remains in all cases within the limits of the FOV.

Instrument corrections, EUV channel

Apart from the common processing described in Subsection 2.2.2, specific procedures to correct the data from the EUV solar observations were necessary. The first 2 and the last 17 channels of the EUV detector (wavelengths: 561.229, 561.833 and 1171.84 - 1181.54 Å) presented no counts systematically and so they were eliminated from the array. Other corrections include background subtraction and wavelength registration. These corrections were performed separately for each detector line containing the source image, after the onboard binning and before adding the lines. These lines are, in all cases, lines 4 and 5 (index starting with 0).

Measured counts at a particular wavelength originating from photons not emitted by the Sun, or emitted by the Sun but at a different wavelength from that considered are regarded as background. There are many sources of background:

(1) The RTG background commented already in Subsection 2.2.2, can be neglected

(2) Photons coming from Interplanetary Hydrogen (IPH) emissions and other sources.

(3) Scattered light. This contribution can itself be divided into 3:

1. Light dispersed by the grating. Photons are not dispersed into only one angle as would happen in an ideal grating, but they spread across the whole detector. This behavior is characterized by the Point Spread Function (PSF) of the whole imaging system (basically, mirrors + diffraction grating). Therefore, photons of any wavelength can contribute to

counts in other wavelengths too. This effect is particularly important for very intense features in the source spectrum, as is the cases of Ly-α emission from the Sun.

2. Internal reflections. Photons scattered inside the instrument can reflect in the instrument case and reach the detector at any wavelength channel.

3. Glints. The idea of a contribution to the BKG from eventual glints is motivated by the observation of some features in UVIS EUV detector images corresponding to observations of the interplanetary medium. Occasionally, light can leak onto the detector through apertures in the instrument case, falling onto the detector directly, or after being scattered by the grating or internal reflections. This contribution is listed for completeness, but it is not characterized, rare, almost impossible to differentiate from the others, and expected to be a negligible fraction of the scattered light (McClintock personal communication).

The analysis presented accounts for contribution (2), and a part of contributions (3.1) and (3.2), the part that comes from long wavelength radiation. Contribution (2) is estimated from observations made when all solar light is completely extinguished by atmospheric absorption. All counts corresponding to altitudes lower than $\sim$ 300 km are averaged, giving in all cases a negligible contribution at a rate of a few 10^{-2} counts/sec/pixel; it is nevertheless subtracted from the raw data. Ajello et al. (2007); Steffl (2005) also found background counts from Inter-Planetary Hydrogen (IPH) scattered Ly-α to be negligible compared with other sources of background. The exact source, spectral and time variation of the scattered light (contribution (3) above) was unknown; the spectral and temporal characteristics of the data reveal the presence of at least two manifestations of this contribution. The first varies with time in the same manner as the count rate at the long wavelength end of the spectrum. This can be seen in Figure 2.15, showing the light curve for bins around the solar lines at 584 Å and 630 Å, and for a bin covering the range 1100 - 1160 Å. The time dependence of the counts in this

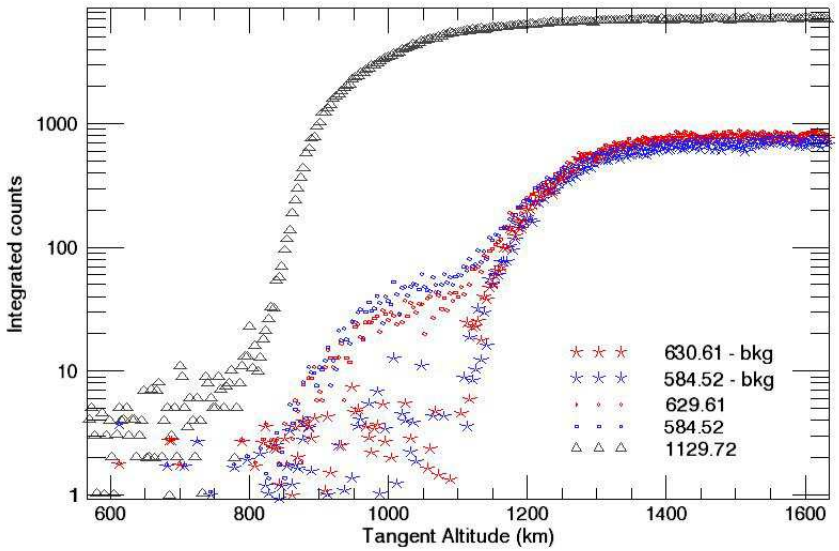

Figure 2.15: Light curves for 7-channel bins centered in two solar lines before (○) and after (⋆) the BKG correction. Light curve for a 100-channel bin in the long wavelength end of the detector used as proxy for one of the sources of BKG (△). The wavelengths corresponding to the center of the bins are shown in the plot, in Å. Data from the T53 flyby.

bin is supposed to be similar to that of the the Ly-α line at 1216 Å (whose behavior was unknown), based on the flatness of the methane absorption cross sections, and the negligible contribution of other absorbers in the wavelengths/altitudes involved. At low altitudes the light curve for the short wavelength bins show background counts that vanish for lower altitudes in a similar fashion to that

of the counts in the long wavelength bin. It is therefore hypothesized that this background is due to light scattered by the instrument from longer wavelengths, probably including the intense solar Ly-α line. The Ly-α line is orders of magnitude more intense than the lines in the EUV region and is not yet completely absorbed by methane at altitudes where radiation of short wavelengths is completely absorbed by nitrogen. This long wavelength contribution is more important longward of 1125 Å and shortward of 780 Å, where the signal is smaller (Ajello et al., 2007; Steffl, 2005). Accordingly with this analysis, this background was subtracted from the spectrum below 780 Å by assuming that it is proportional to the count rate in the 1100 - 1160 Å region, and requiring that the modified count rate in the 584 Å and 630 Å lines go to zero for altitudes where these lines have been extinguished by atmospheric absorption. Above 780 Å the average of the background in the 774 - 780 Å region was subtracted as a constant background. The total background (i.e. after adding all the relevant lines in the detector) as a function of altitude for the relevant bins involved in the density retrieval, as well as for the bin used as proxy for the background is shown in Figure 2.16, for the case of the T53 solar occultation. In the same figure the background as a function of wavelength is shown. In most of the

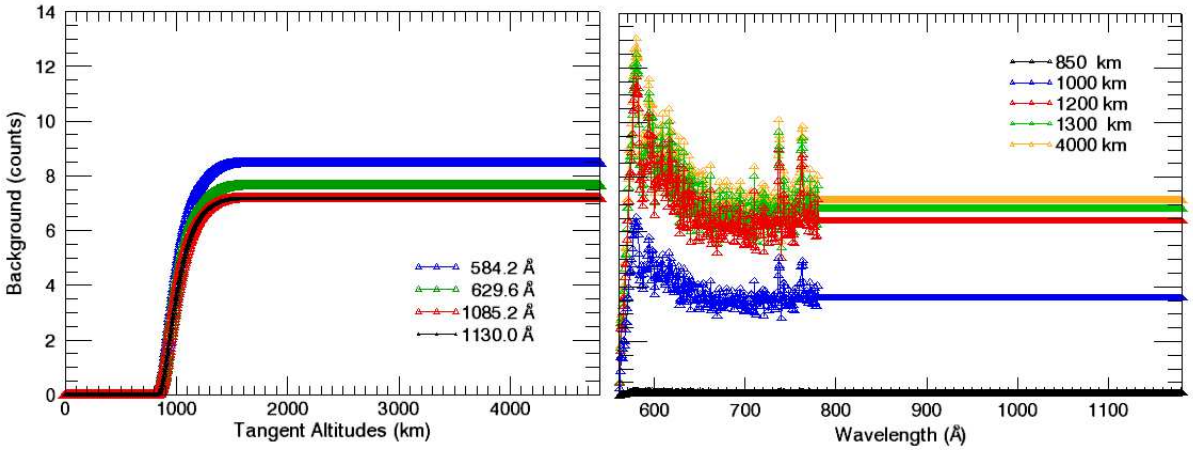

Figure 2.16: Left: The subtracted background as a function of altitude for the relevant bins involved in the retrieval of densities and background determination. Right: The subtracted background as a function of wavelength for different tangent altitudes. The data correspond to the T53 solar occultation.

cases, the transmission in the bin [1100 - 1160] Å was fitted by a continuous curve before scaling it to background value as explained above, to reduce contribution to noise in the background. In cases when the data could not be fitted properly, the data were smoothed, resulting in a noisier background than in cases when the fit was achieved. The background corrected counts for the bins shown in the left plot of Figure 2.16 differ in less than 10% for most of the altitudes when changing from fitting to smoothing the background. After these corrections a residual background remains, particularly next to the measured emission in 584 Å, 630 Å, and 1085 Å used in the analysis (see Figure 2.20). We interpret this second manifestation of this contribution to the background as extended wings of the instrument PSF. The temporal behavior of this second type of background is precisely the same as that of the spectral emissions features themselves—the absorption cross section in the spectral regions of our interest vary smoothly. Therefore, as this background has no effect on the analysis, it is not corrected. Moreover, the analysis is based on bins including only the core of the lines of interest, and excluding the wings, to minimize any contribution of residual background contamination. The corrected light curves for bins around 584 and 630 Å are shown in Figure 2.15. The background corrected solar spectrum is shown in Figure 2.20.

Other important data correction is the wavelength calibration and registration. For the solar

occultations the Sun can be imaged off the slit center in the dispersion direction, and it can drift further during the observation. This resulted in spectra from different samples suffering from a wavelength- and time-dependent shift with respect to the calibration provided in th PDS archive. Thus, after the PDS wavelength calibration, wavelength registration was needed. Based on the position of well known and strong solar emission lines a recalibration (also called correction in the following) mapping UVIS channel to wavelengths was performed individually on each sample (i.e., on each measured spectra). During the image drift in the detector, the flux of a spectral feature moves from one detector pixel to the other. This shift was first seen either as a slope or a strong fluctuation of the signal in some of the light curves, for altitudes outside the atmosphere. The top plots in Figure 2.17 show the light curves before and after background and wavelength correction for a stable (T53) and an unstable (egress leg of T62) occultation. The bottom plots of the same figure show counts in the UVIS/EUV channel corresponding to 629.61 Å (representative of a solar emission line) and to detector line 5 (as determined from the Gaussian fits, see below) as a function of observation time. In the case of T53, no perturbation

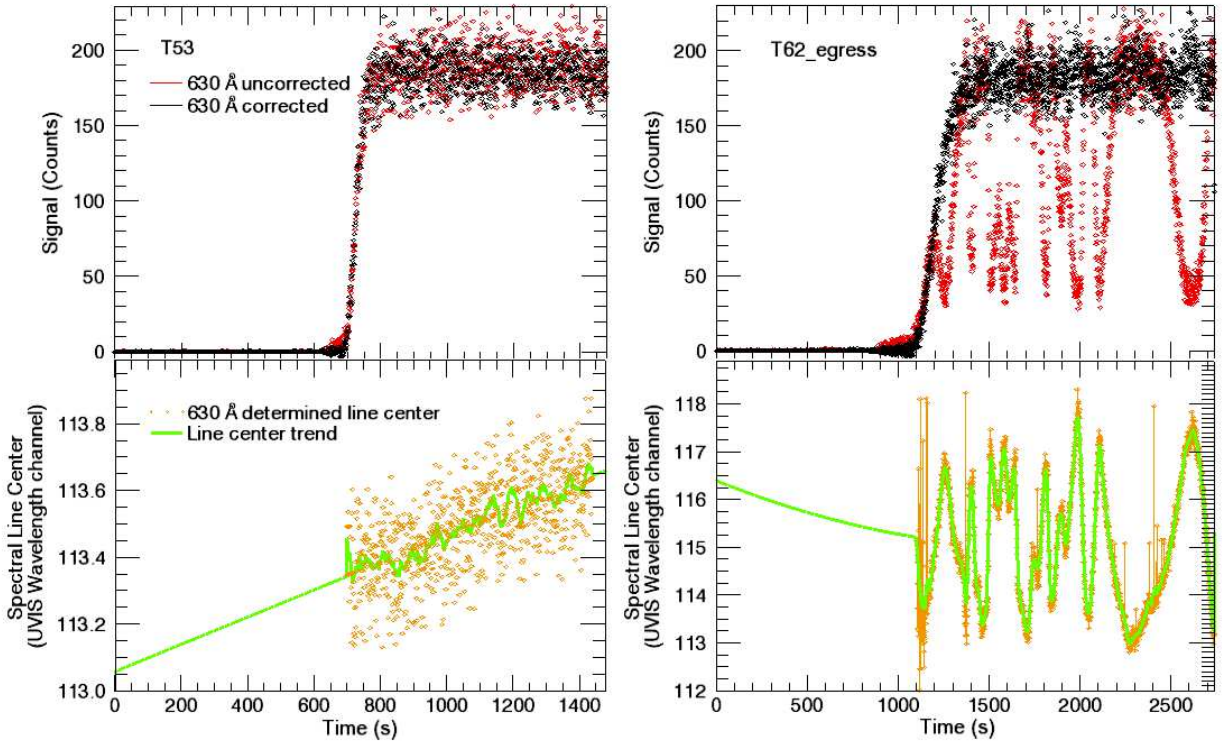

Figure 2.17: Top: Light curves before and after background and wavelength correction for UVIS/EUV channel 113, corresponding to 629.61 Å(representative of a solar emission line). Bottom: UVIS/EUV channel corresponding to the 629.61 Å emission line and to detector line 5 (as determined from the Gaussian fits, see text) as a function of observation time. The plots on the left and right correspond to the T53 and egress leg of T62 solar occultations, respectively.

is clear from a visual inspection of the light curves, but the analysis performed during the wavelength calibration described below shows a small, sub-pixel wavelength shift. For the unstable occultation case shown in the figure, the light curve is clearly spoiled by the shift. The recalibration procedure not only confirms the correlation of the fluctuations in the light curve with the shift of the line center in the detector—which, moreover, also correlates with the pointing drifts shown in Figure 2.14—but also correct the light curves. The slope of the light curves for all wavelength channels in the detector is shown for T53 in Figure 2.18 (Left). The relative dispersion—standard deviation over mean—of the part of the light curves above TOA, for all channels in the detector, is shown for the egress leg of T62

in Figure 2.18 (Right). The effects of wavelength shifts are more evident for stronger solar emission

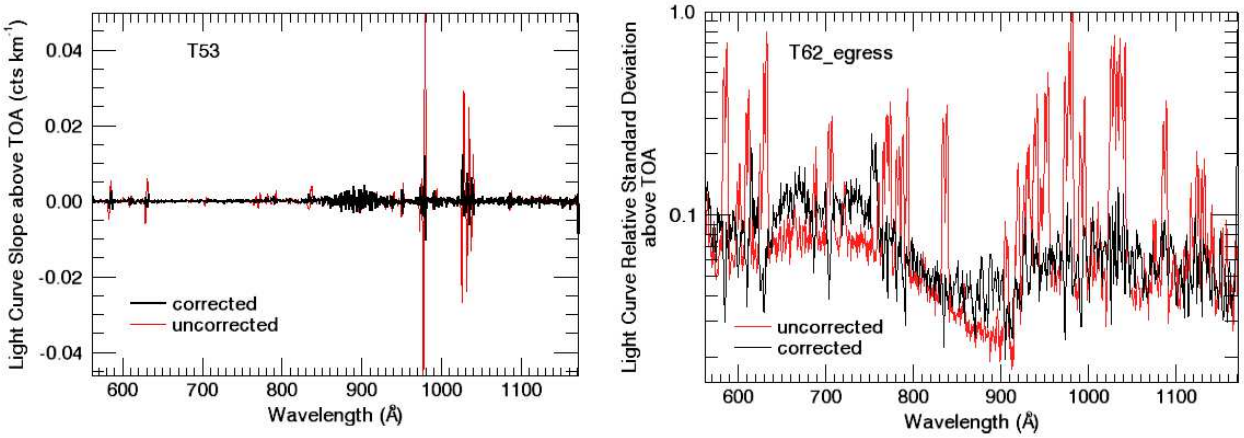

Figure 2.18: Left: Slope of the light curves for altitudes above TOA for all the EUV wavelength channels before and after wavelength correction. Data are from T53 solar occultation. Right: The relative dispersion of the data around the mean for altitudes above TOA for all the EUV wavelength channels before and after wavelength correction. Data are from the egress leg of the T62 solar occultation.

lines. It has to be kept in mind that these are extreme cases (particularly pathological in the case of T62) that are shown just to give an idea of the methods used to quantify the defects and the results of the corrections. Each observation has its own characteristics and these methods are more or less effective in each case.

The wavelength registration procedure is as follows. A set of solar lines was chosen as reference, based on their clear identification in the UVIS spectra. Bunches of lines with similar intensity unresolved by UVIS were ignored. The chosen solar lines were: 584.33, 629.72, 949.74, 977.03, 1025.73, and 1031.91 Å (see for example Curdt W. et al., 2001). The UVIS channels corresponding to these lines were identified in the UVIS spectra as the center of a Gaussian fitted to the relevant part of the UVIS spectrum. This was done for each altitude for which the reference line was not absorbed (i.e., the transmission in a bin around the solar line measured by UVIS was bigger than 5%). These altitudes differ from line to line. After filtering of outliers, that result for altitudes for which the Gaussian fit was not accomplished properly, the outcome was the centers of the lines, in units of detector channel, as a function of altitude, or observation time, as shown in Figure 2.17 (Bottom). As the movement of the spacecraft, that originated the pointing drift and consequently the variation in the curve, is expected to be smoother than the oscillations observed, the data was smoothed to eliminate these high frequency variations (this smoothed trend is also shown in Figure 2.17). For the lower altitudes, where the lines were absorbed, or high altitudes presenting a strange behavior, a quadratic extrapolation of the behavior at the center altitudes was used. The measured wavelength shift for the reference lines vary from occultation to occultation, being of 3.2 Å ($\sim$ 5 pixels) in the worst case. The residual, defined as the difference between the reference and corrected wavelengths, is up to 0.4 Å in the worst case, but less than 0.2 Å in most of them. This is the accuracy of the wavelength recalibration, which is about 1/3 of an EUV wavelength channel.

A second order wavelength calibration polynomial was then derived for each altitude according to

$$Wl = a_0 + a_1 n + a_2 n^2 \tag{2.10}$$

where n is UVIS channel number, Wl is the corrected wavelength, and the coefficients are altitude (or time) dependent. The calibration coefficients for the T53 occultation are shown in Figure 2.19.

The resulting light curves after the correction presented a notorious improvement with respect to non

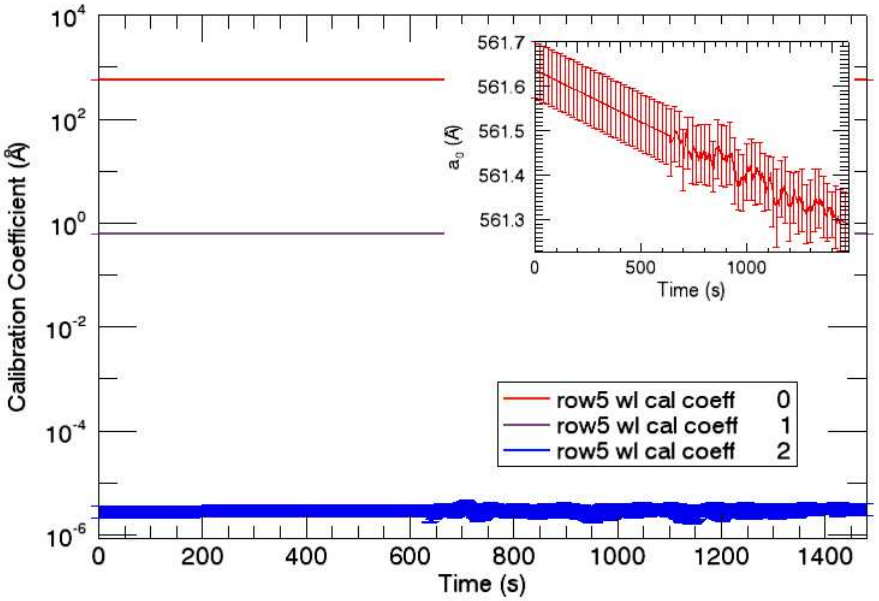

Figure 2.19: Wavelength calibration coefficients as a function of observation time for detector line 5, solar occultation T53. The inset shows the a_0 coefficient, with uncertainties plotted every 20 values for clarity.

corrected data (see Figures 2.17 and 2.18). It is worth noting that the analysis of absorption is based on bins around solar emission lines, and that the flux in a bin of several pixels centered in a solar line is constant with altitude even in the case of a small wavelength shift. However, the wavelength recalibration allows to take a smaller bin centered in the solar line, excluding the wings that could be more affected by background; therefore the wavelength recalibration is worth performing in all cases.

Finally, correction of instrumental effects can also concern the flat field (FF) response of the instrument. Pixel-to-pixel variations in the detector can result in unrealistic variations in the signal. For example, the image of a spectral and spatial uniform source would not be a uniform image. In an occultation analysis the important quantity is the relative variation of the signal (before and after the radiation passed through the atmosphere) and in principle a FF correction is not necessary. Nevertheless, as the position of a finite source in the detector can vary during the occultation, a non-flat detector response would give an unrealistic change in signal with time. Motion in the spatial dimension could result in a false change of intensity for a particular wavelength. Motion in the dispersion direction would result in a wavelength shift combined with a false change of intensity of a particular spectral feature. This is solved with a FF correction, which compensates the pixel-to-pixel variations. There is not known FF correction for the solar occultation port of the EUV channel. Attempts to apply a FF correction corresponding to other slit states (see Steffl, 2005) did not provide satisfactory results (this was evaluated by visual inspection of the resulting spectra after the FF correction: increasing noise in the continuum and deformation of spectral features). Moreover, the detector cube downloaded from the PDS archive is already windowed and binned in the case of solar occultations, discarding the possibility of the application of a FF. The wavelength recalibrated light curves were visually inspected for effects of source motion in a non-flat detector. No change in signal (beyond noise level) was appreciated. Therefore, any eventual pixel-to-pixel variation is expected not to distort the data as to affect the results significantly. The corrected data is ready to be interpreted in terms of absorption of the solar spectrum through the atmosphere.

Solar Spectrum and atmospheric absorption

The solar spectrum was measured by UVIS when the line of sight was outside the atmosphere. The spectrum from the T53 flyby is shown in the upper panel of Figure 2.20 as an example; it is an average of all the corrected samples corresponding to tangent altitudes from 2000 to 4800 km. The attempts to radiometrically calibrate this spectrum with the PDS calibration procedure was unsuccessful, possibly due to the lack of a calibration matrix for the solar occultation port (including the pick-off mirror). The

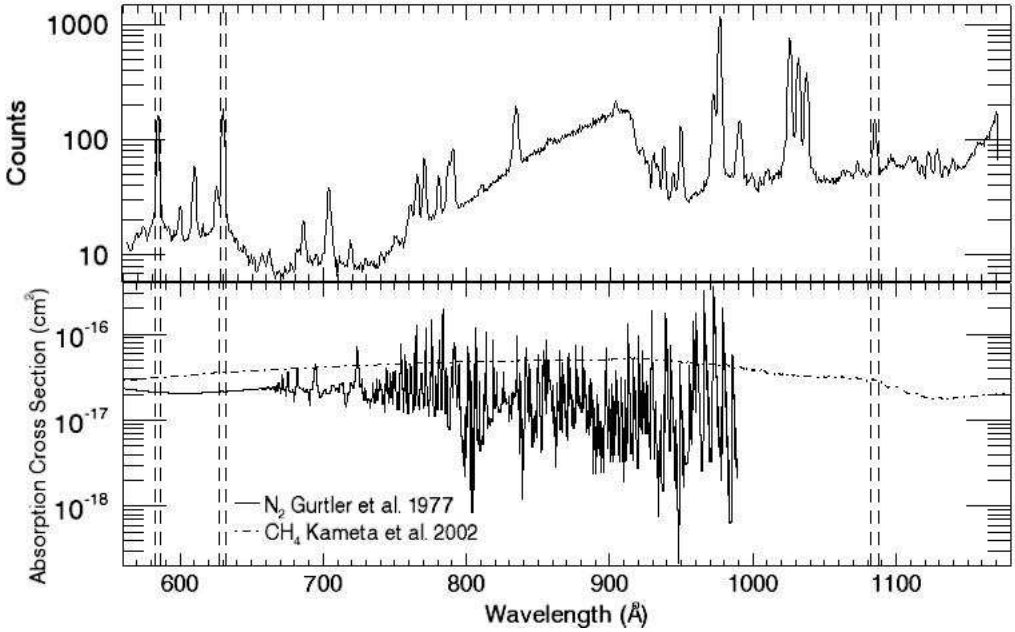

Figure 2.20: Solar spectrum measured during the T53 flyby (top). N_2 and CH_4 absorption cross sections (bottom). The spectral bins used in the analysis are represented by the dashed vertical lines.

spectrum consists mainly of intense solar lines, some continuum emission, and residual background.

Figure 2.20 also shows the absorption cross sections of N_2 (Gurtler et al., 1977)[6] and CH_4 (Kameta et al., 2002), the main EUV absorbers in Titan's atmosphere. The absorption cross sections for N_2 have a resolution of 0.03 Å and there is no comment about the measurement temperature in the reference. The CH_4 absorption cross section have a resolution of 1 to 4 Å and were measured at 298 K. As underlined by De La Haye et al. (2008) (see their Figure 1) nitrogen, by far the dominant atmospheric constituent (98%), is the almost exclusive absorber of photons with energy in its absorption region, 561 - 1000 Å in the UVIS/EUV range. Methane (2%) has a wider absorption region (561 - 1450 Å in UVIS/EUV,FUV ranges), and absorbs most photons in the remaining 1000 - 1450 Å wavelength range. The less energetic photons penetrate deeper into the atmosphere and can be absorbed by minor species (see Subsection 2.3.2). Lavvas et al. (2011) presented a detailed model for photodissociation and ionization of N_2 and CH_4 incorporating the latest photoabsorption cross sections at that time and including contribution from photoelectrons. Ionization dominates for N_2 in the range 500 - 800 Å (range including the bins used in this work to detect molecular nitrogen). N_2 loss is due to photons and electrons, and results mainly in ionization (∼67% of products). The coupled-channel Schroedinger equation calculations fail to reproduce the measurements at wavelengths smaller than 845 Å so the use of measurements, although at lower resolution than the theoretical calculations, is the better

[6]Note that these absorption cross sections are shown for illustrative purposes only, the retrieval of N_2 is done using the absorption cross section values in Samson et al. (1987).

Table 2.3: Wavelength bins used in the analysis of solar occultations.

Wavelength bin, Å	Central UVIS wavelength, Å	Wavelength channels binned
[582.3, 586.3]	584.3	7
[627.7, 631.7]	629.7	7
[1082.2, 1088.2]	1085.2	9

option nowadays (Lavvas et al., 2011). Measurements at higher resolutions, like those possible at the SOLEIL synchrotron facility, could resolve N_2 bands and could be available in the future. The picture for CH_4 loss is different because its absorption extends to longer wavelengths. Ionization peaks at 1000 km. Dissociation peaks at ∼800 km, and dominates above 900 Å for CH_4 (this is the range used to retrieve CH_4 in this work). The loss process is mainly due to photons, and the result is mainly neutral dissociation, with ionization being less important. Absorption cross sections measured are expected to be accurate enough in the region above 900 Å. In this work we retrieve the density profiles of N_2 and CH_4 by using two bins centered on the solar HeI line at 584 Å (582.40 - 586.63 Å) and OV line at 630 Å (627.79 - 631.43 Å), and a bin spanning solar lines around 1085 Å (1082.12 - 1088.19 Å), respectively. This retrieval procedure takes advantage of the facts that CH_4 dominates absorption in the long wavelength bin, that N_2 dominates absorption in the short wavelength bins (although a CH_4 contribution is still important and accounted for, see Chapter 3), and that the cross sections do not change significantly in the wavelength bins used. The corresponding bins are marked with dashed lines in Figure 2.20 and can be consulted, together with the central wavelengths, in Table 2.3.

Transmission measured in a solar occultation

After the instrument corrections, the next step in the analysis is the calculation of the atmospheric transmission according to the procedure described in the preceding sections of this chapter. Figure 2.21 shows an example of atmospheric transmission for three wavelengths bins, measured during the solar occultation that took place in the T53 flyby. The transmissions in the 584 and 630 Å bins are in

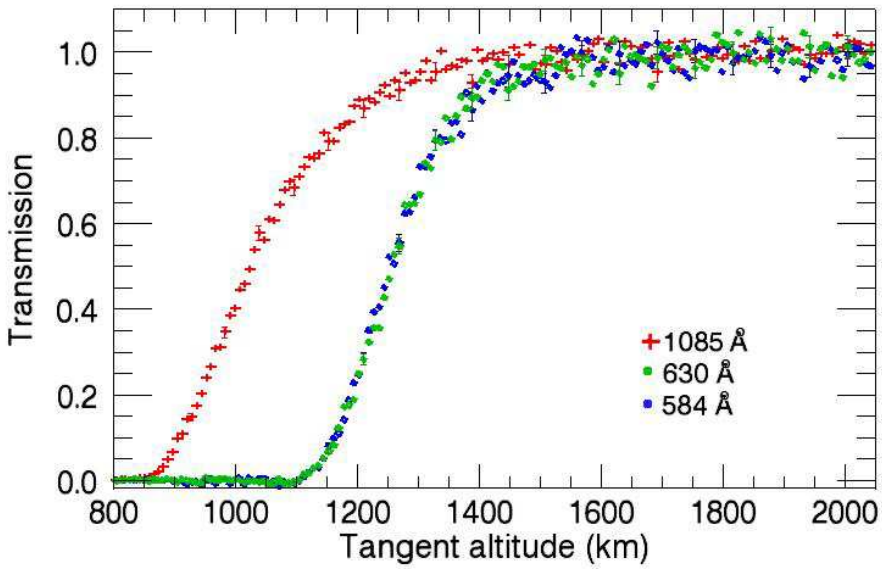

Figure 2.21: Transmission as a function of tangent altitude, corresponding to the solar occultation during flyby T53. The curves correspond to the wavelength bins used in the analysis, centered in the measured emission peaks whose wavelengths are shown in the graph.

excellent agreement, with half-light levels at 1254 km. The half-light level for the 1085 Å bin is at

Table 2.4: Characteristics of stellar occultations analyzed.

Flyby	Data product (FUV <yyyy_doy_hh_mm>)	Star	Lat. (deg) [a]	Lon. (deg W) [a]	Atmosp. in shadow [a]	Altitudes probed (km)	Original sampling (km) [a]	Sc - tg. alt. min. distance (km) [a]
T41	FUV 2008_054_15_36	ϵ CMa	-2 – -10	332 – 334	yes	243 – 2000	0.4	4.7×10^5
T53	FUV 2009_109_21_23	α Eri	38 – 39	294 – 308	no	0 – 4627	1.6	3.8×10^4

[a] for altitudes relevant to absorption measurements

1023 km. It is clear from the figure how radiation in the 584 Å and 630 Å bins is absorbed much higher in the atmosphere than radiation in the 1085 Å bin because of the much higher abundance of N_2. As can be seen from Figure 2.21 there is no sign of absorption layers for the altitudes probed.

2.5 Temporal/spatial coverage of data

This section presents ancillary information about the observations analyzed, to be used for further references in the following chapters, especially the one dealing with atmospheric variability. These metadata include geometrical, geographical, and temporal information derived from the geometry analysis described in Subsection 2.2.2.

Geometric and other ancillary information about the stellar occultations analyzed in this work is presented in Table 2.4. The stars occulted during flybys T41 and T53 were Epsilon Canis Majoris (Adara), and Alpha Eridanus (Achernar), respectively.

The search for solar occultation observations was performed in several ways, with different advantages and disadvantages and obtaining consistent results among them. The search tool provided by the rings node of the PDS[7] was one of the methods used. This tool allows to search for UVIS observations targeting the Sun. However, the PDS label of one of the solar occultation observations have an 'UNKNOWN' target, which has also to be taken into account during the search. A second method was based on the search in all the '.TAB' files for all the UVIS volumes in the PDS. Solar occultations were then identified by the value of some of the fields in the tabulated data (like ODC_ID), then the PDS label of candidate observations can be inspected to see if their DESCRIPTION field identifies them as an observation of solar radiation through Titan's atmosphere. This method gives more control of the search details, but is more complex and time consuming. Finally, all the labels corresponding to EUV observations in the PDS were analyzed in the search of a description matching that of an observation of solar radiation through Titan's atmosphere. Among them, observations with the Sun as target should be identified. This method finds exactly the files of concern, but involves the handling of several thousand files by the user. The result of the search is a list of all the solar occultations through Titan's atmosphere measured with the UVIS/EUV channel by August 2013. Metadata information about the solar occultations analyzed in this work is presented in Table 2.5. In cases when a range is presented, the values are sorted according to increasing time of observation.

This final list merits some comments. In some cases an ingress and egress occultations were measured during the same flyby. This is the case of T10, T62 and T78. The occultations can be in the same data product (same file, like for T10 and T78) or in separate products. The T10 ingress occultation data is unusable, the spacecraft was inside the atmosphere while the occultation took place and the light curves are not appropriate for the analysis. T62_eg also grazed the atmosphere for tangent altitudes higher than 1300 km, but the resulting light curves were appropriate for abundance retrieval. Observations during T10, T26, and both observations during T62 suffer from pointing

[7] OPUS search tool website: http://pds-rings.seti.org/search/

Table 2.5: Characteristics of solar occultations analyzed.

Flyby	Data product (EUV yyyy_doy_hh_mm)	Lat.[a](deg)	Lon.[a](deg W)	LST[b] (hh:mm)	SLT[b] (hh:mm)	Altitudes probed (km)	Original sampling[a] (km)	Sun size in atm.[a](km)	Sc - tg. alt. min. dist.[a] (km)	T (K)
T10_eg	EUV 2006_015_11_25	-62 – -55	0 – 10	20:04	08:29	0 – 5365	2.6 – 2.9	9.7 – 10.8	9483	164
T26	EUV 2007_069_01_05	-76 – -77	39 – 29	23:10	13:46	10185 – 0	5.4 - 5.3	5.6 - 5.4	5300	139
T53	EUV 2009_110_00_11	-21 – -28	237	18:03	22:02	0 – 4802	3.9 – 4.3	5.1 – 4.8	3190	148
T58	EUV 2009_189_15_42	86 – 85	239 – 236	17:40	21:46	6663 – 0	3.2	11.5 – 10.9	9738	119
T62_in	EUV 2009_285_06_27	1 – -5	230	18:00	21:30	5937 – 0	1.3 – 1.2	25 – 23	18680	169
T62_eg	EUV 2009_285_08_15	-68 – -62	48 – 49	06:09	21:36	0 – 2432	1.1 – 0.9	2.7 – 0.0	0	137
T78_in	EUV 2011_255_02_23	28 – 32	162 – 161	18:28	17:31	4021 – 0	5.0 – 4.8	9.4 – 9.2	9217	119
T78_eg	EUV 2011_255_02_23	25 – 20	354 – 353	05:42	17:32	0 – 7914	4.8 – 5.0	7.4 – 7.2	8009	154

[a] for altitudes relevant to CH_4 or N_2 absorption.
[b] for the half light point in the 584 Å bin light curve.

instabilities causing wavelength shifts. In these cases the wavelength recalibration procedure described in Section 2.4.2 allowed to correct the data and to obtain acceptable light curves and spectra, to which the retrieval procedure could be applied. Although flybys T53, T58 and T78 are more stable and the correction is not critical, the wavelength correction was still performed to improve the quality of the data. The solar occultation that took place during the T53 flyby benefits from particularly good pointing stability and small attitude drift. Additionally, UVIS observed a stellar occultation during T53 (Koskinen et al., 2011, see also Table 2.4), providing the opportunity to compare the CH_4 densities derived from each observation. The solar occultation measured during flyby T32 presented pointing instabilities that could not be corrected with the procedures use in this work, therefore no abundances were derived from it. Curiously, misassigned keywords in some PDS labels produced 'false findings' in the search outputs. This is the case for product EUV2008_027_19_32 which is actually a Saturn solar occultation, and the case of product EUV2007_273_08_04 which, judging for the look of the light curves, is probably a Saturn solar occultation too. This might explain why none of these observations were included in the analysis of Saturn solar occultations by Koskinen et al. (2013). All things considered, although the general characteristics of the solar occultations are similar and a common analysis protocol could be established, all present particularities that complicate the study from the search of the observations till the final analysis of the results, calling for especial attention in each case.

The geographical coordinates for relevant altitudes (in terms of absorption) of all the observations analyzed are summarized in Figure 2.22. The latitude coverage is comprehensive, the occultations

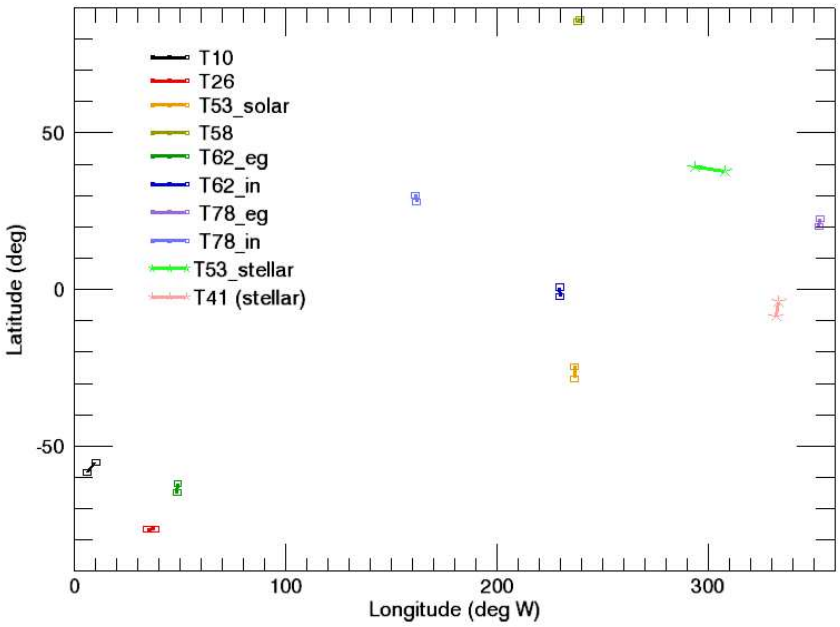

Figure 2.22: Latitude and Longitude for all the observations analyzed.

probed low, mid and high latitudes in both hemispheres. There are however gaps of sampling, most of the occultations accumulating in low/mid latitudes on both hemispheres and longitudes above 150° W, or in high southern latitudes and longitudes below 100° W, leaving unexplored a region known in terms of magnetospheric interaction as the wake region. The Titan Solar Local Time and the position of Titan in Saturn orbit given in terms of the Saturn Local Time, for the solar occultations, are shown in Figure 2.23. Most of the solar occultations took place at the evening terminator, none of them took place while Titan was positioned from Saturn midnight to Saturn sunrise times.

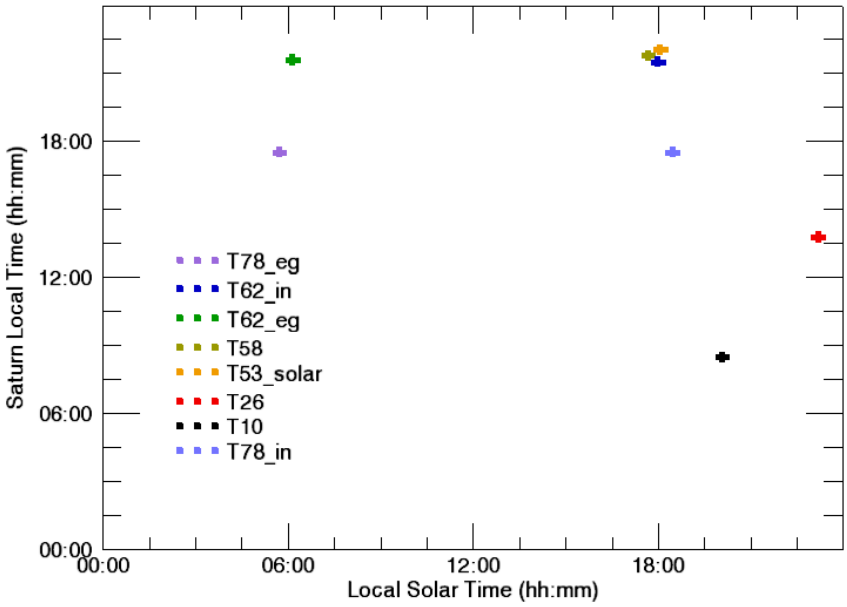

Figure 2.23: Saturn Local Time and Titan Local Solar Time corresponding to the solar occultations analyzed.

2.6 Summary of chapter

The particularities of the UVIS FUV and EUV channels and the corresponding data were outlined. This work deals with time series of spatial-spectral images: spatial-spectral cubes, downloaded from the PDS data archive. Ancillary data necessary for the analysis are provided and handled by SPICE kernels and routines, implemented in the software developed by the author.

The formalism and techniques described in this chapter allow to analyze stellar and solar occultations measured by UVIS, and to derive composition and temperature of Titan's upper atmosphere. The first steps of this analysis, common to both types of occultations, concern geometry calculations and basic operations and checks on the spatial-spectral cubes. Then each type of occultation needs a specific analysis. The differences and similarities of stellar and solar occultations were commented in this chapter, in connection with differences in the source, instrumental, or geometric characteristics.

An introduction to stellar and solar occultations was given, followed by specifics of the analysis for each type. Stellar occultations measured by UVIS have been presented before, showing the potential of the instrument in deriving profiles of minor hydrocarbons, nitriles, and aerosols in Titan's thermosphere. This motivates the continuation and verification of these kind of studies, as will follow in the present work. The analysis of a solar occultation measured by UVIS, on the contrary, was just recently performed by the author of this work (Capalbo et al., 2013), the remaining solar occultations in the archive are presented here. They provide a wonderful opportunity to derive abundance of N_2 and temperatures, and to compare them with the only solar occultation measured before (by UVS on Voyager 1, in 1980) and with INMS results.

The introductions to stellar and solar occultations were followed by analyses specific for each type. These analyses include pointing and instrument corrections. The stellar occultations presented show a stable pointing, some of the solar occultations do not. The most important instrument corrections are the background and the wavelength corrections implemented for the EUV channel. The wavelength correction makes suitable for analysis observations otherwise spoiled by pointing drifts. The analysis involves the absorption or extinction due to the species in the atmosphere. In the case of the stellar

occultations, the absorption spectrum of minor hydrocarbons in the full range of the FUV channel should be considered. On the contrary, the dominant absorption of N_2 and CH_4 in the EUV allows to base the analysis in three representative wavelength bins (582.40 - 586.63 Å, 627.79 - 631.43 Å, and 1082.12 - 1088.19 Å). The end point of the preliminary analysis is transmission as a function of altitude and as a function of wavelength, ready to be the input of the retrieval methods described in Chapter 3.

The last section of this chapter presents all the observations analyzed in this work. This database, containing all the UVIS solar occultations in the PDS archive to the best of the knowledge of the author, serves as a reference for the further reading of the manuscript.

Chapter 3

Retrieval methods

In Section 2.2 it was explained how the measured transmission is related to the atmospheric composition. A column density profile for the constituents was derived from the analysis of the transmission measured at different tangent altitudes, and from the column densities the number densities were obtained. The methods used are explained in this section. These problems are generally ill-posed (the solution might exist but may not be unique nor stable) and therefore measurements do not uniquely determine the solution: the presence of measurement uncertainties means that there is no unique mapping from the measurement space to the solution space and/or the information provided by the equations are not independent. The two separate problems (deriving column densities from the measured transmission and number densities from the column densities) have their own complications: in the first case of spectral analysis, for a particular height, the measurement vector has as many values as wavelength channels and the solution as many elements as species are included in the retrieval. There are generally more measurements than unknowns giving an over-determined problem. Besides, the model relating the measured and unknown quantities is complex. All this calls for a least-squares minimization. For the second case of spatial inversion, from a discrete number of column densities a continuous quantity is searched: the number densities as a function of altitude, therefore several states in the solution space might lead to the measured quantities. Discretization of the problem helps to make it well-determined but it remains ill-conditioned, as the problem suffers from noise amplification, i.e., small noise in the measured quantities would result in huge errors or oscillations of the retrieved quantities. In this second case the quantities are related in a linear form. For these reasons the column density profiles for the constituents were retrieved using a χ^2-minimization technique and the number density profiles were retrieved using a constrained linear inversion method. Very similar procedures have been used before to determine number densities (Vervack et al., 2004; Koskinen et al., 2011; Quemerais et al., 2006) and the technique presented here follows them closely, particularly the ones in the last reference. The first part of the transmission analysis is different for the solar occultations. As only a wavelength bin at a time is involved, there is no need for a least-squares spectral analysis, the column densities are calculated directly from the ratio of measured transmission and the absorption cross section. The resulting column densities and number densities for stellar and solar occultations are presented in Chapter 5.

3.1 Column density retrieval, stellar occultations

In the present study the transmission through the atmosphere is assumed to be the result of absorption by the gaseous constituents and aerosol extinction (see Equation 2.4). With the assumptions made in Section 2.2.1 the transmission can be modeled as in Equation 3.1 (see Equation 2.7).

$$\Gamma_{mod}(\lambda) = \exp(-\tau_l(\lambda)) = exp(-\sum_{s=1}^{S} \sigma_s(\lambda) N_{tot_{l,s}}) \tag{3.1}$$

$N_{tot_{l,s}}$ is the sum of the column densities of species s over all traversed atmospheric layers while the tangent altitude corresponds to the middle point of layer l (Equation 2.9). The procedure to derive the column densities from the transmission can be seen as the search of a set of column densities N (the parameters in our model, subscripts $_{tot_{l,s}}$ will be omitted for clarity) that will maximize the probability density function (p.d.f.) $\mathrm{P}(N|\Gamma_{meas})$ for the probability that the column densities are N given a measured transmission Γ_{meas} (see for example Kyrola et al., 1993). Under the assumption of normally distributed N and Γ values, the logarithm of this p.d.f. can be expressed in terms of the negative of a cost function involving the measurements (Γ_{meas}) and its covariance matrix ($S_{\Gamma_{meas}}$), the modeled transmission (Γ_{mod}) according to Equation 3.1 and convoluted with the UVIS-FUV

instrument function, the previous knowledge of the parameters N_a and their covariance matrix (S_{N_a}) (see Rodgers (2000); Koskinen et al. (2011) and Equation 3.2). The instrument function was modeled as a Gaussian with a 2.38 Å width and two lorentzians (See the UVIS User's guide NASA-PDS, 2012).

$$-2\ln(P(N|\Gamma_{meas})) = (\Gamma_{meas}-\Gamma_{mod})^T S^{-1}_{\Gamma_{meas}}(\Gamma_{meas}-\Gamma_{mod})+(N-N_a)^T S^{-1}_{N_a}(N-N_a)+constant \quad (3.2)$$

Minimization of the cost function would be equivalent to maximization of the probability and would give the most likely set of parameters N. The model used to obtain Γ_{mod} is non linear, involving an exponential and a convolution with the instrument response (see Equations 2.7 and 3.3 below). A linearization could be an alternative way to deal with this problem, but the non linear approach was chosen because it is a more trustful representation of the measurements and based on the fact that it gave better results according to the study in Kyrola et al. (1993). The main difference with the approach in this last reference is that here the convolution is done after exponentiation, and not before as in Kyrola et al. (1993). In the present case any prior information about the N values, represented by the second term on the right in Equation 3.2, is ignored ($S_{N_a} \to \inf$). Moreover, to solve the problem for the column densities the cost function was written as a χ^2 quantity in the form of Equation 3.3,

$$\chi^2 = \sum_{\lambda} \frac{(\Gamma_{meas,\lambda} - \Gamma_{mod,\lambda})^2}{\sigma^2_{meas,\lambda}}, \quad (3.3)$$

where σ^2_{meas} are the diagonal elements of $S_{\Gamma_{meas}}$ (which is supposed to be diagonal, meaning no cross correlation among transmission at different wavelengths) and represent the uncertainties in the measured transmission. The optimal N were determined as the values that minimize χ^2. This was done implementing a Levenberg-Marquardt (see for example Press et al., 1996) algorithm with the IDL routine MPFIT (Markwardt, 2009).

Some practical considerations are worth mentioning regarding the retrieval procedure. The theoretical transmission for low altitude can have infinitely small values in the region of methane absorption (below 1400 Å), while the measured transmission is normally lower limited by an instrument background, especially when several altitudes are averaged. This can produce big relative discrepancies between the modeled and measured spectra. Although these differences are not very relevant to the overall quadratic residue due to their small absolute value, this region was excluded when the χ^2 minimization was done, keeping only values above a minimum transmission (0.007, or optical depth 5). The column density retrieval was characterized by its associated Q-probability and reduced χ^2. The former represents the probability that the χ^2 be bigger that the one obtained, by chance (Press et al., 1996). This would mean that, with the same uncertainties (which are assumed to be normally distributed), if a bigger value of χ^2 is obtained it is not due to a defect in the model. This Q-probability value varies between 0 and 1 for a statistically very untrustful and a perfectly trustful retrieval. However, due to the fact that the formal assumptions for which this statistics applies (models linear in the parameters, measurement uncertainties normally distributed, etc.) are normally not rigorously fulfilled by the models, the latter can be considered acceptable even with Q values several orders of magnitude below 1. The reduced χ^2 is defined as the value of the χ^2 quantity divided by the degrees of freedom, which in turn is equal to the number of wavelength channels in the spectrum contributing to χ^2 minus the number of parameters involved. The characteristics of the χ^2 distribution make this value be close to 1 in cases of good fits. To avoid border effects caused by the convolution with the instrument function to affect the fits, 6 spectral channels in the short wavelength end of the spectrum (∼3.6 Å) and 5 in the long wavelength end (∼3 Å) were not included in the calculation of the residues defining χ^2 (Equation 3.3). Even after the exclusion of very low transmission values commented above, the MPFIT routine produces sometimes unacceptable results (some parameters are not retrieved, re-

trieved as negative values or with uncertainty greater or equal than 100%). In cases when the final reduced χ^2 was greater than a threshold (set arbitrarily to 15), the whole retrieval was repeated with a new initial guess. If the reduced χ^2 was smaller than the threshold but some parameters (N values) were not properly retrieved, the retrieval was repeated with a new initial guess for those parameters, conserving the retrieved values and uncertainties for the others. In all cases the best retrieved set of parameters was kept. In any iteration the new initial value was obtained from the old one multiplying by $2^{iter(-1)^{iter}}$. Taking into account a compromise of improvement of the result and processing time, the simulations showed that only 2 iterations are worth doing (see Appendix B).

3.2 Column density retrieval, solar occultations

As the 1085 Å bin is dominated by CH_4 absorption, column densities along the line of sight, N, are related to transmission through Equation 3.4,

$$N = -\frac{\ln(T_\lambda)}{\sigma_\lambda} = \frac{\tau_\lambda}{\sigma_\lambda}, \tag{3.4}$$

where σ_λ is the absorption cross section, and T_λ and τ_λ are the measured transmission and optical depth of the atmosphere, respectively. The contribution of methane to the net optical depth was subtracted before the calculation of nitrogen column densities from the 584 Å and 630 Å bins. The ratio of the CH_4 to N_2 optical depths in these bins varies between 0.07 and 0.7 for altitudes between 1100 and 1400 km. The methane opacity was calculated using a linear fit to the natural logarithm of the derived column densities in the upper part of their altitude range (this varies from occultation to occultation, being approximately between 1100 - 1300 km). The absorption cross sections used for these calculations are from (Samson et al., 1987), measured with a bandpass of 1 to 3 Å and having an uncertainty of ±3%. The average values of the N_2 absorption cross section in the short wavelength bins (see Figure 2.20) are $(2.24\pm0.05)\times10^{-17}$ and $(2.34\pm0.07)\times10^{-17}$ cm^2. The average value of the CH_4 absorption cross section in the long wavelength bin is $(2.90\pm0.02)\times10^{-17}$ cm^2 (from Kameta et al., 2002). This procedure allows to retrieve abundances without using the complicated band structure in the N_2 absorption cross section, where it varies several orders of magnitude in narrow lines (0.007 Å, Lewis et al., 2008).

As for the other species involved in the retrievals, it is valid to ask if the abundances derived with the techniques used correspond to nitrogen and methane or other isotope with similar values of absorption cross section. As underlined in Lavvas et al. (2011), isotopic substitution results in small shifts in the rotational and vibrational levels of the molecules, which translates to small shifts in their photoabsorption cross sections. Lavvas et al. (2011) found that N_2 isotopic substitution have a negligible impact on the photolysis rates of N_2 and CH_4. So, in principle, we could be detecting a combination of N_2 and $^{15}N^{14}N$; similarly, a combination of CH_4 and $^{13}CH_4$. The isotopic ratios in Titan's atmosphere for $^{12}C/^{13}C$ and $^{14}N/^{15}N$ being ~ 82 and ~ 183 respectively (Niemann et al., 2005), it can be assumed that the abundances derived with the analysis just described are, indeed, mainly from molecular nitrogen and methane.

3.3 Altitude range for column densities retrieved from stellar or solar occultations

The column densities for stellar and solar occultations were calculated for an altitude range wide enough to include the first light of the light curves at the same time as the highest altitudes, where

absorption starts. But while for the higher altitudes the small absorption due to the dilute atmosphere resulted in transmission values very close to unity; the lack of signal decreased the S/N for the lower altitudes. As a result, the corresponding number densities lack physical significance or suffer from enormous uncertainties. Consequently the column density profiles were altitude-filtered before the number density calculations. The valid altitudes for a particular profile were defined as those for which the transmission in the relevant wavelength bin satisfied:

$$T + \sigma_T \leq 0.99 \qquad and \qquad T - \sigma_T \geq 0.01, \tag{3.5}$$

where T and σ_T represent the transmission and its uncertainty, respectively. For the solar occultations the relevant bins are those in Table 2.3. For the case of stellar occultation the situation is more complicated as the absorption features for the different species overlap. In this case, some bins were defined as 'characteristic bins' for a particular species and the criteria in Equation 3.5 evaluated for all these bins, resulting in a pair of limiting altitudes for each bin. For each species, the median among the lower limits was chosen as the lower limiting altitude, the median among the upper limits as the upper one. The bins used for the species retrieved are detailed in Table 3.1, the wavelength limits for these bins where defined as the wavelengths for which the absorption decreased in 1/2 from the maximum in the bin, except for the bins corresponding to N_2 absorption and CH_4 absorption, where the factors 1/3 and 1/4 were used instead. An example of transmission curves as a function of altitude for 4 of these bins can be seen in Figure 2.11. Spatial subsetting not only avoided unnecessary

Table 3.1: Characteristic absorption bins in the FUV for each species, used to determine altitude limits for a valid column density retrieval.

Species	Wavelength bins (Å)
CH_4	[1200.00, 1362.23]
C_2H_2	[1436.53, 1442.13], [1474.03, 1484.38], [1518.13, 1520.58]
HCN	[1397.63, 1399.18], [1412.93, 1414.33], [1429.23, 1430.78]
C_2H_4	[1686.93, 1695.2300], [1699.68, 1706.63], [1727.83, 1732.83], [1742.03, 1745.98]
C_4H_2	[1400.33, 1406.03], [1442.93, 1449.13], [1577.78, 1597.48], [1636.88, 1649.83]
HC_3N	[1377.08, 1469.1]
C_6H_6	[1740.38, 1818.63]
CH_3	[1497.50, 1503.50]
AER	[1800.00,1900.00]

processing time but, as the results of the different layers is not independent (see section on spatial inversion below), avoided unrealistic results from very high or low layers to spoil potentially good results from other layers.

Further filtering of the column densities was necessary before the number densities could be calculated. Outliers were eliminated applying a median filter of 5-altitude width to the column density profiles. Infinite column densities, those with uncertainty bigger than 100% or equal to zero, were interpolated assuming a decreasing exponential behavior as a function of altitude. Unreal uncertainties of less than 0.01% were set to 0.01% to avoid numerical problems in the spatial inversion. No values were extrapolated, causing the limits of the valid altitude range of the profiles to be values originally retrieved, without any of the pathologies that trigger a filter.

3.4 Number density and aerosol extinction retrieval

For the calculation of number densities the formalism is similar to the one described above. For a given species Equation 3.2 would take the form

$$-2\ln(P(n|N)) = (N - F(n))^T S_N^{-1}(N - F(n)) + (n - n_a)^T \Pi (n - n_a) + constant \tag{3.6}$$

The information in the measurements is not enough to identify the solution and some additional resource is necessary; the matrix Π represents, in a general case, this additional information about n. This can take different forms. If this is the inverse of the covariance matrix (S_a^{-1}) of the a-priori profile (n_a) then the solution is given by the Maximum A-posteriori Probability (MAP) formula (Rodgers, 2000). The use of prior information is not a good option in this case: as the available number density profiles for the upper atmosphere of Titan are scarce, a statistically trustable a-priori profile and covariance matrix are not available. The additional information can be based on assumptions about the solution for n, like smoothness. This approach was explored in this work. N and n have as many elements as altitudes probed and the model $F(n)$ is linear and given by:

$$\mathbf{N} = \mathbf{D}\, n + \sigma_N = F(n) + \sigma_N, \tag{3.7}$$

where D is the distance matrix that represents the discretization of the atmosphere (see Figure 2.5 and Equation 2.6). The densities are assumed to be constant in each layer. Equation (3.7) is the matrix form of the equality used to arrive to the last member of Equation (2.7), with the addition of the uncertainty in the column densities, σ_N. Among the possible choices for the matrix Π, a smoothness constraint was used, implemented via an *L-1* $\times$ L second derivative operator given in Equation 3.8,

$$B = \frac{1}{h^2}\begin{vmatrix} -1 & 2 & -1 & 0 & 0 & ... & 0 \\ 0 & -1 & 2 & -1 & 0 & ... & 0 \\ ... & ... & ... & ... & ... & ... & ... \\ 0 & ... & 0 & -1 & 2 & -1 & 0 \\ 0 & ... & 0 & 0 & -1 & 2 & -1 \end{vmatrix}, \tag{3.8}$$

where h is the distance between atmospheric layers. This uses as prior information that the n profile is smooth and that a linear function is a good approximation of it. The additional information matrix is then

$$\Pi = \Lambda B^T B = \Lambda H \tag{3.9}$$

In this way the retrieval is performed using what is called a Tikhonov regularization (see for example Twomey, 1996), with a constrain given by the matrix H and the intensity of the regularization given by the regularization parameter Λ. As the number densities span over several orders of magnitude as a function of height, an altitude dependent regularization parameter is compulsory. Λ is actually a diagonal $L \times L$ matrix.
The optimal value of n, according to Equation 3.6, can be expressed as (Rodgers, 2000)

$$n_r = S_n(\Lambda H n_a + D^T S_N^{-1} N), \tag{3.10}$$

where

$$S_n = (\Lambda H + D^T S_N^{-1} D)^{-1}, \tag{3.11}$$

is the covariance matrix of the retrieved number densities n_r, and n_a is a prior knowledge of this profile, chosen as 0 in the case presented here. As noted before, ΛH is equivalent to the inverse of the

prior profile covariance matrix, S_a^{-1} in the MAP method (see for example Sofieva et al., 2004). The determination of Λ is key in the process, and there are several criteria to do this in the literature. A small value of Λ would result in a noisy profile as discussed above. If Λ is too big, too much smoothing will produce a featureless profile, missing any interesting feature measured. Moreover, the influence of adjacent altitudes over the retrieval at a particular altitude increases, degrading the altitude resolution of the result. The procedure implemented here is based on an iterative increment of the regularization and can be described as follows: with $\Lambda = 0$, n_r is retrieved using Equation 3.10. Then, based on the approach given in Press et al. (1996), $\Lambda_{i,j}$ is set equal to $(D^T S_N^{-1} D)_{i,j}/H_{i,j}/100$. This first guess would set Λ 'on the map'. The factor 10^{-2} is to start with a small enough value to be sure that no unnecessary smoothing is set from the beginning. The values of n_r are then recalculated iteratively, using Equation 3.10, multiplying Λ by 1.4 in every iteration. The iterations are stopped when the condition

$$||Dn_r - N|| \sim ||\sigma_N|| \tag{3.12}$$

is reached, where $||.||$ represents the 2-norm.

The matrix $A = S_n D^T S_N^{-1} D$ is called averaging kernel matrix. Its rows can be seen as smoothing functions, peaking at the corresponding altitude, showing the contribution to this altitude from others, expressing the relationship between the retrieved and true profiles, and with a spread characterizing the resolution of the retrieval. This resolution can be calculated according to different criteria. Here the Backus-Gilbert spread (see for example Rodgers, 2000) was used. In essence, and considering the statistical and arbitrary approaches used to derive the n profile, the definition of a spread that will provide an unambiguous altitude resolution lacks significance, and is somehow arbitrary (within sensible values). It is important to have in mind that features smaller than a certain size can not be retrieved trustfully and that this size will be related to the width of the averaging kernels.

For the aerosols, although the formalism is the same, the quantities involved and derived are different. The extinction cross sections used in the retrieval correspond to a particular aerosol size, and so do the retrieved column densities. To obtain aerosol extinction in a more general case, instead of using the retrieved aerosol column densities as the last element of the vector N in Equation 3.7, the aerosols optical depth, τ_{aer} can be used. Then, the corresponding resulting quantity in the vector n is the aerosol extinction. This was done using the aerosol optical depth in the long wavelength end of the UVIS FUV range: 1800-1900 Å, where extinction is supposed to be mainly due to aerosols (see contributions to optical depth in Section 3.6).

As in the case of the column densities the retrieved number densities needed filtering. Retrieved negative number densities and densities with uncertainties greater or equal to 100% were eliminated. Densities for the highest altitude suffered from a border effect due to the second derivative operator used in the inversion, so points within one resolution width from the top of the profiles were eliminated. The different points in the profile have similar but different altitude resolutions; therefore, for simplicity, the biggest value among the median of the resolutions and the altitude sampling is reported as a characteristic resolution for the whole profile.

3.5 Temperature calculations

The N_2 number density profiles were used to derive temperature in the upper atmosphere of Titan. Nitrogen is relatively inert and, due to its dominance in the upper atmosphere, its averaged temperature can in general be regarded as a good indicator of the averaged temperature of the atmosphere as a whole. Assuming the atmospheric is in hydrostatic and diffusive equilibrium, and using the relation between pressure and temperature given by the ideal gas law, the number density of N_2 can be given

by Equation 3.13 (see for example Salby, 1996),

$$n(z) = n(z_0)\frac{T(z_0)}{T(z)} \exp - \int_{z_0}^{z} \frac{g(z')m}{kT(z')}\, \mathrm{d}z', \tag{3.13}$$

where n and T are the number density and temperature, respectively, m is the nitrogen molecular mass, k the Boltzmann's constant, and g the altitude dependent gravity. The gravity g can be written in terms of the gravity at the surface, g_s, and Titan's radius, R, as

$$g(z) = g_s \left(\frac{R}{R+z}\right)^2. \tag{3.14}$$

Under the assumption of an isothermal upper thermosphere—an assumption which has been shown to be in good agreement locally with the measured N_2 densities (see for example Waite et al., 2005) though it does not hold for large altitude ranges in the thermosphere— and applying the natural logarithm, Equation 3.13 becomes

$$\ln(n(z)) = \ln(n(z_0)) - \int_{z_0}^{z} \frac{g_s m}{kT} \left(\frac{R}{R+z'}\right)^2 \mathrm{d}z'. \tag{3.15}$$

Having measured the number densities, the temperature can be calculated from Equation 3.15 in different ways. Three methods were studied in this work and are presented in Appendix A. The method chosen to derive the temperatures that are shown in this report consists in solving the integral in the equation above and equate the temperature. The method used calculates T varying z in all the altitudes covered by the measurements, one of them fixed as z_0. Sequentially all the values are chosen as z_0 and the calculation of T repeated each time. The calculated temperatures are filtered and a final value is calculated as a weighted average. The uncertainty is determined as the weighted mean absolute deviation of the averaged values. As the other procedures used (see Appendix A), and as noted in Westlake et al. (2011), this method is based upon the simple assumptions of a hydrostatic, diffusive, isothermal, and N_2 dominated atmosphere, and is in general not susceptible to uncertainties due to systematic density perturbations occurring outside of the altitude range studied.

3.6 Simulations

The routines developed to retrieve the number densities from the measured transmission were tested with simulated data. The calibrated spectra of the star Epsilon Canis Major measured in high dispersion mode by the International Ultraviolet Explorer (IUE, data product ID sp35165) was used as source spectrum. It was multiplied by a simulated transmission spectrum, the latter calculated based on the absorption cross section and extinction spectra of the species included in the model (see section 3.6.1 and Table 2.2 for some examples), and their vertical abundance profiles in Titan's upper atmosphere from photochemical models. The resulting attenuated spectra, corresponding to different altitudes, were transformed into simulated UVIS counts. This synthetic UVIS observation was then processed by the analysis routines that implement the retrieval process described in Sections 3.1 and 3.4 to calculate column densities and number densities. Finally, the retrieved number densities were compared with the 'true' value from which the simulation started. The different steps in the data simulation and the tests of the routines are detailed following, and in Appendices A to C. These simulations apply to the stellar occultation technique, although the validation of the spatial inversion applies to the solar occultations as well.

3.6.1 Choice of Species

As was commented in a previous chapter, many molecules present absorption features in the UV, but this does not guaranties their identification. The detectability of a particular species depends on the combination of the intensity and wavelength dependence of its absorption cross section, its relative abundance in the atmosphere, and on instrument resolution and S/N. So, which species could be included in a first approach of upper atmosphere characterization through UVIS/VUV absorption?. To try to answer this question this work presents a preliminary survey of candidate molecules. The choice of species was based on their appearance in the reaction paths in photochemical models, the model-predicted abundances (e.g. De La Haye et al. (2008); Krasnopolsky (2009), Lavvas personal communication), and their absorption cross section in the FUV (also from several sources). Table 3.2 summarizes the analysis done. The abundance values reported are in most of the cases approximate values read from plots of mixing ratio profiles or converted from plots of number density profiles, from measurements or photochemical models. The conversion to mixing ratio was done assuming an atmospheric total density equal to the N_2 density, the latter being also approximate values read from plots of N_2 profiles used in different photochemical models. The altitudes in Table 3.2 are close to the maximum in production rate of many species (De La Haye et al., 2008; Lavvas et al., 2008b, 2011), and also close to the unit optical depth measured during UVIS stellar occultations for wavelengths in the range 1400 - 1700 Å. The absorption cross sections given in the table are in many cases approximate values read from prominent features in the absorption spectrum plots or read from tabulated data in the references. From the values in the first columns of Table 3.2, absorption coefficients (see Equation 2.5) for each species considered were roughly estimated; providing merely an order of magnitude for most cases (in some cases not even so), except for the main constituents for which the models can be closer to the real abundances in Titan's atmosphere. Species with a resulting absorption coefficient of the order of 10^{-11} or bigger are considered to be worth of an attempt to be retrieved. For species whose absorption was estimated in the EUV wavelength range the absorption coefficient should be bigger ($\gtrsim 10^{-8}$), or they will most likely be masked by N_2 and CH_4.

Some molecules merit particular comments. Although the detectability of C_2H_6 is promising, in practice it is masked by CH_4 (Koskinen et al., 2011) and therefore it is not included in the retrieval using real data. Based on Table 3.2, the detectability of HCN is low, furthermore it was not retrieved in the simulations in Subsection 3.6.3. Nevertheless, paradoxically, it was included in the model atmosphere used for the analysis of real data. As noted by Westlake et al. (2011), the cooling ability of HCN is unmatched in Titan's thermosphere and is the major controller of the thermal structure (Yelle, 1991). The production of HCN seems to effectively mitigate the UV solar heating, in a chemical feedback system involving UV-enhanced production of $HCNH^+$. Moreover, the description of HCN evolution and profiles by photochemical models is deficient (see the discussion in Lavvas et al. (2008b), for example), the mole fractions being normally bigger than the measured values, particularly in the upper atmosphere. Finally, HCN number density profiles were derived from UVIS/FUV measurements in Koskinen et al. (2011), showing that its detection is indeed possible, if its abundance in the probed region is high enough. For these reasons, HCN was given a 'second chance' in the retrieval applied to real data. Although absorption cross section for CH_3 for the whole UVIS/FUV range were not found in the bibliography, the scarce measurements show up prominently among the absorption of the other species. This, added to its predicted high abundance compared with other radicals (Krasnopolsky, 2009) and to its relevance to the photochemical evolution of the upper atmosphere (see for example Lavvas et al., 2008b), motivated its inclusion in the retrieval analysis. Fray et al. (2010) simulated a UVIS/FUV absorption spectrum based on measured abundances of some hydrocarbons and assuming an upper limit for the HC_5N column density of 5×10^{14} cm^{-2}. They found some features in the

Table 3.2: Analysis of detectability by UV absorption in Titan's upper atmosphere for several species. Unless otherwise stated mixing ratios and N_2 density are from De La Haye et al. (2008), Ta flyby. nE-10 means n×10^{-10}.

Species	Altitude (km)	N_2 density (cm^{-3})	Mixing ratio	ACS (cm^2)	Wavelength (Å)	ACS reference	Absorption coefficient (cm^{-1})	Worth trying
N_2	850	1.3E+11	1.0E+00	2.2E-17	584	Samson et al. (1987)	2.9E-06	YES
CH_4	850	1.3E+11	2.0E-02	1.7E-17	1300	Chen and Wu (2004)	4.4E-08	YES
				6.7E-19	1400	Chen and Wu (2004)	1.7E-09	YES
H_2	1300	2.0E+08	8.0E-03	6.1E-18	580	Lee et al. (1976)	9.8E-12	NO
	1300	2.0E+08	8.0E-03	5.0E-18	1100	Chan et al. (1992)	8.0E-12	NO
H	860	1.5E+11	2.8E-03	0.0E+00	1000-1050	Schunk and Nagy (2009)	0.0E+00	NO
				3.5E-18	900-950	Schunk and Nagy (2009)	1.5E-09	NO
				5.2E-18	850	Beynon (1965)	2.2E-09	NO
HCN	850	1.3E+11	9.0E-05	2.9E-17	1398	Bénilan (unpublisheda)	3.3E-10	YES
CH_3	850	1.3E+11	4.0E-05	5.7E-18	1215	Taatjes et al. (2008)	3.0E-11	YES
	850	1.3E+11	4.0E-05	1.4E-16	1500	Pilling et al. (1971)	7.4E-10	YES
C_4H_2[a]	850	8.0E+10	3.0E-05	7.1E-17	1610	Ferradaz et al. (2009)	1.7E-10	YES
C_2H_2	850	1.3E+11	1.7E-04	4.7E-16	1519	Wu et al. (2001)	1.0E-08	YES
C_2H_6	850	1.3E+11	1.0E-04	3.0E-17	1340	Chen and Wu (2004)	3.9E-10	YES
C_2H_4	850	8.0E+10	4.0E-04	3.1E-17	1610	Wu et al. (2004)	9.9E-10	YES
C_2H_5	850	8.0E+10	2.0E-10	3.0E-19	1500	Gans et al. (2011)	4.8E-18	NO
C_3H_8[c]	1050	3.1E+09	7.2E-06	6.0E-17	1450	Koch and Skibowski (1971)	1.3E-12	NO
C_3H_8[a]	850	8.0E+10	1.0E-05	6.0E-17	1450	Koch and Skibowski (1971)	4.8E-11	YES
CH_3C_2H	850	1.3E+11	5.0E-06	1.0E-16	1348	Ho and Lin (1998)	6.5E-11	YES
				2.5E-16	1550	Ho and Lin (1998)	1.6E-10	YES
$CH_2C_2H_2$	850	1.3E+11	3.0E-06	1.0E-16	1700	Chen et al. (2000)	3.9E-11	YES
C_6H_6	850	1.3E+11	1.0E-06	4.2E-16	1790	this work	5.4E-11	YES
C_2N_2	850	1.3E+11	3.5E-09	3.2E-17	1582	Bénilan (unpublishedb)	1.5E-14	NO
CH_3CN[a]	850	8.0E+10	1.5E-06	3.1E-19	1650	Suto and Lee (1985)	3.7E-14	NO
	850	8.0E+10	1.5E-06	6.5E-18	1650	Suto and Lee (1985)	7.8E-13	NO
C_4N_2[a]	850	8.0E+10	1.7E-05	6.3E-16	1610	Bénilan (unpublishedb)	8.6E-10	YES
HC_3N	850	1.3E+11	4.0E-07	2.4E-16	1450	Ferradaz et al. (2009)	1.2E-11	YES
HC_3N[a]	850	8.0E+10	6.0E-05	2.4E-16	1450	Ferradaz et al. (2009)	1.1E-09	YES
C_2H_3CN[a]	850	8.0E+10	8.0E-06	3.1E-17	1850	Eden et al. (2003)	2.0E-11	YES
HC_5N[a]	850	1.3E+11	1.0E-05	3.0E-16	1750	Fray et al. (2010)	3.9E-10	YES
$CH_2CHCHCH_2$[b]	851	1.9E+11	6.7E-09	7.9E-17	1866	Fahr and Nayak (1994)	9.9E-14	NO
CH_3CCCH_3[a]	850	8.0E+10	6.0E-07	1.0E-16	1575	Palmer and Walker (2007)	4.8E-12	NO
CO[a]	850	8.0E+10	5.0E-05	7.8E-16	1510	(Jolly pers. comm)	3.1E-09	YES
H_2O[a]	850	8.0E+10	8.0E-07	5.0E-18	1700	Yoshino et al. (1996)	3.2E-13	NO
NH_3[b]	850	1.9E+11	5.1E-09	5.2E-17	1350	Yu-Jong et al. (2007)	5.0E-14	NO
	850	1.9E+11	5.1E-09	1.2E-17	1540	Cheng et al. (2006)	1.2E-14	NO
C_6H_2[a]	850	8.0E+10	5.0E-06	4.2E-16	1830	Shindo et al. (2003)	1.7E-10	YES
CH_3CHCH_2[a]	850	8.0E+10	2.0E-06	4.5E-17	1720	Fahr and Nayak (1996)	7.2E-12	NO
Ar	1180	1.0E+09	8.0E-06	3.7E-17	600	Souza and Srivastava (1994)	3.0E-13	NO

[a] Mixing ratio and N_2 density from Krasnopolsky (2009).
[b] Mixing ratio and N_2 density from (Lavvas personal comm.)
[c] N_2 density from Table 7, and mixing ration from Toublanc et al. (1995) in Table 10, of Magee et al. (2009).

simulated spectrum that could be attributed to HC_5N. However, according to Table 3.2, this species' contribution to the optical depth is negligible.

Species included in the simulations and their absorption

Based on Table 3.2 a preliminary list of 18 species to be included in the simulations was established: CH_4, C_2H_2, HCN, C_2H_4, C_2H_6, CH_3C_2H, C_4H_2, HC_3N, C_2N_2, HC_5N, C_6H_6, C_3H_8, $CH_2C_2H_2$, C_4N_2, C_2H_3CN, CO, CH_3, and AER. Particular cases of this preliminary selection are C_2N_2 which, although undetectable according to Table 3.2, was included in the preliminary list motivated by its previous inclusion in a similar analysis (Capalbo, 2010); and C_6H_2, which was included in the table after the simulations were performed (and therefore is not in the list). Profiles for CO, C_4N_2, C_3H_8, and CH_3 were calculated from mixing ratios retrieved from Krasnopolsky (2009) and converted to number densities using the N_2 profile from the same reference. The aerosol profile is from Lavvas et al. (2010), it is a profile for size changing particles in the range 0 - 1081 km. Other profiles are from other photochemical models (Lavvas personal communication) in the range 0 - 1364 km. The profiles were extrapolated from their original highest altitude up to 2000 km, assuming hydrostatic equilibrium (exponential behavior). When the number densities were smaller than 10^{-10} they were set to 10^{-10} to avoid computational over/underflows (e.g. the aerosols). From the number density profiles column densities were generated according to Equation 3.7, with $\sigma_N = 0$. With this column densities and the absorption cross sections, optical depth spectra were calculated for all the altitudes. The altitude grid used is not fundamental for the calculations and was varied from one simulation to another. To give an idea of the values involved, a typical altitude grid had 2000 points between 200 and 2000 km. The absorption cross sections are brought to a common grid covering the wavelength range 1200 - 1910 Å with a step of 0.1 Å[1]. With the abundances and absorption cross sections used, the theoretical optical depth is close to 1 in the central region of the FUV wavelength range for altitudes close to 800 km. The theoretical contribution of each of the 18 species to the optical depth at 800 km is shown in Figure 3.1. Species not visible in the figure have contributions below the lower limit of the plots. It should be noted that for the purpose of these simulations, any profile representative of the order of magnitude of the profiles of the species in Titan's thermosphere is sufficient. The real abundances in the planet might vary significantly from those used for the simulation, which aims to characterize the retrieval routines; therefore it should be used with caution when deriving conclusions for particular species and/or altitudes in the real atmosphere.

Based on the contribution of the 18 species to the total optical depth and on the visual comparison of a simulated optical depth spectrum with a stellar absorption spectrum measured by UVIS, the list was reduced to 11 species: CH_4, C_2H_2, HCN, C_2H_4, C_4H_2, HC_3N, C_6H_6, C_4N_2, CO, CH_3, and AER. The profiles of these species can be seen in Figure 3.2.

3.6.2 Simulation of UVIS data and column density retrieval

From the simulated total optical depth, transmission was calculated (Equation 2.8), convolved with the UVIS/FUV instrument function[2], binned according to the UVIS channels, reversed calibrated according to the instrument calibration, altered with random Gaussian noise simulating the instrument uncertainty and converted to integer to simulate the digitization process. The noise was added as random values with zero mean and a standard deviation equal to the square root of the simulated counts (Poisson uncertainties). The data was averaged in altitude as would be in a real occultation

[1]This step, chosen for convenience in the computations, is smaller than the resolution of some of the absorption cross sections used. However, the discrepancies between the original values and those resulting after translation to a common grid is, for most of the species and relevant wavelengths, less than 3%. This is fulfilled, particularly, for most of the values greater than 10^{-17} in the CO absorption cross section.

[2]Except for CO, most of the lines or bands in the measured absorption cross sections are larger than the 0.1 Å step of the wavelength grid used for the calculations; therefore, the use of this grid is expected not to affect the convolution significantly.

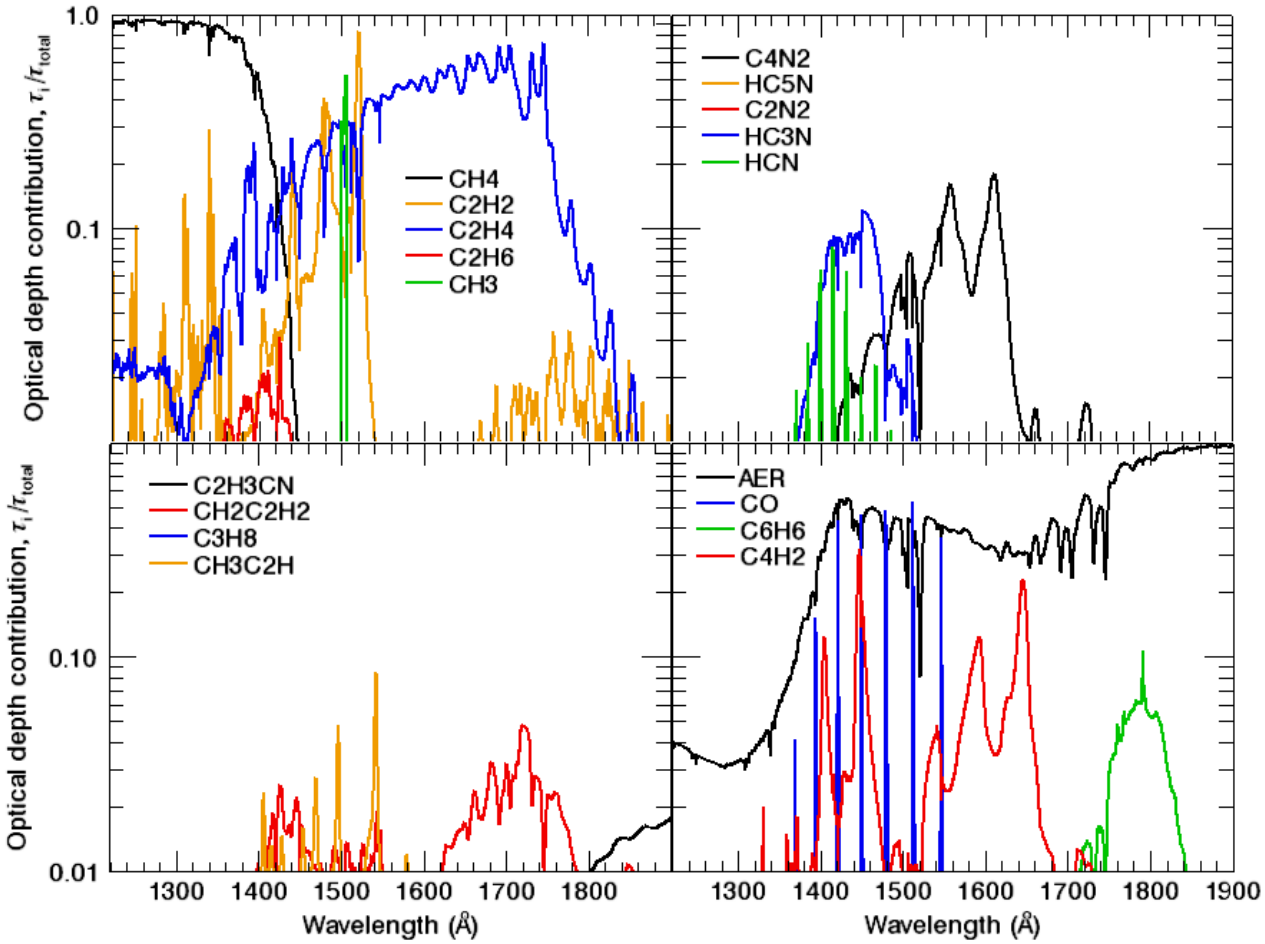

Figure 3.1: Relative contribution to the optical depth from each of the 18 species initially considered as candidates for detection by UVIS/FUV, at 800 km. Species not visible in the figure have contributions below the lower limit of the plots.

analysis. In this case, 10 altitudes were averaged, giving a sampling interval of some 9 km. The synthetic source spectrum in count units calculated from values corresponding to altitudes above 1500 km (I_0 in Equation 2.4), together with spectra at lower altitudes, are shown in Figure 3.3. As the profiles of the species have a few molecules per centimeter square even at the highest altitude, the simulated data—from which the I_0 value is calculated—do not really have samples corresponding to the unabsorbed source spectrum. Nevertheless, the abundances are so small above 1500 km that the simulated samples above this altitude could be considered as measured out of the atmosphere for the purposes of this simulations. Moreover, the flatness of the simulated light curves validates this statement. The slope of the light curves above 1500 km is null for most of the wavelengths, except for the wavelengths below $\sim$ 1300Å for which the average slope is negligible at a rate of $\sim 10^{-3}$ counts/km. The synthetic transmission spectrum and transmission as a function of altitude are shown in Figure 3.4. This transmission was the input of the retrieval routines that implement the retrieval process described in Section 3.1 to calculate column densities. The technique uses an initial guess of the column density profile of each species to start the minimization of the χ^2 quantity (Equation 3.3). This initial guess comes normally from a photochemical model. For this simulations, the initial guess was derived from the simulated column densities perturbed adding to it Gaussian noise, with a mean value of zero and a standard deviation equal to 5% of the unperturbed value. Besides a bias factor was applied to all altitudes, producing a solid shift of the profile in the column density dimension. This

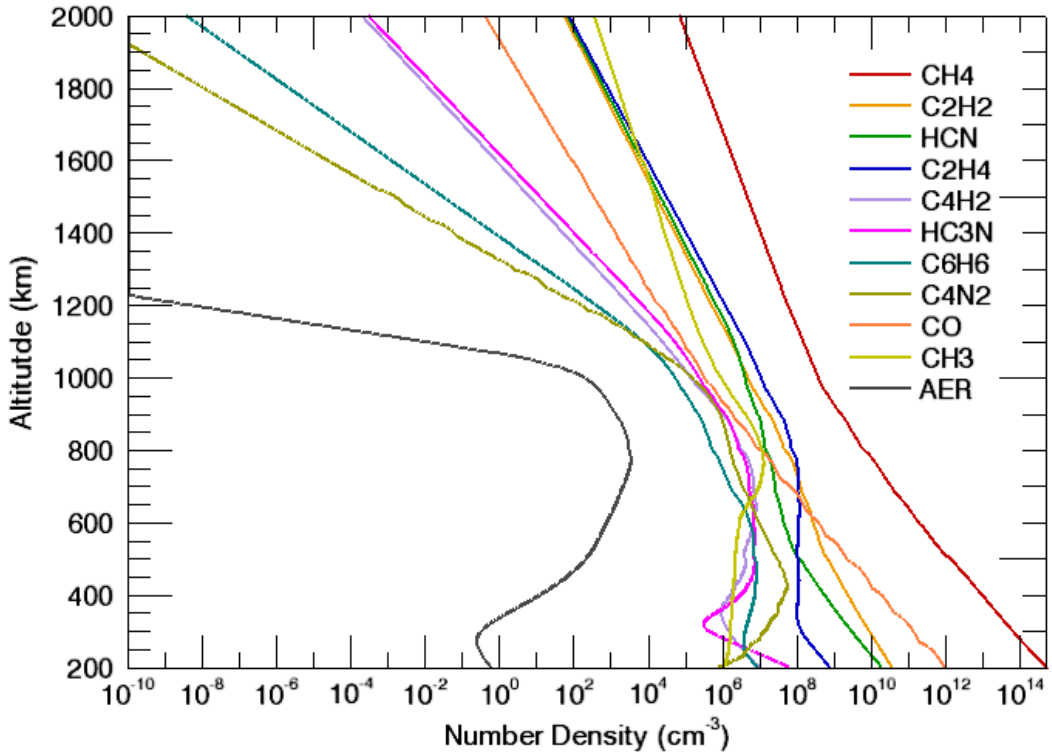

Figure 3.2: Number density profiles of the 11 species used in the data simulations.

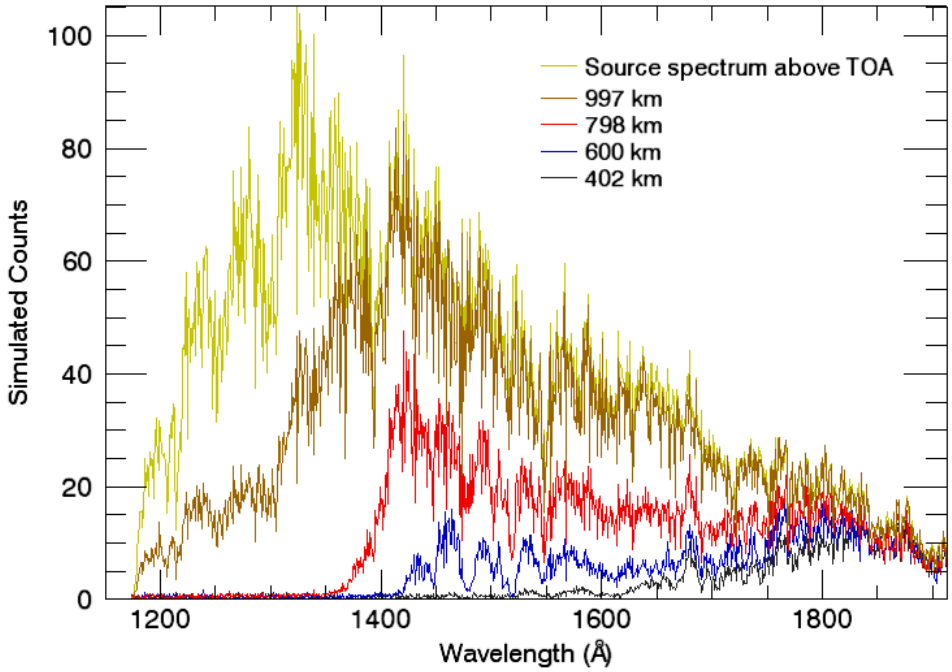

Figure 3.3: Synthetic source spectrum in count units calculated from values corresponding to altitudes above 1500 km. Also shown are spectra corresponding to lower altitudes as absorbed by the simulated atmosphere. Data were binned every 2 wavelength channels and averaged every 10 altitudes.

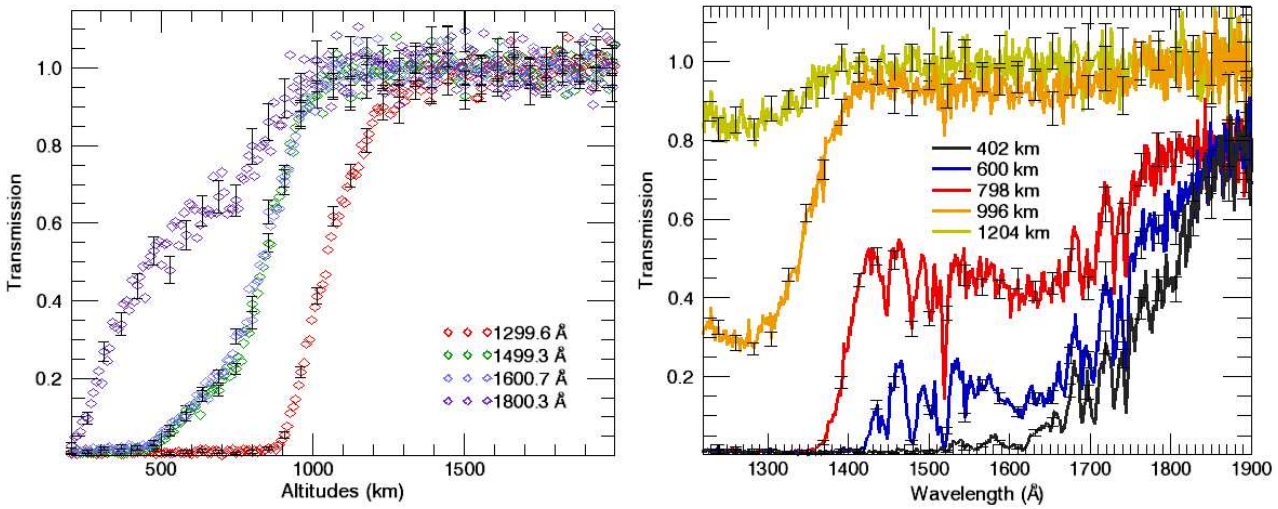

Figure 3.4: Left: Calculated transmission as a function of altitude for several wavelengths. Right: Calculated transmission spectrum for several altitudes. Transmission was calculated form simulated data binned every 2 UVIS wavelength channels and averaged every 10 altitudes. Only some uncertainty bars are shown for clarity.

bias was varied to study the response of the retrieval procedure as a function of the different initial guesses.

Before engaging in the column density retrieval, the core routine used to determine the column densities that minimize the χ^2 quantity, MPFIT, was tested. Although the minimization algorithm is a robust and well behaved one in a general sense, it can suffer from slow convergence or convergence to an undesired local minimum if a poor initial guess is used. The routine was wrapped with the transmission filtering and iteration algorithms described in Section 3.1. For the first test to the routine, in contrast, no re-iteration scheme was used. This allowed to study the response of the routine to different initial guess profiles. Initial guesses biased by a factor 2, 3, 4, 6, 10, 1/2, 1/3, 1/4, 1/6 and 1/10 were used in successive runs. For each run the resulting column densities for 5 altitudes representative of different regions along the full altitude range were compared with the 'true' column densities. The comparison was made taking into account the uncertainties retrieved by MPFIT, an ideal result being one in which the 'true' profile falls within the 1-σ uncertainty interval around the retrieved value. The results of this test are shown in Appendix B. The conclusions from the test are that the routine fails to retrieve the 'true' profiles for some species/altitudes, even when this true profile is used as initial guess. If the initial guess differs in a factor 3 or more than the true profile, or in a factor 0.25 or less, the retrieval as a whole starts to be marginally acceptable. This is somehow worrying because the photochemical model profiles used as initial guess to analyze real data can differ up to a factor of 10 from the measurements. This motivated the iteration scheme described in Section 3.1, with the hope that re-scaling the initial guess would favor converge to an appropriate set of column densities. It should be kept in mind, however, that the re-iteration algorithm has its limitations itself. Depending on the result from MPFIT, only some of the initial guess profiles might be altered, not necessarily the ones differing the most from the 'true' profile. Moreover, all altered profiles are so by the same factor. The iteration can then result in a pointlessly delay of the retrieval, so it was limited to only a few iterations. The results of this test are shown in Appendix B. The conclusion from this test is that the iteration scheme improves marginally the results, retrieving some species at some altitudes that were not retrieved in the case of MPFIT running once. The improvement might be, in part, a consequence of the fixation of the profiles of some well retrieved species. Moreover, only 2 iterations are sufficient, in most cases, to obtain the final result, so this is the maximum number of iterations used for the real

data analysis.

Another important characterization of the MPFIT routine in the context of this work concerns the uncertainties provided by it. Under the assumptions stated in Section 3.1 about the distribution of the uncertainties in the measured data, the uncertainties in the derived column densities should be the formal 1-σ uncertainty, computed from their covariance matrix. However, as the retrieved uncertainty intervals around the retrieved values did not include the true column density value for some species/altitudes, a Monte Carlo simulation was performed to characterized the output uncertainties. The distribution of the column densities for 800 km given by MPFIT in 3150 realizations were compared with the 'true' values and the uncertainty given by MPFIT in one realization of the ones described in the previous paragraph. The result was an underestimation of the uncertainties by MPFIT by less than 35% for most species, about 90% for the aerosols, and an overestimation of the uncertainty in the case of CH_4 and HCN. Moreover, the true value was not contained within the 1-σ interval around the mode of the distribution for CH_4, which means that the true value was not recovered for this species. As the results correspond to only one altitude—for which some of the species might not be retrievable for some data sets, as is the case of HCN—no systematic corrections of the column densities or uncertainties derived from MPFIT was implemented. Nevertheless, it is worth keeping in mind that the MPFIT uncertainties shown in some of the results might be underestimated, and consider a safer 2-σ interval when interpreting the results. The simulations described above were performed binning the simulated data every 2 UVIS wavelength channels. The simulations for the case of the initial guess being twice the true value was repeated without binning, the resulting transmission spectrum for the corresponding altitudes was almost the same in both cases, binned and unbinned. This showed that the binning of the data is unnecessary. No data binning is performed in the analysis of real occultations.

The whole retrieval procedure (spectral least squares fit + spatial inversion) was tested with the simulated data described previously, without any spectral binning, wrapping MPFIT with a scheme of two iterations. The analysis was limited to the range 400 - 1400 km. Most of the reduced χ^2 values for the fits at different altitudes are within 0.8 and 2, which implies a good fit. Most of the Q-probability values are between 0.2 and 1, which also provides confidence for the fits, although the values very close to 1, above 880 km, may imply an overestimation of the uncertainties.

The resulting column densities are shown in Figure 3.5, the shaded areas represent the altitude and column density intervals containing the filtered final values, the values that are automatically considered well retrieved by the retrieval process. It is the final profiles (labeled '_final' in the plots) that should be considered in the analysis. Species CH_4 is not well retrieved above 1150 km. For C_2H_2, the filters leave out some valid values at high altitudes, this is due to the somehow conservative choice of valid altitudes based on the characteristic bins; the same happens for C_2H_4. HCN is one of the most problematic species, as its absorption peaks are highly masked by CH_4 absorption in the simulation. Many of the values for high altitudes are interpolated for this species. The case of C_4H_2 is the opposite of that of C_2H_2, it is not well retrieved above 875 km, but the final filtered profile includes values above 1000 km. The same happens with HC_3N, which is not well retrieved below 550 km and around 800 km, while the profile provided by the analysis procedure reaches 450 km in its lower limit. C_6H_6 and C_4N_2 present a similar problem, the retrieval failing above 830 km for the first, and below 450 km and above 1020 km for the second. Surprisingly, despite its modest contribution to the optical depth, CO is the only species that is coherently retrieved for all altitudes by the algorithm. This might be due to the structure of its absorption cross section, very thin compared to that of all the other species. On the contrary, the inexactitude of the CH_3 retrieved profile was expected from the lack of information about its absorption cross section. The profile is deficient at different spots in the whole altitude range, particularly around 900 km. Besides, it presents unreal waves below 750 km.

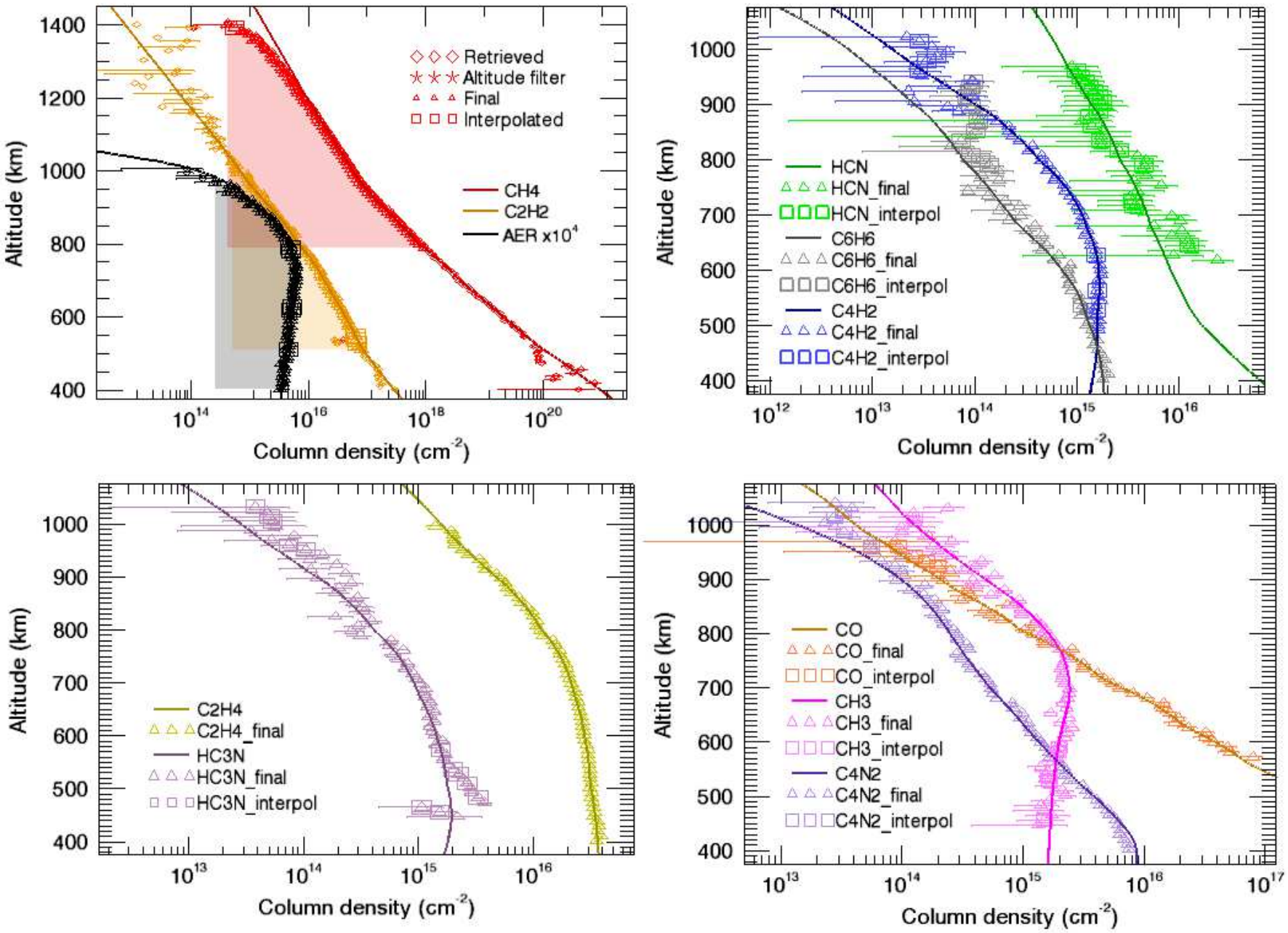

Figure 3.5: Column densities retrieved from simulated data. The raw retrieved values, the intermediate results from the filtering and the final results (shaded areas) are shown for CH_4, C_2H_2 and AER. The final results are shown for the other species. Interpolated values are indicated in all cases. The solid lines are the 'true' column densities used to generate the simulated data. Uncertainty bars are 1-σ uncertainties.

Although not evident from the figure, the aerosols column densities seem to be underestimated from 550 - 700 km; they are also inexact above 900 km.

3.6.3 Simulation of molecular number density and aerosol extinction retrieval

The number densities for the molecular species and the extinction for aerosols, derived from the column densities and optical depth respectively, are shown in Figures 3.6. The shaded areas represent the altitude and number density intervals containing the filtered final values—the values that are automatically considered well retrieved by the retrieval process. The solid lines are the 'true' number densities used to generate the simulated data. The aerosol extinction was calculated from the 'true' aerosol number density and the average absorption cross section in the range 1800-1900 Å. The characteristic vertical resolution for the profiles are either 35 or 55 km, depending on the species considered. The exception is HC_3N, with a resolution of 70 km. In general the profiles present unreal oscillations, most likely due to the scattering of the column density values and the noise amplification inherent of the inversion technique, that was not completely eliminated with the regularization implemented. This eliminates any possibility to identify wave-like structures in the profiles, just well defined absorption layers or depleted regions could be detected. In most of the cases the true profiles are reproduced within the 2-σ confidence interval of the retrieved number densities. Although the CH_4 column densities were not properly retrieved for high altitudes, the true number densities are withing the uncertainty interval of the retrieved number densities. The C_2H_2 retrieved values diverge towards high densities above 968 km; the same happens with C_2H_4 above 978 km. This might be due to the failure of the filter aimed to chop off the border effect. HCN was the only species that could be considered not retrieved by the procedure. Species C_4H_2, HC_3N, C_6H_6, C_4N_2, CH_3 and the aerosol extinction are well retrieved only in a sub-region of the profiles shown. This calls to caution when interpreting the values for high and for low altitudes in the profiles of this species retrieved from real data. As in the case of the column densities, CO is the best retrieved species, with only one outlier, at the highest altitude. To repeat, this simulations are based on sample number densities that are not expected to match but in order of magnitude (in some cases not even so) the average abundances in Titan's atmosphere—except for CH_4 for which the models can be closer to the real abundances. Besides the real abundances can vary from one location in Titan to the other. Relative differences among the densities used could render a species more or less 'retrievable' than the others. Moreover, this is the first time that such a big number of species is included in this kind of analysis, resulting maybe very ambitious in this sense. Most of the absorption cross sections for the different species overlap in the central wavelength region of the measured spectrum: about 1400 - 1800 Å. This largely complicates their identification and maybe pushes the methods and computational routines to their limits of applicability.

Finally, the author performed a second visual comparison of the simulated optical depth obtained with the 11 species with a real spectrum measured by UVIS during T41, both corresponding to a tangent altitude of 800 km. The features in the simulated optical depth due to C_4N_2 and CO are the most difficult to match with measured features. Thus, with the aim of simplifying the analysis, these species could be eliminated from the list of 11 candidates to be retrieved.

3.7 Summary of chapter

The problems of deriving column densities from transmission and number densities from column densities are ill-posed. In this work, the first problem is approached with a least-squares minimization technique. The goodness of the result is characterized by a reduced χ^2 value and a Q-probability

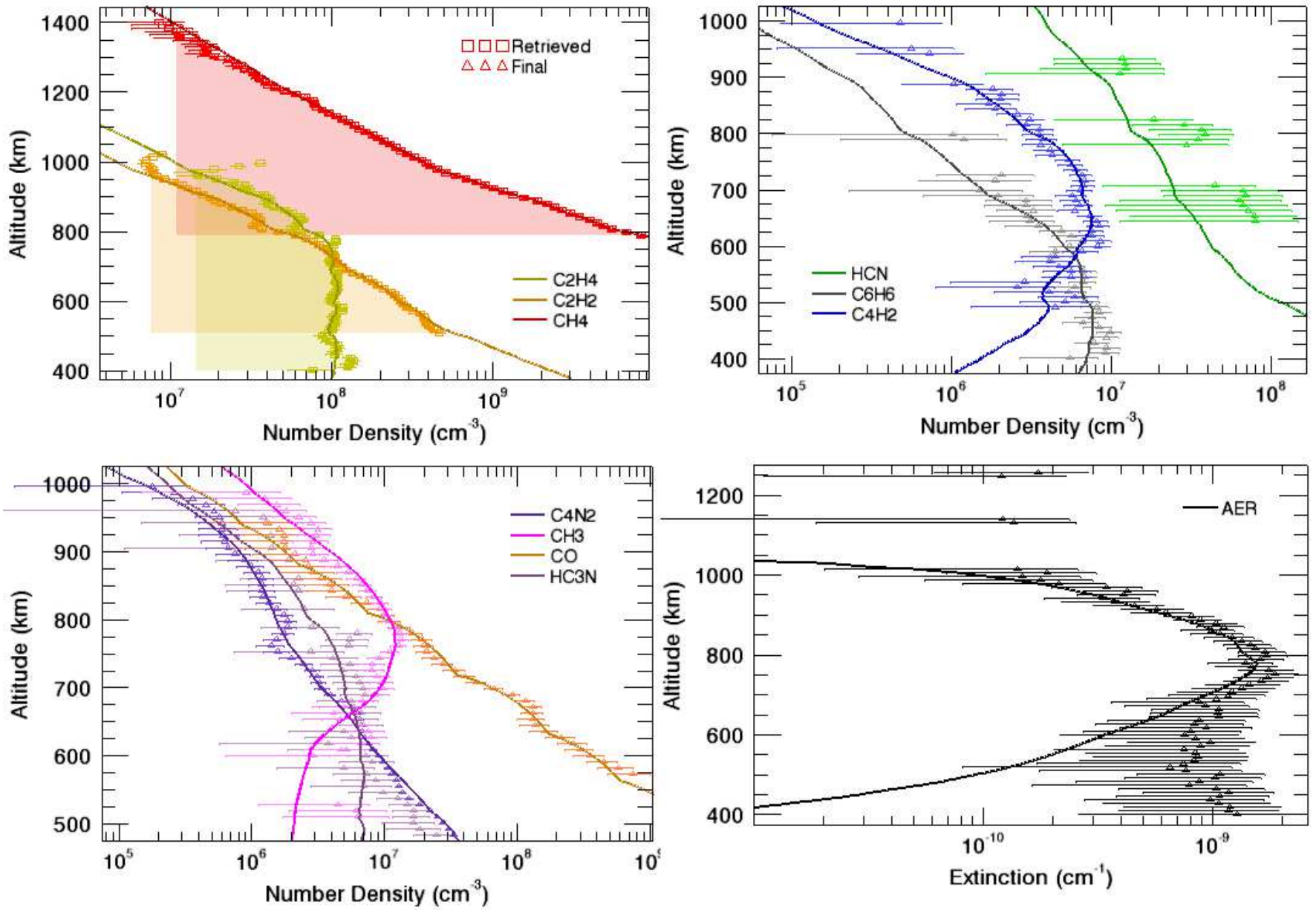

Figure 3.6: Number densities and aerosol extinction retrieved from simulated data. The raw retrieved values, and the final results after filtering (shaded areas) are shown for CH_4, C_2H_2 and C_2H_4. The final results are shown for the other species. The solid lines are the 'true' number densities used to generate the simulated data. The aerosol extinction was calculated from the 'true' aerosol number density and the average absorption cross section in the range 1800-1900 Å. Uncertainty bars are 1-σ uncertainties.

value. In the case of solar occultations there is no need for a least-squares spectral analysis, and the column densities are calculated directly from the ratio of measured transmission and the absorption cross section. The second problem is tackled with the use of a regularized inversion, the altitude resolution of the retrieved number densities is characterized by the spread of the averaging kernels.

The implementation of the column densities derivation includes filtering of the measured transmission and an iteration scheme (2 iterations) to improve retrieval results. The resulting uncertainties provided by the routines were found to be underestimated for most of the species involved. The analyses of the iteration scheme and the uncertainties were performed with simulations of column density retrievals, presented in this chapter. The column densities are filtered previous to the calculation of number densities, according to the transmission in predefined characteristic absorption bins, and other practical criteria (e.g. values with infinite uncertainty). The filtering restricts the altitude span of the final column densities. The retrieved number densities are also filtered using the same practical criteria. The method to derive temperature from the N_2 column densities was also presented in this chapter. The former is based on the integration of the hydrostatic equilibrium equation.

The whole retrieval procedure (spectral least-squares fit + spatial inversion) was tested with simulated data. The choice of species to be included in the simulations was based on their detectability, in turn dependent on the absorption cross section of the relevant species and their abundance in Titan's atmosphere. Eleven species were included in the simulations. Finally, only nine were used in the analysis of real data: CH_4, C_2H_2, HCN, C_2H_4, C_4H_2, HC_3N, C_6H_6, CH_3, and AER. The column densities were well retrieved overall, although for some species the retrieval failed for some altitudes. The same comment applies for the number densities retrieved in the simulations, so results for these altitudes should be taken with caution when analyzing real data. On the other hand, differences between the simulated and real atmosphere might change how a particular species is retrieved (e.g. the case of HCN), and no radical conclusions about the detectability of any of the 11 species should be made from the simulations. The number density profiles present oscillations that do not exist in the original profiles, most likely due to the scattering of the column density values and the noise amplification inherent of the inversion technique, that was not completely eliminated with the regularization implemented. In most of the cases the true profiles fall within the 2-σ confidence interval of the retrieved number densities. The characterization of the retrieval technique, and the analysis of detectability of molecules in Titan's atmosphere by UVIS, are two of the main contributions of this work.

Chapter 4

Benzene absorption cross section in the VUV, relevance for Titan's upper atmosphere

Previous chapters underlined several times the important characteristic of Titan's atmosphere of being a rich reservoir of complex organic molecules. It has also been commented how the identification of these molecules has been pursued with modeling and laboratory experiments, and confirmed in many cases by observations. Among the complex hydrocarbons obtained in the models, experiments, and observed, is C_6H_6. Apart from its detection on Titan (Coustenis et al., 2003), C_6H_6 was also detected in Jupiter, Saturn (Bézard et al., 2001) and in the CRL618 nebula from ISO data (Cernicharo et al., 2001). From all the possible isomers with the formula C_6H_6, this work deals with the cyclic form c-C_6H_6, called benzene. It is the simplest of the aromatic hydrocarbons: a group of hydrocarbons characterized by general alternating double and single bonds between carbons. Benzene can be the precursor to the formation of a whole host of heavier hydrocarbons including polycyclic aromatic hydrocarbons (PAHs). The condensation of Polycyclic Aromatic Compounds (PAC) may contribute to the formation of Titan's haze layers. This pathway competes with the polyacetylene polymers and nitriles polymers pathways for haze formation (Wilson et al., 2003; Wilson and Atreya, 2003; Lebonnois, 2005). As a consequence benzene has a privileged attention among other molecules, a whole chapter in this work. The chapter will follow with an introduction about the presence of benzene on Titan. Due to their relevance for c-C_6H_6 detection with UVIS, an introduction about benzene absorption cross section in the VUV will follow. Our own measurement experiments will be described in Section 4.3, our results and their analysis presented in section 4.4. The measured absorption cross sections were used in the analysis of UVIS FUV data to retrieve benzene abundance in Titan's upper atmosphere. The technique was described in Section 2.3, its application to the case of benzene, the results and comments will be presented in Chapter 5.

4.1 An Introduction to Benzene on Titan

After the detection of benzene among the products of laboratory experiments simulating Titan's atmospheric chemistry, the models started to include this molecule in the reactions considered. The first of those laboratory simulations was carried out by Sanchez et al. (1966). From the reactions in a N_2/CH_4 1 bar mixture subjected to high frequency sparking discharge they found, among other products, C_6H_6. Raulin et al. (1982) mention several experiments simulating Titan's chemistry that also obtained C_6H_6. Coll et al. (1999) detected benzene in a N_2/CH_4 (98:2) gas mixture subjected to high voltage discharges (cold plasma) at temperature and pressure representatives of Titan's atmosphere. Motivated by the detection of polyaromatic compounds in laboratory tholins and theoretical work based on PAHs formation from benzene, Lebonnois et al. (2002) included benzene in their model for Titan's atmosphere and suggested chemical pathways that can link this simple molecule and PAHs to macromolecules, precursors to aerosol particles. However, this aerosol formation pathway was negligible compared to others (polymers of acetylene, polymers of HCN). This might be due to underestimated reaction rates or to the small quantities of benzene in their model compared to the latter measured abundances given in Coustenis et al. (2003), derived from ISO IR spectra. This was the first tentative identification of benzene in the satellite's atmosphere. They determined a benzene mole fraction of $(4 \pm 3)\times10^{-10}$ in the stratosphere. The detection of benzene triggered more attempts to model its production and the inclusion of PAHs in the models for aerosol formation (Wilson et al., 2003; Wilson and Atreya, 2004; Lebonnois, 2005) particularly because of its importance as intermediate link in the gas-aerosol path. Wilson et al. (2003) analyzed mechanisms for the formation of benzene based on recombination of the propagyl radical (C_3H_3) and compared their results with the ISO observations, reproducing the only one value at low altitude provided by this observation if their nominal profile is multiplied by a factor of about 3. Due to the high uncertainties in reaction rates at lower temperatures they used reaction rates for 300 K. They found that the results were highly de-

pendent on the C_3H_3 sinks considered. They also found that an ion pathway dominated the benzene abundance above 750 km. Wilson and Atreya (2003) provided an updated c-C_6H_6 vertical profile, better matching ISO measurements, that they include in their analysis of Titan's thick haze layer. They found that aromatic molecules may play an important role in the haze formation. Wilson and Atreya (2004) present an improved model, also reproducing the ISO measurements of benzene. The aerosols included in this new model act as a shield against benzene photolysis in the stratosphere. The cited work also discusses the influence of solar activity on the benzene profile, abundances decreasing about one order of magnitude from solar maximum to solar minimum conditions. Lebonnois (2005) presents a sensitivity study on c-C_6H_6 and PAHs on Titan and Jupiter. In this model benzene is mainly produced by recombination of the propagyl radical (C_3H_3) and the abundance was higher that in Lebonnois et al. (2002), resulting in a bigger relevance of the PAH's pathway for the formation of aerosols. The predictions of the model agreed with the ISO measurements.

After the Cassini arrival in 2004, models and observations complemented iteratively in an unprecedented way. The presence of benzene in the stratosphere was confirmed by Coustenis et al. (2007) and Vinatier et al. (2007) from CIRS data. The first of these references presents an analysis of data from a Titan northern winter period in which an increase in c-C_6H_6 abundance towards the pole is evident, but lacks from vertical information about the detected constituents. The first vertical profiles in the stratosphere (about 150 - 300 km) were provided in the second reference, limited to 80° N during northern winter. They also provide an upper limit for c-C_6H_6 abundance in the southern hemisphere. These results are consistent with predictions from Lebonnois (2005) and the tentative detection in Coustenis et al. (2003). Latitudinal variations in the c-C_6H_6 mixing ratio profile are derived from CIRS data in Vinatier et al. (2010) for northern latitudes, during northern winter observations. They also derived a lower latitudes upper limit consistent with results in Vuitton et al. (2008). Higher in the atmosphere ($>$ 900 km) unexpected high abundances of complex hydrocarbons, including benzene, were determined from the analysis of INMS data (Waite et al., 2005; Vuitton et al., 2006, 2007) after the first Cassini flybys. Waite et al. (2007) showed the presence of neutrals and ions of several thousand daltons at about 1000 km. They suggest ion-neutral chemistry at high altitude plays a major role in the formation of benzene, which would then form higher order PAHs. They also presented the possibility of benzene condensing onto the surface of aerosols. However, the underestimation of benzene resulting from the applied chemical schemes in Waite et al. (2007) left the questions of an unidentified source and/or a regeneration mechanism compensating the loss. These results may be interpreted as a support of the suggestion of Wilson et al. (2003) about the importance of ionospheric chemistry for c-C_6H_6 formation in the higher layers. This fact of INMS results giving a C_6H_6 abundance some orders of magnitude bigger than the commented models predicted was highlighted in Vuitton et al. (2007). In their analysis of INMS data they provide a c-C_6H_6 mole fraction in the thermosphere derived from measured abundance of protonated benzene. The high concentrations in the thermosphere compared to previous modeled results is associated by the authors to a production of benzene in the higher layers. For Lavvas et al. (2008b) the main production process for benzene in the upper atmosphere is the recombination of two C3H3 radicals. They underline the uncertainties in the reaction rates, as well as the fact that the use of different rates can lead to variations of some orders of magnitude for the mole fraction in the upper atmosphere. Their predictions are below INMS results, supporting the fact that benzene formation might be related to ion chemistry at thermospheric altitudes. Regarding the competition of the different channels to form aerosols, Lavvas et al. (2008b) find that the aromatic pathway is less important than the copolymer and nitrile pathways in haze formation. The formation and distribution of c-C_6H_6 on Titan is the main topic analyzed in Vuitton et al. (2008). They used an ion chemistry model and a neutral chemistry model to analyze the production mechanisms of c-C_6H_6 in the atmosphere. The results were validated by comparison with INMS measurements

from 12 flybys in the upper atmosphere and with CIRS values for the stratosphere. Vuitton et al. (2008), like Vuitton et al. (2007), suggest a main source of benzene in the thermosphere, where it is created by both ion and neutral chemistry. The former authors present an interesting discussion of the discrepancies between their work and those from Lebonnois (2005) and Wilson et al. (2003). Some comments are made in Vuitton et al. (2008) about diurnal variations, found to be mild. De La Haye et al. (2008) developed a 1D ion-neutral rotating model to account for diurnal variations of solar inputs. In their model two main processes are responsible for benzene production: neutral chemistry of C_3H_3 below 700 km, and electron recombination above 700 km. In their study this production mechanism, dominant as in Vuitton et al. (2008), has a peak that depends on the day illumination conditions, shifting from 850 km during the day to 1050 km at night. Krasnopolsky (2009) developed a global-mean model of coupled neutral and ion chemistry of Titan, one of the calculated species is C_6H_6. In their analysis they favor ion chemistry over neutral chemistry for the formation of PAH in the upper atmosphere, which would shift the attention from c-C_6H_6 in this matter towards hydrocarbon ions. More recent relevant measurements include those from Cui et al. (2009). From their analysis of INMS data from 15 flybys that took place from April 2005 till November 2007, they derived globally averaged number density and mixing ratio profiles of various hydrocarbons (including C_6H_6) and nitrogen bearing species, in the range between 950 and 1200 km. Interpretation of these results deserves some caution, since instruments wall effects (like adsorption/desorption and surface chemistry) might affect the measured densities. Latest laboratory experiments include those from Imanaka et al. (2010) who detected benzene by extreme vacuum ultraviolet irradiation of a N_2/CH_4 gas mixture. All this synergy between experiments, models and observations advanced greatly our understanding of benzene in Titan's atmosphere.

At present (September 2013) the presence and relevance of benzene in Titan's atmosphere is undoubted. But the role of this low abundant hydrocarbon and most abundant 'heavy' molecule, as well as the role of other heavy hydrocarbons and their ions, are not fully understood, not to mention extremely complex. The profiles from the photochemical models not only have associated a big uncertainty (Hebrard et al., 2007), but also change dramatically as a function of the background atmospheres used or the chemical reactions involved. The lack of information about these reactions at temperatures relevant for planetary atmospheres is also a drawback. New laboratory measurements and Titan observations, particularly from Cassini, will help to contrast the efforts of the modelers to better understand the atmosphere. The measurements commented on the previous paragraph cover mainly the stratosphere and upper atmosphere above 950 km. As stated in previous chapters, UV stellar occultations absorption measurements allow probing the upper atmosphere in between these limits. The Cassini/UVIS occultation measurements during the regular Titan flybys can detect benzene from its VUV absorption features. The study of several of these occultations corresponding to different spatial/temporal coordinates would allow to study benzene variability. Benzene profiles in the upper atmosphere in the range 550 - 900 km were provided by Koskinen et al. (2011), the first identifications of benzene in the upper atmosphere of Titan from UVIS data. They used the c-C_6H_6 absorption cross section presented here and found that the inclusion of benzene in the forward model of their analysis significantly reduces the residuals between the modeled and measured optical depth. The same UVIS observations were re-analyzed here with an identical technique. The resulting benzene profiles are presented in Section 5. These results were derived with the absorption cross section measurements presented in this chapter.

4.2 Introduction to benzene absorption cross sections

To interpret the absorption measured from star occultations it is imperative to count with the absorption cross section spectra of the molecules of interest (see Chapter 2). Unfortunately the absorption cross section spectra for many molecules of planetological interest is unknown, or poorly known. The absorption spectrum of benzene is an exception, its interpretation has long served as a benchmark for the development and testing of theoretical approaches to describe π-electron systems. They also provide useful information in a large number of scientific contexts, including studies in aeronomy, astrophysics, planetary science, radiation chemistry, physics, and biology. As a consequence, numerous experimental and theoretical studies have been carried out on this, the simplest aromatic molecule, particularly in the VUV. Some of these experiments will be referred next to provide a context to our own measurements, without pretending to be a full bibliographical review on the topic. In some cases there are no comments about resolution, uncertainties or temperature used in the experiments (they are assumed to be performed at room temperature, approximately 298 K). The reader is referred to the extensive bibliography within the references cited here for more details.

Many of the discussions and experiments about the VUV absorption of benzene started by the mid 1950s. The first measurements were that from Price and Wood (1935), who photographed the absorption spectra of C_6H_6 and C_6D_6 in the range 1000 - 2000 Å. They first identified Rydberg transitions in the shorter wavelength range but mention only marginally the big absorption feature around 1800 Å. They do tackle this region later (Price and Walsh, 1947) when they argue that at least two electronic transitions are concerned in the 1600 - 2000 Å region. Hammond et al. (1950) supports this statement and comment on different transitions that could be responsible for the two features around 1790 Å and 2000 Å. These works do not present absolute absorption cross sections as a function of wavelength. Pickett et al. (1951) present a short review of the work done up to the beginning of the 1950s, including propositions by different authors on assignment of the bands around 1790 and 2000 Å. These former authors themselves provided for the first time absolute values of extinction coefficient measured in the range 1560 - 2200 Å using a photographic method. Their analysis of the temperature variation of some of the bands in the 2000 Å band system found no measurable difference between spectra at room temperature and those at ∼253 K. Hammond and Price (1955) used a photoelectric detector to determine absorption cross sections in the range 1650 - 2150 Å. From the plots in these last two cited works, both resolutions are coarse compared to the present study (see below). Wilkinson (1956) obtained higher-resolution (0.026 to 0.065 Å) absorption spectra of benzene and deuterated benzene using a more appropriate continuum as source that facilitated the identification of many new weak bands with respect to Price and Wood (1935). The former authors identified four Rydberg series, each with 8 to 10 members. All four series were found to converge to the same ionization potential of 9.25 eV. Vibrational progressions were found to be associated with each Rydberg transition except in the diffuse region close to the ionization limit. They also re-interpreted some of the vibrations observed by Price and Wood (1935). Koch and Otto (1972) provide benzene absorption cross section measured with the spectral continuous synchrotron radiation from the electron accelerator DESY in the photon energy range of 6 - 35 eV (350-2060 Å). Wavelength resolution ranged between 1-4 Å. In this work they note assigned Rydberg states, vibrational structures and review first ionization values available at that time. Pantos et al. (1978) measured benzene extinction coefficient at room temperature, from 1350 - 2700 Å, at several resolutions. The resolution of the benzene spectrum showed in their work is 2.5 Å. Their extinction measurements have an uncertainty of 10%.

By the end of the 20th century new experimental techniques and theoretical studies allowed to further investigate the absorption in the UV and review old interpretations. Grubb et al. (1985) performed four-photon absorption spectroscopy measurements. They reported on several Rydberg

series in benzene converging to the first ionization potential, some of them seen in our results. Suto et al. (1992) also measured benzene absorption cross sections in the 1060-2950 Å range, at 1 Å resolution and room temperature (24° C). Their results agree with those from Pantos et al. (1978) within the 10% uncertainty in the newer results. They do not make any new identification of bands with respect to previous works. Many other works performed in the '80s and '90s are referred to by Rennie et al. (1998), who measured absolute photoabsorption, photoionization and photodissociation cross-sections and the photoionization quantum efficiency of benzene and hexadeuterobenzene in the range 350 - 1300 Å. The resolution ranged from 1.7 to 2.3 Å in the range overlapping with the shortest wavelength region in our spectra (approximately 1160 - 1340 Å). Rennie also used the Pantos et al. (1978) and other authors' measurements to make a composite spectrum including the whole range covered by our measurements (and even shorter wavelengths). When compared with previous works, their values of the cross section are in general accordance in some cases, though consistently higher in some others. Feng et al. (2002) presented absolute UV and VUV photoabsorption oscillator strengths (cross sections) for the valence shell discrete and continuum regions of benzene from 4 to 56 eV (approximately 3100 - 220 Å) using high resolution (∼0.05 eV FWHM) dipole (e,e) spectroscopy, with an uncertainty of at most 5%. They provide a summary of the available absolute photoabsorption cross sections of benzene at different energy ranges as well as a thorough comparison with previous results. In the region overlapping our measurements, their results agree with some previous measurements and disagree with others. In the present work we present our addition to the knowledge of the c-C_6H_6 absorption cross section in the region 1160 - 2200 Å, at medium resolution (∼1 Å). Absent in the references, the study of temperature variations, mainly in the range 1700 - 1900 Å, is our main original contribution.

To interpret the presented absorption cross section results it is convenient to have in mind the energetic states of the benzene molecule. When the 6 carbon atoms and the 6 hydrogen atoms are used to conform the benzene molecule assuming D_{6h} symmetry, the 1s orbitals of the hydrogen atoms and the 2s and 2p orbitals of the carbon atoms derive into a set of molecular orbitals. The molecular orbitals arising from p atomic orbitals and antisymmetric with respect to the plane of the molecule are called π orbitals. These are the most loosely bound orbitals in benzene and therefore very important in understanding the stability of the molecule. They also determine the ground and lowest excited electronic state of the molecule (Herzberg, 1966), the other orbitals being neglected in usual treatments. The ground state configuration forms the state $^1A_{1g}$. Mulliken (1939) has shown from the electronic selection rules for a molecule of the high symmetry of benzene that the only allowed transition from the ground state is that to the $^1E_{1u}$ state. Excitation energies from the ground state to the first excited states would need to be $\sim$ 7 eV (approximately 1770 Å), higher energies up to the 10.7 eV (some 1150 Å) reached in this study can promote electrons to higher, non π, orbitals. We are going to identify some of these transitions in our measured spectrum and compare them with previous work. But the intention of this work is not to provide a thorough interpretation of the benzene states and transitions—this has been made previously. Nevertheless, our data provides new experimental material to those interested in these identifications. Our focus will be the general absorption features in the measured spectrum in the range relevant for the FUV channel of the UVIS instrument (1115 - 1900 Å), their variations with temperature, and their use to identify benzene in Titan's upper atmosphere.

4.3 Experimental measurements of benzene absorption cross section

The absorption cross sections where derived from absorption measurements of c-C_6H_6 gas contained in a closed cell, irradiated with VUV radiation. The gas used was the product 109646 benzene

from Merck, reference substance for gas chromatography with a purity $\geq$ 99.9 %. No impurities were detected in any of the measurements performed. The pressure and the temperature in the cell were continuously monitored and controlled. Some of the measurement were performed at BESSY II synchrotron facility, Berlin, Germany; others were performed with the 10 m VUV spectrograph at the Meudon Observatory, Meudon, France. The second set of measurements have as prime objective to confirm and further study temperature variations. The different setups and processing are described in the next subsections. In all cases the results of the measurements were transmission as a function of wavelength. From the transmission, the optical depth and absorption cross section are determined via the Beer-Lambert law.

4.3.1 Absorption measurements with Synchrotron radiation, BESSY II facility

Synchrotron electromagnetic radiation from a storage ring can range from Terahertz to hard X-rays. This is a very powerful, continuum and well collimated light source for spectroscopy at short (less than 2000 Å) wavelengths. The experimental setup has already been described in Ferradaz et al. (2009). A schematics is shown in Figure 4.1. Prior to its introduction into the cell, the sample was

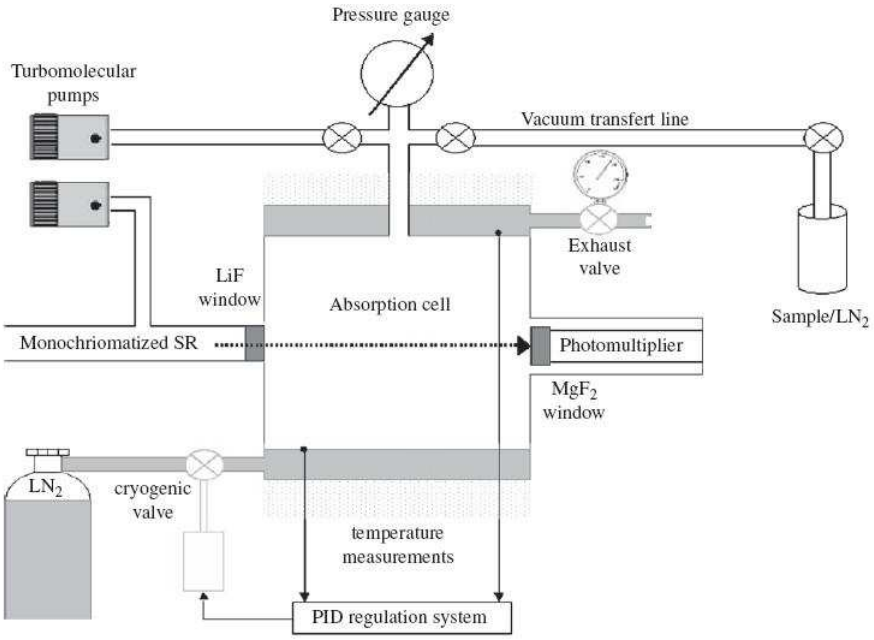

Figure 4.1: Experimental setup used to measure benzene absorption cross section at BESSY II synchrotron facility. From Ferradaz et al. (2009)

held in solid state at liquid nitrogen temperature. The sample was contained in a test tube, connected to the cell by a valve system. In this experiment the sample is irradiated with Synchrotron VUV radiation (SR) from the BESSY II storage ring. The radiation coming from dipole magnets was fed into a 3 m normal incidence monochromator to obtain a VUV beam. Measurements of absorption were performed in the 1150 - 2200 Å range, with resolutions of 1 or 0.5 Å and 3 points per resolution. The wavelength values have a varying precision depending on the wavelength region studied, being of 0.17 Å in the worst case. The vacuum spectra were measured with 0.5 or 0.3 points per resolution to save measurement time, and interpolated during processing to match the benzene spectra points per resolution. The choice of these values was a compromise between resolution and scanning time. The resolution used is sufficient for the applications to the analysis of UVIS spectra. The monochromator provided the wavelength values for the measurements, but a solid shift of 3.1 to 3.3 Å (depending on

the spectrum considered) with respect to the spectra measured in Meudon was performed in post-processing (see next subsection). These last spectra were calibrated based on oxygen absorption bands. Given the configuration of the experiment no stray light is expected from the environment. Stray light from the source itself is minimized by the collimation of the monochromator beam, by adjusting the alignment to avoid internal reflexions, and placing the cell as close as practically possible to the focus of the monochromator optical system. The cell containing the sample during the measurements was a cylinder of about 950 cm^3. The radiation traverses the cell along its revolution axis. The optical path for the radiation was 14.15 cm. The entrance and exit of the cell were covered by LiF and MgF_2 windows respectively. This allowed measurements down to the cutoff wavelength (about 1140 Å). The intensity of the beam at the exit of the cell was measured with an Electron Tubes Ltd 9402B solar blind photomultiplier (PM). The PM chamber was vacuumed to 4.4 μbar and held at room temperature. The cell pressure was measured at the level where the sample enters the cell. The empty cell pressure was about 4.4 μbar. The range of c-C_6H_6 pressure used was 6 - 375 μbar, much lower than the saturation pressure at the temperatures used ($\sim$1000 μbar at 230 K). The pressure increased a few μbar during the measurements due to air leaks and outgasing. Abrupt minima in pressure were also observed during the measurements at low temperature, probably due to fast sample condensation-evaporation events in the cell walls. These behaviors were accounted for during the spectra processing.

The temperature was controlled and measured during the low temperature part of the experiment. A nitrogen cryogenic valve with a proportional, integral, derivative (PID) controller was in charge of keeping the system at a desired temperature. This latter quantity was measured with two type-K thermocouples fixed on the inside wall of the cell and located at the opposite flat plates of the cylinder. The temperature stability was about 4 K, the variations due to the liquid N_2 injection by the cryogenic valve. The temperature gradient across the cell was about 15 K. The values given for low temperature measurements correspond to an average value. The wavelength given by the monochromator and the voltage proportional to the radiation out of the absorption cell were digitalized and registered in a text file.

A measurement series to obtain one c-C_6H_6 absorption spectrum at a particular temperature, wavelength range, resolution, and pressure was performed as follows. First a vacuum spectrum was measured, with no sample in the absorption cell. Then the chamber was filled with c-C_6H_6 until the desired pressure was achieved. A spectrum of the sample gas was then measured. After evacuation of the sample a new vacuum spectrum was measured. The ring current in the synchrotron facility diminishes with time between electron injections. From the two vacuum spectra an intermediate interpolated vacuum spectrum was calculated using the ring current linearly interpolated. From the ratio of the benzene and vacuum intensities a transmission was then calculated, the absorption cross section was derived from this transmission (see below).

Different series of absorption cross section spectra were measured in this experiment. These series covered different wavelength ranges, with different resolutions, and temperatures. Moreover, several measurements were performed varying only the pressure to confirm reproducibility and pressure independence of the results. At least 3 different pressures in at least one sub-wavelength region of the whole wavelength range covered by the measurements were explored for a given temperature and resolution. A total of 36 spectra were collected. The series were filtered excluding spectra (or part of them) with very low absorption, spectra which clearly suffered from a systematic error, spectra with particularly high noise levels, and low transmission spectra. The resulting 26 filtered spectra could be arranged in sets, each composed of spectra measured with different pressures and wavelength ranges, but the same resolution and at the same temperature. Spectra in each set were merged, averaging the absorption cross section values in the wavelength regions where the spectra overlapped, to obtain a final spectrum over the whole wavelength range and at the given temperature and resolution. The

resulting spectra are listed in Table 4.3. As an example, data from the filtered series and the final merged spectrum measured at 298 K and 0.5 Å resolution is shown in Figure 4.2.

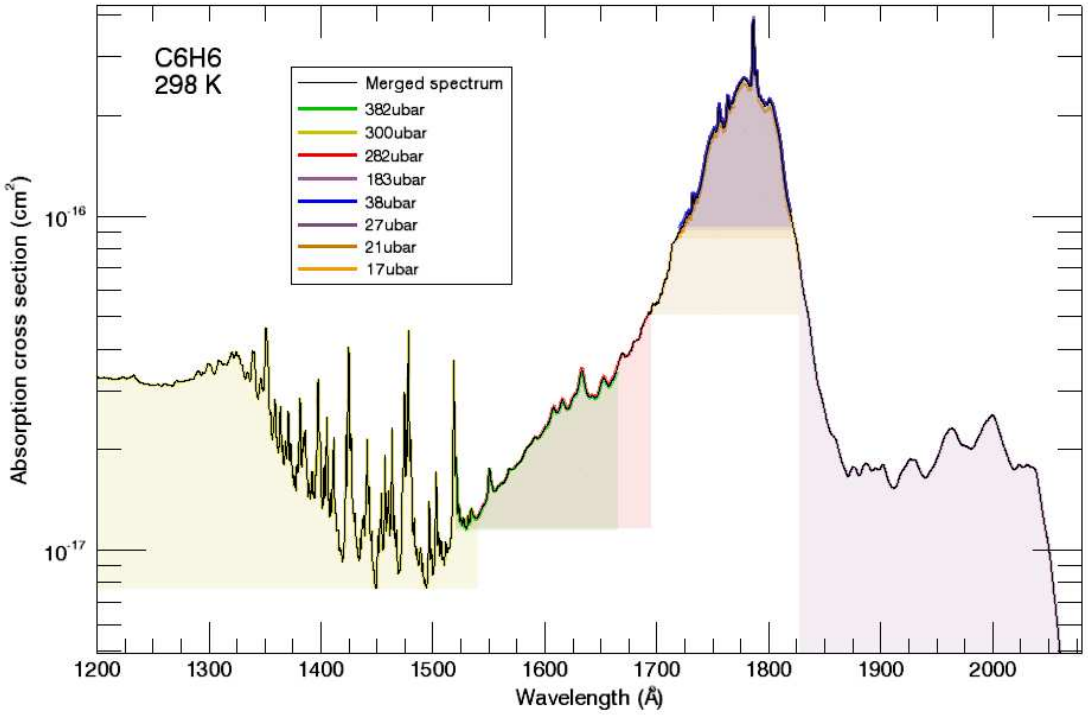

Figure 4.2: Absorption cross section from several filtered measurement series at 298 K, measured at 0.5 Å, with SR as a source. The result of each measurement series is a c-C_6H_6 absorption spectrum at a particular temperature, wavelength range, resolution, and pressure. Different series are identified by the shaded colored regions. The final merged spectrum for the corresponding temperature and resolution is also shown.

4.3.2 Absorption measurements with a deuterium lamp source, Meudon Observatory facility

The schematics of the set up for this experiment is shown in figure 4.3. Prior to its introduction into

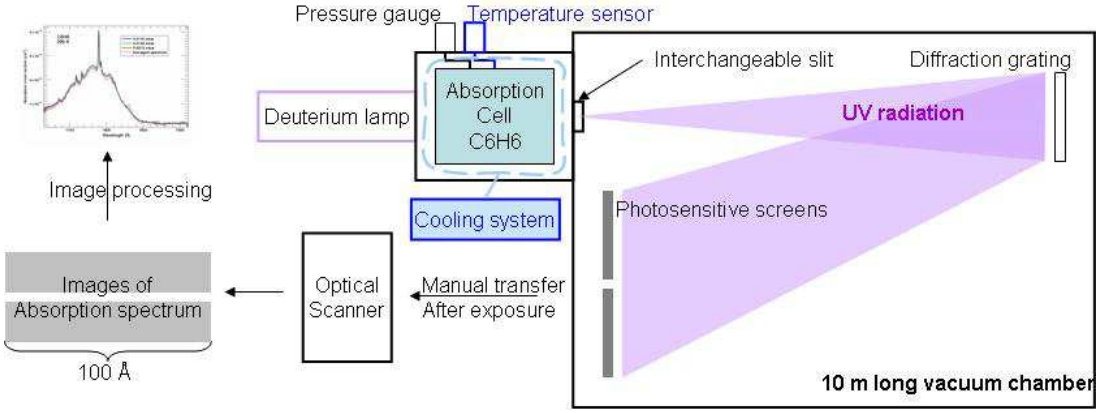

Figure 4.3: Experimental setup used to measure benzene absorption cross section with a deuterium lamp as a source at the Meudon Observatory facility.

the cell, the sample was held in liquid state at room temperature at equilibrium vapor pressure (some

100.18 mbar). The sample was contained in a test tube, connected to the cell by a valve system. Radiation from a Heraeus D200 VUV deuterium lamp was used as a continuum source. The non-collimated radiation enters directly the sample chamber through its few cm aperture. This means the molecules were irradiated with a VUV flux from 1140 to 4000 Å modulated in intensity according to the relative radiance spectrum of the lamp. This motivated the presence of a shutter valve between the source and the absorption cell to minimize photochemistry during sample insertion. All measurements were performed in the 1710 - 1910 Å range, with a relative resolution ($\lambda/\Delta\lambda$) of 2000 and 7 points per resolution. According to the wavelength calibration the wavelengths are accurate to (1 - 6)$\times 10^{-2}$ Å in the measured range. The vacuum spectra were measured at the same resolution and sampling as the benzene spectra. The choice of these values was a compromise between resolution and exposure time of the sensitive image plates where the spectra were registered. The resolution used is sufficient for the application to the analysis of UVIS spectra. The wavelengths values were provided by a calibration based on oxygen absorption bands (see below). The lamp intensity was variable along the slit and wavelength dependent. Therefore the measurements of a same day were performed using the same region of the lamp profile. The source also presented a flux variation of about 0.1%/min, limiting exposure time. Given the configuration of the experiment no stray light is expected from the environment.

The cell containing the sample during the measurements was the same as for the BESSY II measurements. The optical path for the radiation was 17.45 cm, the difference length with respect to the BESSY II case is due to different connectors being used to fix the cell to the whole experiment. The entrance and exit of the cell were covered by MgF_2 windows. This configuration allowed measurements down to the cutoff wavelength (about 1140 Å). After leaving the absorption cell the beam passed an interchangeable slit (2 mm for measurements at a relative resolution of 2000) and reached a 3600 lines/mm reflective concave diffraction grating in a Rowland Circle configuration with a diameter of 10.7 m. The spectrograph has an Eagle in-plane mounting where the slit and the plate holder for detection are in the same plane. The grating and the plate holder have to be rotated and displaced to keep the image in focus when the wavelength range is changed. The spectrum is recorded simultaneously on 2 FUJI image plates, each of them having a maximum useful length of 38 cm and linear response in intensities over five orders of magnitude. The image plates integrate the received flux so unstable or pulsed emission light sources can be used. The characteristics of the spectrograph are summarized in Table 4.1. It is worth noting the similarities between this instrument concept and the UVIS instrument in Cassini, the latter being, roughly, a reduced space version of the former (see UVIS characteristics in Section 2.1).

Table 4.1: Characteristics of the 10 m spectrograph at Meudon Observatory.

Grating	holographic (Jobin-Yvon)
Radius of the grating, m	10.685
Number of lines/mm	3600
λ of maximum efficiency, Å	1200
Plate factor (linear dispersion on the plate), Å/mm	0.25
$\lambda/\Delta\lambda$	2000, 50000, 150000
Wavelength range, Å	250 - 2200, with image plates 500 - 3000, with photographic plates
Maximum range covered in one exposure, Å	$\sim$ 200
Mechanical fittings	ISO-KF, ISO-CF

The cell pressure was measured at the level where the sample enters the cell. The empty cell pressure was less than 0.1 μbar. The range of c-C_6H_6 pressure used was 5-15 μbar, much lower than

the saturation pressure at the temperatures used (7×10^{-2} mbar at 210 K, Fray and Schmitt, 2009). The pressure increased a few μbar during the measurements due to air leaks and desorption. Intensity decrease was observed due to particle deposits on the windows. This limited the exposure time and therefore resolution (as a wider slit was needed to satisfy S/N requirements). The windows of the lamp and cell were regularly cleaned to overcome this problem.

The temperature was controlled and measured during the low temperature part of the experiment. A LAUDA Ultra-Kryomats RUL 80(-D) was in charge of keeping the system at a desired temperature. This latter quantity was measured with a type-K thermocouple fixed on the inside wall of the cell and located at the flat inner plate of the cylinder, in contact with the gas. The temperature uncertainty was 1 K and the stability better than this. There was no temperature gradient across the cell. During measurements at low temperature (below ∼250 K) a heating loop was installed around the entrances of the absorption cell to avoid air leakage due to the vacuum o-rings becoming rigid.

A measurement series to obtain one c-C_6H_6 absorption spectrum at a particular pressure and temperature was performed as follows. First a vacuum spectrum was measured, with no sample in the absorption cell. Then the chamber was filled with c-C_6H_6 until the desired pressure was achieved. A sample spectrum was then measured. After evacuation of the sample a new vacuum spectrum was measured. The exposure time for each of these spectra was 8 min. Then an oxygen spectrum was acquired, measured with a thinner entrance slit for wavelength calibration purposes, exposing during 30 min. The photosensitive image plates were then read on a Scanner Cyclone Plus Storage Phosphor System (Perkin-Elmer). The image plates are scanned by the system's laser focused to less than 43 microns, and the latent image is detected by its optics to create a high resolution 16-bit digitized image with quantitative data. The pixels values should be proportional to the flux received. Curiously, a square root dependence was noted instead in the output from the scanner. This was later confirmed as a bug in the version of the scanner data compression software used. This behavior was corrected during processing. The resulting image contains stripes of some 9000 x 200 (spectral x spatial) pixels corresponding to the different spectra measured during a measurement series. These stripes are cut, the values squared, and the rows averaged to get a spectrum (vacuum, benzene or oxygen). Unexposed regions in the plate are used to estimate a background correction.

The wavelength scale was determined from the Schumann-Runge molecular oxygen absorption bands (1750 - 1950 Å) measured in the same series (and therefore the same plate) as the benzene absorption, though with a higher relative resolution (50000). The oxygen spectrum measured at 215 K was point-to-point calibrated based on the oxygen absorption cross sections in Yoshino et al. (1992), choosing specific calibration reference points in the spectra. A wavelength vs. pixel number, first-order calibration polynomial was fit to the 20 points picked up in the range 1750 - 1880 Å. With this polynomial the benzene spectrum measured in that same measurement series was then calibrated in wavelength. For a particular absorption line, the difference in pixel number from one series to another comes from a different placement of the image plates during the exposures, therefore this difference is considered to be a solid shift in an integer number of pixels. This fact was used to calibrate the remaining of the spectra in the following way. The oxygen spectra measured in the different series, other than the one point-to-point calibrated, were cross correlated with the calibrated series, solid shifted accordingly, the pixel values in the calibration table updated and a new calibration polynomial calculated for each of them. Again, with this polynomial the benzene spectrum measured in the same measurement series was then calibrated in wavelength[1]. This procedure still left a small shift among

[1]In some series the oxygen spectrum was measured with a relative resolution of 2000. In this cases, the measured reference spectrum was smoothed with a boxcar function to allow a successful correlation. In one of the measurement series the oxygen spectrum was saturated, therefore the benzene spectrum was used for the cross correlation with no considerable degradation of the calibration.

all the spectra. Finally, all spectra were solid shifted with respect to the mentioned point-to-point calibrated spectrum to make the maximum of all spectra coincide. This shift was in all cases of the order of 10^{-2} Å.

The processing takes into account possible tilts/deformations in the images and regions with defects in the plates (that deteriorate with each use due to handling); some of these defects are corrected in the procedure. One type of defect was a point defect of a few pixels width at random positions, causing spikes in the spectra. For each spectrum these spikes were filtered out eliminating the values that differed from a smoothed version of the spectrum in more than three times the mean difference between the original spectrum and the smoothed version. Moreover, as the spectra were oversampled (some 90 points/Å), they were binned to achieve 7 points per resolution. This also helped to wash out the point defects. Bigger image plate defects like zones of several square centimeters with decreased sensitivity were not corrected for but are rare, and its importance diminished after further averaging (see below). After the corrections the measurements from the two separate image plates were joined, linearly interpolating the values in the center wavelengths corresponding to the gap between the plates (this gap varies according to the positioning of the plates during the measurement and it can be of some 5 Å in the worst case). The intermediate result of the measurement series was a wavelength-calibrated set of two vacuum spectra, one benzene spectrum and an oxygen spectrum in the range 1700 - 1900 Å. As the source flux varied with time during the measurements, the two vacuum spectra were used to calculate an intermediate interpolated vacuum spectra assuming a linear decay of intensity. From the ratio of the benzene and vacuum intensities a transmission was then calculated, the absorption cross section was derived from this transmission (see below).

Different series of spectra were measured in this experiment at different temperatures. Measurements at different pressure confirmed reproducibility and pressure independence of the results. At least 3 different pressures were explored for a given temperature. About 60 benzene absorption spectra were collected. The series were filtered excluding spectra (or part of them) with very low c-C_6H_6 pressure, spectra which clearly suffered from a systematic error, spectra with particularly high noise levels and saturated spectra. The resulting 12 filtered spectra could be arranged in sets, each composed of spectra measured with different pressures but the same temperature. For each set, values in the spectra differing in more than 4 times the median of the group were iteratively filtered out, further compensating image plate defects. The absorption cross section spectra in each set were then averaged to obtain a final spectrum at the given temperature. The resulting spectra are listed in Table 4.3. As an example, data from the filtered series and the final merged spectrum measured at 298 K and 1 Å resolution are shown in Figure 4.4.

As commented previously, during the measurements performed in Meudon an increasing with time opacity of the chamber windows was noted. This was due to deposited material while the experiment was being performed, motivating the regularly clean up of the windows. For these experiments the sample gas was irradiated with a beam composed by all the wavelengths in the spectrum of the VUV lamp, at once. The irradiation time was 8 min per spectrum. Thus, the question arose about the possibility of generation of chemical products and deposition, triggered by c-C_6H_6 dissociation. The molecular nature of the solid responsible for opacity of the windows was not studied further and remains unknown.

4.3.3 Absorption cross section derivation and uncertainties

From the transmission spectra, the absorption cross section was calculated using the Beer-Lambert law in the form

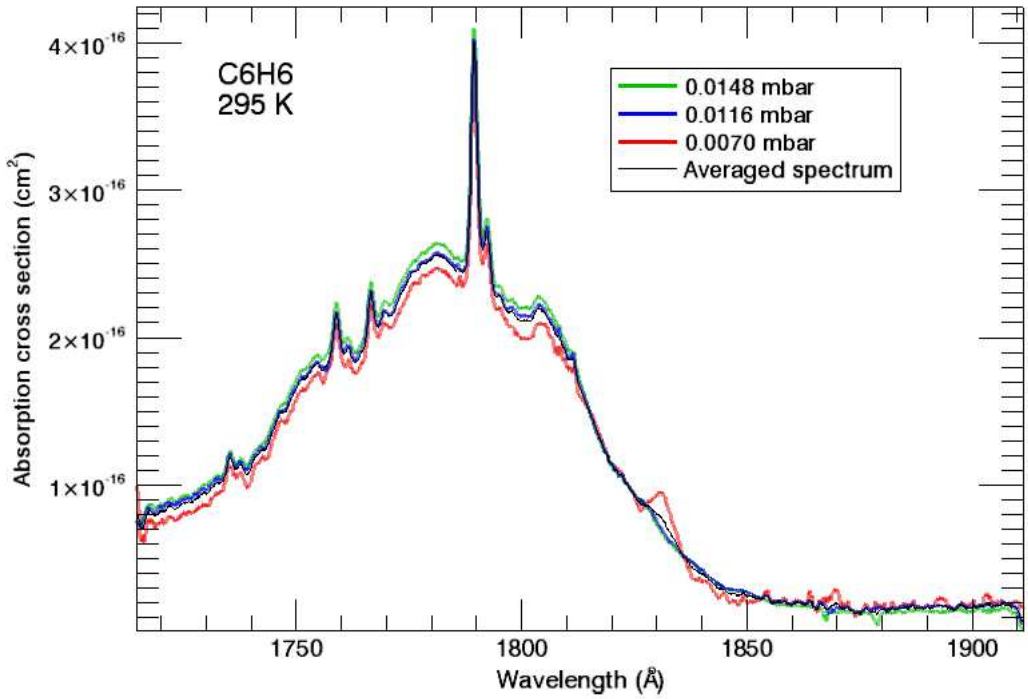

Figure 4.4: Absorption cross section form several filtered measurement series at 298 K, measured at 1 Å, with a deuterium lamp as a source. The result of each measurement series is a c-C_6H_6 absorption spectrum at a particular pressure and temperature. The final merged spectrum is also shown.

$$T = \frac{I}{I_0} = \exp(-\tilde{\sigma} l \frac{p}{T} \frac{T_0}{p_0}) \tag{4.1}$$

where the transmission as a function of wavelength, T, is the ratio of the sample spectra I and the vacuum spectra I_0, as explained in the previous section. The absorption cross section is $\tilde{\sigma}$, in units of amagat^{-1} cm^{-1}. The optical path through the absorption cell is l, p and T are the pressure and the temperature in the cell, $T_0 = 273.15\ K$, and $p_0 = 1013.25{\times}10^3 \mu$bar. The absorption cross section presented in the following sections is calculated according to

$$\sigma = \tilde{\sigma} n_0 \tag{4.2}$$

σ in units of cm^2 and n_0 is the Loschmidt constant $2.6867774{\times}10^{19} cm^{-3}$.

The uncertainty in the derived cross sections is mainly due to the uncertainty in the actual pressure inside the cell. For a particular spectrum the uncertainty is calculated as the relative difference between absorption cross sections measured at two extreme pressures, and is given by Equation 4.3,

$$\delta\sigma_\lambda = \frac{\sigma_{\lambda,plow} - \sigma_{\lambda,phigh}}{\sigma_{\lambda,plow} + \sigma_{\lambda,phigh}} \tag{4.3}$$

where *plow* and *phigh* represent the lowest and highest pressures measured in the wavelength range considered. This results in different uncertainty associated to different spectra and wavelength regions, according to different experimental conditions. For spectral regions where only one pressure was available, the uncertainty can be estimated from measurements in neighboring wavelength regions and/or measurements at similar temperatures. Table 4.2 summarizes the derived uncertainties corresponding to each spectra presented, the limits of the wavelength regions indicated are approximative.

Table 4.2: Uncertainties corresponding to each spectra derived in this work and presented in Table 4.3. The limits of the wavelength regions indicated are approximative.

Absorption cross section uncertainty (%) for measurements with deuterium lamp source				
Temperature (K)	Wavelength range (Å)			
	1710 - 1740	1740 - 1830	1830 - 1910	
295, 245, 215	10	5	20	
Absorption cross section uncertainty (%) for measurements with SR source				
Temperature (K)	Wavelength range (Å)			
	1150 - 1360	1360 - 1600	1600 - 1800	1800 - 2040
298 (1 Å resolution)	4	7	3	3
298 (0.5 Å resolution)			3	
250	<14	<14	<14	
230			7	

It is very difficult to obtain acceptable absorption measurements in a whole wavelength range where the absorption varies significantly within the range. Lower gas pressure in the absorption cell will allow clear measurements of strong absorption regions, but noisy measurements in regions of weak absorption, where the latter cannot be clearly determined. Higher gas pressures in the cell will allow measurements of smaller absorption coefficients, but might saturate strong absorption features. Sometimes experimental constrains, like the positioning of the photosensitive plates in the Meudon Observatory experiment, determine the wavelength region used in the measurements. In the range 1700 - 1900 Å the absorption cross section vary in a factor bigger than 12. The region around the maximum of absorption was given priority in this work. As a result, the measurements from the Meudon experiment above 1840 Å are very noisy. Nevertheless, the whole measured range is kept to provide a comparative value with the measurements performed with the SR source. The instrumental bandwidth is greater than the line width (see for example Pantos et al., 1978) of the Rydberg transitions, therefore the absorption cross section values for the peaks in the spectra are in these cases underestimated due to this experimental constraint. The valence transitions measured do not suffer from this problem.

4.4 Absorption cross section results and interpretation

This section presents the results of the absorption measurements and absorption cross section calculations described in Section 4.3. The characteristics of the final spectra are presented in Table 4.3. These spectra are shown in Figure 4.5.

Table 4.3: List of measured spectra. Spectra from the bibliography shown in Figure 4.6 are also included for reference.

Reference	Temperature (K)	Range (Å)	Resolution (Å)
This work, SR	298	1153 - 2062	1
This work, SR	298	1203 - 2103	0.5
This work, ^2H	295	1715 - 1911	1
This work, SR	250	1153 - 2103	0.5
This work, ^2H	245	1715 - 1912	1
This work, SR	230	1723 - 1823	0.5
This work, ^2H	215	1715 -1912	1
Pickett et al. (1951)	298	1538 - 2119	n[a]
Hammond and Price (1955)	298	1610 - 2130	n[a]
Pantos et al. (1978)	293 - 300	1780 - 2530	2.5
Rennie et al. (1998)	298	348 - 1342	1.7 - 2.3

[a] n = not specified

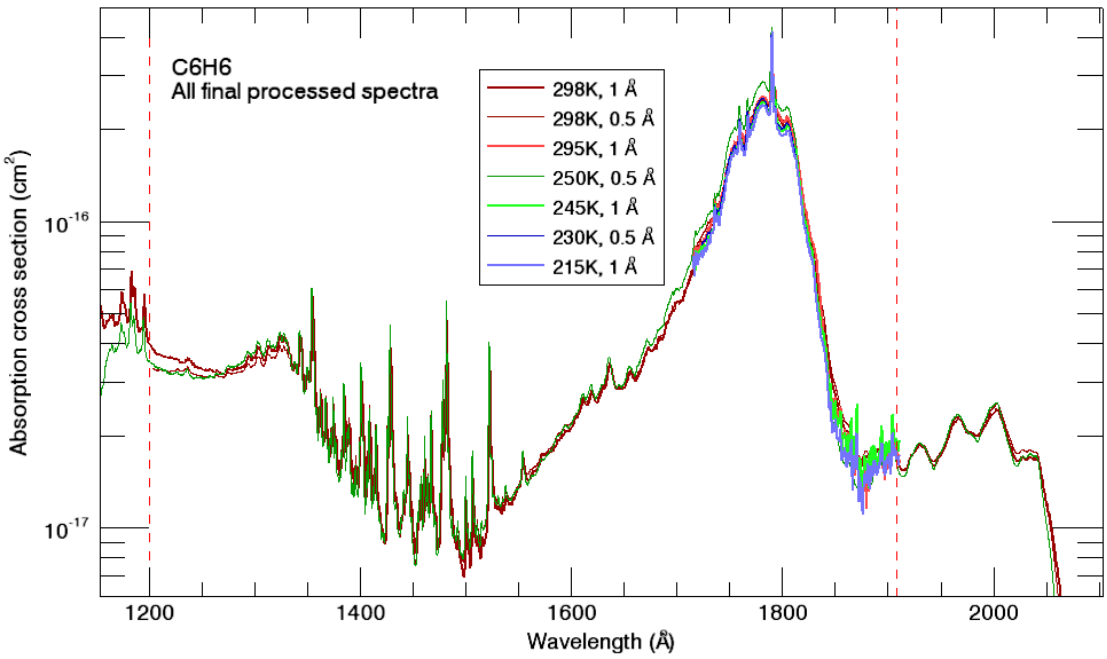

Figure 4.5: Benzene absorption cross section derived from the experiments and analyses described in Section 4.3, at different temperatures and different resolutions. The wavelength range of the UVIS instrument used to retrieve hydrocarbon density profiles (see Subsection 2.1.1) is shown as dashed lines for reference.

The measurements are in general self consistent according to the reported uncertainties and possible temperature effects. The only exception is the spectrum corresponding to 250 K. It presents an unexpected behavior for wavelengths above 1600 Å, the values being systematically about 10% greater than those corresponding to 298 K. This could not be explained and is attributed to some experimental error. Moreover, it was also noted that the measurements from the SR facility measured with 1 Å resolution showed less structure than the ones measured at the Meudon Observatory facility, with the same resolution. This might indicate that the resolution calculated for the monochromator system at the SR facility might have been overestimated. Taking this into account, the wavelength resolution corresponding to the measurements from the SR radiation referenced in this text should be considered nominal. In practice, the measurements with resolution 0.5 Å from the SR experiment will be compared with those at 1 Å from the deuterium lamp experiment.

As can be seen in Figure 4.5, it is difficult to identify band system onsets in the spectrum due to the overlapping of the neighboring systems and the presence of a continuum. In VUV spectroscopy of polyatomic molecules, transitions between states in the valence shell of the molecule mix with transitions to states in which the excited electrons occupy diffuse (Rydberg) orbitals with a principal quantum number larger than that of the valence shell. In single-photon absorption experiments four Rydberg series have been observed converging onto the lowest ionization threshold and at least three more onto higher limits. In addition, transitions into several low-lying valence states have been identified below the ionization threshold. Thanks to multi-photon absorption, the assignments of ten Rydberg series converging onto the first ionization potential (giving state $^2E_{1g}$) have been confirmed (see Rennie et al. (1998) and references within). A detailed description of the Rydberg series is out of the scope of the present work. Grubb et al. (1985) have summarized the ungerade and gerade Rydberg series converging onto the lowest ionization potential (9.25 eV), excited in single- and multi-photon studies. Even at the moderate resolution of the presented measurements some band

systems and transitions can be identified. The ultra-violet absorption spectrum of benzene in the region presented may be divided into 4 regions. The first of these is a diffuse absorption region 2050 - 1850 Å, of maximum about 1980 Å. The second is an extremely strong absorption region covering approximately from 1600 to 1850 Å, with a maximum about 1790 Å. The third region of absorption lies below 1600 Å till approximately 1350 Å. Here series of strong, narrow, bands of Rydberg type occur, converging to the first ionization potential of benzene. Below 1350 Å, the fourth region presents strong bands which are thought to be the first Rydberg bands leading to the second ionization potential of benzene (11.5 eV, Grubb et al., 1985). The absorption below the range covered here corresponds to other Rydberg states (see for example Rennie et al., 1998) converging to higher ionization potentials. Benzene absorption in the wavelength region studied here is 3 order of magnitude bigger than the other well know forbidden absorption region around 2500 Å (see for example Fally et al., 2009). This explains the dramatical fall of the absorption cross section above 2050 Å.

There are two electronic transitions in the region 2050-1700 Å: a system of very diffuse bands between 2050 and 1850 Å (responsible for the absorption of maximum around 1980 Å) and an extremely strong broad absorption with a few sharp peaks and an underlying continuum in 1850-1700 Å (responsible for the strong 1790 Å absorption, as argued already by Price and Walsh, 1947). The absorption in the region from 2000 to 1800 Å was interpreted in three different ways (see Pickett et al. (1951); Herzberg (1966) and references therein). It was believed by Carr and Stücklen (1939) and Hammond et al. (1950) to constitute the first member of the second Rydberg series previously reported by Price and Wood (1935) and co-workers. It has also been associated with the forbidden transition $^1A_{1g} - {}^1B_{1u}$ (see for example Feng et al., 2002; Koch and Otto, 1972). This assignment was already suggested by Nordheim et al. (1940), although these authors also suggest that the system may alternatively be ascribed to a forbidden $^1A_{1g} - {}^1E_{2g}$ π electronic transition. Craig (1949) has supported this assignment. The structure in this region is interpreted as a ring-breathing vibration by Pickett et al. (1951).

The region 1800 - 1600 Å is believed by Pickett et al. (1951) to represent two transitions, a Rydberg series overlying a valence transition of type $^1A_{1g} - {}^1E_{1u}$—this is the only symmetry-allowed transition in the c-C_6H_6 point group (Hammond and Price, 1955). The peak at 1789 Å in our spectrum (1789 Å in Pantos et al., 1978, 1790 Å in Pickett et al., 1951, 1787 Å in Koch and Otto, 1972) and the accompanying sharp bands were suggested to represent the first member of the second Rydberg transition in Price and Wood (1935), converging to the first ionization potential of 9.247 eV (Koch and Otto, 1972). Price and Walsh (1947) were convinced about this assignment both by the position of the band and by its accompanying vibrational pattern. They also suggested the overlaying continuous hump of absorption to come from C-H dissociation. Nordheim et al. (1940) also suggested this association for features observed in 1650 - 1850 Å, the series being assigned to transitions $^1A_{1g} - {}^1E_{1u}$. The continuous background is also interpreted as possibly due to a transition involving a C-H dissociation by the last authors. The association with a $^1A_{1g} - {}^1E_{1u}$ π electron transition is also done in Herzberg (1966) and Pantos et al. (1978). The 'shoulders' with maxima at 1781 Å and 1804 Å in our spectra are confirmed by Koch and Otto (1972) to be part of the underlying π excitation.

The bands in the region region 1600 - 1360 Å get weaker and closer together towards shorter wavelengths, and eventually merge into a weak continuum around 1360 Å. Price and Wood (1935) found that the sharp bands in this region could be arranged into two Rydberg series with their corresponding vibrations, which had approximately the same limit corresponding to an ionization potential of about 9.2 eV. These features are also identifiable in our measured spectra, the discrepancies with the reported wavelengths for the main members of the series being in most of the cases smaller than our spectral resolution (0.5 Å). Price and Wood (1935) mentioned the possibility of more vibrational progressions for some of the electronic bands, due to their high intensities. They did not found any.

The identification of such progressions in our spectra at 0.5 Å resolution might be possible, but was not explored. The intensity of both the Rydberg series definitely points to the fact that they are due to allowed transitions. Both series can be assigned to allowed transitions of symmetry $^1A_{1g} - {}^1E_{1u}$ according to Nordheim et al. (1940). Four Rydberg series were identified by Wilkinson (1956), each with 8 to 10 members, and many with vibrational structure. The assignment to Rydberg series is also done in further references (for example Herzberg, 1966; Pantos et al., 1978; Grubb et al., 1985).

The region 1360 - 1150 Å includes the first ionization potential: 9.25 eV or 1340.4 Å. The features in this region were seen by Price and Wood (1935) considerably more diffuse than those at wavelengths longer than 1360 Å. The first band in the long wavelength end is clear in our spectrum (at about 1355 Å). Also identified by Hammond et al. (1950), this feature corresponds to the first member of a Rydberg series converging to the second ionization potential of ca. 11.5 eV. Koch and Otto (1972) confirm with the help of photoelectron spectra from Turner (1970) that the band groups seen in our spectra are the first (n=3, the group at longer wavelengths) and second (n=4, the group at shorter wavelengths) members of a Rydberg series and associated vibrations, converging to the second ionization potential of 11.45 eV, giving state $^2E_{2g}$. In a latter publication Koch and Otto (1976) identify other 2 Rydberg series, with a first member in the long wavelength structure and a second member at shorter wavelengths still in the range of our measurements. One of these two series converges to a third ionization potential of 11.7 eV (Whetten et al., 1983). This region has been remeasured and interpreted with the aid of photoelectron spectra by Rennie et al. (1998).

Khvostenko et al. (2003) has questioned the conventional assignments proposed in the preceding literature. Correlating measured excited state energies with calculations from MNDO/d they deduced the electronic configuration of the excited states of benzene derivatives, then interpreted the spectrum of benzene on the light of the results. They assigned the bands around 2000 Å to a $\pi \rightarrow \pi* \; E_{1u}$ transition (instead of the conventional B_{1u}) and the bands around 1790 Å to a $\sigma \rightarrow \sigma* \; E_{1u}$ transition (instead of the conventional $\pi \rightarrow \pi*$). Under the lack of further references, to the best of the author's knowledge, that confirm this new assignment I decided to use the conventional one for the discussion above.

Pantos et al. (1978) underlined the importance of the effect of the instrumental bandwidth. The Lambert-Beer law is correctly used to obtain the cross section only when the exciting light bandpass is much less than the inherent line width of an absorption line. This is the case for the $^1B_{1u}$ and $^1E_{1u}$ transitions, for which they found no variation with bandwidth. But for the Rydberg bands our bandwidth is larger than the widths of the lines (line widths of approx 0.1 Å should be expected in the Rydberg region according to Pantos et al., 1978). In these cases the derived absorption cross sections are underestimated. This makes not much harm to the identification of benzene on Titan by means of UVIS observations, as this is based on the large feature associated to the $^1E_{1u}$ valence transition. However, the peak associated to the first member of the second Rydberg series in Price and Wood (1935) is some 1.7 times bigger than the mentioned transition. Thus it can have an influence in the detection. According to the variation of calculated extinction with bandwidth in Pantos et al. (1978), a very important error can be expected in this peak. However, our results imply a less steep variation of extinction with bandpass when passing from 1 Å to 0.5 Å bandwidth, so the error might not be that important. Further analysis should be performed to better estimate this possible deviation from the real absorption cross section and, if this peak is seen to play an important role in the detection of benzene in a future analysis, for example with a higher resolution than that of the UVIS instrument, attention should be paid to the resolution of the absorption cross section used.

Figure 4.6 shows the absorption cross section measured at 298 K and 0.5 Å nominal resolution, and results from other works (Pickett et al., 1951; Hammond and Price, 1955; Pantos et al., 1978;

Rennie et al., 1998). Tabulated data from the first, second and forth references were downloaded[2] already in the units plotted here. Data from the third reference was read from their Fig. 3. For the first three references, extinction coefficients vs. wavenumber have been read from the original work and converted to absorption cross sections (conversion factor 3.8235×10^{-21}) vs. wavelength. The absorption cross section presented in Suto et al. (1992) and measured at 1 Å resolution (not shown here) agree with those from Pantos et al. (1978) within the 10% uncertainty in the newer results. Improved resolution in our work permits to identify vibrational features absent in the old spectra,

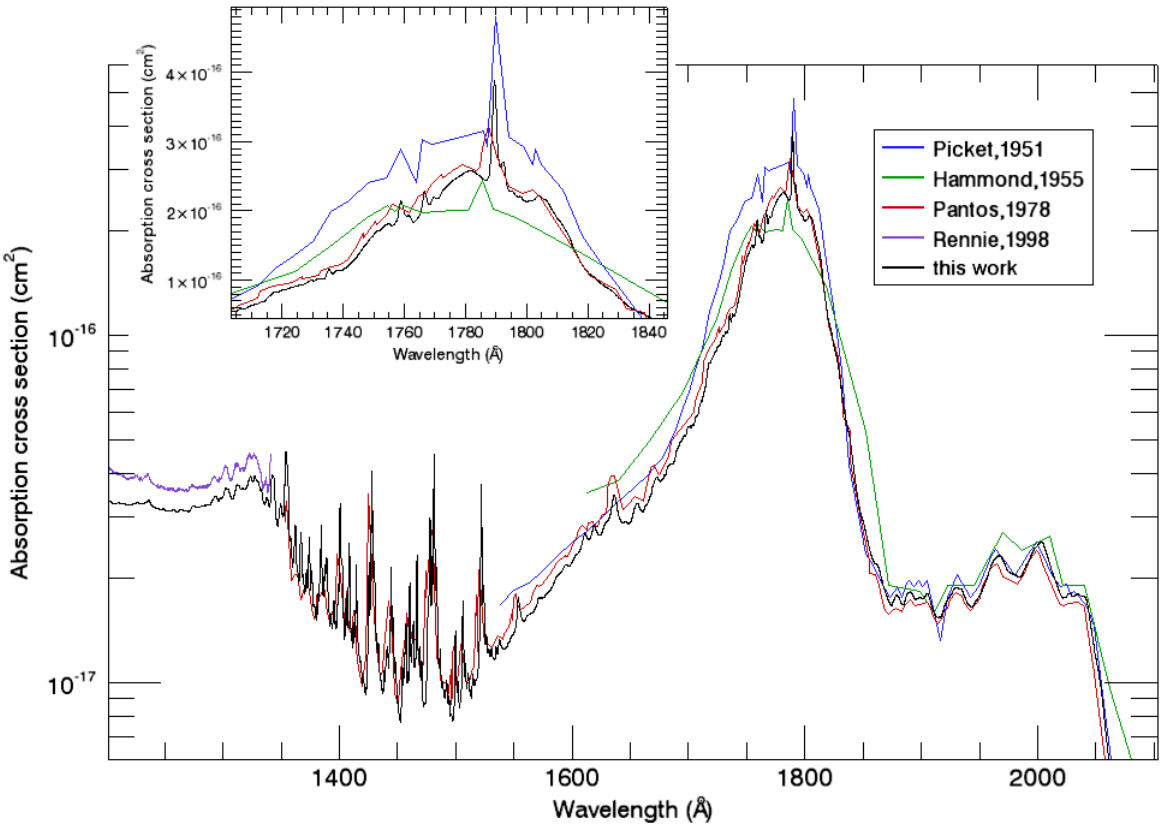

Figure 4.6: Benzene absorption cross section measured with SR as a source, at 298 K and nominal 0.5 Å resolution. Measurements from other work are shown for comparison (see text for references). The inset better shows differences in absolute values and resolutions.

particularly the bands around 1759 Å and 1767 Å. The best agreement in absolute value is with the data from Pantos et al. (1978). There is a shift in wavelength between our curve and theirs, maybe due to the reading process or the higher resolution in our data. The peaks at 1781, 1789 and 1804 Å in our data agree well with the values of 6.96, 6.93 and 6.87 eV assigned to different transition in Bolovinos et al. (1981, 1982). In this last reference the benzene spectrum from Pantos et al. (1978) is included for reference.

4.4.1 Temperature variations

One of the main motivations for doing the presented spectroscopic measurements was to study the temperature behavior of the benzene absorption cross section. From the pure spectroscopic point of view, even at the moderate resolution of our measurements, this would be useful to see the reaction of

[2]Downloaded from http://www.atmosphere.mpg.de/

the different band systems to lower temperatures and compare with theoretical calculations. The relevance of the temperature variation in the absorption cross sections for atmospheric VUV spectroscopy has been commented in Chapter 2. In that chapter it was underlined the importance of being in possession of absorption cross sections measured at temperatures relevant for the upper atmosphere of Titan ($\sim$ 150 K, see Section 5.2), or to have the confirmation of the absence of significant variations with temperature, at least at the resolutions concerned. Pickett et al. (1951) mentioned that the relative intensity of the first two bands in the 2000 Å region (reading the spectrum from the long wavelength end) measured at 253 K showed no measurable change, with respect to the measurements at room temperature. Apart from this comment, no systematic study of temperature variations of the benzene absorption cross section in the VUV region studied here was found in the bibliography consulted. For these reasons we measured absorption at different temperatures in Berlin and Meudon and analyzed the variation in the absorption cross sections as a function of temperature. The results are presented in this subsection.

To quantify temperature effects it is convenient to calculate a percentage fractional change in absorption cross section (see for example Ferradaz et al., 2009). This coefficient is given by equation 4.4,

$$P_{c,T} = 100 \times \frac{\sigma_T - \sigma_{298}}{\sigma_{298}} \tag{4.4}$$

where a positive value means the absorption cross section at temperature T is greater than that at room temperature. Figure 4.7 shows the $P_{c,T}$ coefficient calculated for some of the spectra in Table 4.3, in the region 1735 - 1820 Å, the region for which measurements at more than two different temperatures are available. Accordingly to the previous discussion about the resolution of the spectra, the measurements with the deuterium lamp source at 1 Å resolution are compared with the measurements with SR at nominal 0.5 Å. The maximum uncertainty in the absorption cross section is also shown in Figure 4.7. The reference used for the calculation of the $P_{c,T}$ in this case is the absorption cross section spectrum measured at 298 K using SR as a source.

Even though most of the variations observed remain within the measurement uncertainty, significant variations as a function of temperature are observed for some of the curves. Among those curves within the uncertainty limits, the variability observed for the measurement at 295 K does not represent a real variation with temperature but a measure of the repeatability of the measurements (with 2 different instruments). Indeed, this curve and the reference correspond to the same spectra, at almost the same temperature, performed with the two different experimental setups presented in the previous section. The fact that the pink solid curve is within the limits marked by the uncertainty in the measurements verifies the coherence of the results, and validates further comparison of results derived from the different experiments. The curve corresponding to the measurements at 250 K is shown for completeness, yet the problems commented before for these measurements eliminate all validity from the temperature variation observed in the figure. The curves for 245, 230, and 215 K present a common overall behavior. The absorption cross section decreases with decreasing temperature in most of the wavelength range shown, the bigger decrease observed for wavelength at the local minima in the absorption cross section. For some of the local maxima the behavior is opposite, the absorption increasing with decreasing temperature, while the width of the associated peak diminishes. This is evident for the local maxima around 1760 Å (only for the 230 K curve) and for the global maximum in the region, close to 1790 Å. This maximum is one of the significant variations, reaching out of the uncertainty limits. This behavior is what can be expected for transitions involving low energy states, which become more populated, and therefore more absorptive, when the temperature decreases. Some peaks representing weaker transitions, at the sides of a stronger one, decrease with decreasing temperature. These correspond to transitions from higher energy levels, whose population

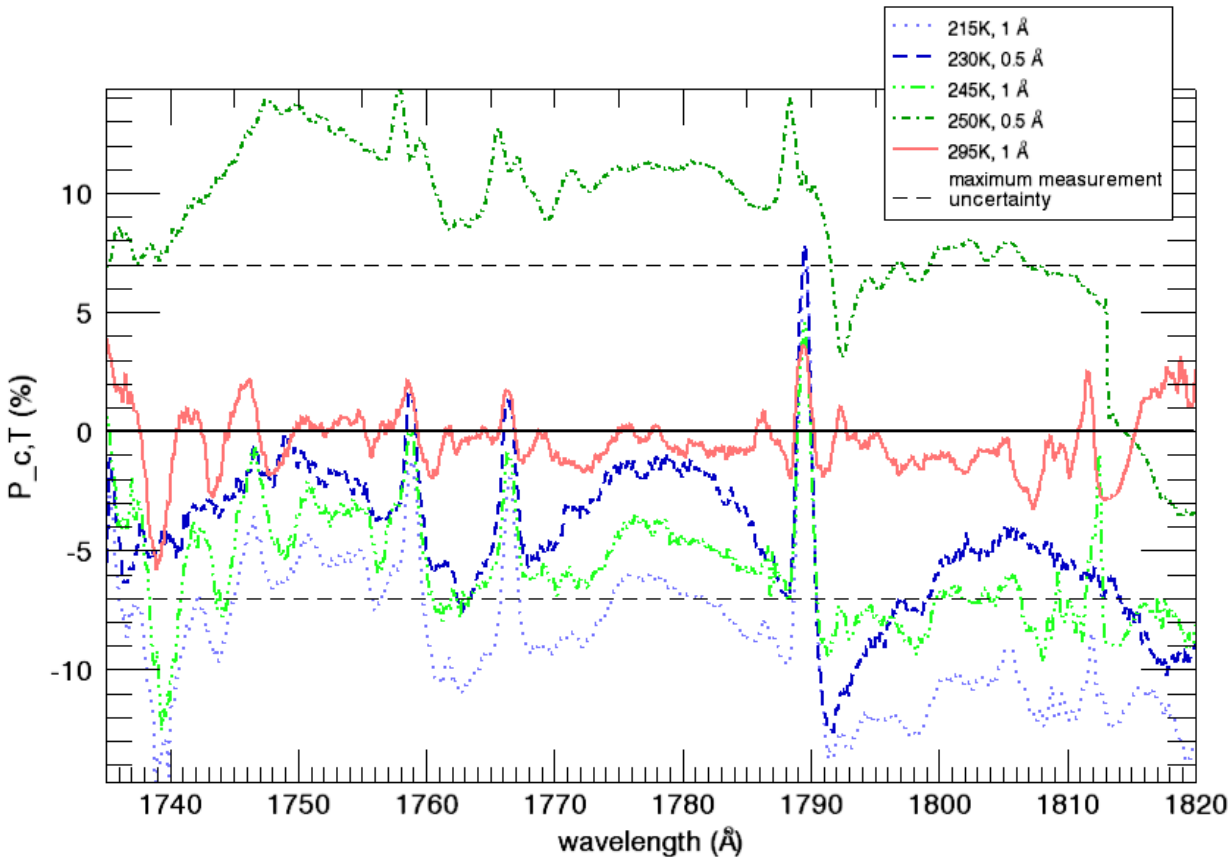

Figure 4.7: Fractional change in absorption cross section, $P_{c,T}$, for some of the spectra in Table 4.3, in the region 1735 - 1820 Å. The maximum uncertainty in the absorption cross section is also shown.

decreases with decreasing temperature and consequently the intensity of the associated absorption. Other significant variations are seen for some of the minima, mainly for the curve corresponding to measurements at 215 K. Nonetheless, the variation for the three lowest temperatures remain significant for the minimum on the long wavelength side of the absolute maximum of absorption.

The $P_{c,T}$ coefficient calculated for the spectra measured at 250 K is shown in Figure 4.8, for the region 1210 - 1650 Å. Some variations are attributed to the fact that the peaks get thiner and thus increase in height when the temperature decreases. Although some of the significant variations observed correspond to real changes with temperature (see Figure 4.9), variations in wavelength smaller than the 0.17 Å measurement precision should not be taken into account.

The data presented in this work, particularly the temperature variations measured, are a valuable new addition to the benzene absorption cross section databases. The relevant variations observed happen at separate wavelength intervals within the spectral range covered by the $A_{1g} - E_{1u}$ continuum absorption, and are at most of some 14%. The identification of benzene in the UVIS spectrum is based on the $A_{1g} - E_{1u}$ continuum absorption, and in less extent on the over-imposed Rydberg peaks. The noise in the optical depth measured by UVIS in this region is bigger than the relevant temperature variations shown here (see for example Koskinen et al., 2011). Therefore, the effects of the observed temperature variations on the detection of benzene on Titan with UVIS should be negligible. On the other hand, the lowest temperature explored here is 215 K, while Titan's thermosphere can be as cold as ∼120 K (see Section 5). Thus, an absorption cross section temperature effect affecting the UVIS c-C_6H_6 retrieval can not be fully discarded until absorption measurements at lower temperatures are

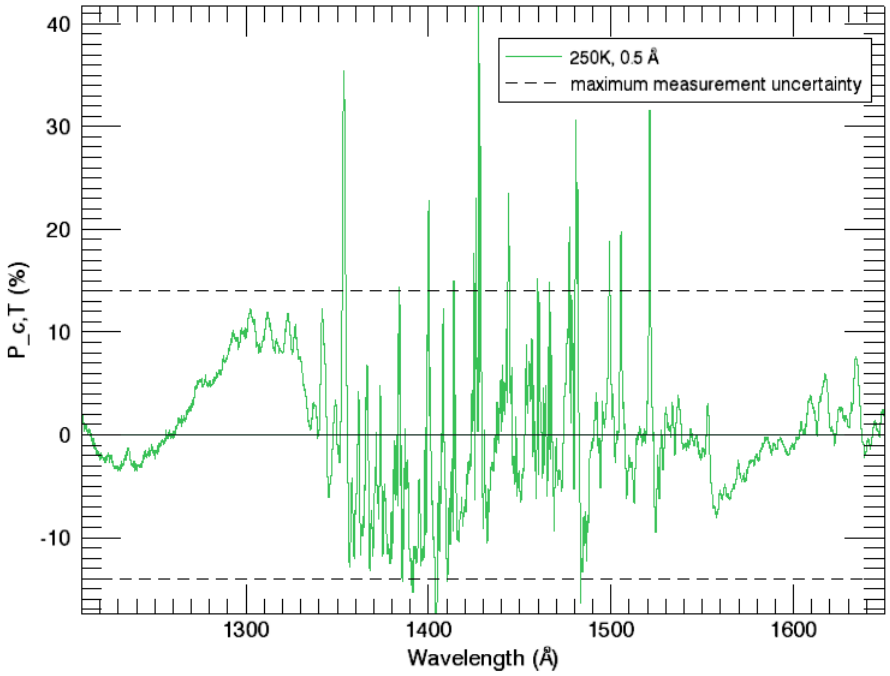

Figure 4.8: Fractional change in absorption cross section, $P_{c,T}$, for the spectra measured at 250 K, for the region 1210 - 1650 Å. The maximum uncertainty in the absorption cross section is also shown.

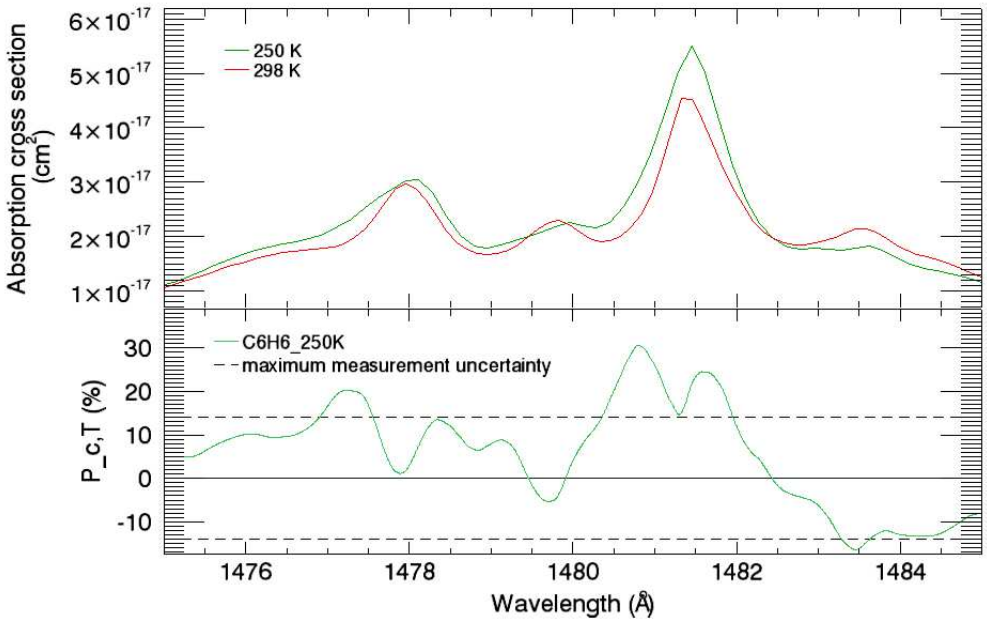

Figure 4.9: Fractional change in absorption cross section, $P_{c,T}$, for the spectra measured at 250 K, zooming in one of the band system. The maximum uncertainty in the absorption cross section is also shown.

available.

4.5 Summary of chapter

Benzene has been detected in experiments modeling Titan's atmosphere, included in models of it, and actually detected in the atmosphere itself. Its importance for Titan's atmospheric chemistry is based on the fact that it can be the precursor to the formation of a whole host of heavier hydrocarbons, including polycyclic aromatic hydrocarbons. Benzene density profiles in the upper atmosphere were obtained from the analysis of UVIS data. The knowledge of the benzene absorption cross section is mandatory for its detection with UVIS. The absorption cross sections have been thoroughly explored in the past, but an analysis of their temperature dependence was lacking, and presented in this chapter.

This chapter presented absorption cross sections in the range 1153 - 2103 Å, at 1 Å resolution and covering 5 temperatures in the range 215 - 298 K. The absorption cross sections were obtained in two different international facilities, the BESSY II synchrotron in Berlin, and the Meudon Observatory spectrograph in Meudon. The measurements are self consistent and compare well with previous work. The absolute values reported here for sharp transitions might be underestimated due to the experimental bandwidth being larger than the width of some of the transition. This is expected not to affect significantly the detection of benzene by the UVIS instrument. No significant variation of the absorption cross sections with temperature was observed. The effect of this insignificant variation on the detection of benzene on Titan with UVIS should be negligible. Nevertheless, an effect of an absorption cross section variation with temperature on the retrieval of benzene from UVIS data can not be fully discarded, until absorption measurements at lower temperatures than those presented here are available.

Chapter 5

Atmospheric composition and variability

This chapter presents the composition and temperature of Titan's upper atmosphere derived from the stellar and solar occultation analyzed, in the form of column density profiles and number density profiles, and averaged temperatures. Synergy among the FUV and EUV channels in UVIS is underlined, as well as comparison of CH_4 and N_2 profiles with measurements derived from data of other instruments. Particular attention is called on the C_6H_6 profile derived using the absorption cross section presented in Chapter 4. The last section presents the temperature values as a function of several geometric and temporal variables, accompanied with brief discussions about variability of the atmosphere.

5.1 Column density and number density profiles

5.1.1 Abundance of minor constituents, from stellar occultations measured in the FUV

The column densities of the minor constituents derived from stellar occultations measured during the T41 and T53 flyby are shown in Figure 5.1 and 5.2, respectively. The Q-probabilities associated

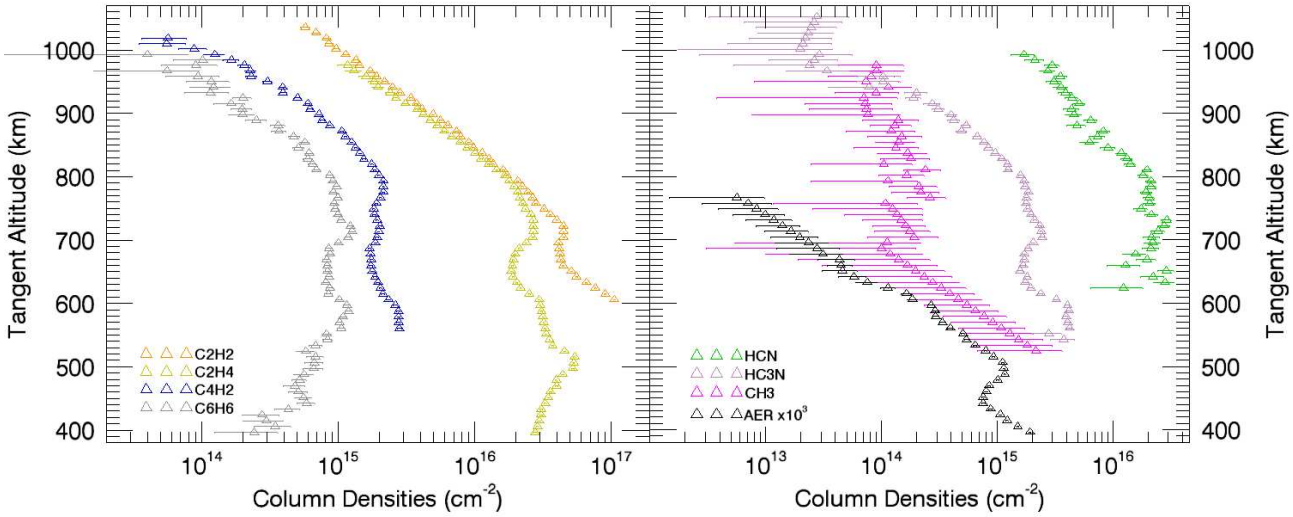

Figure 5.1: Column densities derived from a stellar occultation during flyby T41.

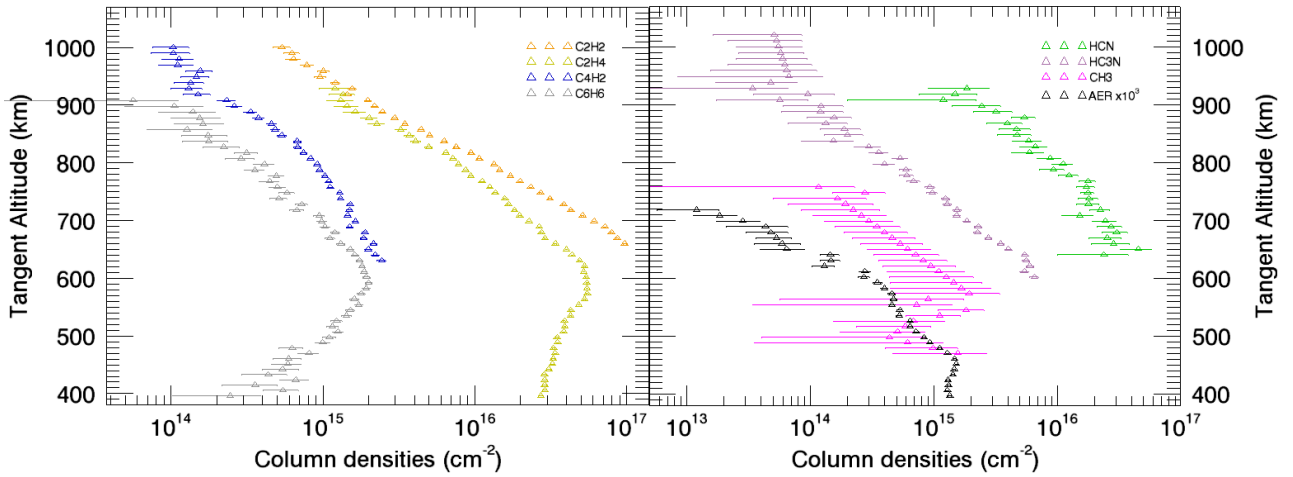

Figure 5.2: Column densities derived from a stellar occultation during flyby T53.

to the χ^2 start to be bigger than 10^{-9} for altitudes above 924 km for T41, and 827 km for T53,

which would mean that fits for lower altitudes are not good. However, the reduced χ^2 for most of the altitudes in T41 fall in the range 0.75 - 2.5, the range being 0.8 - 1.6 for T53, implying a good fit. This casts doubts on the applicability of the Q-probability criteria used, or its implementation in this work. Based on the χ^2 values obtained, the overall results of the simulations and the general agreement of the number densities with previous works (see below), most of the column densities shown are considered to describe well the state of the atmosphere at the different altitudes. Figures 5.1 and 5.2 show the column densities after the filtering commented in Section 3.3, which determines the altitude range of the profiles. For the case of T41, most of the CH_3 column densities are interpolated values, which means that for most of the altitudes the procedure could not find appropriate values to fit the data. The profile, therefore, lacks of physical significance. The same applies for the profile of HC_3N above 1000 km and the AER profile above 685 km. For the rest of the species and altitudes, only a few of the values shown are interpolated results. The CH_3 column densities from T53 deserve the same comments as the CH_3 profile from T41. The same applies for the T53 profile of C_2H_4 below 440 km, HC_3N above 928 km, and the AER profile above 660 km. For the rest of the species none or only a few of the altitudes contain interpolated values.

The number densities of the minor constituents derived from stellar occultations measured during the T41 and T53 flyby are shown in Figure 5.3 and 5.4, respectively. The figures show the profiles after

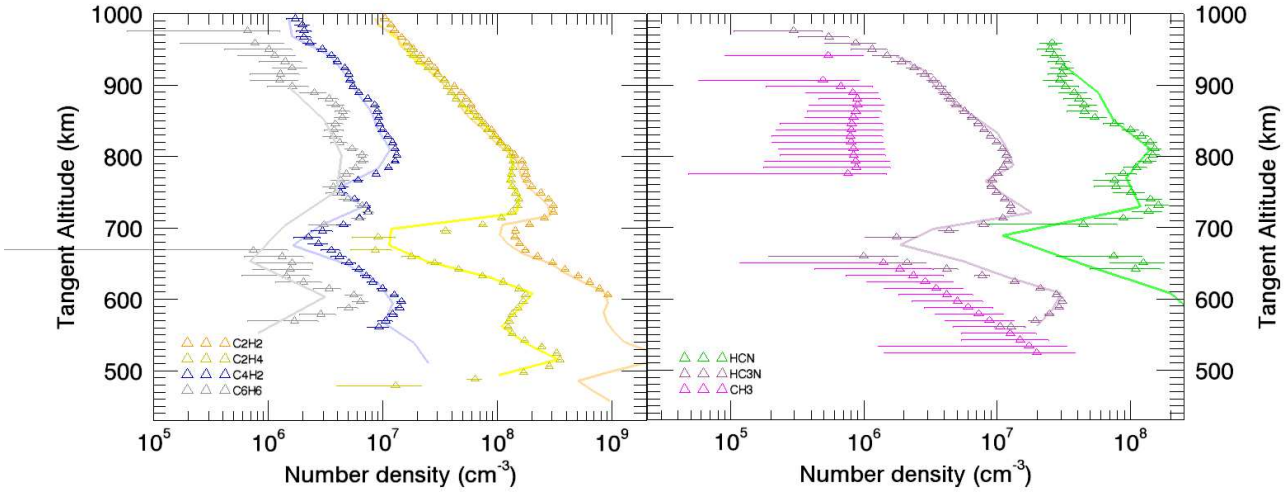

Figure 5.3: Number densities derived from a stellar occultation during flyby T41. Solid lines are profiles from Koskinen et al. (2011).

the filtering commented in Section 3.4, which determine the altitude range of the profiles. Results for CH_3 are shown for completeness, but following the comments for the corresponding column densities above, they lack physical significance.

The several sources of uncertainties were briefly described along with the analysis procedure in Chapter 3. The uncertainty coming from the Poisson counting statistics affecting the detector measured counts is propagated in the calculation of transmission and optical depth. The uncertainty in the column densities is that given by the MPFIT routine as the 1-σ uncertainty of the calculated parameters. The systematic uncertainty coming from the measured absorption cross sections (up to 10% in the worst cases), are not taken into account for the calculation of the uncertainty bars shown in the plots. Finally, the uncertainties in the derived number densities is the square root of the diagonal elements of the number density covariance matrix (Equation 3.11), dependent on the column density covariance matrix, and calculated during the column density inversion. Note that for some altitudes in the column density or number density profiles, the calculated 1-σ uncertainties are smaller than the symbol used for the plots. According to the simulations presented in Section 3.6, it is the 2-σ uncer-

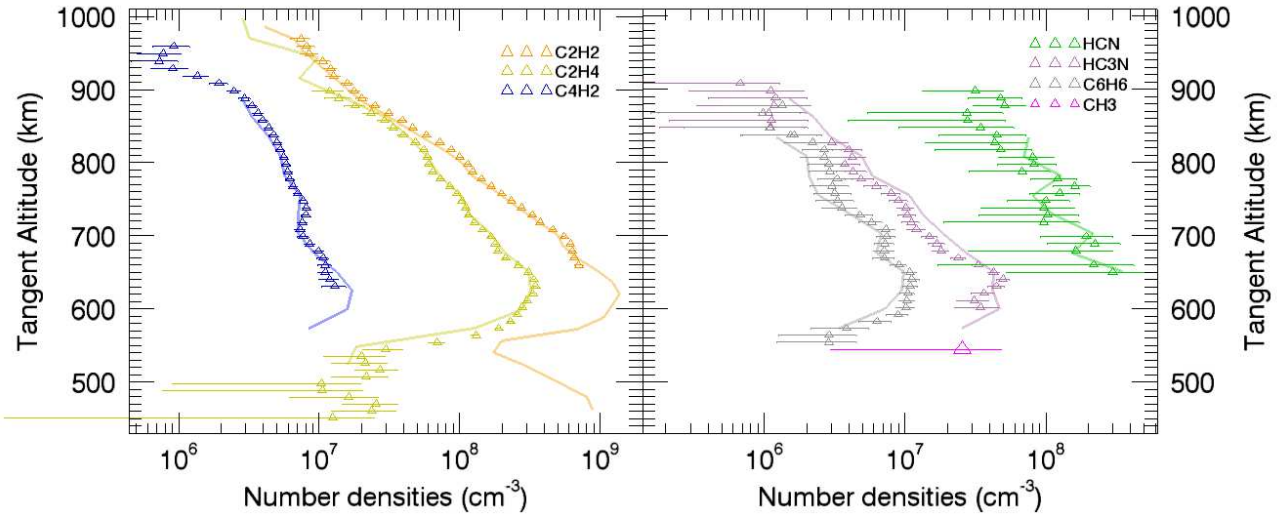

Figure 5.4: Number densities derived from a stellar occultation during flyby T53. Solid lines are profiles from Koskinen et al. (2011).

tainty interval that better characterizes the results. Similar considerations apply to the uncertainties in the abundances of the major constituents (see below). The uncertainties in the spectral fitting, however, do not apply in the case of solar occultations, the uncertainties in the column densities are derived through traditional error propagation in these cases.

The number density profiles in Figures 5.3 and 5.4 are in good agreement with those from Koskinen et al. (2011), shown as solid lines in the plots, derived with the same techniques but different implementations. Some differences are, however, worth noting. The altitude coverage of the profiles derived here is similar to that in Koskinen et al. (2011), although for some species the profiles in this reference reach lower altitudes—especially for C_2H_2, extending 150 km lower—and, rarely, higher altitudes—like for C_2H_4 extending some 50 km higher. This might be due in part to the conservative criteria used in this work to limit the altitudes considered to have valid transmission values (see Section 3.3). For species HC_3N and C_6H_6 it is the profiles from this work that cover higher altitudes than those in Koskinen et al. (2011), some 40 km and 80 km, respectively. The C_2H_4 profile from this work goes a few km lower. Although the profiles from the present work show a denser altitude sampling it should be kept in mind that the altitude resolution is dictated by the spread of the averaging kernel characterizing the column density inversion. This resolution, calculated according to the procedure described in Section 3.4, is about 20 - 30 km for the profiles shown in Figure 5.3 (T41), except for HC_3N (∼35 km); and 15 - 25 km for the profiles shown in Figure 5.4 (T53), except for C_6H_6 and HC_3N that have resolutions of about 30 km and 35 km, respectively. Number density variations along several tenths of km are coincident in the profiles from this work and those from Koskinen et al. (2011), but some of the profiles derived here present more oscillations. This might be artifacts of the inversion technique, caused by the dispersion in the column densities (see for example the column densities of C_6H_6 for altitudes above 800 km, in Figure 5.1).

The number density profiles present maxima of abundance, the most prominent located about 510 km, 600 km and 730 km for T41. These coincide with strong absorption observed in the transmission as a function of altitude for the corresponding observation, motivating their interpretation as absorption layers. This kind of absorption is clear in Figure 2.11 (corresponding to T53) for one of the characteristic absorption bins of C_4H_2. Unfortunately, the retrieved number densities do not reach that low, probably, again, due to the conservative altitude filtering. There are also depleted regions. Many profiles present an overall leveling-off below 800 km (T41) or 640 km (T53). A level

off in hydrocarbon column densities was also observed by Shemansky et al. (2005) in data from the Tb flyby. There are also several depletion layers, the most prominent located about 560 km and 670 - 690 km for T41. This is less evident for T53 because the retrieved profiles do not reach such low altitudes as in the case of T41. Nevertheless, the increase in transmission around 520 km evident from Figure 2.11 for the characteristic absorption bin of C_6H_6 can be correlated with its depletion seen in Figure 5.4. Koskinen et al. (2011) presented an interpretation of these layers in terms of gases-dominated absorption at high altitudes and aerosol-dominated extinction at low altitudes. This interpretation is further validated by the characteristics of the measured aerosol extinction.

The aerosol extinction is shown in Figure 5.5. As the extinction is derived using the measured

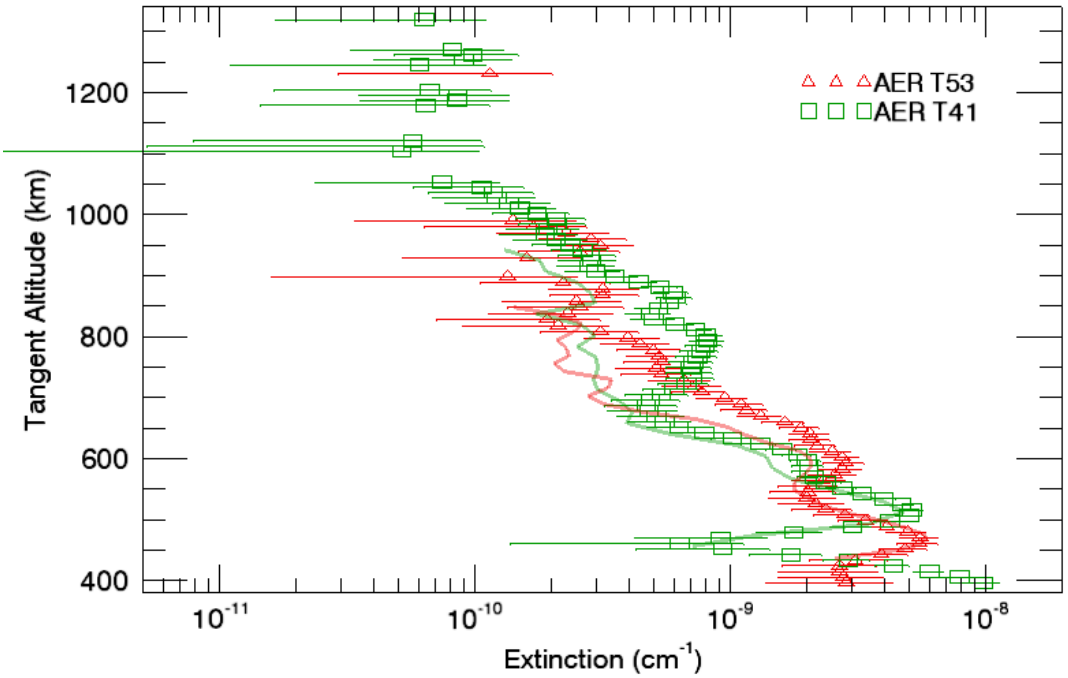

Figure 5.5: Aerosol extinction derived from stellar occultations during flybys T41 and T53. Solid lines are profiles from Koskinen et al. (2011).

optical depth and not the filtered column densities, the aerosol profiles can extend to lower and higher altitudes with respect to those from the molecular species. Nevertheless, the values higher than 1000 km present big uncertainties and are in a region where the procedures failed to retrieve extinction in the simulated data (see Section 3.6). Below 1000 km the profiles from the two occultations seem to be anticorrelated. Both present an oscillating behavior, with clear extrema. The more evident maxima happen at 515 km and 800 km for T41 and at 465 km and 595 km for T53. The peak in extinction at 465 km correlates well with the dip in the curve of transmission as a function of altitude for the wavelength bin [1800, 1900] Å (see Figure 2.11), that is supposed in this work to be dominated by aerosol extinction, and that was indeed used to derive the extinction in Figure 5.5. The second maximum at about 595 km correlates better with the dip in the transmission of the C_6H_6 wavelength bin [1740, 1819] Å, which overlaps 20 Å with the AER bin (although the maximum in C_6H_6 absorption is about 1790 Å). Therefore, for the interpretation of this high altitude maximum in terms of extinction layers, the consideration of a combination of aerosols and hydrocarbons could be more appropriate to interpret the results. For T41 a similar analysis can be done, although in this case the layer at 515 km correlates not only with a dip in the AER bin, but also with the C_6H_6 and C_4H_2 bins. Moreover, the maximum of extinction at about 800 km has no evident counterpart dip in the transmission curves.

It should be noted that the simulations suggest that extinction is not well retrieved below 675 km, but the agreement of the profiles with the previous work motivates a reconsideration of the validity of the values for these altitudes. Aerosol extinction profiles for T41 and T53 derived with the same techniques as here but different implementations are presented in Koskinen et al. (2011); they are reproduced as solid lines in Figure 5.5. The profiles presented here are in good agreement with those from the cited reference from 450 km till 700 km in the case of T41, and till 550 km in the case of T53. Koskinen et al. (2011) used the bin [1850, 1900] Å to characterize aerosol extinction, which leaves out the eventual extinction below 1850 caused by hydrocarbons. This might be the reason for the difference in the profiles above 700 km (T41) or above 550 km (T53). The discrepancies mentioned call for a more detailed analysis of the atmospheric extinction in the long wavelength end of the FUV detector, which is certainly a challenge considering the low S/N ratio in this part of the spectrum.

Benzene

An introduction about benzene in Titan was made in Section 4.1, where the relevance of this molecule in the context of Titan's upper atmospheric chemistry was put into evidence. The number density profiles for C_6H_6 in the upper atmosphere obtained in this work from stellar occultation measurements are plotted in Figure 5.6. It is reminded once more that high frequency oscillations should be

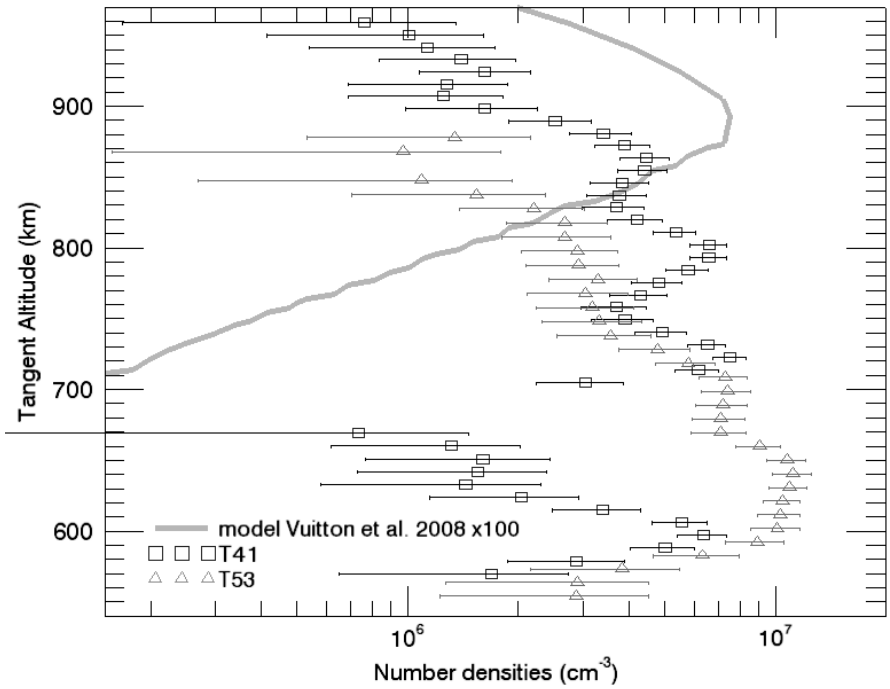

Figure 5.6: Benzene number density profiles derived from stellar occultations during flybys T41 and T53. The solid line is a profile calculated from those in Vuitton et al. (2008), scaled by a factor 100.

interpreted with caution, as they might be due to artifacts of the retrieval technique. The two profiles agree in the range 560 - 600 km and from 715 - 775 km. They present a marked difference in the region between these two, with a depletion of an order of magnitude in the T41 profile. Above 780 km it is difficult to identify real differences, although the T41 profile is bigger than the T53 profile by a factor ∼2.

Vuitton et al. (2008) proposed a formation of benzene via $C_6H_7^+$ electron recombination (also used by Wilson et al. (2003) but with a different reaction list, obtaining a very low benzene production rate) near 900 km, the main formation region; and from neutral radical reaction in the stratosphere where a

second peak of production is predicted in their model. Benzene is then rapidly depleted by photolysis, the main loss process according to them, producing C_6H_5, the main photodissociation product (3 times more abundant than C_6H_6). This radical diffuses downward and is converted through reactions with other radicals to heavier aromatics in the 800 - 350 km region. This process is responsible for the rapid decrease in benzene mole fraction below 900 km. The model in Vuitton et al. (2008) was constrained with INMS and CIRS data, the resulting C_6H_6 mole fraction profiles reproduce well the measurements of these instruments around 1000 km and 100 km, respectively. From the C_6H_6 mole fraction profile and N_2 number density profile used in the neutral chemistry model in Vuitton et al. (2008), a C_6H_6 number density profile was calculated assuming a pure N_2 atmosphere. The solid line in Figure 5.6 represents this calculated profile multiplied by a factor 100 (small oscillations in the profile come from the digitalization process). Even when the photochemical models are subject to several uncertainties including those in reaction rates, and even when they are sometimes limited to particular geometrical and illumination conditions, the discrepancy with the profiles derived here is striking and calls for further analysis in the future.

The retrieval techniques used to derive the density profiles of the species are based on their absorption cross section. But the technique itself is unable to determine the identity of a molecule given an absorption cross section spectrum, the identity of the molecule is determined by the 'user', based on confidence of not only the absorption cross section corresponding to the molecule of interest, but the correlated features in the measured spectrum too. The question might then arise about the true identity of a particular species, particularly when isotopic substitution or substituted molecules (like substituted benzenes) can lead to absorption spectra similar to the molecule of interest. The sets of absorption bands obtained in both light and heavy benzene are essentially similar (Price and Wood, 1935; Rennie et al., 1998). However, those of the latter suffer a small shift to the violet relative to those of the former. Moreover, the H/D ratio measured for Titan by different techniques is about 10^{-4} (Table 10.4 in Soderblom et al., 2009b). Other benzene derivatives present absorption cross sections similar to that of benzene (see for example Hammond et al., 1950; Suto et al., 1992). But the main valence transition and the over-imposed Rydberg transition around 1790 Å in the benzene absorption cross section (see Chapter 4), that actually determines its characterization in the UVIS spectrum, is shifted in the references commented beyond the UVIS spectral resolution (except maybe for benzotrifluoride). The absorption of halogen-substituted benzenes is reported to be similar to that of c-C_6H_6 (Herzberg, 1966). However, these species are barely mentioned in the literature regarding detections and modeling of Titan's atmosphere. It can be therefore concluded that the absorption features in the UVIS/FUV spectrum associated to benzene in this work are indeed so and, correspondingly, the profiles shown in this section.

5.1.2 Abundance of major constituents, from FUV stellar and EUV solar occultations

The column densities of the major constituents were derived from the stellar occultations described in Table 2.4 and solar occultations described in Table 2.5. The column densities for CH_4 are shown in Figure 5.7, the N_2 column densities in Figure 5.8. The CH_4 column densities from solar occultations were derived from the absorption in the bin around 1085 Å. The N_2 column densities for each solar occultation shown in Figure 5.8 is calculated as the mean of the column densities derived from each bin involved in the analysis (584 Å and 630 Å) for altitudes where the column densities overlap. For altitudes with results from only one bin, this value was taken as the column density for that altitude. The uncertainty from the individual column densities was propagated to the averaged value.

Figure 5.9 and 5.10 (Left) show the CH_4 and N_2 number densities, respectively. The N_2 number

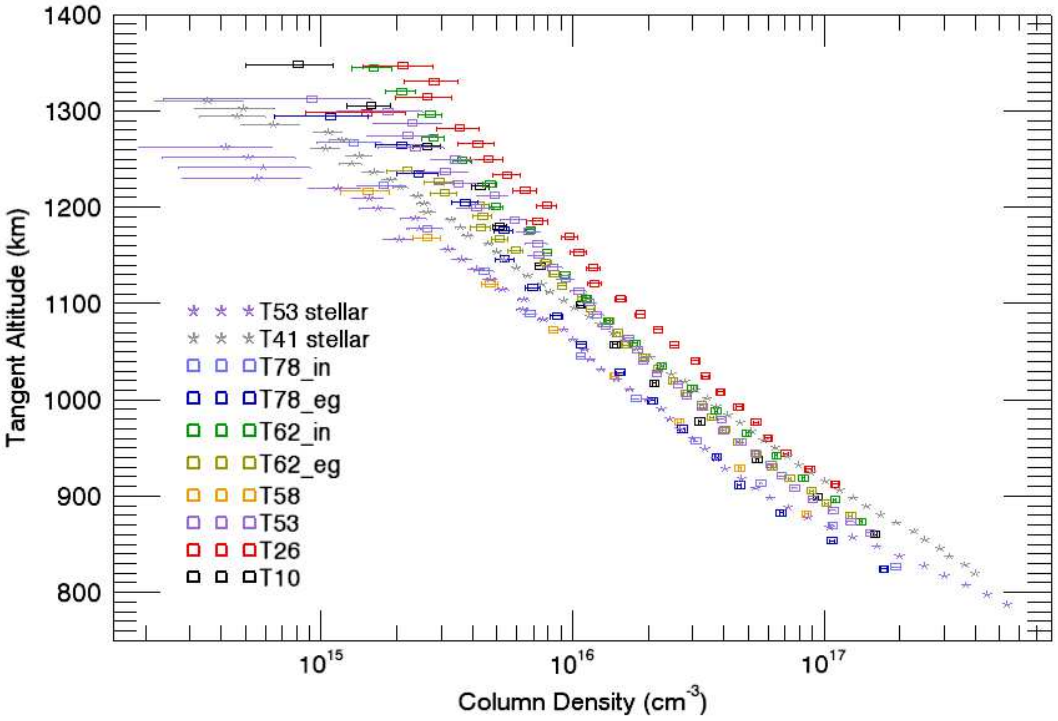

Figure 5.7: Methane column density profiles derived from all stellar occultations and all solar occultations analyzed in this work.

densities are determined separately from the column densities for each of the two bins involved in the analysis (584 Å and 630 Å). The CH_4 profiles derived from stellar occultations reach a few tens of kilometers lower in the atmosphere thanks to smaller CH_4 absorption cross section in the FUV, compared to that in the EUV bin used in the case of solar occultations (see Figures 2.10 and 2.20). There are some oscillations in some of the profiles, for example in that from T26. These should be interpreted with caution, as might be due to divergences from the real profile caused by the noise in the column densities, not smoothed by the regularization procedure. Koskinen et al. (2011) derived CH_4 number density profiles from the same UVIS stellar occultations analyzed here: T41 and T53. The profiles are shown as solid lines in Figure 5.9. The results agree well for most altitudes. The profiles from this work reach some 100 km higher; those from the mentioned reference extend to lower altitudes, till 610 km. The results for N_2 are consistent: on most of the cases, either the number density values derived from one bin are comprised in the uncertainty interval of the number densities derived from the other, or the uncertainty intervals overlap. Effective N_2 number densities for each occultation were calculated as the mean of the number densities derived from each bin for altitudes where the number densities overlap. For altitudes with results from only one bin, this value was taken as the number density for that altitude. The uncertainty from the individual number densities was propagated to the averaged value. The final number densities are shown in Figure 5.10 (Right). It is worth noting the dispersion of the values for a given altitude. Even for profiles derived from one flyby but different occultations (like data from T62) the profiles not only do not overlap but present a different scale height. Further analysis of the differences is presented in Section 5.2.

The resolution associated with the CH_4 number densities is about 20 - 30 km for T10, T26, T53 and T62 egress; about 60 km for T62 ingress and T78 egress; and some 100 km and 90 km for T58 and T78 ingress, respectively. The resolution associated to the N_2 number densities is about 20-35 km for T26, T53, T58 and T62 egress; around 20-50 km for T62 ingress, 60-75 km for T10 and T78 egress; and 50-100 km for T78 ingress. The final altitude resolution depends on the width of the averaging

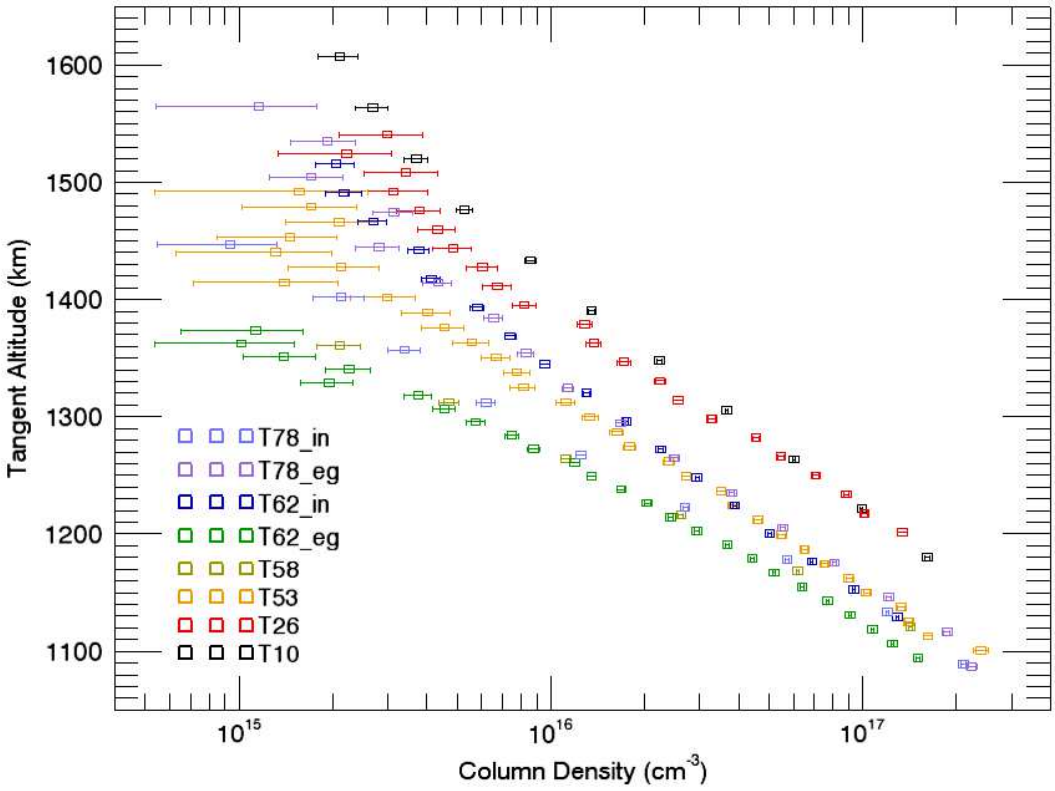

Figure 5.8: Nitrogen column density profiles derived from all the solar occultations analyzed in this work.

kernels (which in turn depends on the amount of regularization or smoothing applied by the retrieval process), and on the effective atmospheric sampling (after the altitude averaging of the measured intensities). An averaging kernel (AVK) for a particular altitude for each species is overplotted in Figure 5.12. The AVK of the N_2 inversion using the 584 Å or the 630 Å bin are almost identical, but this is not always the case, resulting in the span of values for the N_2 profile resolution commented above. In some cases, the characteristics of the column density profiles requires more iterations of the regularization procedure to achieve convergence. As every iteration degrades altitude resolution of the derived number densities, they can present low altitude resolution (the T58 CH_4 number densities are an example of this). The altitude averaging is performed based on the size of the Sun at the atmosphere level, aiming to reduce the effect of overlapping projected disks (see Subsection 2.4.2). As a consequence, occultations with bigger projected Sun (like T78 ingress) will have a sparse effective altitude sampling and their number density profiles will have lower altitude resolution.

One of the main contributions of this work is the simultaneous derivation of N_2 and CH_4 number density profiles for the same location in the atmosphere. This provides an independent measurement of the profiles of these main components at mid and high altitudes in the upper atmosphere; from them the mixing ratio of CH_4 can be derived directly, an important parameter to constrain photochemical models. Moreover, stellar occultations and solar occultations can take place during the same flyby. These happen at different locations, providing a measurement of CH_4 abundances at two different, well defined, geographical coordinates within a time span of some hours. An example of this happened during the T53 flyby, when UVIS measured a stellar occultation before measuring a solar one (see Tables 2.4 and 2.5). The N_2 and CH_4 profiles from the solar occultation and the CH_4 profile from the stellar occultation during flyby T53 are shown in Figure 5.11. These results from the solar occultation are a revisited version of those from Capalbo et al. (2013). The profile derived from the same stellar occultation by Koskinen et al. (2011) is also shown as a solid line. Interestingly, the CH_4 profile from

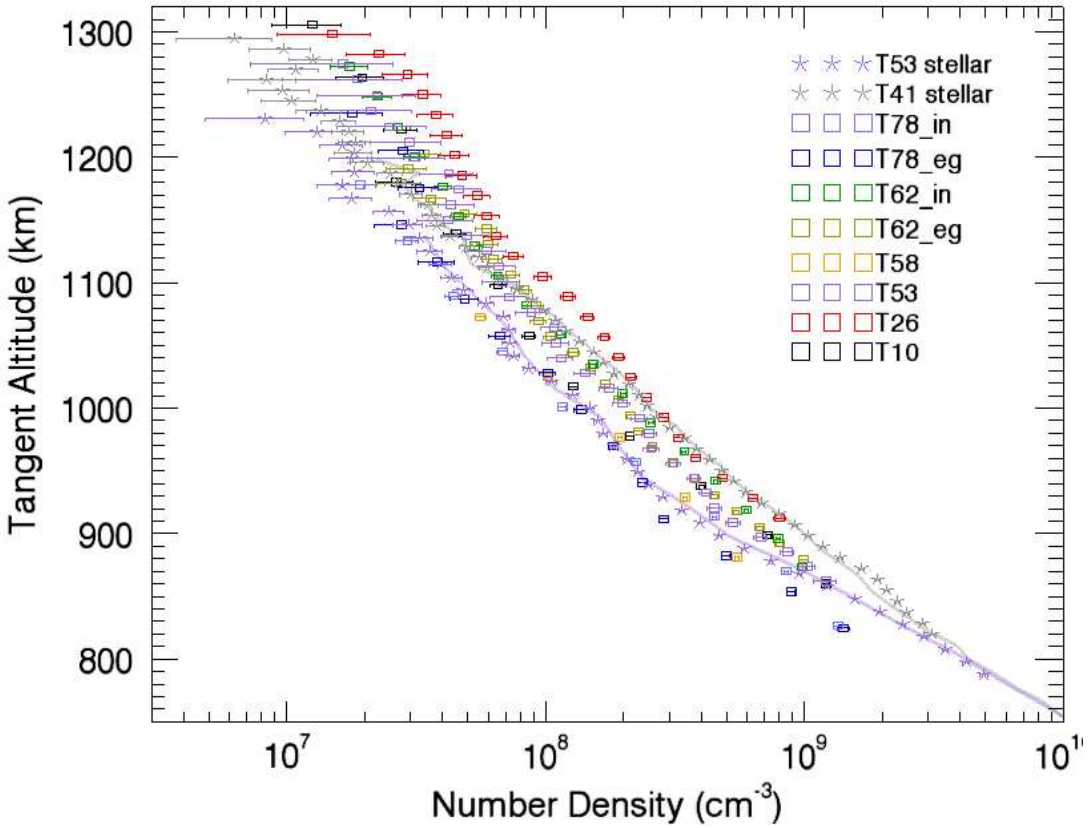

Figure 5.9: Methane number density profiles derived from all the stellar occultations and all the solar occultations analyzed in this work. Solid lines are CH_4 number density profiles derived in Koskinen et al. (2011) from the T41 and T53 stellar occultations.

the solar occultation differs from the UVIS stellar occultation profile by a factor of about 1.5 from 900 km to 1100 km, and up to 2.5 above that. The profiles are closer at lower altitudes and coincide near 860 km, the lower altitude in the CH_4 profile derived from the solar occultation. It is possible that the factor of 1.5 arises because the stellar and solar occultations probed different latitudes under different illumination conditions.

The measurements in Figure 5.9 and 5.10 complement the measurements from other instruments, like INMS and UVS. As commented earlier the optimal measurement conditions for INMS and UVIS are different, so it is uncommon to have both type of measurements in the same flyby. However, INMS performed measurements of N_2 and CH_4 in the upper atmosphere during flybys T26 and T58. The profiles from the inbound and outbound legs of these flybys are compared with the UVIS solar occultation results in Figure 5.12. The INMS profiles shown include a 2.9 factor increase in the density measured by INMS (see for example Koskinen et al., 2011; Snowden et al., 2013). Also shown in the figure are the N_2 density profile derived from the Huygens Atmospheric Structure Instrument (HASI) mass profile (Fulchignoni et al., 2005), assuming an atmosphere composed of nitrogen and 5% of methane; and the N_2 and CH_4 density profiles from Vervack et al. (2004) derived from UVS data. Table 5.1 presents temporal and geographical information for the data in Figure 5.12. The HASI-derived N_2 profile, measured close to the Equator and the only one measured close to Titan northern winter season, is above all the other profiles shown, measured close to Titan Vernal Equinox. The UVS profile agrees well with the T26 UVIS profile, measured almost 27 years later and at higher latitude. Assuming no instrumental artifacts nor systematic errors, the differences between UVIS and INMS, both measurements corresponding to the same flyby, should be due to spatial variations in the atmosphere, or fast variations that could take place during the hours that might take a flyby.

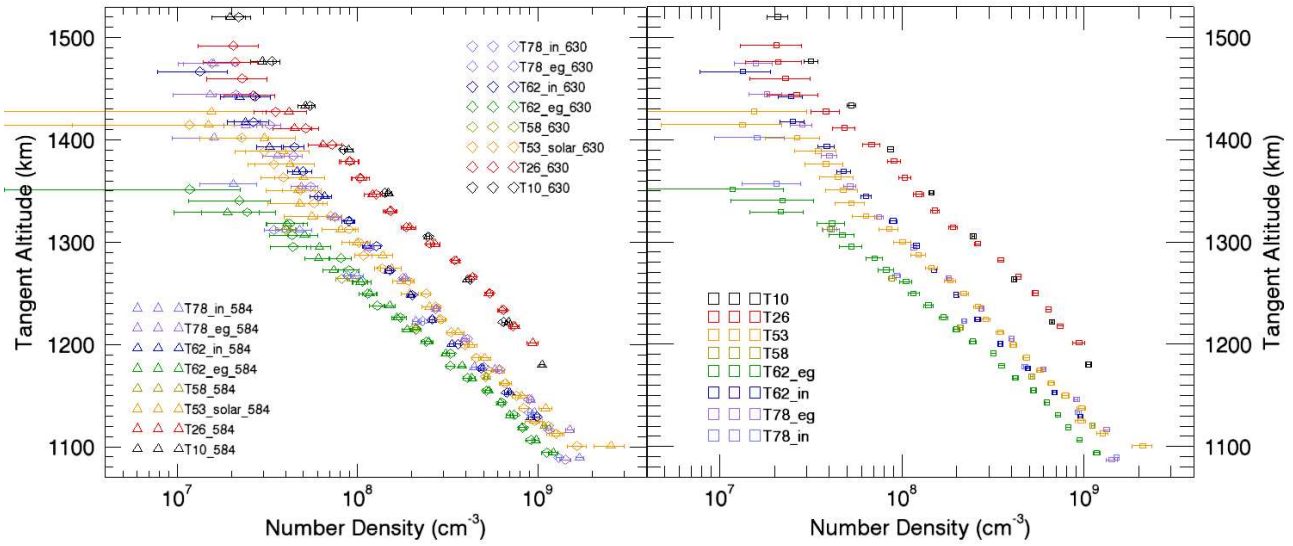

Figure 5.10: Nitrogen number density profiles derived from all the solar occultations analyzed in this work. Left: N_2 number densities determined separately from the column densities for each of the two bins involved in the analysis (584 Å and 630 Å). Right: N_2 number densities calculated as the mean of the number densities derived from each bin (see text for details).

Table 5.1: Temporal and geographical characteristics for the set of measurements shown in Figure 5.12. For INMS the latitude and longitude correspond to closest approach.

Measurement	Time (mm/yy)	Close to Titan Season	Solar Activity	Latitude (deg)	Longitude (deg W)
UVIS T26 solar occ.	03/07	Vernal Equinox	Low	-76 – -77	39 – 29
UVIS T58 solar occ.	07/09	Vernal Equinox	Low	86 – 85	239 – 236
HASI	01/05	Northern winter	Low	-9.5	186.2
UVS solar occ.	11/80	Vernal Equinox	High	4	107
INMS T26	06/07	Vernal Equinox	Low	31.7	358
INMS T58	07/09	Vernal Equinox	Low	-52.2	178

The geographical information in Table 5.1 corresponds to Cassini's closest approach. The spacecraft coordinates may vary significantly during the flyby and so the INMS profile corresponds to a range of latitudes/longitudes. For example, the INMS N_2 number densities at 1300 km for T26 corresponds to 10° in latitude; for T58, to -30° (inbound) and -69° (outbound). The N_2 profile derived from the solar occultation during T58 corresponds to a latitude of 85°. Similar comments apply for CH_4. Further comparison of UVIS/EUV solar occultation results with INMS, UVS and HASI results is presented in Capalbo et al. (2013). There, the T53 CH_4 and N_2 densities are compared with corresponding INMS results from the inbound and outbound passes in flybys T51 and T55, that took place some months before and after T53, respectively. As noted in the cited reference, comparison of results with densities derived by other experiments is complicated by the possibility of temporal and geographic variations as well as differences in retrieval methods or uncertainties in instrument calibrations (see e.g. Cui et al., 2009). Nitrogen and methane densities measured at 1100 km by INMS can vary between Titan encounters by factors of ∼5.5 (Westlake et al., 2011) and ∼2.7 (Magee et al., 2009), respectively. Considerable variability in CH_4 structure between flybys has also been observed from analysis of INMS data by Cui et al. (2012). From the analysis of different data sets, a study of the atmospheric variability in Titan's upper atmosphere has been emerging in the last years.

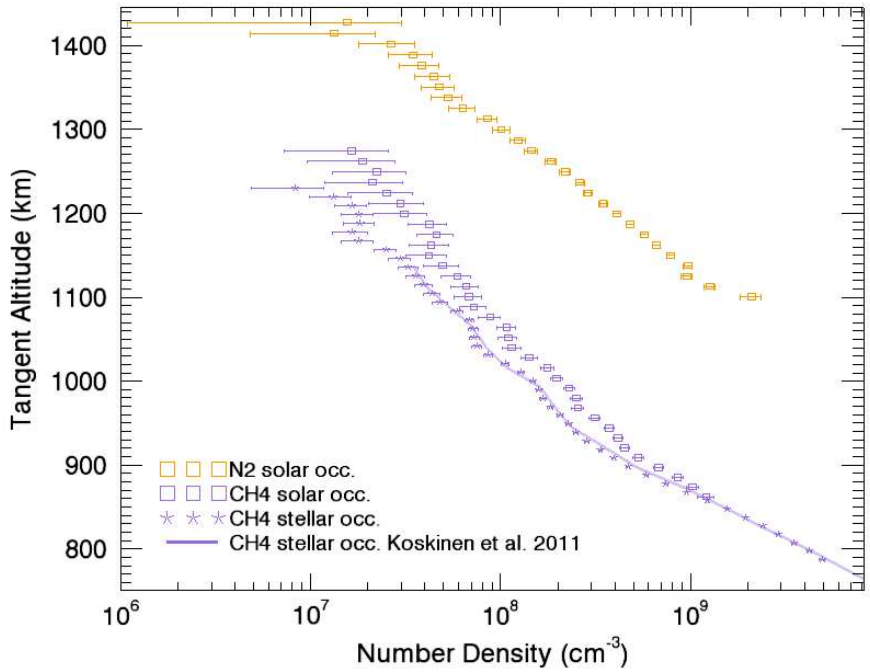

Figure 5.11: Nitrogen and methane number density profiles from the solar occultation and the methane profile from the stellar occultation during flyby T53. Solid line is the methane profile derived in Koskinen et al. (2011) from the same stellar occultation.

5.2 Temperature and variability

Average temperature in the upper atmosphere was calculated from the N_2 number densities derived from EUV solar occultations, with the procedures described in Section 3.5. For each occultation two temperatures were calculated, each from densities derived from a different bin of the two that characterized N_2 absorption (584 Å and 630 Å). A representative temperature for each observation was calculated as the mean of the two temperatures, uncertainty propagated accordingly. The temperatures for each flyby are shown in Figure 5.13. It is worth noting that temperatures for the upper atmosphere were not measured before for most of the flybys whose data was analyzed here and, moreover, the information derived from the T78 flyby is the most up-to-date sample of Titan's thermospheric temperature the author is aware of. The content of this section provides therefore an important contribution to the analysis of the thermospheric structure. The temperatures for particular flybys also analyzed in previous work are shown in Table 5.2. The average global temperature is also shown. It should be noted that the global average of (144 ± 2) K derived in this work comes

Table 5.2: Global temperature derived averaging all temperatures obtained from the UVIS EUV solar occultations and temperatures for specific flybys. Comparison is done with equivalent temperatures from previous work that based the analysis in INMS data.

Reference	This Work	Cui et al. (2009)	Westlake et al. (2011)	Snowden et al. (2013)
Global average	144 ± 2	151.0 ± 0.5	153.0 ± 1.2	150.7 ± 4.2
T26	139 ± 7	-	142.9 ± 1.3	141.0 ± 6.5 [b]
T58	119 ± 3	-	∼140[a]	118.1 ± 0.6 [c]
Instrument	UVIS	INMS	INMS	INMS

[a] Approximate value from Figure 4 in the reference.
[b] Inbound leg, high altitude density level.
[c] Inbound leg, low altitude density level.

from only 8 measurements, the other references in Table 5.2 use temperatures determined from several tens of flybys. Moreover, in the case of Snowden et al. (2013) the value (150.7 ± 4.2) K shown here

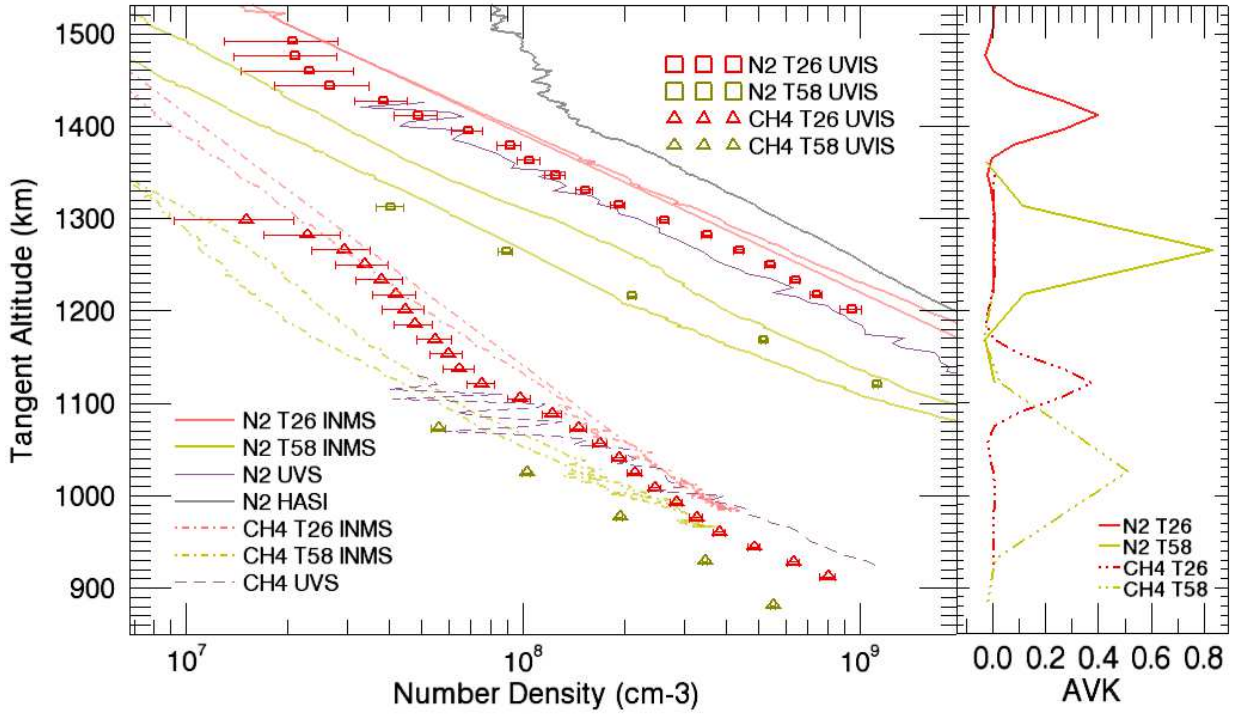

Figure 5.12: Methane and nitrogen number density profiles derived from solar occultations T26 and T58. On the right, the AVK for a particular altitude for each species and from each occultation. Also shown are the profiles for both species measured by UVS in Voyager 1 during a solar occultation in 1980, the profiles from INMS measured during T26 and T58, and a nitrogen profile calculated from the density measurements performed by the HASI instrument during the Huygens probe descent through Titan's atmosphere, in January 2005.

corresponds to values for a particular height of a temperature profile, and not to an average of the upper thermospheric temperature as in this work. All global temperatures derived from INMS data are about 4% higher than the value derived here, the uncertainty interval of this value does not overlap with those from the references. On the other hand, it should be noted that the standard deviation of the set of 8 temperature values derived here is 19 K.

As was commented in the introduction, variability is important in Titan's atmosphere. This is also evident from Figures 5.9 and 5.10 presenting all CH_4 and N_2 profiles derived. In the present work, the study of variability is limited to the analysis of possible effects on the measured temperatures. Measured temperatures can vary roughly between 100 - 200 K (see for example Snowden et al., 2013) from flyby to flyby. The combined effects from the different variables affecting the behavior of the atmosphere (day/night, season, position in the magnetosphere, etc.) are very complex, the variables cannot be easily decoupled, especially when dealing with limited data sets, with poor statistic and easily biased by outliers, like in the present case. Nevertheless, this section presents the temperatures derived as a function of those variables to see if some correlation is evident.

Figure 5.14 shows the temperatures from all the solar occultations as a function of latitude. The measurements present a good latitude coverage, with a gap only for mid northern latitudes. Equatorial and mid latitude temperatures are in general bigger than high latitude ones. An exception, showing the opposite behavior, is the temperature measured during T10. The temperature as a function of longitude is shown in Figure 5.15. The longitude coverage leaves gaps around 100° and 300° W, leaving the wake region of Titan local plasma interactions unexplored by the observations. No correlation is evident from the figure; three different temperatures, spanning the whole range of temperatures measured, correspond to longitudes in the region 230° - 240° W.

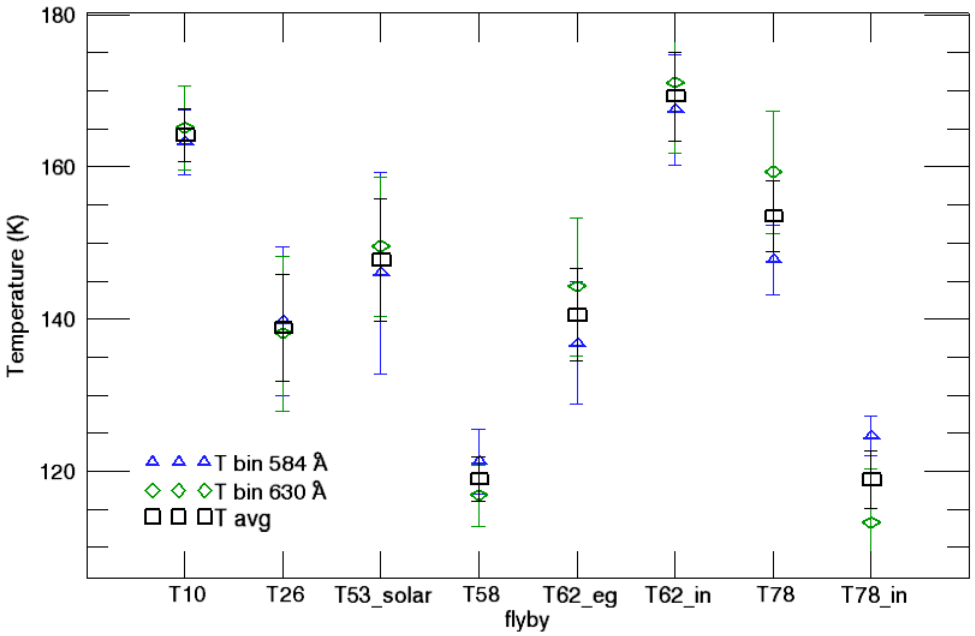

Figure 5.13: Upper atmosphere temperatures for all flybys analyzed in this work. Temperatures calculated from densities derived from each of the two bins that characterized N_2 absorption, as well as the mean temperature for each occultation are shown.

Müller-Wodarg et al. (2008) used data from 13 targeted flybys of Titan (T5 - T32, between April 2005 and June 2007, i.e. 2.5 years, just after the northern hemisphere Winter solstice) to construct an empirical model based on INMS observations that describes the mean state of the thermosphere in the northern hemisphere. By fitting density and CH_4 mixing ratio for different latitudes and then interpolating in altitude, they extended the information from INMS measurements onto a grid in those variables. This permits to overcome the effect on derived temperatures of the error associated to calculations from densities taken along any single trajectory (Müller-Wodarg et al., 2006). Considerable latitude differences are present in the temperatures below 1200 km. Near 1000 km altitude, temperatures reach (164 ± 6) K at 20° N and (131 ± 6) K near 80° N. In contrast, Titan's thermosphere appears in their analysis nearly isothermal with latitude above 1200 km with an average temperature of (146 ± 13) K. The temperatures for the northern hemisphere determined in this work are either some 15 K above or some 20 K below 140 K. Again, it has to be taken into account that the sampling of the northern hemisphere is sparse in this work, that average temperatures for an altitude range of approximately 1200 - 1500 km are presented, and that the corresponding flybys took place from mid 2009 on. Due to the characteristics of the spatial and temporal coverage of the data sets, Müller-Wodarg et al. (2008) did not investigate variations with other geographical or temporal variables (like longitude, time of the day, or season).

Cui et al. (2009) studied composition and thermal structure of the upper atmosphere based on the analysis of INMS data from 15 Titan flybys spanning 2.5 years, from April 2005 till November 2007. They classified the temperatures obtained according to bins in latitude, longitude, magnetospheric environment, etc. Although based on different procedures to derive temperature than Müller-Wodarg et al. (2008), both works show that the equatorial region in Titan's thermosphere appears to be warmer than the north polar region. Cui et al. (2009) give a temperature difference between the equator and north pole of ∼10 K. These authors, in contrast to Müller-Wodarg et al. (2008), make notes about zonal variations. Their results show that the magnetospheric ram side (270° W longitude)

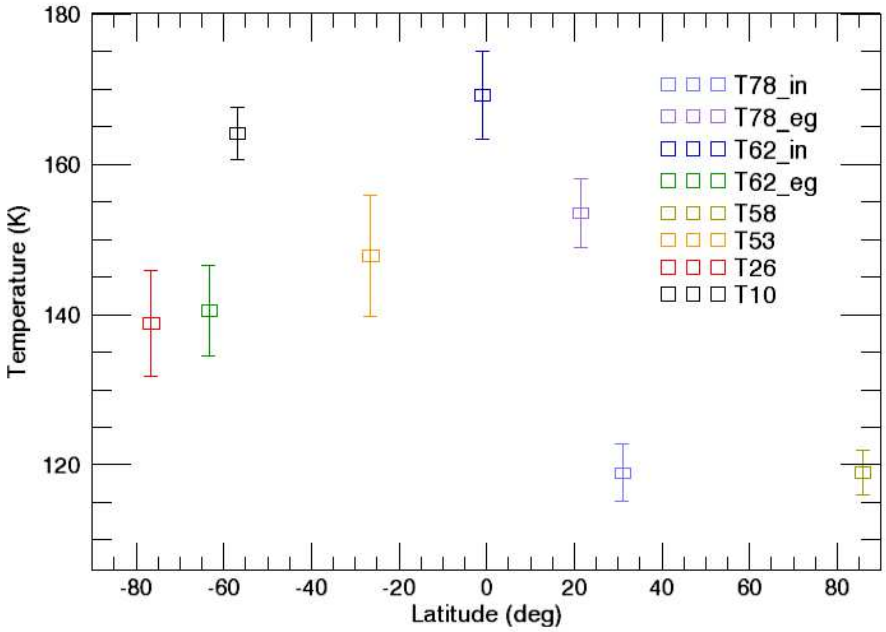

Figure 5.14: Upper atmospheric temperatures as a function of latitude.

and facing-Saturn side (0° W longitude) of Titan appear to be warmer than the wake side (90° W longitude) and anti-Saturn side. However, Titan's wake side is poorly sampled in the data set they used. Therefore the interpretation of a cooler wake side on Titan deserves some caution. Cui et al. noted that the restricted sampling of the available INMS data at the time of publication did not allow a firm conclusion on the realistic horizontal variations to be made.

Westlake et al. (2011) presented an analysis of INMS data from 29 flybys, taking place from October 2004 till August 2009. The authors studied mainly how the upper atmospheric thermal structure responds to the different plasma environments, though they also classified flybys according to other variables like latitude and longitude. Their results refer mainly to 1100 km upwards, with the most important differences happening above 1250 km, therefore overlapping with the region studied in this work. Although thermal plasma processes energy deposition is dominant over solar processes only above 1300 km, throughout the flybys covered in the mentioned study the Sun was in a particularly quiet solar minimum, and the external heating from solar EUV/UV photons is expected to have a diminished effect on the resulting temperatures. Although they observed a decrease in temperature from their low northern latitude group of measurements to their high northern latitude group, Westlake et al. (2011) find no global correlation with latitude that would indicate that the upper thermospheric structure is solar driven. They suggest that the coincidental correlation between the plasma environment and the latitude may have led to the assessment in Müller-Wodarg et al. (2008) that the thermospheric structure was latitudinally dependent rather than dependent on the plasma environment. This is a variable that is not going to be studied in the present work and yet worth mentioning briefly. Westlake et al. (2011) concluded that a magnetospheric effect on Titan's thermospheric structure is likely. The 29 K effective temperature increase observed between encounters taking place in the plasma sheet versus those in the plasma lobes is indicative of the large magnitude of the heating, and was the largest deviation observed between data groupings used in Westlake et al. (2011). On the other hand, Snowden et al. (2013) found that although at low altitudes Titan's thermosphere is colder when Titan is observed in Saturn's magnetospheric lobes compared to Saturn's plasma sheet, at higher altitudes the lobe passes are hotter than the plasma sheet passes. Moreover, they found

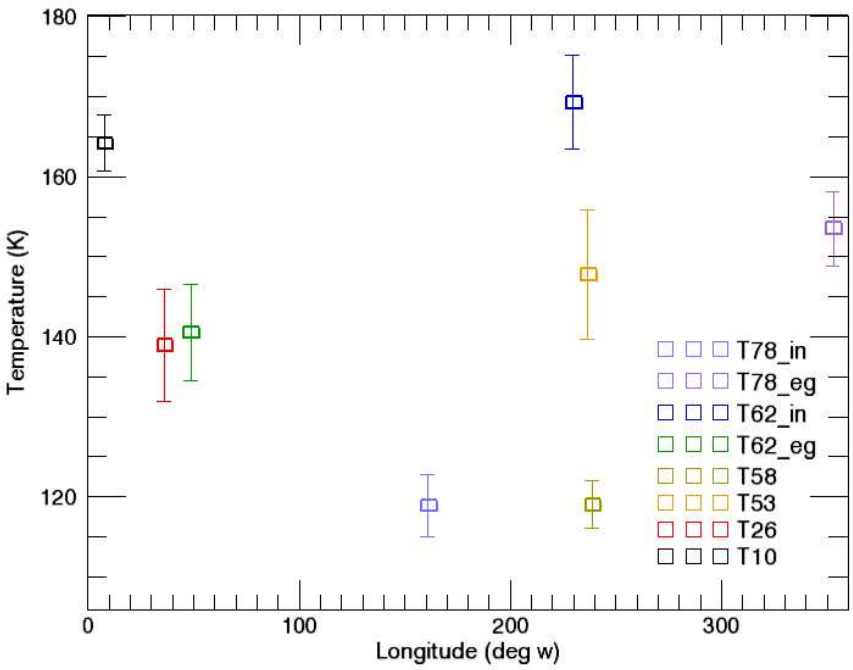

Figure 5.15: Upper atmosphere temperatures as a function of longitude.

no correlation between the temperature of Titan's thermosphere and ionospheric signatures of enhanced particle precipitation, which suggests that the correlation between position in the plasma and temperature is not indicative of a physical connection.

Snowden et al. (2013) derived vertical temperature profiles from INMS N_2 density measurements from 32 Cassini passes, from mid 2006 till mid 2010. They derived temperatures fitting with the hydrostatic equilibrium equation the average N_2 density profiles for several regions of Titan's atmosphere. The authors found a similar trend with latitude in the northern hemisphere as Cui et al. (2009) and Westlake et al. (2011): the temperature of the northern high latitude region is coldest and the equatorial region is warmest. However, the same trend does not hold in the southern hemisphere, where the mid-latitude region is warmer than the low latitude region. This is consistent with the temperature derived here from the T10 flyby being warmer than that derived from the T53 flyby (see Figure 5.14). Finally, they find an insignificant difference in the temperature calculated in different longitude regions. Snowden et al. (2013) also derived temperature profiles. They found that the median temperature of Titan's thermosphere varies significantly from pass-to-pass between 112 and 175 K. To investigate the horizontal structure of Titan's thermosphere they also plot the temperature at two N_2 density levels (representing Titan's mid to lower thermosphere and Titan's upper thermosphere) versus latitude, longitude, date of flyby, and magnetospheric environment. They found no strong correlation of temperature with latitude or longitude.

Titan's atmosphere presents also temporal variability. The temperatures derived here from the solar occultations are presented following as a function of temporal variables. Figure 5.16 shows temperature as a function of Titan Local Solar Time (LST). Logically, the temperatures correspond to either the morning or evening terminator, although due to Titan's orbit inclination these do not always correspond to 06:00 and 18:00 hs, respectively; particularly for occultations at high latitudes. Measurements in the morning terminator could be considered representative of an atmosphere coming out the night, and those from the evening terminator representative of an atmosphere coming from a day period. No day/night differences are evident in the results presented, measurements in the evening

terminator span across the whole range of temperature measured. Muller-Wodarg et al. (2000), using

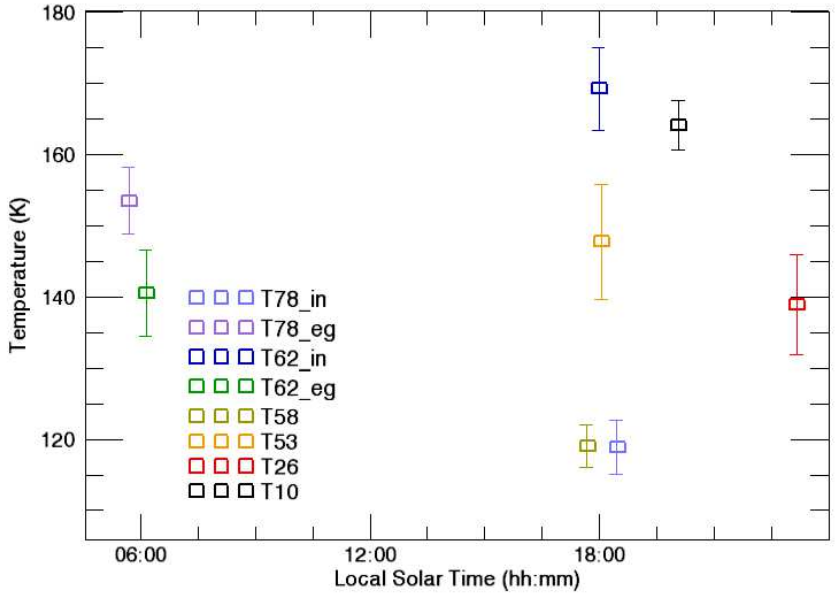

Figure 5.16: Upper atmosphere temperatures as a function of Titan Local Solar Time.

a 3-D General Circulation Model (GCM) of Titan's thermosphere, found diurnal and hemispheric variability of up to 10-20 K in thermospheric temperatures, resulting from solar EUV heating; the variability was largest above 1300 km. On the contrary, Cui et al. (2009) found the nightside to be warmer than the dayside. A similar trend is found in Westlake et al. (2011) and Snowden et al. (2013); although the day/night temperature difference found by the latter is smaller than in previous calculations and their final conclusion is that no relevant dependence on local time can be derived from the observations. Figure 5.17 shows the span of the measured temperatures in time, the vertical line showing approximately Titan's Vernal Equinox in August 2009. Again, no correlation with time or Solar activity is apparent, as neither is from the temporal trend shown in Westlake et al. (2011). Snowden et al. (2013) state that the average temperature of Titan's thermosphere may have decreased by about 10 - 15 K in mid-2007, or around T32; this is not evident from the data set presented here. Finally, Figure 5.18 shows the temperatures as a function of the position of Titan with respect to Saturn in terms of its Saturn Local Time. Although not directly correlated to the position of Titan in the magnetosphere of Saturn, this plot can provide qualitative information about it. For instance, for positions close to Saturn midday, Titan can not be in the magnetospheric lobes; in the same way, for positions close to Saturn midnight, Titan can be in the lobes or in the plasma sheet. No evident correlation of temperature with SLT exists in the data set presented. Although Titan's thermospheric temperature vary considerably as a function of time and location, this variability might result from a combined effect of the variables used here to study it, taking only one of them at a time could be misleading.

5.3 Summary of chapter

The number density profiles, derived from stellar occultations, of minor constituents in Titan's thermosphere are valuable information about its composition. At the same time, it is worth underlying that the main contribution of the present work in this respect are not the profiles themselves, but the analysis of the detectability of different species and the characterization of the retrieval technique

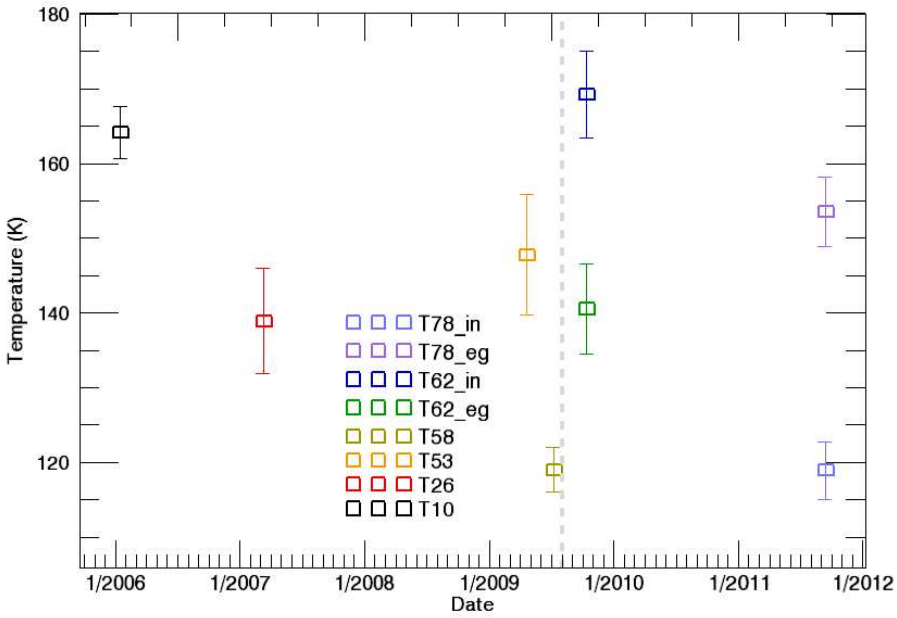

Figure 5.17: Upper atmospheric temperatures as a function of time. The vertical line shows, approximately, Titan's Vernal Equinox in August 2009.

(performed in Chapter 3). The fact that the profiles are in good agreement with equivalent profiles derived in Koskinen et al. (2011) validates the results presented here. Results like the aerosol extinction are useful to study the evolution of extinction layers. However, this kind of analysis needs to be deepen in order to understand the discrepancies of the extinction profiles presented here and in the cited work; this would include the better identification of absorbers in the far FUV region. The differences between modeled and measured benzene profiles shown in this chapter put in evidence the complexity of the behavior of this molecule. The density profiles, derived from solar occultations, of N_2 and CH_4 provide an independent and low uncertainty measure of the abundance of these main constituents. This allows direct calculation of CH_4 mixing ratios.

Valuable and in many cases new information about the temperature of the upper atmosphere was presented. The poor sampling of the data set did not permit to draw any conclusion about atmospheric variability, but the values presented, for different times and locations, are to complement the existing measurements and help in the study of this variability.

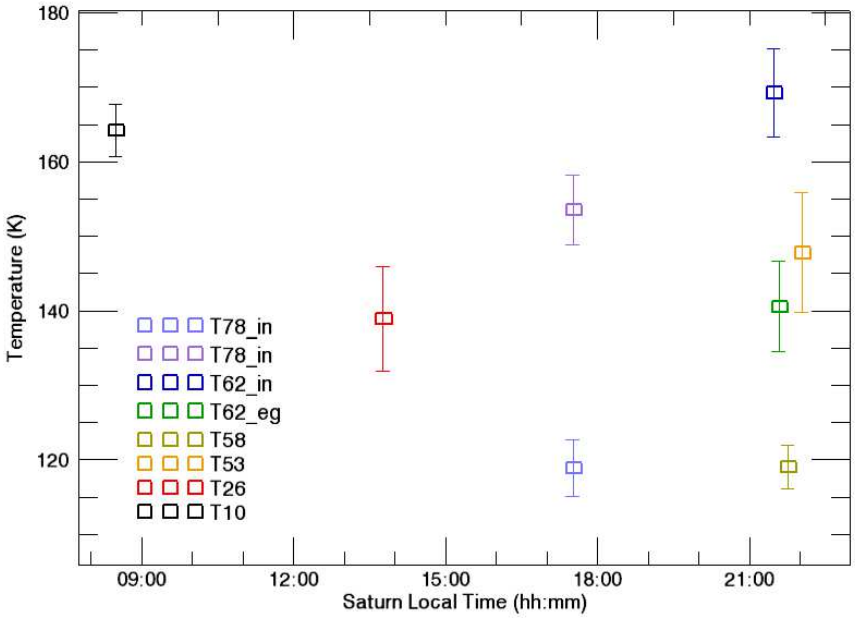

Figure 5.18: Upper atmosphere temperatures as a function of Saturn Local Time.

Chapter 6

Conclusions and further work

This work dealt with observations of Titan's atmosphere from the FUV and EUV channels of the UVIS instrument, in the form of 2 stellar and 8 solar occultations, respectively. The EUV data needed to be corrected from background and wavelength misregistration, the latter due to pointing instabilities. The procedures developed successfully accounted for these two corrections. In some cases, the wavelength recalibration implemented permitted the analysis of observations that, the correction had not been made, would be useless for the purpose of atmospheric composition derivation.

A technique to retrieve atmospheric composition based on atmospheric radiative transfer theory was implemented via a Levenberg-Marquardt (routine MPFIT) minimization algorithm and a regularized (constrained or Tikhonov) inversion algorithm. A study about species detectability permitted to determine a list of 11 molecules that could possibly be detected by UVIS. Although not exhaustive, this study is expected to provide a basis for future analysis of UVIS absorptive occultation data. Using the 11 candidate molecules, the retrieval techniques were characterized with simulated UVIS data. To improve its performance MPFIT was wrapped in an iteration scheme that fixes successfully retrieved parameters and re-retrieve the others. Retrieval results were observed to be dependent of the initial guess, the output becoming unacceptable if the initial guess differs in a factor 3 or more than the true profile, or in a factor 0.25 or less. The uncertainties for most of the column densities derived from MPFIT were seen to be underestimated—by 35% for most of the species, about 90% for the aerosols—in comparison with uncertainties derived from a Monte Carlo analysis, performed for one altitude. MPFIT uncertainties are overestimated by less than 15% for CH_4 and HCN. The column densities returned by MPFIT were filtered according to several criteria, including an altitude filtering based on the transmission in characteristic absorption bins of the species included. Apart from the limitations commented above, the technique retrieves well column density and number density profiles, although the altitude coverage of the final results might be over-restricted by the altitude filtering implemented, and the derived number density profiles present oscillations around the real profiles used to simulate the data. These oscillations are artifacts of the procedure, most likely due to the noise in the retrieved column densities, that is not efficiently reduced in the regularized inversion. On the other hand, an 11-species retrieval at UVIS resolution may be pushing the technique to its limits, the use of less, but still appropriate species in terms of their features being identifiable in the absorption spectrum, led to better retrieval results.

This work presents for the first time medium resolution absorption cross section spectra for benzene at different temperatures. More than a year of measurements at Berlin and Meudon were invested for this task. Although the variation with temperature observed is of the order of the measurement uncertainty, some temperature effects could be qualitatively and quantitatively analyzed. These temperature variations are expected to be insignificant for the analysis of UV absorption by Titan's atmosphere at UVIS resolution. Actually performing a retrieval with absorption cross sections measured at a different temperature and observing the effect on the resulting column densities could serve to validate this assumption. In addition, larger variations of the Rydberg peak at 1790 Å in higher resolution measurements can not be discarded. The measured absorption cross sections will become part of a more extensive data base of absorption spectra of molecules of astrophysical interest available online to the scientific community[1].

The benzene absorption cross sections measured were added to a bigger set of laboratory results and used in the processing of two stellar occultations by Titan's atmosphere (T41 and T53), to derive column densities and number densities of hydrocarbons and nitriles, and aerosol extinction, in the upper thermosphere. These results directly match the last main objective of this work, stated in the introduction, about detection of species in Titan's thermosphere. The local maxima in the number

[1] Available at http://www.lisa.univ-paris12.fr/GPCOS/SCOOPweb/lesmoleculesdeSCOOP.htm

density profiles of C_2H_4, C_6H_6, and in the extinction profiles of aerosols could be correlated with dips in the transmission curves measured at wavelengths representative of absorption (or extinction) by those species. The resulting number densities agree well with those in Koskinen et al. (2011), derived from the same occultations, and the only previous work that presented this kind of results. Only one new molecule, CH_3, was added to the model atmosphere in the present work; its retrieval failing for both occultations. This might be due to the lack of sufficient information about its absorption cross sections, and/or its low abundance in the regions probed. Although no significant new information was added in the analysis of the two stellar occultations, the results obtained serve as a validation of the retrieval procedure implemented here. The short altitude-scale oscillations shown in the profiles should be interpreted with caution, in view of the known artifacts produced by the procedure, commented above. Benzene was one of the species for which number density profiles were obtained from the stellar occultations. The profiles obtained showed marked differences between each other, and with a model profile calculated from a mole fraction profile in Vuitton et al. (2008). The discrepancy with the profile in this reference is striking and calls for further analysis. This points to complex, unknown, chemical and dynamical processes affecting the benzene vertical distribution, revealed by measurements but out of reach by current models. Vertical profiles like the ones derived for benzene are a fundamental reference to contrast and constrain the models, and improve our understanding of Titan's upper atmosphere.

This work also presented column and number density profiles of CH_4 derived from 2 stellar occultations and 8 solar occultations, and N_2 profiles derived from the solar occultations. The occultations analyzed sampled different latitude and longitude combinations, with a comprehensive coverage in latitude. This is a strong point of the data set in view of a global and variability analysis. The profiles vary in density and scale height from flyby to flyby, denoting atmospheric variability. A similar comment applies when comparing the profiles derived here with those from other measurements at different times/locations. A further exploration of atmospheric variability in terms of abundance of CH_4 and N_2 was deferred to a future work. The data presented here not only complement measurements from other instruments but also demonstrates the potential of the synergy between stellar and solar occultations with the case study of flyby T53. In this flyby, two CH_4 profiles were derived within hours, one from a stellar occultation and one from a solar occultation, at two different locations in Titan's atmosphere. Oscillations in the CH_4 profiles presented might be artifacts from the technique. A future simulation of density determination from a solar occultation might be useful to determine if this is the case.

Three different methods to derive temperature from N_2 densities were proposed and analyzed with a Monte Carlo procedure. The technique that integrates the hydrostatic equilibrium equation and calculates a weighted average temperature, varying the reference altitude value, was chosen to derive the temperatures in this work due to its robustness. The upper atmosphere average temperature was calculated for each of the solar occultations analyzed, in many cases corresponding to times and locations for which no experimental thermospheric temperatures were available in the bibliography. This, together with the density profiles presented, fully fulfills the first objective of this work related to the provision of observational data to constrain photochemical models. Some of the temperatures where compared with temperatures derived from the same flyby but from other instruments, with a good agreement in general. It has to be taken into account that a direct comparison is difficult as different measurements correspond to different locations. Analysis of the eight temperatures as a function of different geographical and temporal variables showed no evident correlation, except for a small trend of temperature decrease towards the poles. This analysis matches the second objective of this work, contributing to the observations of upper thermospheric temperature variability.

All the solar occultations in the PDS archive by August 2013 (to the best of the knowledge of the

author) were commented in this report, all that could be analyzed were so. There are many stellar occultations that are still waiting to be analyzed. The techniques implemented are ready for this task. This could help in the further characterization of the absorption in the long wavelength region of the FUV channel, where aerosols dominate. Furthermore, Cassini arrived at the Saturnian system in 2004 and the mission is planned to be continued till 2017, so FUV and EUV observations during 4 more years are expected to be available. The study of the influence of a full solar cycle on the atmosphere during the Cassini mission could be a goal for future variability studies. Comparison of the high altitude results derived here with results for the lower atmosphere, for instance from the CIRS instrument, would allow to further constrain the future photochemical models of Titan's atmosphere, and may provide an insight on the coupling of these two atmospheric regions. In terms of laboratory work, high resolution absorption cross section measurements in the FUV and EUV ranges for N_2 and CH_3 (just to mention some) would be very useful to deepen the analyses presented here.

Acknoledgements

The achievement of my PhD lies on more than the last three years of efforts and qualifications. I want to thank my mother, Maria Rosa Santarossa, and my father Carlos Salvador Capalbo, for all they gave me, at all levels in life, and still give me today. Their help was fundamental to achieve every of the steps that led me to this point.

About three years ago my life lost its color. I am very lucky to count with the lovely help of Viktoriya Byelova to color it back again. Thank you Vik.

I want to thank my supervisor Yves Bénilan, for his help in the professional as well as in the personal domain. For guiding me during my research with his knowledge and experience, at the same time that trusting me and letting me explore different options my own way. Similarly, I want to thank Roger Yelle for his supervision and personal assistance, and Tommi Koskinen for our discussions and time together, all very helpful from the professional and personal point of view, especially during my stay in the University of Arizona.

I reserve special gratefulness for Marie-Claire Gazeau, who helped me in uncountable ways since my arrival to LISA in 2010. I also want to thank Marc David, Nicolas Fray and Robert Sternberg, from LISA, for their always kind assistance and warm presence, particularly during this last year 2013.

During the benzene absorption measurements at Meudon, the help of Norbert Champion was invaluable for the good achievement of the task, I am very grateful for that. I also thank the help of my colleagues at LISA for they guidance, and the technical personnel at BESSY II, Berlin, for their assistance, during our measurements in this facility.

I thank Greg Holsclaw and William E. McClintock from the UVIS team for fruitful discussions about the instrument.

I thank the members of the jury for their advise and contributions to enrich my work.

I acknowledge the opportunity to perform my PhD research provided by the Université Paris Est, through a research grant from the Research and Higher Education Ministry.

During these years I went through amazing, countless paperwork and administration. In all cases I had the kind and efficient help of the administration at LISA, and LPL during my stay in Arizona. Thank you to all of them for their help.

Finally, I am very thankful to all those people, anonymous in this report, who contributed directly or indirectly in this scientific and life adventure, with a happy ending.

Appendices

Appendix A

Temperature calculations

The calculation of the temperature in the upper thermosphere of Titan from the N_2 number densities was a subject of study during this PhD. In this appendix, a brief analysis of three methods to perform that calculation is presented. The three methods assume a constant temperature in the altitude range considered. The first and second method consist in calculating the integral in equation 3.15 and equating the temperature as in Equation A.1,

$$T = \frac{g_s m R^2}{kT}\left(\frac{1}{R+z} - \frac{1}{R+z_0}\right)\frac{1}{(\ln(n) - \ln(n(z_0)))}, \tag{A.1}$$

where the quantities are explained in Section 3.5. As the atmosphere may not fulfill the assumptions made, and also due to the measurement uncertainties, the measured values do not follow exactly the behavior of an isothermal, hydrostatic and diffusive atmosphere—particularly at the lowest and highest altitudes. Thus, the value of the resulting temperature might be biased. Moreover, it depends on the z_0 (and correspondingly $n(z_0)$) chosen for the calculation. Several temperatures where then calculated and weighted-averaged to obtain a final value; the weight used was the inverse of the calculated uncertainty in the temperature values.

Method 1 calculates T varying z over all the altitudes covered by the measurements, and using the lowest value as z_0 in each calculation. The infinite value corresponding to $n = n(z_0)$ is excluded from the resulting values. A weighted mean temperature was calculated, iteratively filtering out the values whose uncertainty interval did not overlap with the weighted mean absolute deviation interval corresponding to all temperatures calculated. The uncertainty for the final mean temperature was calculated via error propagation from the weighted mean average formula.

Method 2 calculates T varying z in all the altitudes covered by the measurements, one of them fixed as z_0. Sequentially all the values are chosen as z_0 and the calculation of T repeated each time. This results in N×N values of temperature, where N is the number of altitudes in the measurement vector. The infinite values corresponding to $n = n(z_0)$ were filtered out, as were all values with uncertainty interval overlapping zero or negative values. A weighted mean temperature was calculated, iteratively filtering out the values whose uncertainty interval did not overlap with the weighted mean absolute deviation interval corresponding to all temperatures calculated. The uncertainty for for the final mean temperature was calculated via error propagation from the weighted mean average formula.

Method 3 is radically different from the other two. First the physical altitude is replaced by a geopotential altitude, that takes into account the variation of g with altitude. In this case, the new variable and the new form of Equation 3.15 are

$$y - y_0 = \frac{z}{1 + \frac{z}{R}} \qquad and \qquad \ln(n(z)) = \ln(n(z_0)) - \frac{g_s m}{kT}\int_{y_0}^{y} \mathrm{d}y', \tag{A.2}$$

where the quantities are explained in Section 3.5. After a readily integration, a linear relation is obtained between the logarithm of the number densities and the geopotential altitude y, with the slope given by Equation A.3,

$$-\frac{1}{H_g} = -\frac{m g_s}{kT}, \tag{A.3}$$

where H_g is an effective scale height that will be call geopotential scale height. In this way H_g can be obtained from the measured number densities by a linear fit, and then T can be calculated from it, its uncertainty derived from the uncertainty of the parameters in the fit and error propagation. This method has been used before to derive temperatures from INMS measurements (Cui et al., 2009; Westlake et al., 2011; Snowden et al., 2013). As noted in Westlake et al. (2011), this method relies on the assumption of an hydrostatic, diffusive, isothermal, and N_2 dominated atmosphere; moreover

it does not dependent on boundary conditions, and is in general not susceptible to uncertainties due to systematic density perturbations occurring outside of the altitude range studied.

The methods were tested with a Monte Carlo (MC) simulation. A synthetic isothermal number density profile was generated using altitudes, temperature and abundances representative of a purely nitrogen Titan's upper atmosphere. The number densities were perturbed in each run with Gaussian random numbers centered on the unperturbed value of the profile and with a standard deviation equal to 10% of this value. The uncertainties were modeled based on the uncertainties in the T53 number density profile. They were modeled as a second degree polynomial in altitude, being minimum at the half light point, being 20% of the theoretical number densities at the lowest altitude, and 80% of the number densities at the highest altitude. The uncertainties were also perturbed in each run adding to them random Gaussian values with a mean equal to the value of the theoretical uncertainty and a standard deviation equal to 5% of this value. A theoretical profile for a particular run is shown as an example in Figure A.1.

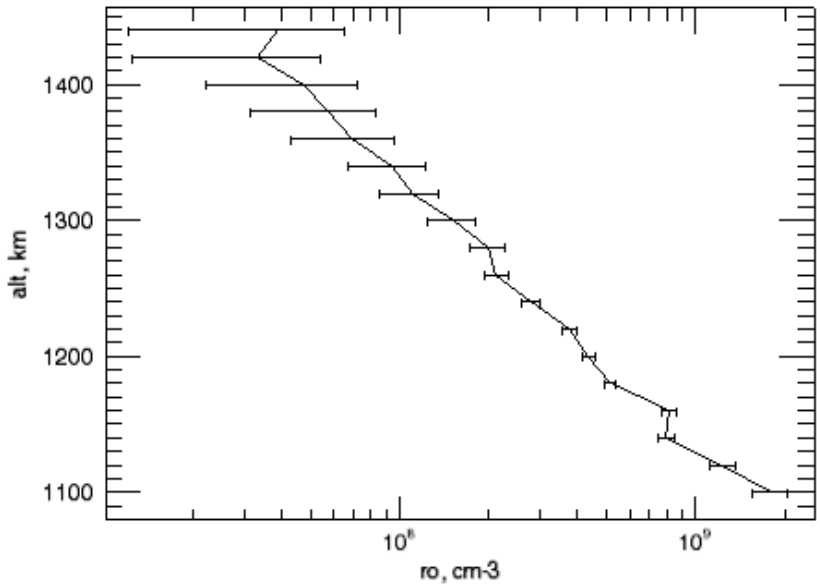

Figure A.1: Example of simulated number densities to test the temperature calculation procedures.

The results of the MC simulations, consisting of 40000 runs each, for the three methods, are shown in Figure A.2. In each plot, the histogram of the calculated temperature values is fitted with a Gaussian function (red curve). Also shown are vertical lines corresponding to the theoretical temperature used to generate the profiles ± the median of the calculated uncertainties (blue lines). Finally, each plot also shows vertical lines corresponding the mean value of the fitted Gaussian ± its standard deviation (red lines).

Method 1 works well, although it underestimates the uncertainty that is implied by the MC simulations—the blue vertical lines are closer to each other than the red vertical lines. Therefore, it would be reasonable to take the standard deviation of the fitted Gaussian as the uncertainty for this method, instead of the uncertainty calculated in the method as described above. Method 2 also underestimates the uncertainty. Moreover, it has a systematic bias to lower temperatures. The reason is unknown, although it might be due to the averaging of a bigger number of temperatures than in method 1, which could have a similar effect of an averaging of many number densities in an altitude profile. If the standard deviation of the fitted Gaussian would be taken as the uncertainty for this method, it would be more precise than method 1. Method 3 also performs acceptably well, although the systematic bias to lower temperatures is again present. The precision of the method falls between those of the other two.

Based on Figure A.2, method 1 seems to be, marginally, the better method, mainly because of the absence of a bias. However, strange results were obtained with this method, in some cases, when applied to a single data set. For example, after one or two iterations, very large temperature values with very large uncertainties biased the final average, in spite of the weighting of the values by the inverse of their uncertainty and despite the filtering. This led to a result of (162 ± 5) K. If the weighted mean absolute deviation of the averaged temperatures is used as uncertainty instead, the result was (162 ± 10) K. In any case, the 150 K corresponding to the synthetic atmosphere was not recovered. Although this particular case could belong to the tail of the distribution obtained in the MC analysis and, therefore, not invalidate the method, the erroneous result is possibly due to the fragility of the iteration procedure. Such a fault in the method is not acceptable because when dealing with real data, only one 'run' is available; thus, such a fragility could led to a completely wrong temperature. The second best choice could then be method 3 which, although biased, seems to underestimate less the uncertainty than method 2. However, this method also fails for individual retrievals. For example, one of the results obtained was (159 ± 5) K. Using the same set of synthetic number densities, method 2 gives (154 ± 2) K. At the same time, if the weighted mean absolute deviation of the averaged temperatures is used as uncertainty instead, the result is (154 ± 11) K. For these reasons, although method 2 could slightly overestimate the calculated uncertainty, and keeping in mind the dispersion and uncertainty in the measured values for some of the solar occultations on which the method will be applied, it was decided to use method 2 for the temperature calculations in the occultation analyses.

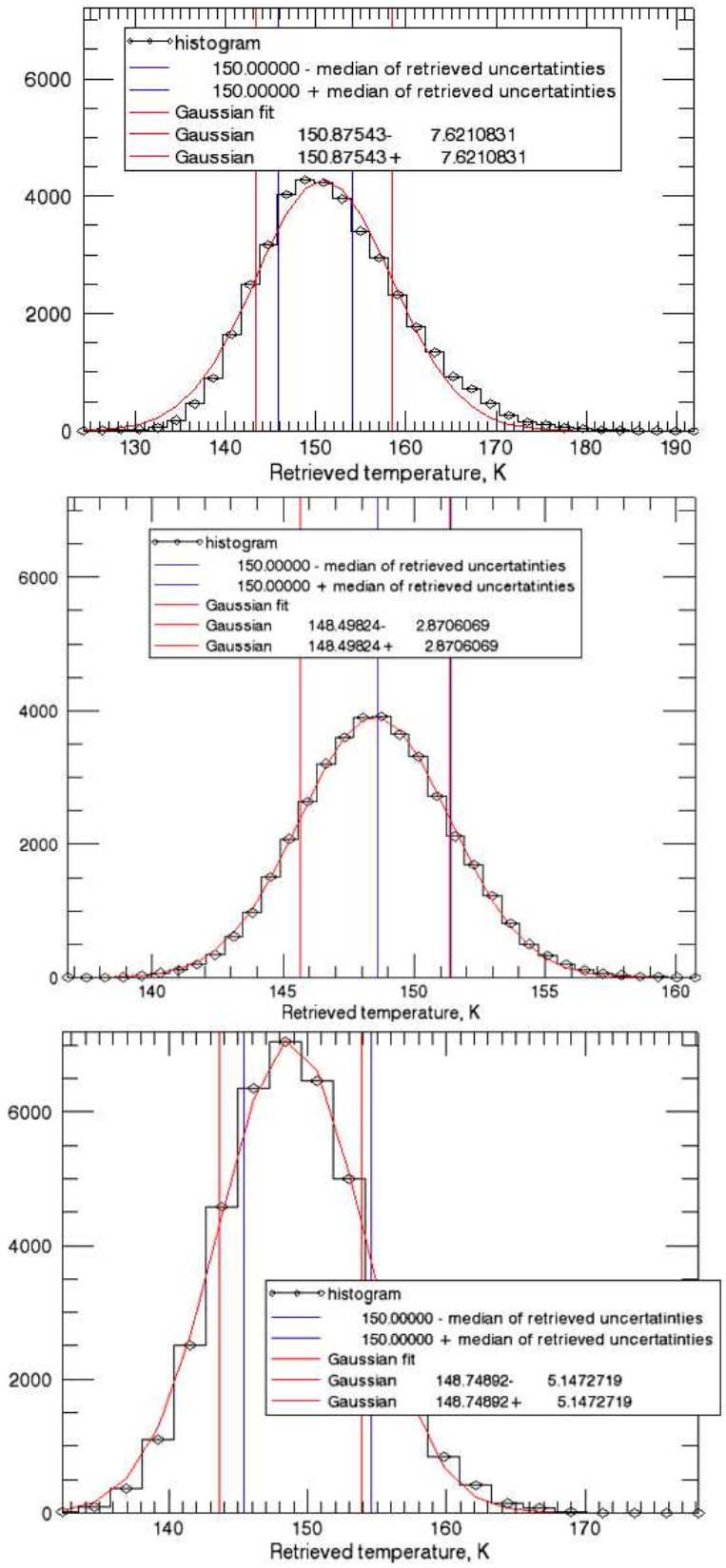

Figure A.2: Results from the Monte Carlo simulations, calculating temperature with method 1 (top), method 2 (middle) and method 3 (bottom). The histogram of the calculated temperature values (black) is fitted with a Gaussian function (red curve). Also shown are the theoretical temperature ± the median of the calculated uncertainties (blue vertical lines), and the mean value of the fitted Gaussian ± its standard deviation (red vertical lines).

Appendix B

MPFIT, dependence of column density retrieval on initial guess

Although MPFIT implements a robust and well behaved minimization algorithm in a general sense, it can suffer from slow convergence or convergence to an undesired local minimum if a poor initial guess is used. For this reason, a study of the output of this routine for different initial guesses used as input was done, using synthetic UVIS data generated according to the procedure described in Section 3.6. The analysis and results of the behavior of MPFIT to different initial guesses are presented in this appendix. The procedure used could be summarized as follows:

a_ The use of MPFIT alone, run once (the routine itself might perform iterations which are transparent to the user, and not modified in any way in this work)

b_ The use of a different column density profile as initial guess in each run mentioned in a_. These initial guesses were: the true column density profile used to simulate UVIS data, the true profile multiplied by a factor 2, 3, 4, 6, 10, 1/2, 1/3, 1/4, 1/6, and 1/10.

c_ For each run of MPFIT with a particular initial guess, column densities for 5 altitudes were retrieved, representative of different regions along the full altitude range: 400, 600, 800, 1000, and 1200 km.

d_ Elapsed times, uncertainties, real errors (comparison with true profile), were taken into account in the analysis of how well MPFIT handles different initial guesses.

The MPFIT routine was wrapped with the transmission filtering described in Section 3.1. The comparison of results was made taking into account the uncertainties given by MPFIT, an ideal result being one in which the 'true' profile falls within the 1-σ uncertainty interval around the retrieved value. To evaluate the results a 'retrieval matrix' was generated. The rows of this matrix represent each altitude studied, the columns, each species studied. The niches in the matrix are colored depending on the output of MPFIT according to Table B.1. In summary, a full green matrix means a perfect

Table B.1: Table showing the criteria used to interpret the 'retrieval matrices' and evaluate the response of MPFIT to different initial guesses.

Green	$error \leq \sigma$	good retrieval
Orange	$\sigma < error \leq 2\sigma$	acceptable retrieval
Red	$2\sigma < error \leq 5\sigma$	MPFIT uncertainties probably highly underestimated
Violet	$5\sigma < error$	unacceptable retrieval
Light grey	$\sigma > 100\%$	species not retrieved
Dark grey	$\sigma = 0$	species not retrieved

technique, every orange niche means that the 2-σ uncertainties should be considered to characterize the results, the other colors are marginally acceptable or unacceptable results, and grey niches mean a failure of MPFIT to provide a result.

Figure B.1 shows, as an example, some of the resulting matrices obtained for the different initial guesses used. For altitudes 400, 1000 and 1200 km, the results were worst: most species not retrieved, huge differences with real values and huge or zero uncertainties. It is worth noting that even giving the routine the true profile did not guarantee a good retrieval. When the initial guess is a factor of 3 or more bigger than the true profile, the general picture for altitudes 400 km and 600 km is worst, although improving for some species. There is no much change when passing from a factor 3 to a factor 6. When the initial guess is a factor of 1/4 or smaller, the retrieval is equal to the case of the initial guess being equal to the true profile, but the lower layers are sequentially lost. This is somehow worrying because the photochemical model profiles used as initial guess to analyze real data can differ up to a factor of 10 from the measurements. This motivated the iteration scheme described in Section 3.1, with the hope that re-scaling the initial guess would favor convergence to an appropriate set of column densities. It should be kept in mind, however, that the re-iteration algorithm has its limitations itself. Depending on the result from MPFIT, only some of the initial guess profiles might

be altered, not necessarily the ones differing the most from the 'true' profile. Moreover, all altered profiles are so by the same factor. The iteration can then result in a pointless delay of the retrieval, so only 4 iterations were used.

The next step was then to repeat steps a_ - d_ above but wrapping MPFIT with the iteration scheme described in Section 3.1. In this case the initial guesses used were the true column density profile used to simulate UVIS data, the true profile multiplied by a factor 2, 4, 10, 0.5, 0.25, and 0.1. Figure B.2 shows, as an example, some of the resulting matrices obtained for the different initial guesses used. The iteration scheme seems to be of little help and it takes much more time (sometimes 4 times more) than MPFIT running on its own, although in some cases it recovers some species/altitudes from a bad retrieval. A close look at the results after each iteration revealed that the values and errors did not change for good after the 2^{nd} iteration, the 3^{rd} and 4^{th} being useless (REM: in each iteration the new initial value was obtained from the old one multiplying by $2^{iter(-1)^{iter}}$). Strangely, even when the initial guess is smaller than the real profile, it is the dividing iteration that improves things. This might imply that it is the fact of fixing some parameters that improved the fit, and not the change in the initial guess. Only 2 iterations were used for the real data analysis.

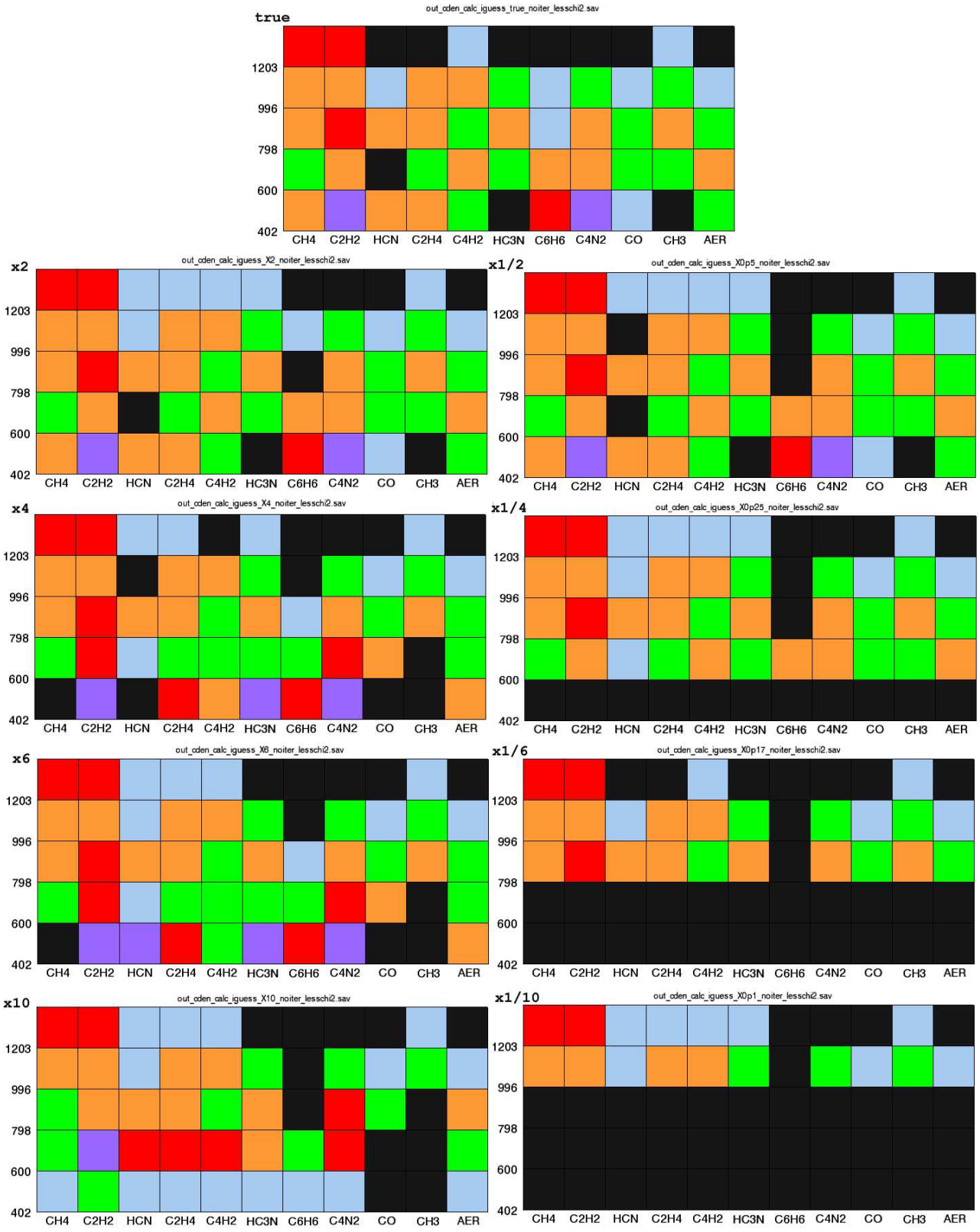

Figure B.1: Retrieval matrices generated to evaluate the results of MPFIT running alone, with no external iteration scheme. The rows of this matrix represent each altitude studied (in km), the columns, each species studied. The niches in the matrix are colored depending on the output of MPFIT, according to the criteria in Table B.1. The value in the upper left of each matrix is the factor multiplying the true column density profile, to get the initial guess used to obtain that retrieval matrix.

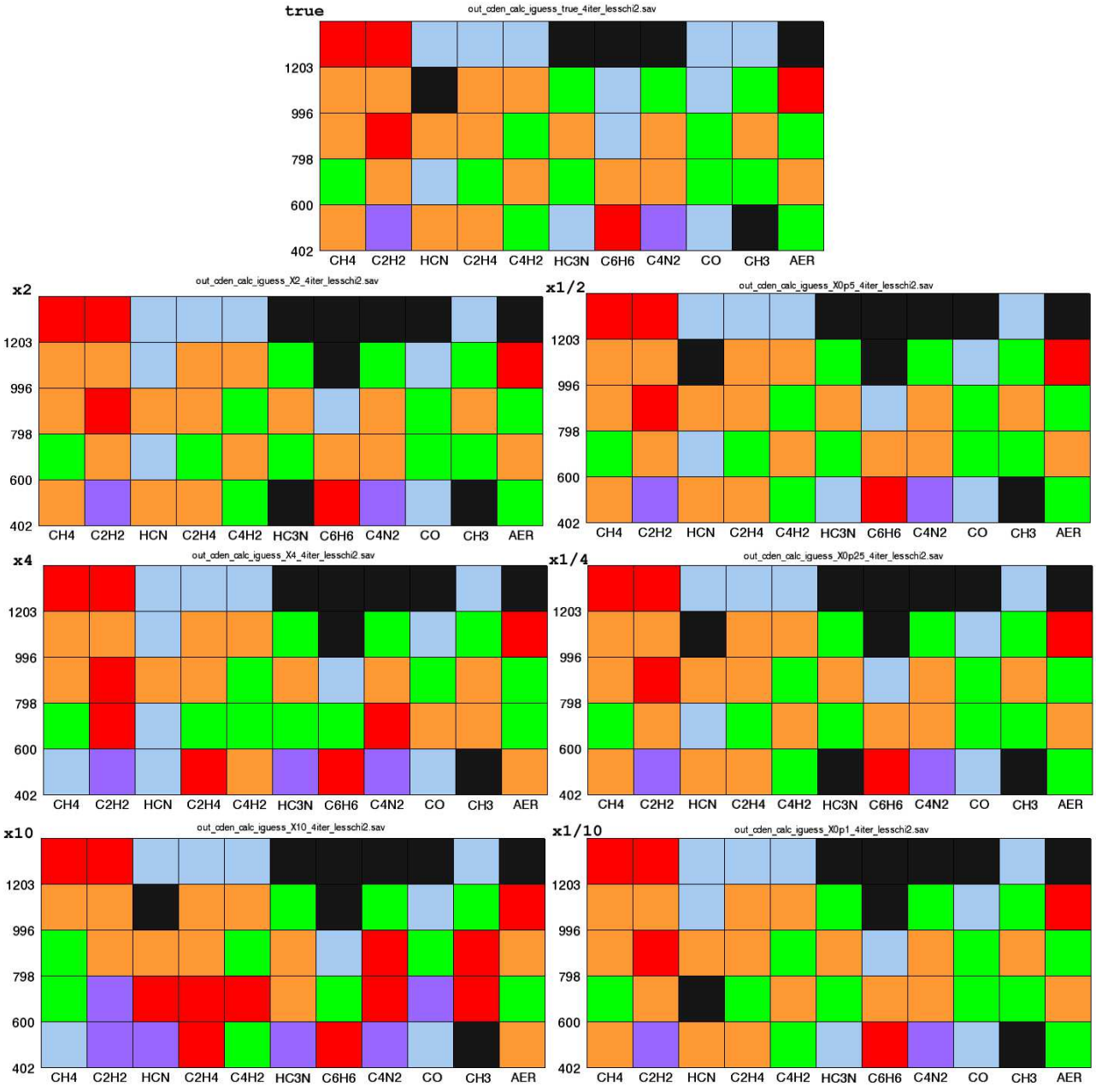

Figure B.2: Retrieval matrices generated to evaluate the results of MPFIT running wrapped with an iteration scheme of 4 iterations. The rows of this matrix represent each altitude studied (in km), the columns, each species studied. The niches in the matrix are colored depending on the output of MPFIT, according to the criteria in Table B.1. The value in the upper left of each matrix is the factor multiplying the true column density profile, to get the initial guess used to obtain that retrieval matrix.

Appendix C

MPFIT, uncertainties in column density retrieval

An important characterization of the MPFIT routine in the context of this work concerns the uncertainties provided by it. Under the assumptions stated in Section 3.1 about the distribution of the uncertainties in the measured data, the uncertainties in the column densities derived with MPFIT should be the formal 1-σ uncertainties, computed from their covariance matrix. However, as the retrieved uncertainty intervals around the retrieved values did not include the true column density value for some species/altitudes for some of the simulations performed, a Monte Carlo simulation was performed to characterized the output uncertainties. The procedure and results are presented in this appendix.

Synthetic UVIS data for 10 altitudes around 800 km were simulated with the procedure described in Section 3.6. The $I0$ spectrum was calculated from a IUE spectrum, convolved, binned and reversed calibrated according to the UVIS/FUV characteristics. Next, the column density retrieval experiment was performed 3150 times, in each case 'drawing' different sets of synthetic measurements thanks to the random perturbations applied to the simulated the data. This noise was added as random values with zero mean and a standard deviation equal to the square root of the simulated counts (Poisson uncertainties). The 10 synthetic altitudes were averaged to simulate the altitude binning in the real data analysis, transmission was calculated and the column densities retrieved with the procedures described in Section 3.1, using an initial guess equal to 2 times the true column densities, and wrapping MPFIT with a scheme of 4 iterations as described in Appendix B. For each of the 11 species included in the simulation (CH_4, C_2H_2, HCN, C_2H_4, C_4H_2, HC_3N, C_6H_6, C_4N_2, CO, CH_3, and AER) the distribution of the column densities was compared with the 'true' values. The uncertainties output by MPFIT when tested with simulated data, with similar initial conditions and iteration scheme (see Appendix B) were compared to the standard deviation of the Monte Carlo results (see Figure C.1).

The general result is acceptable for most of the species: the maximum of the distribution falling within the MPFIT-1-σ interval around the 'true' value. In some of the runs some species were not retrieved. Moreover, the true CH_4 value is not recovered within 1-σ, it is overestimated. Similar comments apply for the aerosols, but their abundance is underestimated. Although the truth is recovered for HCN, low values are not retrieved, which imposes a lower limit for detectability, the same happens for C_6H_6. In this last case, moreover, MPFIT did not return proper uncertainties (see the 800 km row in the 'retrieval matrix' in Appendix B). The comparison of MPFIT uncertainties and the standard deviation from the fitted Gaussian is shown in Figure C.2. The relative uncertainty in the value of the standard deviation of the fitted Gaussian (MC sigma in the graph) is of the order of 10^{-2} for most species, and 10^{-1} for HCN, HC_3N, and C_6H_6. MPFIT uncertainties are systematically too low for most of the species by less than 35%, about 90% for the aerosols. MPFIT uncertainties are overestimated for CH_4 and HCN. As the results correspond to only one altitude, for which some of the species might not be retrievable for some data sets (e.g. HCN), no systematic correction of the column densities or uncertainties derived from MPFIT was implemented in the analysis of real data. Nevertheless, it is worth keeping in mind that the MPFIT uncertainties shown in some of the results might be underestimated, considering a safer 2-σ interval when interpreting the results.

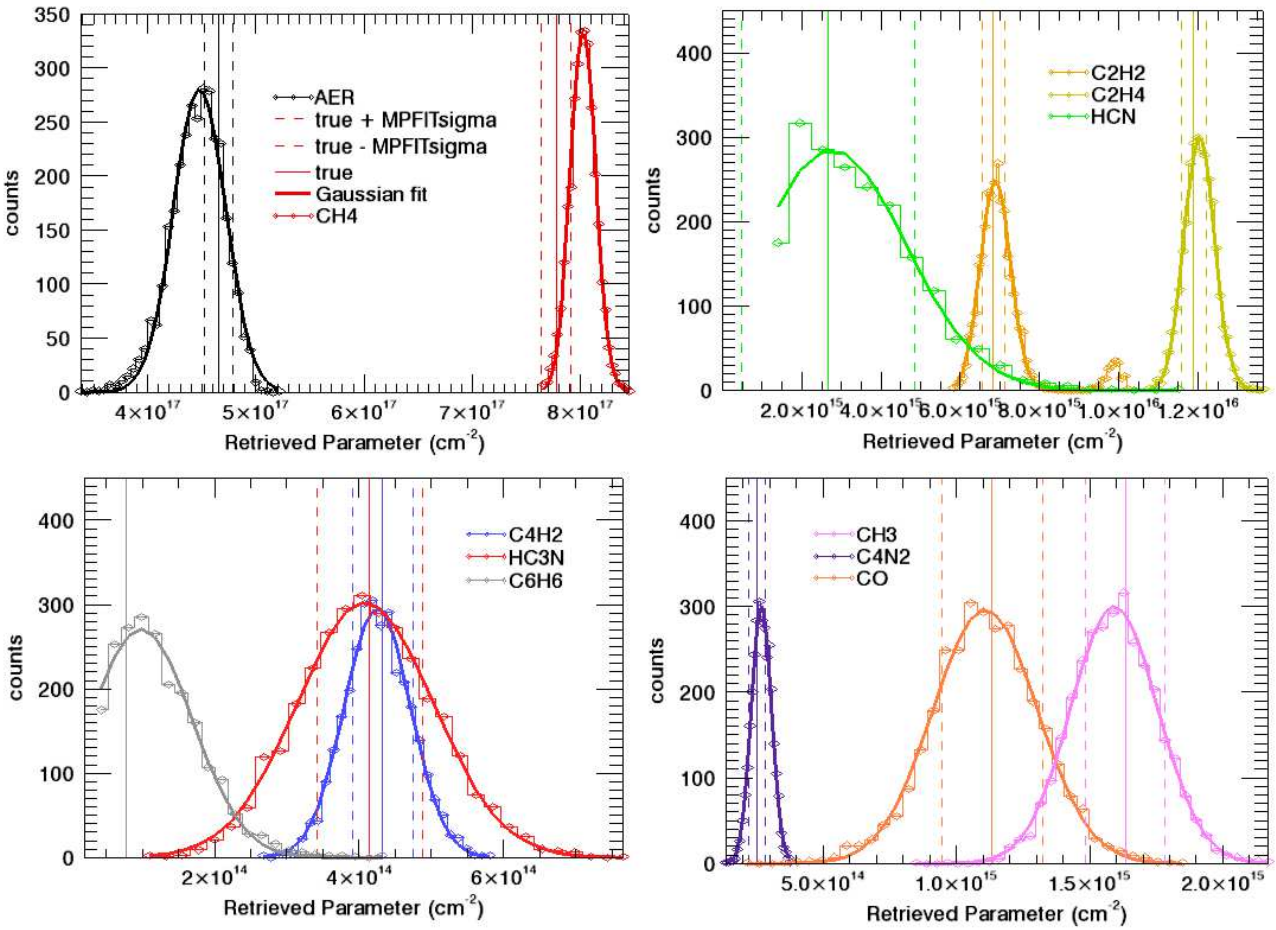

Figure C.1: Distribution of column densities obtained with the Monte Carlo simulations. Overplotted, a Gaussian fit. Solid vertical bars are the 'true' column densities used to simulate the UVIS data. Dashed vertical bars are uncertainties derived by MPFIT in one of the retrievals with simulated data commented in Appendix B, for the same altitude used in the MC simulations presented in this Appendix.

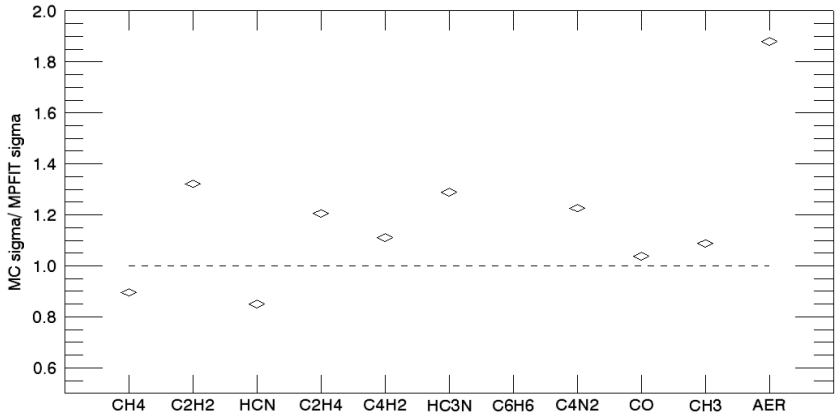

Figure C.2: Comparison of standard deviation of the number density distribution obtained in the Monte Carlo simulation, with the uncertainty derived by MPFIT in one of the retrievals with simulated data commented in Appendix B, for the same altitude used in the MC simulations presented in this Appendix.

Bibliography

Acton, C. H., 1996. Ancillary data services of nasa's navigation and ancillary information facility. Planetary Space Science 44 (1), 65 – 70. 22

Ajello, J., Gustin, J., Stewart, I., Larsen, K., Esposito, L., Pryor, W., McClintock, W., Stevens, M., Malone, C., Dziczek, D., 2008. Titan airglow spectra from the Cassini ultraviolet imaging spectrograph: Fuv disk analysis. Geophysical Research Letters 35 (6). 15, 25

Ajello, J., Stevens, M., Stewart, I., Larsen, K., Esposito, L., Colwell, J., McClintock, W., Holsclaw, G., Gustin, J., Pryor, W., 2007. Titan airglow spectra from Cassini ultraviolet imaging spectrograph (UVIS): Euv analysis. Geophysical Research Letters 34 (24). 15, 25, 30, 43, 44

Bénilan, Y., unpublisheda. 28, 36, 64

Bénilan, Y., unpublishedb. 64

Beynon, J. D. E., 1965. An experimental determination of the photo-ionization cross-section of atomic hydrogen. Nature 207 (4995), 405. 64

Bézard, B., Coustenis, A., McKay, C. P., 1995. Regular article: Titan's stratospheric temperature asymmetry: A radiative origin?. Icarus 113, 267 – 276. 6, 12

Bézard, B., Drossart, P., Encrenaz, T., Feuchtgruber, H., 2001. Benzene on the giant planets. Icarus 154 (2), 492 – 500. 76

Bolovinos, A., Philis, J., Pantos, E., Tsekeris, P., Andritsopoulos, G., 1981. The methylbenzenes vis-a-vis benzene. comparison of their spectra in the rydberg series region. Journal of Chemical Physics 75 (9), 4343 – 4349. 92

Bolovinos, A., Philis, J., Pantos, E., Tsekeris, P., Andritsopoulos, G., 1982. The methylbenzenes vis-a-vis benzene. comparison of their spectra in the valence-shell transitions region. Journal of Molecular Spectroscopy 94 (1), 55 – 68. 92

Broadfoot, A., et al., 1977. Ultraviolet Spectrometer experiment for Voyager mission. Space Science Reviews 21 (2), 183 – 205. 38

Caldwell, J., Cunningham, C., Anthony, D., White, H., Groth, E., Hasan, H., Noll, K., Smith, P., Tomasko, M., Weaver, H., 1992. Titan: evidence for seasonal change-a comparison of hubble space telescope and voyager images. Icarus 97 (1), 1 – 9. 6, 12

Capalbo, F., Bénilan, Y., Yelle, R., Koskinen, T., Sandel, B., Holsclaw, G., McClintock, W., 2013. Solar occultation by titan measured by Cassini/UVIS. Astrophysical Journal Letters 766 (2), (5 pp.). 7, 15, 16, 40, 53, 105, 107

Capalbo, F. J., 2010. Titan's atmospheric composition from Cassini ultraviolet imaging spectrograph data analysis. Master's thesis, Lulea University of Technology/University Paul Sabatier. 22, 28, 65

Carr, E. P., Stücklen, H., 1939. An electronic transition of the rydberg series type in the absorption spectra of hydrocarbons. Journal of Chemical Physics 7 (8), 631. 90

Cernicharo, J., Heras, A., Tielens, A., Pardo, J., Herpin, F., Guelin, M., Waters, L., 2001. Infrared space observatory's discovery of c4h2, c6h2, and benzene in crl 618. Astrophysical Journal, Letters 546 (2). 76

Chan, W., Cooper, G., Brion, C., 1992. Absolute optical oscillator strengths (11-20 ev) and transition moments for the photoabsorption of molecular hydrogen in the lyman and werner bands. Chemical Physics 168 (2), 375 – 388. 64

Chen, F., Judge, D., Wu, C., 2000. Temperature dependent photoabsorption cross sections of allene and methylacetylene in the vuv-uv region. Chemical Physics 260 (1), 215 – 223. 64

Chen, F. Z., Wu, C. Y. R., 2004. Temperature-dependent photoabsorption cross sections in the VUV-UV region. I. Methane and ethane. Journal of Quantitative Spectroscopy and Radiative Transfer 85 (2), 195 – 209.
URL http://www.sciencedirect.com/science/article/B6TVR-48XJFHK-5/2/1cf0eda27823be637a4378115dcab8a6 36, 64

Cheng, B.-M., Lu, H.-C., Chen, H.-K., Bahou, M., Yuan-Pern, L., Mebel, A., Lee, L., Mao-Chang, L., Yung, Y., 2006. Absorption cross sections of nh3, nh2d, nhd2, and nd3 in the spectral range 140-220 nm and implications for planetary isotopic fractionation. Astrophysical Journal 647 (2), 1535 – 1542. 64

Coates, A. J., Wellbrock, A., Lewis, G. R., Jones, G. H., Young, D. T., Crary, F. J., Jr., J. H. W., 2009. Heavy negative ions in titan's ionosphere: Altitude and latitude dependence. Planetary and Space Science 57, 1866 – 1871. 7, 10

Coll, P., Coscia, D., Smith, N., Gazeau, M.-C., Ramírez, S., Cernogora, G., Israël, G., Raulin, F., 1999. Experimental laboratory simulation of titan's atmosphere: aerosols and gas phase. Planetary and Space Science 47, 1331 – 1340. 6, 76

Coll, P., Raulin, F., 1998. Investigation on planetary atmospheres using laboratory simulation experiments: the example of saturn's moon (titan). Earth, Moon, and Planets 80 (1), 113 – 133. 6

Conklin, E. K., Ulich, B. L., Dickel, J. R., 1977. 3mm observations of titan. Bulletin Americal Astronomical Society 9, 471. 4

Coustenis, A., Achterberg, R. K., Conrath, B. J., Jennings, D. E., Marten, A., Gautier, D., Nixon, C. A., Flasar, F. M., Teanby, N. A., Bézard, B., Samuelson, R. E., Carlson, R. C., Lellouch, E., Bjoraker, G. L., Romani, P. N., Taylor, F. W., Irwin, P. G. J., Fouchet, T., Hubert, A., Orton, G. S., Kunde, V. G., Vinatier, S., Mondellini, J., Abbas, M. M., Courtin, R., 2007. The composition of titan's stratosphere from Cassini/CIRS mid-infrared spectra (english). Icarus (New York, NY) 189 (1), 35 – 62. 77

Coustenis, A., Atreya, S., Balint, T., Brown, R., Dougherty, M., Ferri, F., Fulchignoni, M., Gautier, D., Gowen, R., Griffith, C., Gurvits, L., Jaumann, R., Langevin, Y., Leese, M., Lunine, J., McKay, C., Moussas, X., Muller-Wodarg, I., Neubauer, F., Owen, T., Raulin, F., Sittler, E., Sohl, F., Sotin, C., Tobie, G., Tokano, T., Turtle, E., Wahlund, J.-E., Waite, J., Baines, K., Blamont, J., Coates, A., Dandouras, I., Krimigis, T., Lellouch, E., Lorenz, R., Morse, A., Porco, C., Hirtzig, M., Saur, J., Spilker, T., Zarnecki, J., Choi, E., Achilleos, N., Amils, R., Annan, P., Atkinson, D., Bénilan, Y., Bertucci, C., Bézard, B., Bjoraker, G., Blanc, M., Boireau, L., Bouman, J., Cabane, M., Capria, M., Chassefiere, E., Coll, P., Combes, M., Cooper, J., Coradini, A. a., 2009a. Tandem: Titan and enceladus mission. Experimental Astronomy 23 (3), 893 – 946. 15

Coustenis, A., Bézard, B., 1995. Titan's atmosphere from voyager infrared observations. iv. latitudinal variations of temperature and composition. Icarus 115, 126 – 140. 6

Coustenis, A., Bézard, B., Gautier, D., 1989a. Titan's atmosphere from voyager infrared observations. i. the gas composition of titan's equatorial region. Icarus; (USA), 54. 5

Coustenis, A., Bézard, B., Gautier, D., 1989b. Titan's atmosphere from voyager infrared observations. ii. the ch3d abundance and d/h ratio from the 900-1200/cm spectral region. Icarus; (USA), 67. 5

Coustenis, A., Bézard, B., Gautier, D., Marten, A., Samuelson, R., 1991. Titan's atmosphere from voyager infrared observations; iii, vertical distributions of hydrocarbons and nitriles near titan's north pole. Icarus 89 (1), 152 – 167. 5

Coustenis, A., Gendron, E., Lai, O., Véran, J.-P., Woillez, J., Combes, M., Vapillon, L., Fusco, T., Mugnier, L., Rannou, P., 2001. Images of titan at 1.3 and 1.6 μm with adaptive optics at the cfht. Icarus 154 (2), 501. 6

Coustenis, A., Lellouch, E., Sicardy, B., Roe, H., 2009b. Titan from Cassini-Huygens. Springer, Ch. 2. 4

Coustenis, A., Salama, A., Schulz, B., Ott, S., Lellouch, E., Encrenaz, T., Gautier, D., Feuchtgruber, H., 2003. Titan's atmosphere from iso mid-infrared spectroscopy. ICARUS 161 (2), 383. 5, 76, 77

Coustenis, A., Taylor, F. W. (Eds.), 2008. Titan, Exploring an Earthlike world, second edition Edition. World Scientific. xiii, 3

Craig, D. P., 1949. Energy levels of aromatic hydrocarbons. Journal of Chemical Physics 17 (12), 1358. 90

Cravens, T. E., Robertson, I. P., Waite, J. H., J., Yelle, R. V., Vuitton, V., Coates, A. J., Wahlund, J.-e., Agren, K., Richard, M. S., De La Haye, V., Wellbrock, A., Neubauer, F. M., 2009. Model-data comparisons for titan's nightside ionosphere. Icarus (New York, NY) 199 (1), 174 – 188. 23

Cui, J., Yelle, R., Vuitton, V., Waite, J., Kasprzak, W., Gell, D., Niemann, H., Müller-Wodarg, I., Borggren, N., Fletcher, G., Patrick, E., Raaen, E., Magee, B., 2009. Analysis of titan's neutral upper atmosphere from Cassini ion neutral mass spectrometer measurements. ICARUS 200 (2), 581 – 615. 8, 11, 12, 13, 29, 33, 38, 78, 107, 108, 110, 111, 112, 113, 126

Cui, J., Yelle, R. V., Strobel, D. F., Müller-Wodarg, I. C. F., Snowden, D. S., Koskinen, T. T., Galand, M., 2012. The ch4 structure in titan's upper atmosphere revisited. Journal of Geophysical Research. Planets 117 (E11), n/a. 107

Curdt W., Brekke P., Feldman U., Wilhelm K., Dwivedi B. N., Schühle U., Lemaire P., 2001. The sumer spectral atlas of solar-disk features. A&A 375 (2), 591–613.
URL http://dx.doi.org/10.1051/0004-6361:20010364 46

Danielson, R. E., Caldwell, J. J., Larach, D. R., 1973. Inversion in atmosphere of Titan. ICARUS 20 (4), 437–443. 4

De La Haye, V., WAITE, J. H., J., Cravens, T. E., Robertson, I. P., Lebonnois, S., 2008. Coupled ion and neutral rotating model of titan's upper atmosphere (english). Icarus (New York, NY) 197 (1), 110 – 136. 11, 13, 48, 63, 64, 78

De La Haye, V., Waite, J. H., Johnson, R. E., Yelle, R. V., Cravens, T. E., Luhmann, J. G., Kasprzak, W. T., Gell, D. A., Magee, B., Leblanc, F., Michael, M., Jurac, S., Robertson, I. P., 2007. Cassini ion and neutral mass spectrometer data in titan's upper atmosphere and exosphere: Observation of a suprathermal corona. Journal of Geophysical Research. Space Physics 112 (A7), n/a. 13

Eden, S., Limao-Vieira, P., Kendall, P., Mason, N. J., Hoffmann, S. V., Spyrou, S. M., 2003. High resolution photo-absorption studies of acrylonitrile, c[sup]2[/sup]h[sup]3[/sup]cn, and acetonitrile, ch[sup]3[/sup]cn (english). The European physical journal. D, Atomic, molecular and optical physics (Print) 26 (2), 201 – 210. 64

ESA, 2005. Seeing, touching and smelling the extraordinarily Earth-like world of Titan. Web site, retrieved 10 May 2010.
URL http://www.esa.int/SPECIALS/Cassini-Huygens/SEMHB881Y3E_0.html 3

Esposito, L. W., Barth, C. A., Colwell, J. E., Lawrence, G. M., Mcclintock, W. E., Stewart, A. I. F., Keller, H. U., Korth, A., Lauche, H., Festou, M. C., Lane, A. L., Hansen, C. J., Maki, J. N., West, R. A., Jahn, H., Reulke, R., Warlich, K., Shemansky, D. E., Yung, Y. L., 2004. The Cassini ultraviolet imaging spectrograph investigation (english). Space science reviews 115 (1-4), 299 – 361. ix, 15, 20, 21, 22

Fahr, A., Nayak, A., 1994. Temperature dependent ultraviolet absorption cross sections of 1,3-butadiene and butadiyne. Chemical Physics 189 (3), 725 – 731. 36, 64

Fahr, A., Nayak, A., 1996. Temperature dependent ultraviolet absorption cross sections of propylene, methylacetylene and vinylacetylene. Chemical Physics 203 (3), 351 – 358. 64

Fally, S., Carleer, M., Vandaele, A., 2009. Uv fourier transform absorption cross sections of benzene, toluene, meta-, ortho-, and para-xylene. Journal of Quantitative Spectroscopy and Radiative Transfer 110 (9), 766 – 782. 90

Feng, R., Cooper, G., Brion, C., 2002. Dipole (e,e+ion) spectroscopic studies of benzene: absolute oscillator strengths for molecular and dissociative photoionization in the vuv and soft x-ray regions. Journal of Electron Spectroscopy and Related Phenomena 123 (2), 211 – 223. 80, 90

Ferradaz, T., Bénilan, Y., Fray, N., Jolly, A., Schwell, M., Gazeau, M. C., Jochims, H.-W., 2009. Temperature-dependent photoabsorption cross-sections of cyanoacetylene and diacetylene in the mid- and vacuum-UV: Application to Titan's atmosphere. Planetary and Space Science 57, 10 – 12. x, 28, 36, 64, 81, 93

Flasar, F. M., Conrath, B. J., 1990. Titan's stratospheric temperatures : a case for dynamical inertia? (english). Icarus (New York, NY) 85 (2), 346 – 354. 6

Fray, N., Bénilan, Y., Gazeau, M.-c., Jolly, A., Schwell, M., Arzoumanian, E., Ferradaz, T., Es-sebbar, E., Guillemin, J.-C., 2010. Temperature-dependent photoabsorption cross section of cyanodiacetylene in the vacuum uv (english). Journal of geophysical research 115 (E6). 63, 64

Fray, N., Schmitt, B., 2009. Sublimation of ices of astrophysical interest: A bibliographic review. PlanetaryandSpaceScience 57, 2053 – 2080, doi:10.1016/j.pss.2009.09.011. 85

Fulchignoni, M., et al., 2005. In situ measurements of the physical characteristics of Titan's environment. Nature 438, doi:10.1038/nature04314. 3, 13, 38, 106

Galand, M. b. b. a., YELLE, R., JUN CUI [b1], a., WAHLUND, J.-E., Vuitton, V., WELLBROCK, A., COATES, A., 2010. Ionization sources in titan's deep ionosphere. Journal of geophysical research 115 (A7). 23

Gans, B., Garcia, G. A., Boyé-Péronne, S., Loison, J.-C., Douin, S., Gaie-Levrel, F., Gauyacq, D., 2011. Absolute photoionization cross section of the ethyl radical in the range 8-11.5 ev: synchrotron and vacuum ultraviolet laser measurements. The Journal Of Physical Chemistry. A 115 (21), 5387 – 5396. 64

Gillett, F., 1975. Further observations of the 8-13 micron spectrum of titan. Astrophysical Journal. Letters to the Editor 201 (1). 4

Gillett, F., Forrest, W., Merrill, K., 1973. 8-13 micron observations of titan. Astrophysical Journal. Letters to the Editor 184 (2). 4

Grubb, S. G., Otis, C. E., Whetten, R. L., Grant, E. R., Albrecht, A. C., 1985. Higher excited states of benzene: Symmetry assignments of six gerade rydberg series by four-photon absorption spectroscopy. Journal of Chemical Physics 82 (3), 1135. 79, 89, 90, 91

Gurtler, P., Saile, V., Koch, E., June 1977. High resolution absorption spectrum of nitrogen in the vacuum ultraviolet. Chem. Phys. Lett. 48 (2). 48

Hammond, V. J., Price, W. C., 1955. Oscillator strengths of the vacuum ultra-violet absorption bands of benzene and ethylene. Transactions of the Faraday Society 51, 605. 79, 88, 90, 91

Hammond, V. J., Price, W. C., Teegan, J. P., Walsh, A. D., 1950. The absorption spectra of some substituted benzenes and naphthalenes in the vacuum ultra-violet. Discussions of the Faraday Society 9, 53. 79, 90, 91, 103

Hebrard, E., Dobrijevic, M., Bénilan, Y., Raulin, F., 2007. Photochemical kinetics uncertainties in modelling Titan's atmosphere: First consequences. Planetary and Space Science 55, 1470 – 1489. 78

Herzberg, G., 1966. Molecular spectra and molecular structure. Vol. III. Electronic Spectra and Electronic structure of polyatomic molecules. D. Van Nostrand Company Inc. 80, 90, 91, 103

Ho, G. H., Lin, M. S., 1998. Photoabsorption and photoionization of propyne. Journal of Chemical Physics 109 (14), 5868. 64

Hourdin, F., Talagrand, O., Sadourny, R., Courtin, R., Gautier, D., Mckay, C. P., 1995. Numerical simulation of the general circulation of the atmosphere of titan. Icarus 117 (2), 358. 6

Hunten, D., 1973a. The escape of h2 from titan. Journal of the Atmospheric Sciences 30 (14), 726 – 732. 4

Hunten, D., 1973b. The escape of light gases from planetary atmospheres. Journal of the Atmospheric Sciences 30 (8), 1481 – 1494. 4

Hunten, D. M., Morrison, D. (Eds.), 1978. A Titan atmosphere with a surface of 200 K. The Saturn System. NASA Conference Publication 2068. 4

Imanaka, H., Khare, B. N., Elsila, J. E., Bakes, E. L., McKay, C. P., Cruikshank, D. P., Sugita, S., Matsui, T., Zare, R. N., 2004. Laboratory experiments of titan tholin formed in cold plasma at various pressures: implications for nitrogen-containing polycyclic aromatic compounds in titan haze. Icarus 168, 344 – 366. 6

Imanaka, H., Smith, M. A., Turro, N. J., 2010. Formation of nitrogenated organic aerosols in the titan upper atmosphere. Proceedings of the National Academy of Sciences of the United States of America (28), 12423. 78

Ityaksov, D., Linnartz, H., Ubachs, W., 2008. Deep-uv rayleigh scattering of n2, ch4 and sf6. Molecular Physics 106 (21), 2471 – 2479. 26

Jaumann, R., Kirk, R. L., Lorenz, R. D., Lopes, R. M., tofan, E. S., Turtle, E. P., Keller, H. U., Wood, C. A., Sotin, C., Soderblom, L. A., Tomasko, M. G., 2009. Titan from Cassini-Huygens. Springer, Ch. 5. 3

Jeans, J. H., 1931. The dynamical theory of gases. 3d edition. (Dover reprint)., 3rd Edition. Dover reprint. 4

Kameta, K., Kouchi, N., Ukai, M., Hatano, Y., 2002. Photoabsorption, photoionization, and neutral-dissociation cross sections of simple hydrocarbons in the vacuum ultraviolet range. J. Electron Spectrosc. Relat. Phenom. 123, 225 – 238. 48, 58

Kammer, J. A., Shemansky, D. E., Zhang, X., Yung, Y. L., 2013. Composition of titan's upper atmosphere from Cassini UVIS euv stellar occultations. Planetary and Space Science. 32

Khare, B., Sagan, C., Arakawa, E., Suits, F., Callcott, T., Williams, M., 1984. Optical constants of organic tholins produced in a simulated titanian atmosphere: from soft x-ray to microwave frequencies. Icarus 60 (1), 127 – 137. 5, 9, 36

Khare, B. N., Sagan, C., Ogino, H., Nagy, B., Er, C., Schram, K. H., Arakawa, E. T., 1986. Amino acids derived from titan tholins. Icarus 68 (1), 176 – 184. 5, 9

Khvostenko, O. G., Tzeplin, E. E., Dzhemilev, U. M., 2003. A first example of application of photoelectron spectroscopy to interpretation of the uv absorption spectra of benzenes. Doklady Chemistry 389 (4), 101. 91

Koch, E., Otto, A., 1972. Optical absorption of benzene vapour for photon energies from 6 ev to 35 ev. Chemical Physics Letters 12 (3), 476 – 480. 79, 90, 91

Koch, E., Otto, A., 1976. Vacuum ultra-violet and electron energy loss spectroscopy of gaseous and solid organic compounds. International Journal of Radiation Physics and Chemistry 8 (1), 113 – 150. 91

Koch, E., Skibowski, M., 1971. Optical absorption of gaseous methane, ethane, propane and butane and reflection of solid methane and ethane in the vacuum ultraviolet. Chemical Physics Letters 9 (5), 429 – 432. 64

Koskinen, T., Yelle, R., Snowden, D., Lavvas, P., Sandel, B., Capalbo, F., Bénilan, Y., West, R., 2011. The mesosphere and lower thermosphere of titan revealed by Cassini/UVIS stellar occultations. Icarus 216 (2), 507 – 534. x, 7, 8, 9, 10, 15, 16, 21, 25, 33, 34, 36, 37, 52, 56, 57, 63, 78, 94, 99, 100, 101, 102, 104, 105, 106, 108, 114, 119

Koskinen, T. T., Sandel, B. R., Yelle, R. V., Capalbo, F. J., Holsclaw, G. M., McClintock, W. E., Edgington, S., 2013. The density and temperature structure near the exobase of saturn from Cassini UVIS solar occultations. Icarus 226, 1318 – 1330. 52

Krasnopolsky, V. A., 2009. A photochemical model of titan's atmosphere and ionosphere (english). Icarus (New York, NY) 201 (1), 226 – 256. 63, 64, 65, 78

Kuiper, G., NOV 1944. Titan: A satellite with an atmosphere. ASTROPHYSICAL JOURNAL 100 (3), 378–383. 4

Kunde, V. G., Ade, P. A. R., Barney, R. D., Bergman, D., Bonnal, J.-F., Borelli, R., Boyd, D., Brasunas, J. C., Brown, G. V., Calcutt, S. B., Carroll, F., Courtin, R., Cretolle, J. B., Crooke, J. A., Davis, M. A., Edberg, S., Fettig, R. K., Flasar, M., Glenar, D. A., Graham, S., Hagopian, J. G., Hakun, C. F., Hayes, P. A., Herath, L., Spilker, L., Jennings, D. E., Karpati, G., Kellebenz, C., Lakew, B., Lindsay, J., Lohr, J., Lyons III, J. J., Martineau, R. J., Martino, A. J., Matsumura, M., McCloskey, J., Melak, T., Michel, G., Morrell, A., Mosier, C., Pack, L. G., Plants, M., Robinson, D., Rodriguez, L., Romani, P., Schaefer, B., Schmidt, S. M., Trujillo, C., Vellacott, T., Wagner, K., Yun, D. (Eds.), 1996. Cassini infrared Fourier spectroscopic investigation. Vol. 2803.
URL http://dx.doi.org/10.1117/12.253416 15

Kyrola, E., Sihvola, E., Kotivuori, Y., Tikka, M., Tuomi, T., APRIL 1993. Inverse theory for occukation measurements 1. spectral inversion. Journal of Geophysics Research 98 (D4), 7367–7381. 56, 57

Lara, L. M., Lellouch, E., Lopez-Moreno, J. J., Rodrigo, R., 1996. Vertical distribution of titan's atmospheric neutral constituents (english). Journal of geophysical research 101 (E10), 23261 – 23283. 6, 39

Lavvas, P., Coustenis, A., Vardavas, I., 2008a. Coupling photochemistry with haze formation in titan's atmosphere, part i: Model description. Planetary & Space Science 56 (1), 27 – 66. 7

Lavvas, P., Coustenis, A., Vardavas, I., 2008b. Coupling photochemistry with haze formation in titan's atmosphere, part ii: Results and validation with Cassini/Huygens data. Planetary & Space Science 56 (1), 67 – 99. 7, 9, 63, 77

Lavvas, P., Sander, M., Kraft, M., Imanaka, H., 2011. Surface chemistry and particle shape: Processes for the evolution of aerosols in titan's atmosphere (english). The Astrophysical journal 728 (2). 9, 23, 24, 48, 49, 58, 63

Lavvas, P., Yelle, R., Griffith, C., 2010. Titan's vertical aerosol structure at the Huygens landing site: Constraints on particle size, density, charge, and refractive index. ICARUS 210 (2), 832 – 842. 33, 65

Lavvas, P., Yelle, R. V., Vuitton, V., 2009. The detached haze layer in titan's mesosphere. ICARUS 201 (2), 626 – 633. 11

Lebonnois, S., 2005. Benzene and aerosol production in titan and jupiter's atmospheres: a sensitivity study. Planetary and Space Science 53 (5), 486 – 497. 76, 77, 78

Lebonnois, S., Bakes, E. L. O., McKay, C. P., 2002. Transition from gaseous compounds to aerosols in titan's atmosphere. ICARUS 159 (2), 505. 76, 77

Lebonnois, S., Hourdin, F., Rannou, P., Luz, D., Toublanc, D., 2003. Impact of the seasonal variations of composition on the temperature field of titan's stratosphere. ICARUS 163 (1), 164. 6, 12

Lee, A. Y. T., Yung, Y. L., Cheng, B.-M., Bahou, M., Chung, C.-Y., Lee, Y.-P., 2001. Enhancement of deuterated ethane on jupiter. The Astrophysical Journal Letters 551 (1), L93.
URL http://stacks.iop.org/1538-4357/551/i=1/a=L93 36

Lee, L., Carlson, R., Judge, D., 1976. The absorption cross sections of h2 and d2 from 180 to 780 aring. Journal of Quantitative Spectroscopy and Radiative Transfer 16 (10), 873 – 877. 64

Lellouch, E., Coustenis, A., Gautier, D., Raulin, F., Dubouloz, N., 1989. Titan's atmosphere and hypothesized ocean - a reanalysis of the voyager 1 radio-occultation and iris 7. 7-micron data. Icarus; (USA), 328. 5

Lewis, B. R., Heays, A. N., Gibson, S. T., Lefebvre-Brion, H., Lefebvre, R., 2008. A coupled-channel model of the $^3\pi_u$ states of n_2: Structure and interactions of the $3s\sigma_g f_3\ ^3\pi_u$ and $3p\pi_u g_3\ ^3\pi_u$ rydberg states. Journal of Chemical Physics 129 (16), 10.1063/1.2990656. 32, 58

Lewis, J., 1971. Satellites of the outer planets: their physical and chemical nature. Icarus 15 (2), 174 – 185. 4

Liang, M.-C., Yung, Y. L., Shemansky, D. E., 2007. Photolytically generated aerosols in the mesosphere and thermosphere of titan. The Astrophysical Journal. 10, 11, 16, 33

Lindal, G., Wood, G., Hotz, H., Sweetnam, D., Eshleman, V., Tyler, G., 1983. The atmosphere of titan: An analysis of the voyager 1 radio occultation measurements. Icarus 53, 348 – 363. 5

Lockwood, G. W., Thompson, D. T., 2009. Seasonal photometric variability of titan, 1972-2006 (english). Icarus (New York, NY) 200 (2), 616 – 626. 12, 13

Lutz, B. L., Owen, T., Cess, R. D., 1976. Laboratory band strengths of methane and their application to atmospheres of Jupiter, Saturn, Uranus, Neptune, and Titan. Astrophysical Journal 203 (2), 541–551. 4

Macala, G. A., 2002. Design of the reaction wheel attitude control system for the Cassini spacecraft. In: AAS/AIAA Space Flight Mechanics Meeting. 42

Magee, B. A., Waite, J. H., Mandt, K. E., Westlake, J., Bell, J., Gell, D. A., 2009. INMS-derived composition of titan's upper atmosphere: Analysis methods and model comparison. Planetary and Space Science 57, 1895 – 1916. 7, 11, 38, 64, 107

Markwardt, C. B., 2009. Non-linear least-squares fitting in idl with mpfit. In: Bohlender, D. A., Durand, D., Dowler, P. (Eds.), Astronomical Data Analysis Software and Systems XVIII. Vol. 411. ISBN: 978-1-58381-702-5. 57

McClintock, W. E., Lawrence, G. M., Kohnert, R. A., Esposito, L. W., December 1993. Optical design of the ultraviolet imaging spectrograph for the Cassini mission to saturn. Opt. Eng. 32 (12), 3038–3046x'. 40

Mckay, C., Pollack, J., Courtin, R., 1989. The thermal structure of titan's atmosphere. Icarus; (USA), 23. 5, 9

Miller, S. L., 1953. A production of amino acids under possible primitive earth conditions. Science (3046), 528. 2

Müller-Wodarg, I. C. F., Yelle, R. V., Borggren, N., Waite, J. H., 2006. Waves and horizontal structures in titan's thermosphere. Journal of Geophysical Research. Space Physics 111 (A12), n/a. 13, 110

Müller-Wodarg, I. C. F., Yelle, R. V., Cui, J., Waite, J. H., 2008. Horizontal structures and dynamics of titan's thermosphere. Journal of Geophysical Research. Planets 113 (E10), n/a. 7, 11, 12, 16, 23, 28, 109, 110, 111

Muller-Wodarg, I., Yelle, R., Mendillo, M., Young, L., Aylward, A., 2000. The thermosphere of titan simulated by a global three-dimensional time-dependent model. Journal of Geophysical Research 105 (A9), 20833 – 20856. 7, 113

Mulliken, R. S., 1939. Intensities of electronic transitions in molecular spectra v. benzene. Journal of Chemical Physics 7 (5), 353. 80

NASA-PDS, 2012. Cassini UVIS User's Guide. PlanetaryDataSystem, http://pds-rings.seti.org/cassini/uvis/index.html. 30, 35, 57

Niemann, H., Atreya, S., Bauer, S., Carignan, G., Demick, J., Frost, R., Gautier, D., Haberman, J., Harpold, D., Hunten, D., Israel, G., Lunine, J., Kasprzak, W., Owen, T., Paulkovich, M., Raulin, F., Raaen, E., Way, S., DEC 8 2005. The abundances of constituents of Titan's atmosphere from the GCMS instrument on the Huygens probe. NATURE 438 (7069), 779–784. 58

Nordheim, G., Sponer, H., Teller, E., 1940. Note on the ultraviolet absorption systems of benzene vapor. Journal of Chemical Physics 8 (6), 455 – 458. 90, 91

Palmer, M. H., Walker, I. C., 2007. The electronic states of but-2-yne studied by {VUV} absorption, near-threshold electron energy-loss spectroscopy and ab initio configuration interaction methods. Chemical Physics 340 (1-3), 158 – 170.
URL http://www.sciencedirect.com/science/article/pii/S0301010407003710 64

Pantos, E., Philis, J., Bolovinos, A., 1978. The extinction coefficient of benzene vapor in the region 4.6 to 36 ev. Journal of Molecular Spectroscopy 72 (1), 36 – 43. 79, 80, 88, 90, 91, 92

Pickett, L. W., Muntz, M., McPherson, E. M., 1951. Vacuum ultraviolet absorption spectra of cyclic compounds .1. Cyclohexane, cyclohexene, cyclopentane, cyclopentene and benzene. Journal of the American Chemical Society 73 (10), 4862–4865. 79, 88, 90, 91, 93

Pilling, M., Bass, A., Braun, W., 1971. Oscillator strengths of ch2 and ch3 in the vacuum ultraviolet. Chemical Physics Letters 9 (2), 147 – 148. 36, 64

Press, W. H., Teukolsky, S. A., Vetterling, W. T., Flannery, B. P., 1996. Numerical Recipes in Fortran 90, 2nd Edition. Vol. 2 of Fortran Numerical Recipes. Press Syndicate of the University of Cambridge. 57, 61

Price, W. C., Walsh, A. D., 1947. The absorption spectra of benzene derivatives in the vacuum ultra-violet. i. Proceedings of the Royal Society of London. Series A, Mathematical and Physical Sciences (1024), 22. 79, 90

Price, W. C., Wood, R. W., 1935. The far ultraviolet absorption spectra and ionization potentials of c6h6 and c6d6. Journal of Chemical Physics 3 (8), 439. 79, 90, 91, 103

Quemerais, E., Bertaux, J.-L., Korablev, O., Dimarellis, E., Cot, C., Sandel, B. R., Fussen, D., 2006. Stellar occultations observed by spicam on mars express. Journal of Geophysics Research 111, doi:10.1029/2005JE002604. 56

Ramirez, S. I., Navarro Gonzalez, R., 2002. The gas- and condensed-phase products of corona discharges on titan. Origins of Life and Evolution of the Biosphere 32 (5-6), 531. 6

Ramírez, S., Navarro-González, R., Coll, P., Raulin, F., 2001. Possible contribution of different energy sources to the production of organics in titan's atmosphere. Advances in Space Research 27 (2), 261. 6

Rannou, P., Cabane, M., Chassefiere, E., Botet, R., McKay, C. P., Courtin, R., 1995. Titan's geometric albedo: Role of the fractal structure of the aerosols. Icarus 118 (2), 355. 6

Rannou, P., Hourdin, F., McKay, C., 2002. A wind origin for titan's haze structure. Nature 418 (6900), 853 – 856. 6, 12

Rannou, P., Hourdin, F., McKay, C., Luz, D., 2004. A coupled dynamics-microphysics model of titan's atmosphere. Icarus 170, 443 – 462. 6

Raulin, F., 2005. Exo-astrobiological aspects of Europa and Titan: From observations to speculations. Space Science Reviews 116 (1-2), 471–487, Workshop on Comparative Study of the Outer Planets before the Exploration of Saturn, ISSI, Bern, SWITZERLAND, JAN 12-14, 2004. 2, 3

Raulin, F., 2005b. L'environnement de la Terre Primitive, 2nd Edition. Presses Universitaires de Bordeaux, Ch. 15. 2

Raulin, F., McKay, C., Lunine, J., Owen, T., 2009. Titan from Cassini-Huygens. Springer, Ch. 9. 3

Raulin, F., Toupance, G., Mourey, D., 1982. Organic-syntheses from chsub4-nsub2 atmospheres: Implications for titan. Origins of Life 12 (3), 267. 5, 9, 76

Rees, W. G., 2001. Physical Principles of Remote Sensing, 2nd Edition. Cambridge University Press, ISBN 0 521 66034 3 hard back. 24

Reisse, J., 2005. L'environnement de la Terre Primitive, second edition Edition. Presses Universitaires de Bordeaux, Ch. ch 14. 2, 4

Rennie, E., Johnson, C., Parker, J., Holland, D., Shaw, D., Hayes, M., 1998. A photoabsorption, photodissociation and photoelectron spectroscopy study of c6h6 and c6d6. Chemical Physics 229 (1), 107 – 123. 80, 88, 89, 90, 91, 92, 103

Rodgers, C. D., 2000. Inverse methods for atmospheric sounding: theory and practice. World Scientific Publishing Co. Pte. Ltd. 57, 60, 61

Salby, M. L., 1996. Fundamentals of Atmospheric Physics. Academic Press, iSBN-13:978-0-12-615160-2. 62

Samson, J. A. R., Masuoka, T., Pareek, P. N., Angel, G. C., June 1987. Total and dissociative photoionization cross sections of n2 from threshold to 107 ev. Journal of Chemical Physics 86 (11), 6128 – 6132. 48, 58, 64

Samuelson, R. E., Hanel, R. A., Kunde, V. G., Maguire, W. C., 1981. Mean molecular weight and hydrogen abundance of titan's atmosphere. Nature 292 (5825), 688. 5

Sanchez, R. A., Ferris, J. P., Orgel, L. E., 1966. Cyanoacetylene in prebiotic synthesis. Science (3750), 784. 76

Sarani, S., 2009. Reconstruction of titan atmospheric density using Cassini guidance, navigation, and control data. In: Proceedings of the AIAA Guidance, Navigation, and Control Conference. Am. Inst. of Aeronaut. and Astronaut., New York, abstr. 5763. 38

Schunk, R., Nagy, A., 2009. Ionospheres. Physics, Plasma Physics, and Chemistry, 2nd Edition. Cambridge University Press. 64

Selsis, F., Parisot, J.-P., 2005. L'environnement de la Terre Primitive, 2nd Edition. Presses Universitaires de Bordeaux, Ch. ch 10. 2

Shemansky, D. E., Stewart, A. I. F., West, R. A., Esposito, L. W., Hallett, J. T., Liu, X., 2005. The Cassini UVIS stellar probe of the titan atmosphere. Science (New York, N.Y.) 308 (5724), 978 – 982. 7, 8, 10, 15, 16, 21, 33, 101

Shindo, F., Bénilan, Y., Guillemin, J.-C., Chaquin, P., Jolly, A., Raulin, F., 2003. Ultraviolet and infrared spectrum of c6h2 revisited and vapor pressure curve in titan's atmosphere. Planetary and Space Science 51 (1), 9 – 17. 64

Sicardy, B., Ferri, F., Roques, F., Lecacheux, J., Pau, S., Brosch, N., Nevo, Y., Hubbard, W. B., Reitsema, H. J., Blanco, C., Carreira, E., Beisker, W., Bittner, C., Bode, H.-J., Bruns, M., Denzau, H., Nezel, M., Riedel, E., Struckmann, H., Appleby, G., Forrest, R. W., Nicolson, I. K. M., Hollis, A. J., Miles, R., 1999. The structure of titan's stratosphere from the 28 sgr occultation. Icarus 142 (2), 357. 6, 28

Smith, G. R., Hunten, D. M., 1990. Study of planetary atmospheres by absorptive occultations. Reviews of geophysics (1985) 28 (2), 117 – 143. 25

Smith, G. R., Strobel, D. F., Broadfoot, A. L., Sandel, B. R., Shemansky, D. E., Holberg, J. B., 1982. Titan's upper atmosphere: Composition and temperature from the euv solar occultation results. Journal of Geophysical Research. Space Physics 87 (A3), 1351. 5, 6, 39

Sneep, M., Ubachs, W., 2005. Direct measurement of the rayleigh scattering cross section in various gases. Journal of Quantitative Spectroscopy & Radiative Transfer 92 (3), 293 – 310. 26

Snowden, D., Yelle, R., Cui, J., Wahlund, J.-E., Edberg, N., Å gren, K., 2013. The thermal structure of titan's upper atmosphere, i: Temperature profiles from Cassini INMS observations. ICARUS 226 (1), 552 – 582. 11, 12, 13, 29, 106, 108, 109, 111, 112, 113, 126

Soderblom, L. A., Barnes, J. W., Brown, R. H., Clark, R. N., Janssen, M. A., McCord, T. B., Niemann, H. B., Tomasko, M. G., 2009a. Titan from Cassini-Huygens. Springer, Ch. 6. 3

Soderblom, L. A., Barnes, J. W., Brown, R. H., Clark, R. N., Janssen, M. A., McCord, T. B., Niemann, H. B., Tomasko, M. G., 2009b. Titan from Cassini-Huygens. Springer, Ch. 10. 8, 103

Sofieva, V. F., Tamminen, J., Haario, H., Kyrola, E., Lehtinen, M., 2004. Ozone profile smoothness as a priori information in the inversion of limb measurements. Ann. Geophys. 22, 3411–3420. 61

Souza, A. C. A., Srivastava, S. K., 1994. Photoabsorption cross sections of ar, n2 and si(ch3)4 derived from electron energy loss spectroscopy. J. Braz. Chem. Soc. 64

Steffl, A. J., 2005. The io plasma torus during the Cassini encounter with jupiter: Temporal, radial and azimuthal variations. Ph.D. thesis, University of Colorado. 43, 44, 47

Stevens, M. H., Gustin, J., Ajello, J. M., Evans, J. S., Meier, R. R., Kochenash, A. J., Stephan, A. W., Stewart, A. I. F., Esposito, L. W., McClintock, W. E., Holsclaw, G., Bradley, E. T., Lewis, B. R., Heays, A. N., 2011. The production of titan's ultraviolet nitrogen airglow. Journal of Geophysical Research. Space Physics 116 (A5), n/a. 15, 38

Stofan, E. R., Elachi, C., Lunine, J. I., Lorenz, R. D., Stiles, B., Mitchell, K. L., Ostro, S., Soderblom, L., Wood, C., Zebker, H., Wall, S., Janssen, M., Kirk, R., Lopes, R., Paganelli, F., Radebaugh, J., Wye, L., Anderson, Y., Allison, M., Boehmer, R., Callahan, P., Encrenaz, P., Flamini, E., Francescetti, G., Gim, Y., Hamilton, G., Hensley, S., Johnson, W. T. K., Kelleher, K., Muhleman, D., Paillou, P., Picardi, G., Posa, F., Roth, L., Seu, R., Shaffer, S., Vetrella, S., West, R., JAN 4 2007. The lakes of Titan. NATURE 445 (7123), 61–64. 3

Strobel, D. F., 1974. The photochemistry of hydrocarbons in the atmosphere of titan. Icarus 21 (4), 466 – 470. 4

Strobel, D. F., 1982. Chemistry and evolution of titan's atmosphere. Origins of Life and Evolution of Biospheres (Formerly Origins of Life and Evolution of the Biosphere) 12 (3), 244. 5

Strobel, D. F., Summers, M. E., Zhu, X., 1992. Titan's upper atmosphere structure and ultraviolet emissions. icarus. 39

Suto, M., Lee, L. C., 1985. Photoabsorption cross section of ch3cn: Photodissociation rates by solar flux and interstellar radiation. Journal of Geophysical Research. Atmospheres 90 (7), 13037. 64

Suto, M., Xiuyan, W., Jun, S., Lee, L., 1992. Quantitative photoabsorption and fluorescence spectroscopy of benzene, naphthalene, and some derivatives at 106-295 nm. Journal of Quantitative Spectroscopy and Radiative Transfer 48 (1), 79 – 89. 80, 92, 103

Taatjes, C. A., Pratt, S. T., Osborn, D. L., Selby, T. M., Meloni, G., Fan, H., 2008. Absolute photoionization cross-section of the methyl radical. Journal of Physical Chemistry A 112 (39), 9336 – 9343. 36, 64

Teanby, N. A., Irwin, P. G. J., Nixon, C. A., De Kok, R., Vinatier, S., Coustenis, A., Sefton-nash, E., Calcutt, S. B., Flasar, F. M., 2012. Active upper-atmosphere chemistry and dynamics from polar circulation reversal on titan (english). Nature (London) 491 (7426), 732 – 735. 11

Tobie, G., Grasset, O., Lunine, J., Mocquet, A., Sotin, C., JUN 2005. Titan's internal structure inferred from a coupled thermal-orbital model. ICARUS 175 (2), 496–502. 3

Tomasko, M., Doose, L., Engel, S., Dafoe, L., West, R., Lemmon, M., Karkoschka, E., See, C., 2008. A model of titan's aerosols based on measurements made inside the atmosphere. Planetary & Space Science 56 (5), 669 – 707. 10

Toublanc, D., Parisot, J. P., Brillet, J., Gautier, D., Raulin, F., McKay, C. P., 1995. Photochemical modeling of titan's atmosphere. Icarus 113 (1), 2. 6, 64

Trafton, L., 1972a. Bulk composition of Titan's atmosphere. Astrophysical Journal 175 (1), 295–&. 4

Trafton, L., 1972b. Possible detection of H2 in Titan's atmosphere. Astrophysical Journal 175 (1), 285–&. 4

Turner, D. W., 1970. Molecular phoroelectron spectroscopy, a handbook of the 584 Åspectra. Wiley. 91

Twomey, S., 1996. Introduction to the Mathematics of Inversion in Remote Sensing and Indirect Measurements. DOVERM Publications, 0-486-69451-8. 60

Vervack, J. R. J., Sandel, B. R., Strobel, D. F., 2004. New perspectives on titan's upper atmosphere from a reanalysis of the voyager 1 uvs solar occultations. ICARUS 170 (1), 91 – 112. 6, 8, 10, 33, 39, 41, 56, 106

Veverka, J., 1973. Titan- polarimetric evidence for an optically thick atmosphere?. Icarus 18 (4), 657 – 660. 4

Vinatier, S., Bézard, B., Nixon, C. A., Mamoutkine, A., Carlson, R. C., Jennings, D. E., Guandique, E. A., Teanby, N. A., Bjoraker, G. L., Flasar, F. M., Kunde, V. G., 2010. Analysis of Cassini/CIRS limb spectra of titan acquired during the nominal mission. i. hydrocarbons, nitriles and co2 vertical mixing ratio profiles. Icarus 205, 559 – 570. 7, 8, 11, 77

Vinatier, S., Bózard, B., Fouchet, T., Teanby, N. A., de Kok, R., Irwin, P. G., Conrath, B. J., Nixon, C. A., Romani, P. N., Flasar, F. M., Coustenis, A., 2007. Vertical abundance profiles of hydrocarbons in titan's atmosphere at 15° s and 80° n retrieved from Cassini/CIRS spectra. Icarus 188, 120 – 138. 7, 8, 29, 77

Vuitton, V., Doussin, J.-F., Bénilan, Y., Raulin, F., Gazeau, M.-C., 2006. Experimental and theoretical study of hydrocarbon photochemistry applied to titan stratosphere (english). Icarus (New York, NY) 185 (1), 287 – 300. 77

Vuitton, V., Lavvas, P., Yelle, R., Galand, M., Wellbrock, A., Lewis, G., Coates, A., Wahlund, J.-E., 2009. Negative ion chemistry in titan's upper atmosphere. Planetary & Space Science 57 (13), 1558 – 1572. 9

Vuitton, V., Yelle, R. V., Cui, J., 2008. Formation and distribution of benzene on titan. Journal of Geophysical Research 113 (E5), @CitationE05007. 7, 77, 78, 102, 103, 119

Vuitton, V., YELLE, R. V., McEwan, M. J., 2007. Ion chemistry and n-containing molecules in titan's upper atmosphere (english). Icarus (New York, NY) 191 (2), 722 – 742. 7, 77, 78

Waite, J.H., J., Lewis, W., Kasprzak, W., Anicich, V., Block, B., Cravens, T., Fletcher, G., Ip, W.-H., Luhmann, J., Mcnutt, R., Niemann, H., Parejko, J., Richards, J., Thorpe, R., Walter, E., Yelle, R., 2004. The Cassini ion and neutral mass spectrometer (INMS) investigation. Space Science Reviews 114 (1-4), 113–231.
URL http://dx.doi.org/10.1007/s11214-004-1408-2 15

Waite, J.H., J., Niemann, H., Yelle, R., Kasprzak, W., Cravens, T., Luhmann, J., McNutt, R., Wing-Huen, I., Gell, D., De La Haye, V., Muller-Wordag, I., Magee, B., Borggren, N., Ledvina, S., Fletcher, G., Walter, E., Miller, R., Scherer, S., Thorpe, R., Jing, X., Block, B., Arnett, K., 2005. Ion neutral mass spectrometer results from the first flyby of titan. Science 308 (5724), 982 – 986. 62, 77

Waite, J. H., Young, D. T., Cravens, T. E., Coates, A. J., Crary, F. J., Magee, B., Westlake, J., 2007. The process of tholin formation in titan's upper atmosphere. Science (5826), 870. ix, 9, 77

West, R. A., Balloch, J., Dumont, P., Lavvas, P., Lorenz, R., Rannou, P., Ray, T., Turtle, E. P., 2011. The evolution of titan's detached haze layer near equinox in 2009. Geophysical Research Letters 38 (6), n/a. 33

West, R. A., Lane, A. L., Hart, H., Simmons, K. E., Hord, C. W., Coffeen, D. L., Esposito, L. W., Sato, M., Pomphrey, R. B., 1983. Voyager 2 photopolarimeter observations of titan. Journal of Geophysical Research. Space Physics 88 (A11), 8699. 10

West, R. A., Smith, P. H., 1991. Evidence for aggregate particles in the atmospheres of titan and jupiter. Icarus (New York, NY) 90 (2), 330 – 333.
URL http://search.ebscohost.com.biblioplanets.gate.inist.fr/login.aspx?direct=true&db=pcl&AN=19786260&lang=fr&site=eds-live 6

Westlake, J. H., Bell, J. M., Waite, J. H., Johnson, R. E., Luhmann, J. G., Mandt, K. E., Magee, B. A., Rymer, A. M., 2011. Titan's thermospheric response to various plasma environments. Journal of Geophysical Research. Space Physics 116 (A3), n/a. 7, 13, 23, 29, 31, 62, 63, 107, 108, 111, 112, 113, 126

Whetten, R., Ke-Jian, F., Grant, E., 1983. Ultraviolet two-photon spectroscopy of benzene: a new gerade rydberg series and evidence for the 11e2g valence state. Journal of Chemical Physics 79 (6), 2626 – 2640. 91

Wilkinson, P. G., 1956. Absorption spectra of benzene and benzene-d6in the vacuum ultraviolet. Canadian Journal of Physics 34 (6), 596. 79, 91

Wilson, E., Atreya, S., 2003. Chemical sources of haze formation in titan's atmosphere. Planetary & Space Science 51 (14/15), 1017. 6, 9, 76, 77

Wilson, E. H., Atreya, S. K., Coustenis, A., 2003. Mechanisms for the formation of benzene in the atmosphere of titan (english). Journal of geophysical research 108 (E2), 8.1 – 8.10. 6, 76, 77, 78, 102

Wilson, E. H. b. a., Atreya, S. K., 2004. Current state of modeling the photochemistry of titan's mutually dependent atmosphere and ionosphere (english). Journal of geophysical research 109 (E6), E06002.1 – E06002.39. 76, 77

Wu, C., Chen, F., Judge, D., 2001. Measurements of temperature-dependent absorption cross sections of C2H2 in the VUV/UV region. Journal of Geophysical research. Planets 106 (E4), 7629 – 7636. 28, 36, 64

Wu, C. Y. R., Chen, F. Z., Judge, D. L., 2004. Temperature-dependent photoabsorption cross sections in the VUV-UV region: Ethylene. J. Geophys. Res. 109 (E07S15), doi:10.1029/2003JE002180. 28, 36, 64, 158

Yelle, R., 1991. Non-lte models of titan's upper atmosphere. Astrophysical Journal 383 (1), 380 – 400. 63

Yelle, R. V., Cui, J., Mueller-Wodarg, I. C. F., 2008. Methane escape from titan's atmosphere (english). Journal of geophysical research 113 (E10).
URL http://search.ebscohost.com.biblioplanets.gate.inist.fr/login.aspx?direct=true&db=pcl&AN=20869388&lang=fr&site=eds-live 8

Yelle, R. V., Strobell, D. F., Lellouch, E., Gautier, D., 1997. Engineering models for Titan's atmosphere. In: Wilson, A. (Ed.), Huygens: Science, Payload and Mission, Proceedings of an ESA conference. pp. 243 – 256, eSA SP-1177. 39

Yoshino, K., Esmond, J., Cheung, A.-C., Freeman, D., Parkinson, W., 1992. High resolution absorption cross sections in the transmission window region of the schumann-runge bands and herzberg continuum of o2. Planetary and Space Science 40 (2), 185 – 192. 85

Yoshino, K., Esmond, J., Parkinson, W., Ito, K., Matsui, T., 1996. Absorption cross section measurements of water vapor in the wavelength region 120 to 188 nm. Chemical Physics 211 (1), 387 – 391. 64

Yu-Jong, W., Hsiao-Chi, L., Hong-Kai, C., Bing-Ming, C., Yuan-Pern, L., Lee, L. C., 2007. Photoabsorption cross sections of nh3, nh2d, nhd2, and nd3 in the spectral range 110 - 144 nm. Journal of Chemical Physics 127 (15), 154311. 64

Yung, Y., Allen, M., Pinto, J., 1984. Photochemistry of the atmosphere of titan: Comparison between model and observations. Astrophysical Journal Supplement Series 55 (3), 465 – 506. 5, 39

Index